JAERI-M
93-032

ASSESSMENT OF TRAC−PF1/MOD1 CODE FOR CORE THERMAL HYDRAULIC BEHAVIOR DURING REFLOOD WITH CCTF AND SCTF DATA

March 1993

Hajime AKIMOTO, Akira OHNUKI, Michitaka KIKUTA*
and Yoshio MURAO

日本原子力研究所
Japan Atomic Energy Research Institute

JAERI-Mレポートは，日本原子力研究所が不定期に公刊している研究報告書です。
入手の問合わせは，日本原子力研究所技術情報部情報資料課（〒319-11茨城県那珂郡東海村）あて，お申しこしください。なお，このほかに財団法人原子力弘済会資料センター（〒319-11茨城県那珂郡東海村日本原子力研究所内）で複写による実費頒布をおこなっております。

JAERI-M reports are issued irregularly.
Inquiries about availability of the reports should be addressed to Information Division, Department of Technical Information, Japan Atomic Energy Research Institute, Tokai-mura, Naka-gun, Ibaraki-ken 319-11, Japan.

© Japan Atomic Energy Research Institute, 1993

編集兼発行　日本原子力研究所
印　　刷　㈱原子力資料サービス

Assessment of TRAC-PF1/MOD1 Code for Core Thermal Hydraulic Behavior during Reflood with CCTF and SCTF Data

Hajime AKIMOTO, Akira OHNUKI, Michitaka KIKUTA*
and Yoshio MURAO

Department of Reactor Engineering
Tokai Research Establishment
Japan Atomic Energy Research Institute
Tokai-mura, Naka-gun, Ibaraki-ken

(Received January 29, 1993)

Post test calculations for six selected CCTF and SCTF tests were performed to assess the TRAC-PF1 code for core thermal hydraulic behaviors during the reflood in a PWR LOCA. It was found through comparisons of calculated results with measured results that predicted void fraction and core mass with the TRAC-PF1 code showed poor agreement with measured results in quantity and that the TRAC-PF1 code predicted well turnaround time, turnaround temperature and quench time in clad temperature transient including parameter effect of system pressure and core power level. In the calculation for the CCTF best-estimate test, which was performed with low initial clad temperature, the TRAC-PF1 code predicted higher core cooling rate and faster quench propagation than measured results. A study on the interfacial friction model and wall heat transfer model was performed to identify problem areas of the TRAC-PF1 code. It is recommended to improve following models of the TRAC-PF1 code for more realistic prediction of core thermal hydraulic behaviors during the reflood in a PWR LOCA;

(1) Interfacial friction model in the bubbly/slug flow regime,
(2) Interfacial friction model in the vicinity of the flow transition point from the churn flow to the annular/dispersed flow,

---

* Mitsubishi Atomic Power Industry

(3) Wall heat transfer model in the film boiling regime, and

(4) Wall heat transfer model on the criteria for the boiling transition from the film boiling to the transition boiling at low initial clad temperature.

Keywords: Reactor Safety, Heat Transfer, Two-phase Flow, Reflood, Film Boiling, Numerical Simulation, TRAC code

円筒炉心試験および平板炉心試験データによる再冠水時炉心内熱水力挙動に対するTRAC－PF1／MOD1コードの予測性能評価

日本原子力研究所東海研究所原子炉工学部
秋本　肇・大貫　晃・菊田　充孝*・村尾　良夫

（1993年1月29日受理）

加圧水型原子炉冷却材喪失事故再冠水時の炉心内熱水力挙動に対するTRAC－PF1コードの予測性能を評価するために，円筒炉心試験と平板炉心試験から選んだ6試験に対する試験後解析を行った。計算結果と測定結果を比較した結果から，TRAC－PF1コードにより予測されるボイド率及び炉心蓄水量と測定結果との量的な一致は悪いこと，並びに，被覆管温度履歴におけるターンアラウンド時間・ターンアラウンド温度及びクエンチ時間はTRAC－PF1コードにより良好に予測されていることがわかった。低初期被覆管温度で実施された円筒炉心最適評価試験に対する計算では，TRAC－PF1コードは測定結果と比べて大きな炉心冷却速度とクエンチ伝播速度を予測した。TRAC－PF1コードの問題点を明確にするために，界面剪断応力モデルと壁面熱伝達モデルについて検討した。再冠水時の炉心熱水力挙動についてより精度よく予測するために，TRAC－PF1コードの以下のモデルを改良することを推奨する。

(1) 気泡流／スラグ流領域の界面剪断応力モデル，
(2) チャーン流から環状噴霧流への流動遷移点における界面剪断応力モデル，
(3) 膜沸騰領域の壁面熱伝達モデル，
(4) 低初期被覆管温度である時の，膜沸騰領域から遷移沸騰領域への沸騰遷移条件に関する壁面熱伝達モデル

東海研究所：〒319-11　茨城県那珂郡東海村白方字白根2－4
＊　三菱原子力工業

Contents

1. Introduction 1
2. Test Description 4
2.1 Cylindrical Core Test Facility 4
2.2 Slab Core Test Facility 5
3. Code and Model Description 13
3.1 TRAC Input for CCTF Calculation 13
3.2 TRAC Input for SCTF Calculation 13
3.3 Test Conditions 14
4. Results and Discussion 20
4.1 Assessment for CCTF Base Case Test 20
4.2 Assessment for CCTF Pressure Effect Tests 42
4.3 Assessment for CCTF Power Level Effect Tests 54
4.4 Assessment for CCTF Best Estimate Test 66
4.5 Assessment for SCTF Flat Power Test 75
4.6 Run Statistics 81
5. Conclusions and Recommendations 82
Acknowledgments 82
References 83
Appendix A Outline of Interfacial Friction Model and Wall Heat Transfer Model of TRAC-PF1 Code 85
Appendix B Selected Results 94
(1) CCTF Base Case Test (Run 62) 94
(2) CCTF High Pressure Test (Run 55) 111
(3) CCTF Low Pressure Test (Run 67) 128
(4) CCTF Low Power Test (Run 63) 145
(5) CCTF Best Estimate Test (Run 71) 162
(6) SCTF Flat Power Test (Run 619) 174

目　　次

1. 緒　　言 …… 1
2. 試験装置 …… 4
2.1 円筒炉心試験装置 …… 4
2.2 平板炉心試験装置 …… 5
3. 計算コードと入力モデル …… 13
3.1 ＣＣＴＦ計算のためのＴＲＡＣ入力モデル …… 13
3.2 ＳＣＴＦ計算のためのＴＲＡＣ入力モデル …… 13
3.3 試験条件 …… 14
4. 結果と考察 …… 20
4.1 ＣＣＴＦ基準試験による性能評価 …… 20
4.2 ＣＣＴＦ圧力効果試験による性能評価 …… 42
4.3 ＣＣＴＦ出力効果試験による性能評価 …… 54
4.4 ＣＣＴＦ最適評価試験による性能評価 …… 66
4.5 ＳＣＴＦ平坦出力試験による性能評価 …… 75
4.6 計算時間 …… 81
5. 結論と今後の課題 …… 82
謝　　辞 …… 82
参考文献 …… 83
付録Ａ　ＴＲＡＣ－ＰＦ１コードの界面剪断応力モデルと壁面熱伝達モデルの概要 …… 85
付録Ｂ　主要な比較結果 …… 94
(1) ＣＣＴＦ基準試験　(Run 62) …… 94
(2) ＣＣＴＦ高圧力試験　(Run 55) …… 111
(3) ＣＣＴＦ低圧力試験　(Run 67) …… 128
(4) ＣＣＴＦ低出力試験　(Run 63) …… 145
(5) ＣＣＴＦ最適評価試験　(Run 71) …… 162
(6) ＳＣＴＦ平坦出力試験　(Run 619) …… 174

List of tables

Table 1.1.1 ICAP assessment matrix in Japan
Table 3.3.1 Major test conditions
Table 4.6.1 Run statistics

List of figures

Fig. 2.1.1 Schematics of Cylindrical Core Test Facility (CCTF)
Fig. 2.1.2 Vertical cross section of pressure vessel of CCTF
Fig. 2.1.3 Horizontal cross section of pressure vessel of CCTF
Fig. 2.1.4 Heater rods of CCTF

Fig. 2.2.1 Schematics of Slab Core Test Facility (SCTF)
Fig. 2.2.2 Vertical cross section of pressure vessel of SCTF
Fig. 2.2.3 Heater rods on SCTF

Fig. 3.1.1 TRAC noding schematics of CCTF-II calculation
Fig. 3.1.2 Axial power profile of CCTF-II calculation

Fig. 3.2.1 TRAC noding schematics of SCTF-II calculation
Fig. 3.2.2 Axial power profile of SCTF-II calculation

Fig. 4.1.1 Overall mass balance at core in CCTF base case test
Fig. 4.1.2 Core void fractions in CCTF base case test
Fig. 4.1.3 Calculated core void fractions in CCTF base case test
Fig. 4.1.4 Water and steam mass flow rates at core outlet in CCTF base case test
Fig. 4.1.5 Calculated steam and water mass flow rates and void fraction at core outlet in CCTF base case test
Fig. 4.1.6 Clad temperature along a high power rod in CCTF base case test
Fig. 4.1.7 Turnaround temperature and turnaround time along a high power rod in CCTF base case test

Fig. 4.1 8 Quench envelope along a high power rod in CCTF base case test
Fig. 4.1.9 Clad temperature and heat transfer coefficient at elevation of 1.83 m along a high power rod in CCTF base case test
Fig. 4.1.10 Calculated heat transfer at elevation of 1.83 m along a high power rod in CCTF base case test
Fig. 4.1.11 Effect of flow quality on void fraction at steady state with TRAC interfacial friction model
Fig. 4.1.12 Interfacial friction, wall friction and gravity forces in TRAC model
Fig. 4.1.13 Core void fraction
Fig. 4.1.14 Effect of total mass flow rate on void fraction at steady state with TRAC interfacial friction model
Fig. 4.1.15 Comparison of wall heat transfer coefficient between measured and calculated results

Fig. 4.2.1 Comparison of core outlet pressure between low and high pressure tests
Fig. 4.2.2 Comparison of core power between low and high pressure tests
Fig. 4.2.3 Comparison of core inlet mass flow rate between low and high pressure tests
Fig. 4.2.4 Comparison of core inlet mass flow between low and high pressure tests
Fig. 4.2.5 Comparison of core inlet fluid temperature between low and high pressure tests
Fig. 4.2.6 Comparison of core inlet subcooling between low and high pressure tests
Fig. 4.2.7 Effect of system pressure on core inlet mass flow
Fig. 4.2.8 Effect of system pressure on core mass
Fig. 4.2.9 Effect of system pressure on steam mass flow at core outlet
Fig. 4.2.10 Effect of system pressure on water mass flow rate at core outlet
Fig. 4.2.11 Effect of system pressure on void fractions in core
Fig. 4.2.12 Effect of system pressure on clad temperature at elevation of 1.83 m along a high power rod

Fig. 4.2.13 Effect of system pressure on heat transfer coefficient at elevation of 1.83 m along a high power rod
Fig. 4.2.14 Effect of system pressure on quench front propagation along a high power rod

Fig. 4.3.1 Comparison of core power between low and high power tests
Fig. 4.3.2 Comparison of core outlet pressure between low and high power tests
Fig. 4.3.3 Comparison of core inlet mass flow rate between low and high power tests
Fig. 4.3.4 Comparison of core inlet mass flow between low and high power tests
Fig. 4.3.5 Comparison of core inlet fluid temperature between low and high power tests
Fig. 4.3.6 Comparison of core inlet subcooling between low and high power tests
Fig. 4.3.7 Effect of power level on core inlet mass flow
Fig. 4.3.8 Effect of power level on core mass
Fig. 4.3.9 Effect of power level on steam mass flow at core outlet
Fig. 4.3.10 Effect of power level on water mass flow at core outlet
Fig. 4.3.11 Effect of power level on void fractions in core
Fig. 4.3.12 Effect of power level on clad temperature at elevation of 1.83 m along a high power rod
Fig. 4.3.13 Effect of power level on heat transfer coefficient at elevation of 1.83 m along a high power rod
Fig. 4.3.14 Effect of power level on quench front propagation along a high power rod

Fig. 4.4.1 Core power in CCTF best estimate test
Fig. 4.4.2 Core outlet pressure in CCTF best estimate test
Fig. 4.4.3 Core inlet mass flow rate in CCTF best estimate test
Fig. 4.4.4 Core inlet fluid temperature in CCTF best estimate test
Fig. 4.4.5 Initial clad temperature in CCTF best estimate test

Fig. 4.4.6 Core mass in CCTF best estimate test
Fig. 4.4.7 Void fractions in core of CCTF best estimate test
Fig. 4.4.8 Clad temperature in CCTF best estimate test
Fig. 4.4.9 Wall heat transfer regime along a heater rod in CCTF best estimate test
Fig. 4.4.10 Boiling curve and quench behavior

Fig. 4.5.1 Core power in SCTF flat power test
Fig. 4.5.2 Core outlet pressure in SCTF flat power test
Fig. 4.5.3 Core inlet mass flow rate in SCTF flat power test
Fig. 4.5.4 Core inlet fluid temperature in SCTF flat power test
Fig. 4.5.5 Void fractions in core of SCTF flat power test
Fig. 4.5.6 Clad temperature at elevation of 1.905 m in SCTF flat power test
Fig. 4.5.7 Heat transfer coefficient at elevation of 1.905 m in SCTF flat power test
Fig. 4.5.8 Quench envelope in SCTF flat power test

1 Introduction

The International Thermal-Hydraulic Code Assessment and Application Program (ICAP) is conducted by several countries and coordinated by the United States Nuclear Regulatory Commission (USNRC).[1] The purpose of ICAP is to make qualitative and quantitative statement regarding the accuracy of the current thermal-hydraulic computer programs developed under the auspices of the USNRC.

Japan's contributions to ICAP include the assessment of TRAC-PWR, TRAC-BWR and RELAP5 codes. The assessment matrix is shown in Table 1.1.1. The assessment calculations are conducted by Japan Atomic Energy Research Institute (JAERI) and industrial groups.

The Large Scale Reflood Test Program is operated at JAERI to demonstrate the effectiveness of emergency core cooling system(ECCS), to verify computer codes, and to collect information to improve thermal hydraulic models in analysis codes during the refill and reflood phases of a loss-of-coolant accident (LOCA) in a pressurized water reactor(PWR).[2] In the program, two major test facilities are used, that is the Cylindrical Core Test Facility (CCTF) and the Slab Core Test Facility (SCTF).

The CCTF is a test facility designed to provide information on the thermal hydraulic behaviors during the refill and reflood phases in a PWR LOCA with integral system simulation. This facility has a full-height core section with about 2,000 electrically heated rods arranged in a cylindrical configuration and has four primary loops with reactor component simulations. The system integral effects and the core cooling characteristics are investigated with the CCTF.

The main objective of the SCTF is to study two-dimensional thermal hydraulic behaviors in the core during the refill and reflood phases in a PWR LOCA. The SCTF has a full-height, full-radius and one-bundle-width core. The core includes about 2,000 electrically heated rods as well as the CCTF.

The PWR version of the Transient Reactor Analysis Code (TRAC) is being developed at Los Alamos National Laboratory (LANL) to provide an advanced best-estimate predictive capability for the analysis of postulated accidents in PWRs.[3] The TRAC code uses the two fluid model of the two phase flow as the basic model for the hydraulic analysis with constitutive relations dependent on the flow pattern of the two phase flow. To get reasonable prediction, it is essential to use physical models consistent with actual

phenomena in such a prediction.

The objectives of this study is to assess the core thermal hydraulic model of the TRAC-PF1 code during the reflood phase in a PWR LOCA with data from CCTF and SCTF tests. In the previous studies at JAERI, the integral predictive capability of the TRAC-PF1 code was assessed in the calculation of the CCTF base case test with the model including the primary loops by Kikuta et al.[4] and the two-dimensional core cooling behavior was assessed with the SCTF data using two dimensional VESSEL model by Ohnuki et al.[5] In this study, a simplified model only the core and part of the upper plenum is used in the calculation to assess the predictive capability of the TRAC-PF1 code for the parameter effect on the core thermal hydraulic behaviors during the reflood phase in a PWR LOCA. To eliminate the errors in the boundary conditions, the measured core inlet mass flow rate and fluid temperature are specified as input data as well as the core power and core outlet pressure.

In this study, version 12.5 of the TRAC-PF1/MOD1 code was used, which was the latest version available on JAERI's FACOM M-780 computer when this assessment study was performed. Several parameter tests of CCTF tests are selected to assess the TRAC code. The base case test,[6] the high and low pressure tests,[7] the low power test[8] and the best-estimate(BE) test[9] are used. To check the effect of the core radial size, the flat radial power test of the SCTF test[10] is also used.

In section 2, the outline of selected CCTF and SCTF tests will be described as well as the configuration of the facility. In section 3, the TRAC input data used in this study will be explained. In section 4, the calculated results will be compared with test results. Finally, the conclusions and recommendation will be summarized in section 5. Comparisons of major data between measured and calculated results are presented in Appendix B for each tests.

Table 1.1.1 ICAP assessment matrix in Japan

	LOCA type	TRAC-P				RELAP5				TRAC-B				
		88	89	90	91	88	89	90	91	88	89	90	91	
CCTF	PWR LB	9	1				5				5			Reflood
SCTF	PWR LB	3	5	3			1				1			Reflood
ROSA-II	PWR LB								2					Blowdown
ROSA-III	BWR LB/SB										1	1		Blowdown
ROSA-IV	PWR SB	1	1(0)			1	0(1)							
TBL	BWR LB/SB										1	1		Blowdown
Total		13	7(6)	3		1	6(7)		2		8	2		42

2 Test Description

2.1 Cylindrical core test facility

Figure 2.1.1 shows the schematics of the CCTF. The facility is designed to simulate a 1100 MWe PWR with integral system simulation. The vertical dimension and the flow path of each system component are scaled to the actual PWRs by factor of 1/1. The flow area of each system component is scaled down in proportion to the core flow area scaling factor of 1/21.4 to simulate the fluid velocity in the component.

The core of the CCTF consists of 32 bundles arranged in cylindrical configuration. Each bundle contains 57 heater rods and 7 non-heated rods. The heater rods are heated electrically. The core power supply to the heater rods can be changed at a programmed rate to simulate the power decay curve in the actual PWRs. The axial power distribution of each heater rod simulate the cosine profile.

The facility is equipped with four primary loops;three intact loops and a broken loop. Each loop has a hot-leg-piping section, an active steam generator, a cross-over-leg section, a pump simulator, an emergency core cooling (ECC) water injection port and a cold-leg-piping section. Each pump simulator is equipped with an orifice plate to simulate the flow resistance of the locked pump in a PWR.

The ECCS of the CCTF consists of the accumulator(Acc) and the low pressure coolant injection(LPCI) systems. Each system is connected to ECC water injection ports located at the lower plenum, the top of the downcomer, the upper plenum and each of four cold-leg-piping sections. The injection location can be switched by flow control valves in ECC water injection lines.

Figure 2.1.2 shows the vertical cross section of the pressure vessel of the CCTF. The height of the pressure vessel is the same as the reference PWR. The flow area is scaled in proportion to the flow area scaling.

Figure 2.1.3 show the cross section of the pressure vessel of the CCTF. The core of the CCTF consists of 32 bundles arranged in cylindrical configuration. Each bundle contains 57 heater rods and 7 non-heated rods. The core is usually subdivided into three regions to achieve a desired radial power distribution. The three region are named high and medium and low power regions, respectively. The local peaking in a bundle is unity, that is, all heater rods in a bundle have the same power density in the CCTF Core-II

facility.

Figure 2.1.4 shows configuration of a heater rod. A heater rod consist of a nichrome heating element, magnesium oxide and boron nitride insulators, and inconel-600 sheath. Boron nitride insulator is used only in the central part of the heated region. The diameter of the heater rod is 10.7 mm and the rod pitch is 14.3 mm, which are identical to the corresponding dimensions of actual PWR fuel rods. The heater rods are heated electrically. The heated length is 3.66 m as in actual PWRs. The cosine profile of the axial power is simulated by varying the helical pitch of the heating element as a 17 steps chopped cosine axial power profile.

2.2 Slab core test facility

Figure 2.2.1 shows schematics of the SCTF. The primary coolant loops consists of a hot leg equivalent to four hot legs, a steam-water separator corresponding to steam generator inlet plenum, an intact cold leg equivalent to three intact cold legs, a broken cold leg of pressure vessel side and a broken cold leg of steam-water separator side. These two broken cold legs are connected to two containment tanks of which pressure is controlled by exhausting steam to the atmosphere. The flow area scaling of primary loops is 1/21.4 to a 1100 MWe PWR.

The SCTF has a full-height, full-radius and one-bundle-width core in the pressure vessel. Figure 2.2.2 shows the vertical cross section of the pressure vessel of the SCTF. The pressure vessel includes a simulated core, an upper plenum, a lower plenum, a core baffle and a downcomer. The simulated core consists of eight bundles arranged in a row, simulating a radial slab extracted from a PWR core with full height, full radius and one bundle width. In Fig. 2.2.2, Bundle 1 correspond to the central bundle and Bundle 8 to the peripheral bundle in an actual PWR core, respectively. Each bundle consists of 234 heater rods and 22 non-heated rods arranged in 16 x 16 array. Figure 2.2.3 shows configuration of heater rods of the SCTF. The pitch, the outer diameter and the heated length of heater rods are 14.4 mm, 10.7 mm and 3.66 m, respectively. These dimensions are identical to those of 15 x 15 type fuel assembly in a Westinghouse PWR. Each heater rod has a seventeen step chopped cosine axial power profile with a peaking factor of 1.40. The core and upper plenum are enveloped by honeycomb thermal insulators to minimize the wall thermal effect.

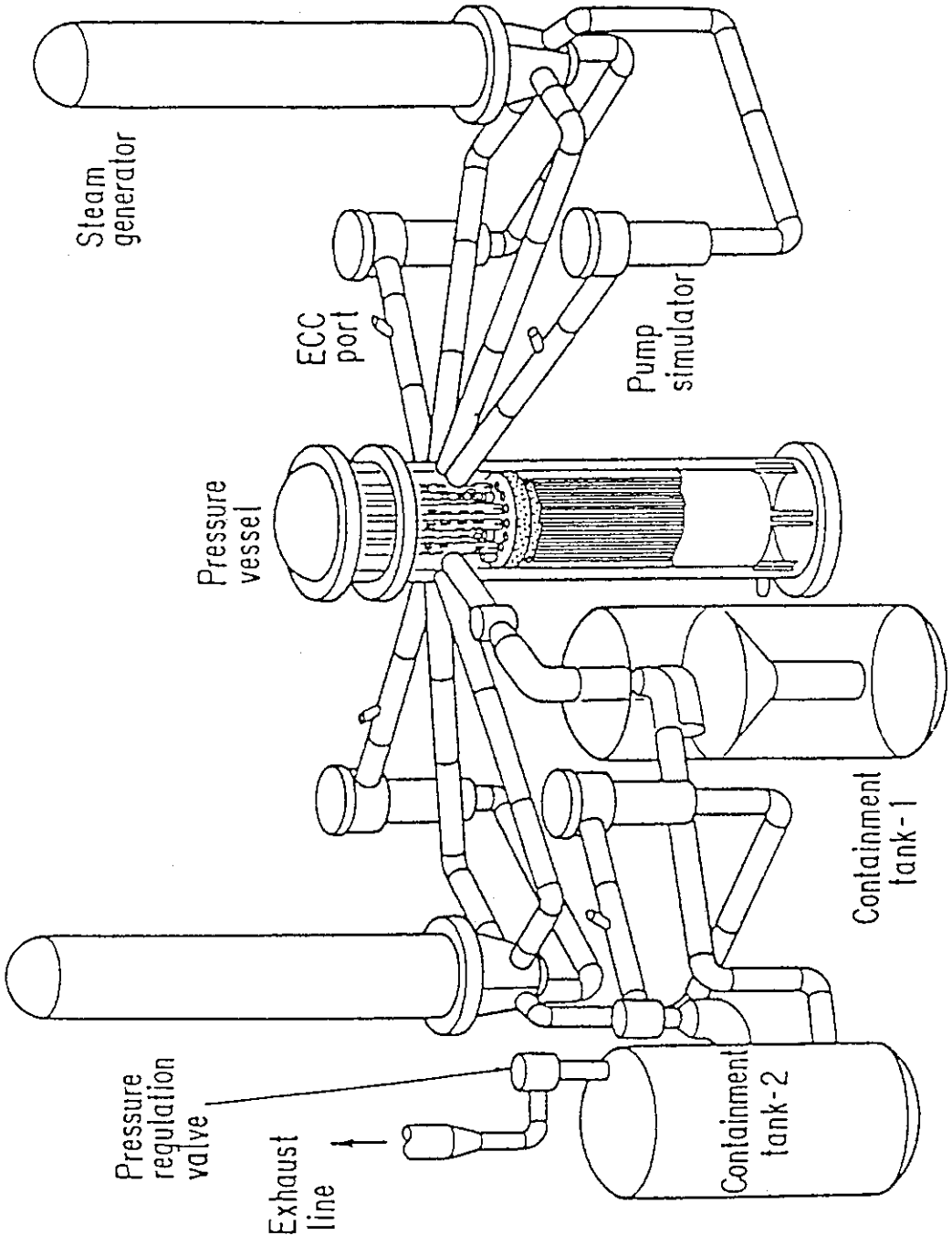

Fig. 2.1.1 Schematics of Cylindrical Core Test Facility (CCTF)

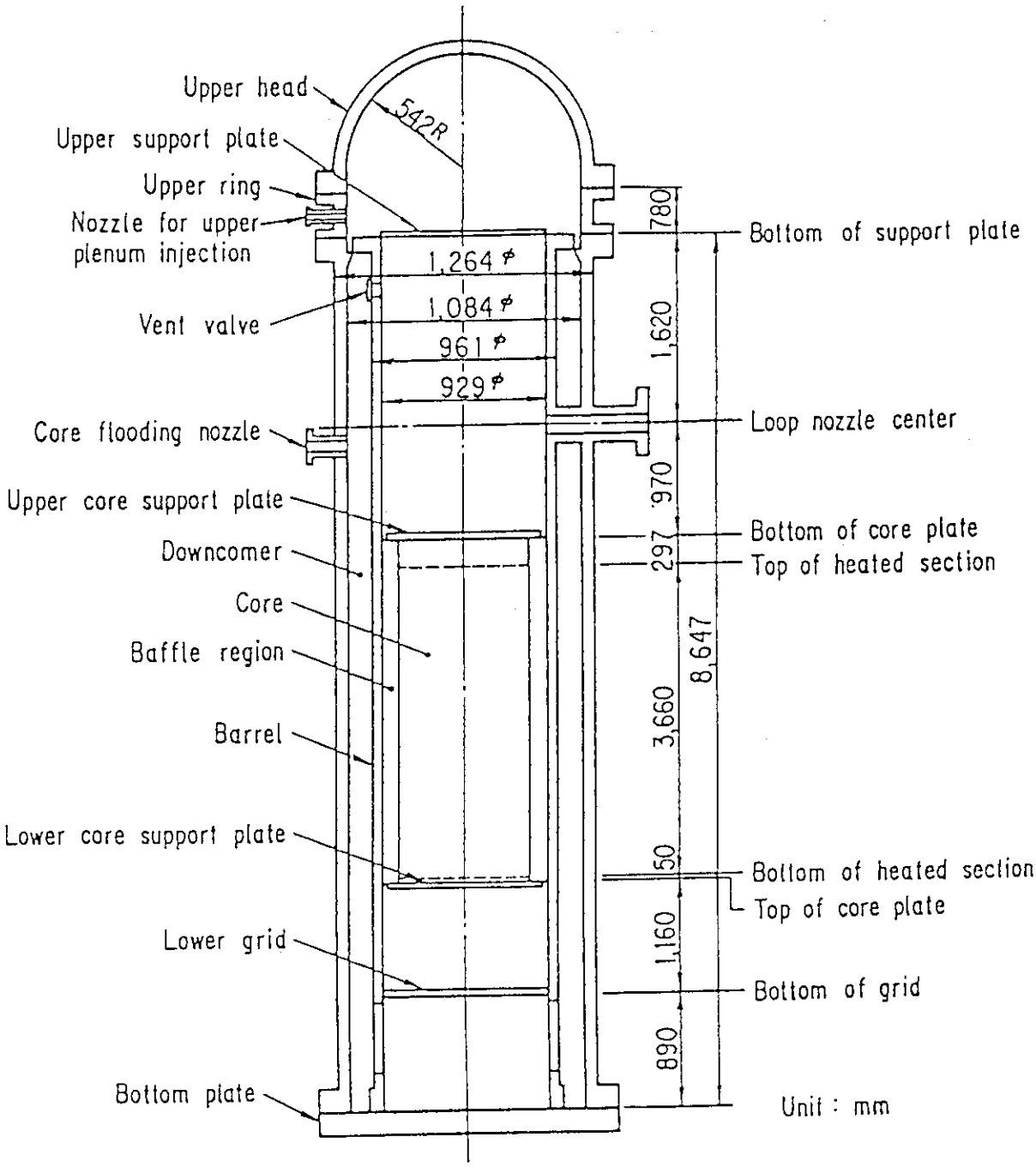

Fig. 2.1.2 Vertical cross section of pressure vessel of CCTF

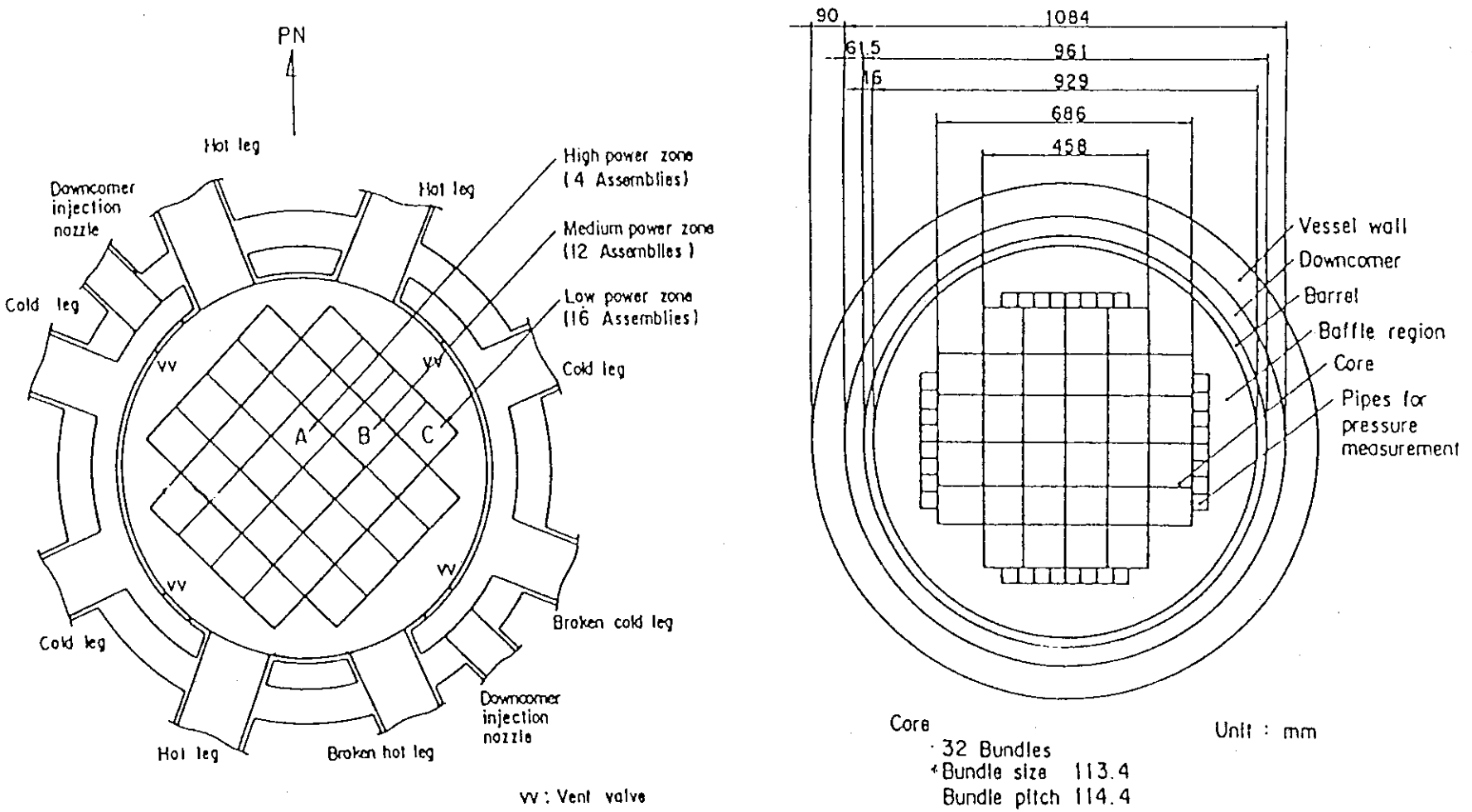

Fig. 2.1.3 Horizontal cross section of pressure vessel of CCTF

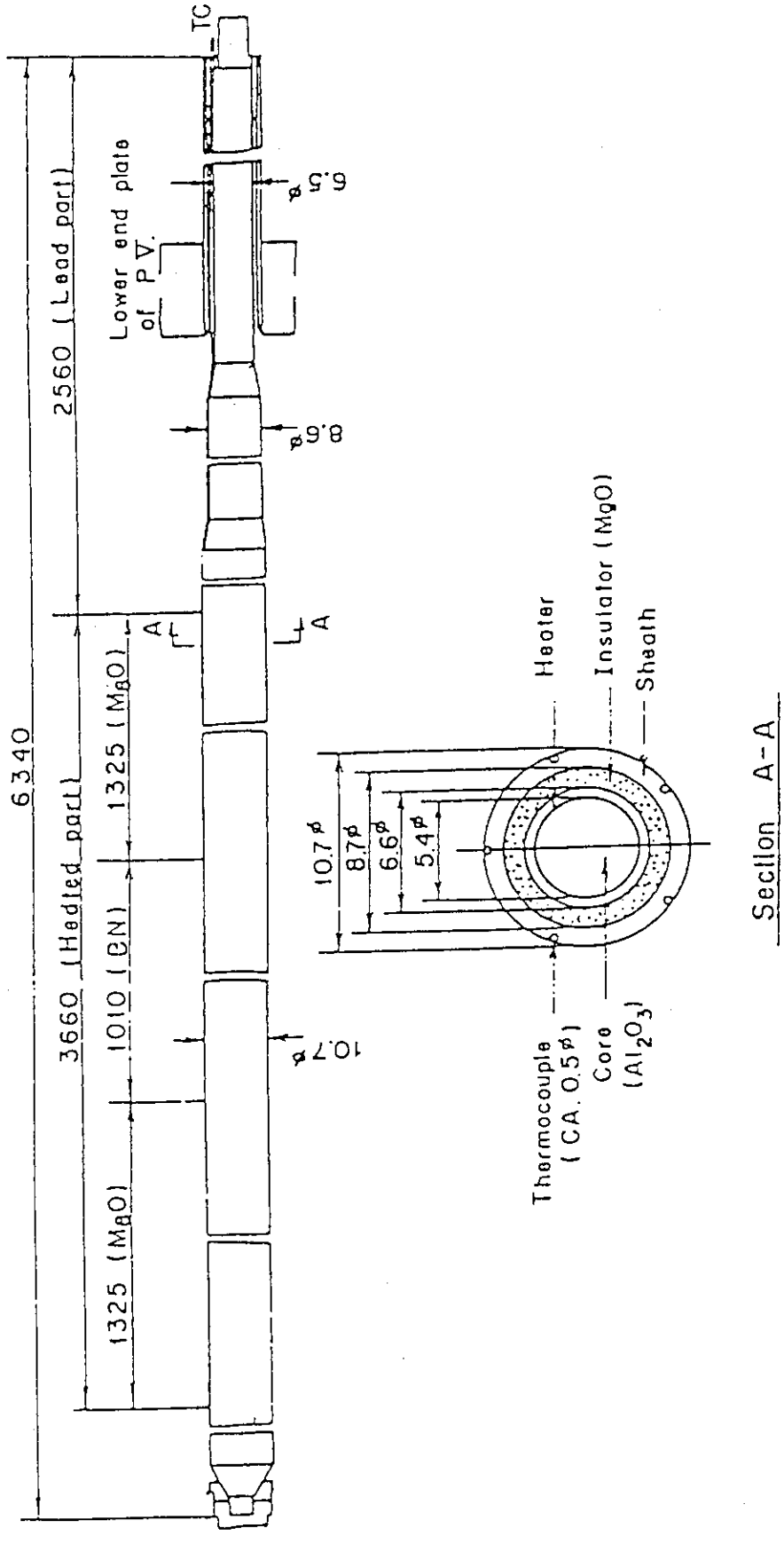

Fig. 2.1.4 Heater rods of CCTF

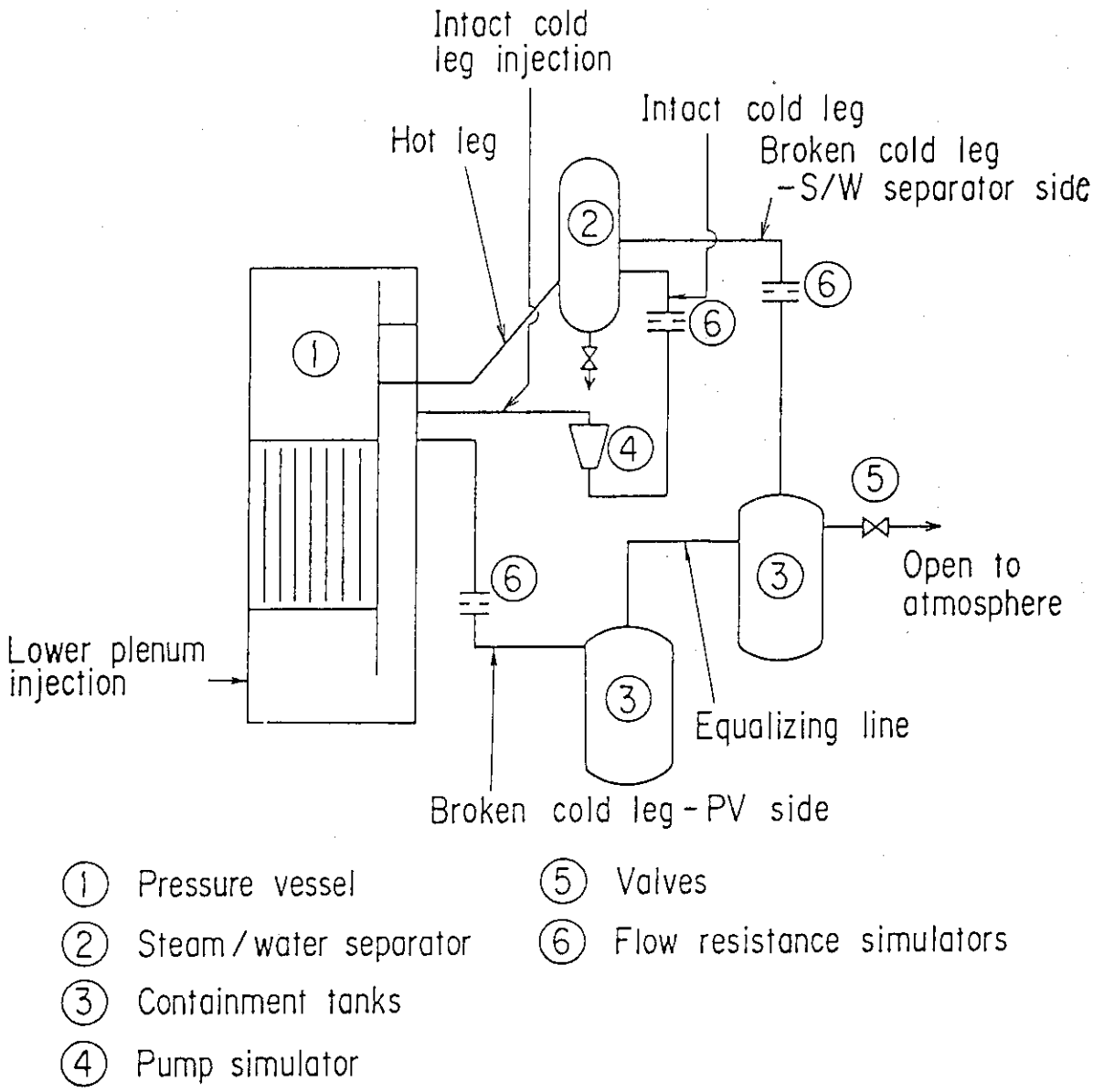

Fig. 2.2.1 Schematics of Slab Core Test Facility (SCTF)

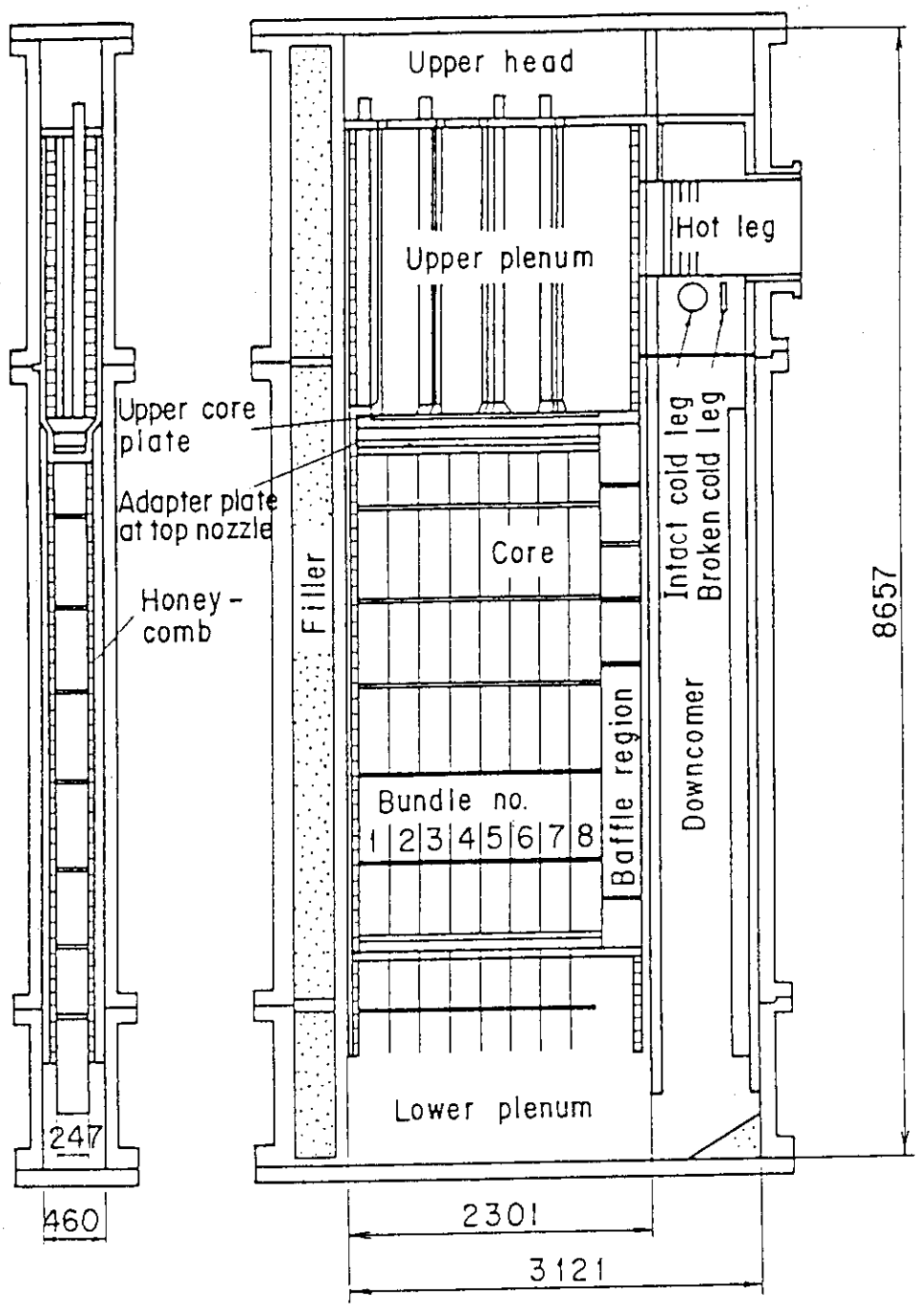

Fig. 2.2.2 Vertical cross section of pressure vessel of SCTF

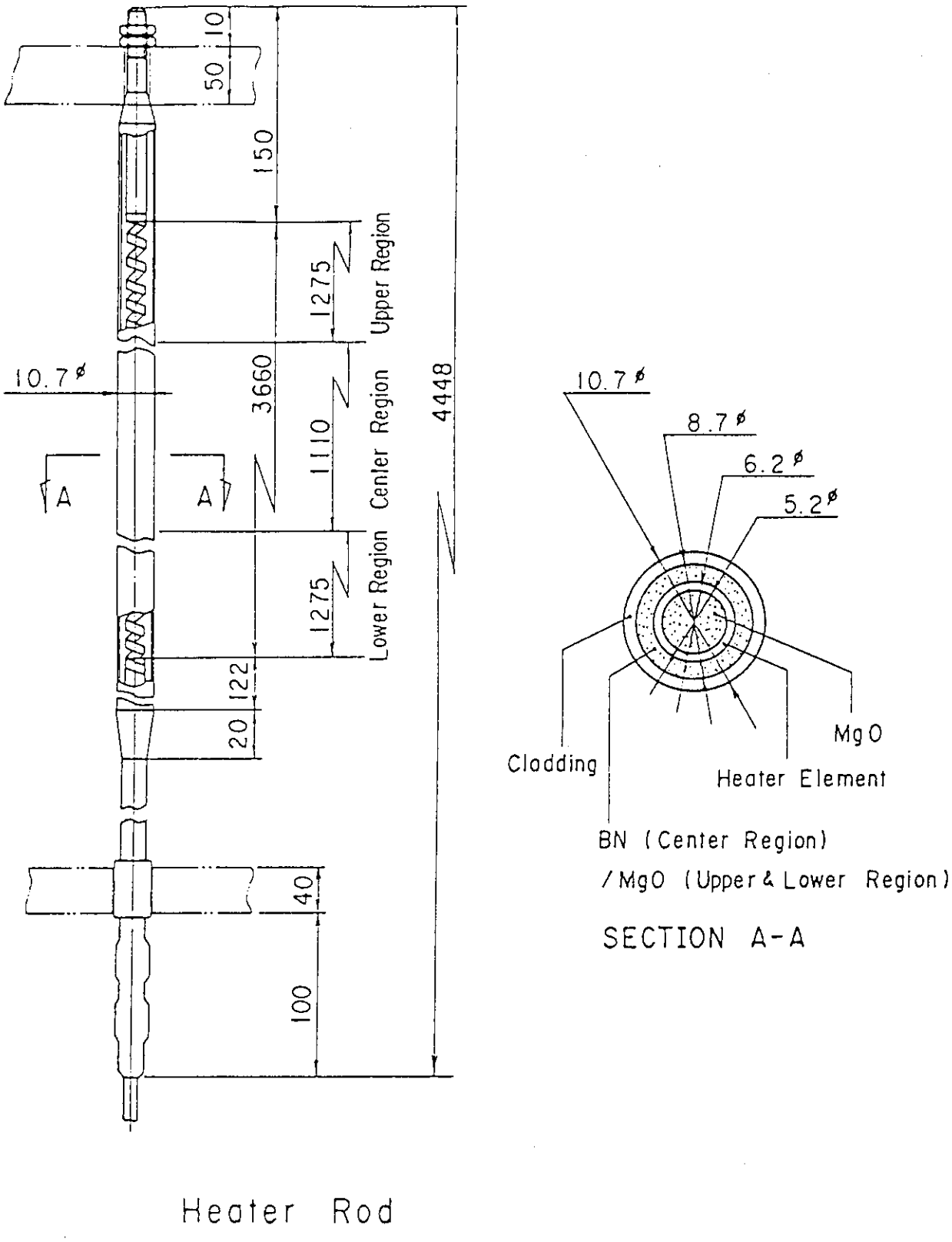

Fig. 2.2.3 Heater rods on SCTF

3 Code and Model Description

3.1 TRAC input for CCTF calculation

Figure 3.1.1 shows TRAC input schematics for the CCTF calculations. Only the core and part of the upper plenum of the CCTF is modeled using the VESSEL component of the TRAC-PF1 code. In the model, the core part corresponds to levels between second and eighth. As boundary conditions, measured core inlet mass flow rate and fluid temperature are input using a FILL component and measured core outlet pressure is input using a BREAK component of the TRAC-PF1 code. The core power supplied to the heater rods is also input using the measured results.

Figure 3.1.2 shows axial power profile of heater rod for the CCTF. Although 17-step chopped cosine power profile is used in the CCTF tests, the power profile is approximated by the linear curves in the TRAC calculation, as shown in Fig. 3.1.2. The approximated profile shows excellent agreement with those of the CCTF. In the CCTF, the radial power profile is not uniform, as described in section 2.1. However, the core part is modeled by single cell per level because the fluid mixing in the radial direction is rapid enough to be treated by the one-dimensional model[(11),(12)] and the TRAC-PF1 code showed no significant dependency on the number of fluid cells per level in the preliminary calculation for a CCTF test. The power and initial temperature for heater rods in high and low power regions were set identical to measured using the additive heater rod capability of the TRAC-PF1 code.

3.2 TRAC input for SCTF calculation

Figure 3.2.1 shows TRAC input schematics of SCTF calculation. As in the CCTF calculations, only the core and part of the upper plenum are modeled with a VESSEL component. The core inlet mass flow rate and fluid temperature are specified with a FILL component of the TRAC-PF1 code using measured results. The core outlet pressure is input with a BREAK component of the TRAC-PF1 code. The core power is input in terms of time using measured result.

Figure 3.2.2 shows axial power profile in the SCTF. The assumed axial power profile in the TRAC calculation shows excellent agreement with that of the SCTF.

3.3 Test conditions

Table 3.3.1 summarizes major test conditions of selected CCTF tests for the assessment of the TRAC-PF1 code. The base case test (Run 62)[6] is a reference test for parameter effect tests in the CCTF-II test series. Test conditions of the base case test was determined based on the reactor safety assessment calculations of PWRs with so called evaluation model. In these tests, the parameter effect of system pressure and the core power level can be studied. The system pressure in the base case test is 0.20 MPa. In the high and low pressure tests,[7] the system pressures are 0.42 and 0.15 MPa, respectively. The core power in the base case test was determined to simulate the decay curve type of (ANS x 1.2 + actinide x 1.1(30 s after scram)). The core power of the low power test[8] was determined to simulate the decay curve type of (ANS x 1.0 + actinide x 1.1(40 s after scram). On the contrary, test conditions of the best-estimate test[9] was determined based on a TRAC calculation for a PWR by Los Alamos. In the TRAC calculation, good core cooling was predicted in the blowdown and refill periods and resulted in the low clad temperature at reflood initiation. To assess predictive capability of the TRAC-PF1 code under a wide range of test conditions, the assessment calculation for the best-estimate test is also included in this study.

Table 3.3.1 Major test conditions

Test name	Peak clad temperature (K)	System pressure (MPa)	Core power (MW)	Radial peaking factor (-)
CCTF base case test[6]	1073	0.20	9.35	1.37
CCTF high pressure test[7]	1073	0.42	9.35	1.37
CCTF low pressure test[7]	1073	0.15	9.35	1.37
CCTF low power test[8]	1073	0.20	7.12	1.37
CCTF best estimate test[9]	580	0.30	7.12	1.00
SCTF flat power test[10]	922	0.20	7.12	1.00

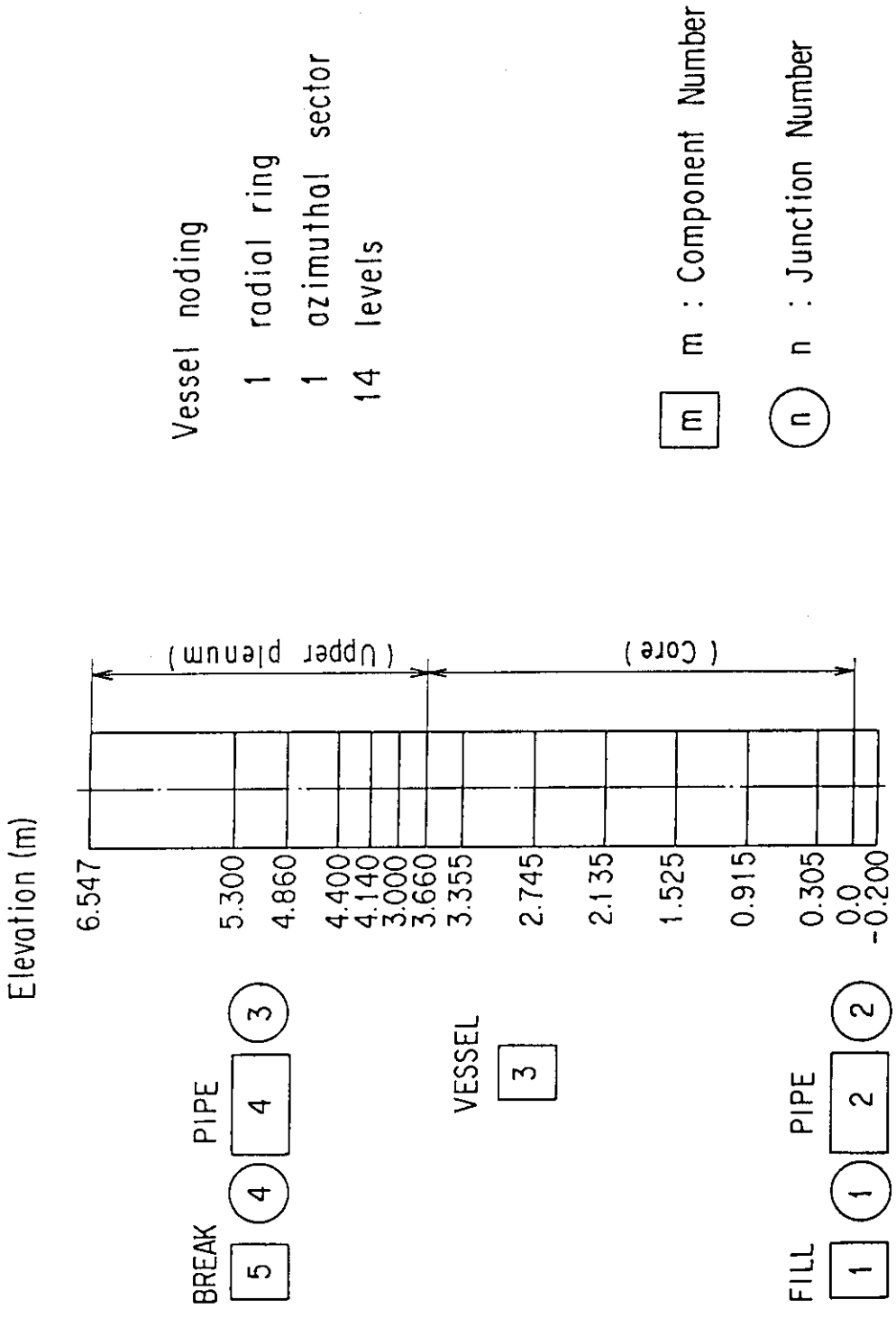

Fig. 3.1.1 TRAC noding schematics of CCTF-II calculation

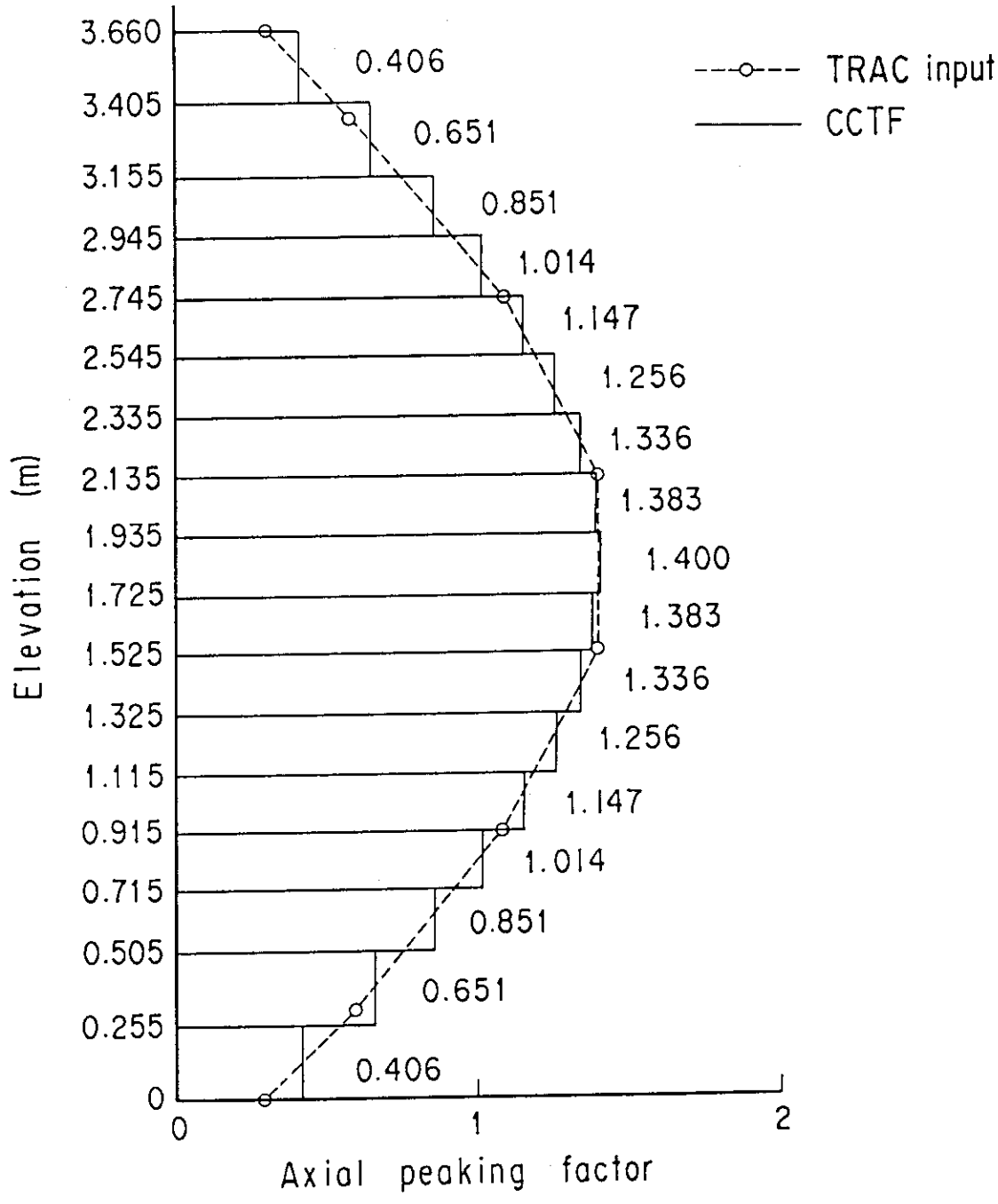

Fig. 3.1.2 Axial power profile of CCTF-II calculation

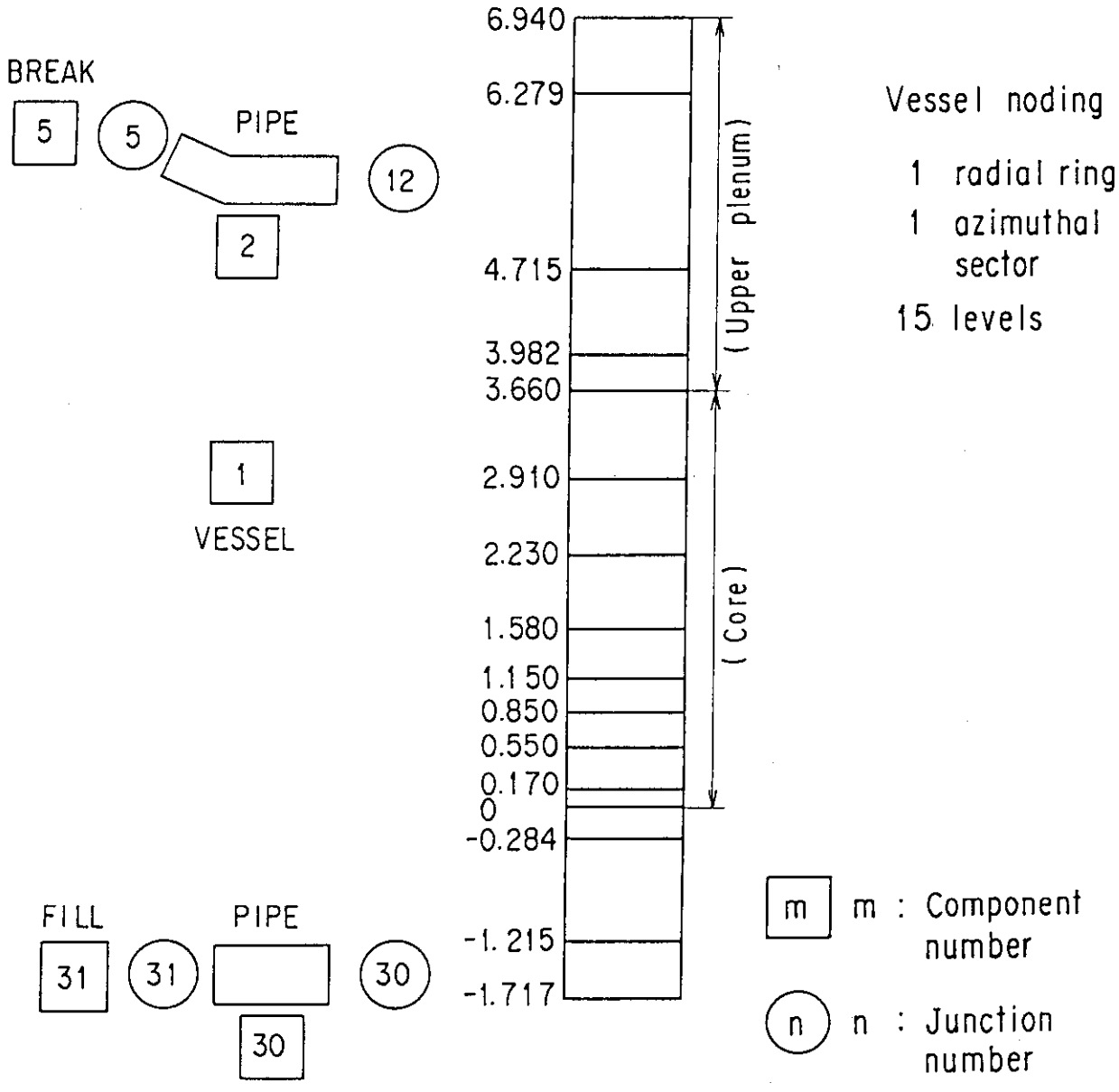

Fig. 3.2.1 TRAC noding schematics of SCTF-II calculation

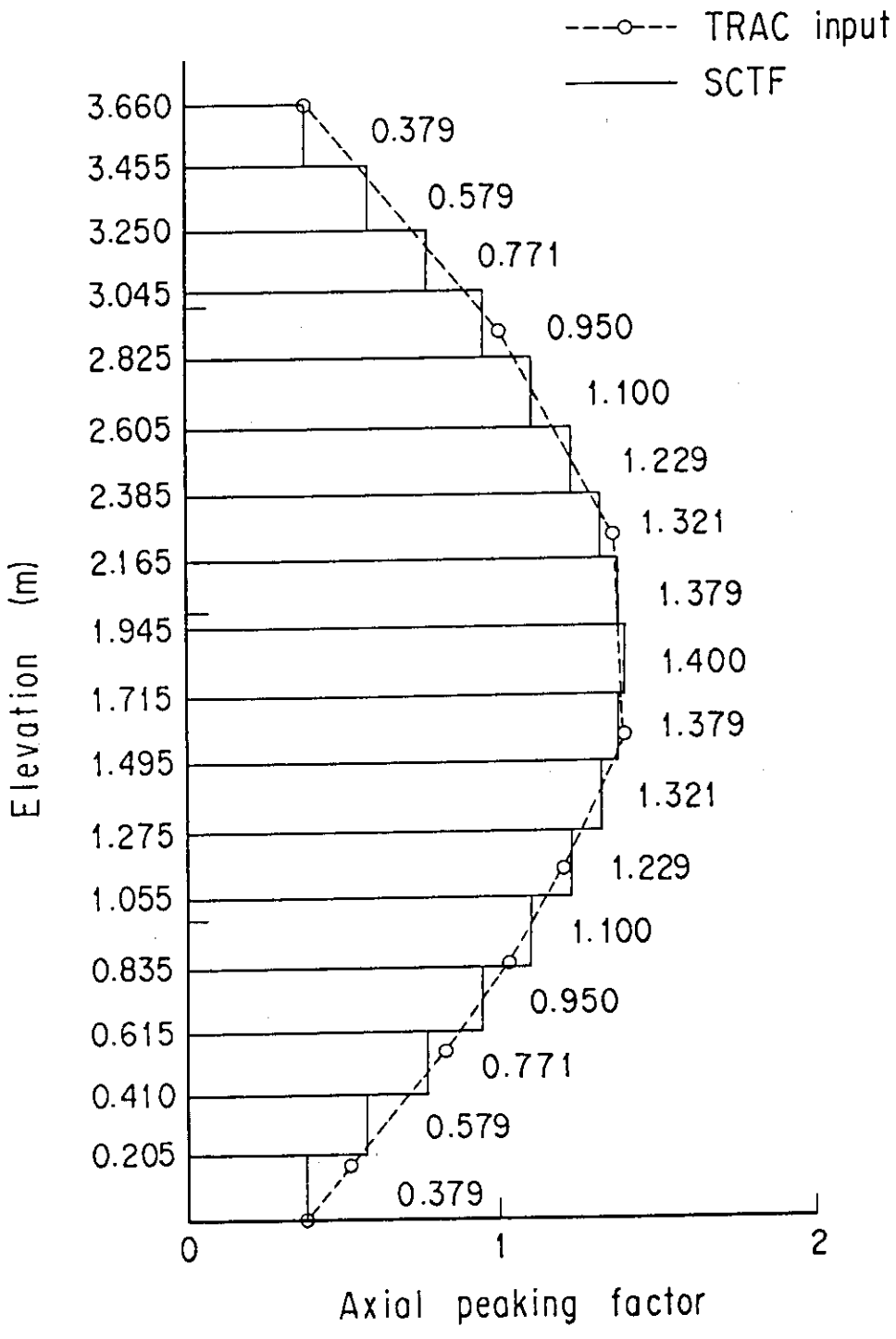

Fig. 3.2.2 Axial power profile of SCTF-II calculation

4 Results and Discussion

4.1 Assessment for CCTF base case test

4.1.1 Hydraulic behavior in core

Figure 4.1.1 illustrates a overall mass balance at core in the CCTF base case test. The inlet mass flow indicates the integrated value of the core inlet mass flow rate with respect to time from reflood initiation. The core mass indicates the total mass accumulated in the core. The outlet mass flow indicates the integrated value of steam or water mass flow rate at core outlet.

In this calculation, the core inlet mass flow rate is specified by a FILL component as a boundary condition, thus the TRAC result shows excellent agreement with measured one. The core mass is underestimated by about 200 kg in the TRAC calculation. The calculated steam mass flow at core outlet is lower than the measured one, while the calculated water mass flow is higher than the measured one. In the TRAC calculation for the CCTF base case test, the water carry-over from core to upper plenum is overestimated.

Figure 4.1.2 shows comparisons of void fractions at various elevations of core. The test results were inferred to differential pressure data assuming no friction and acceleration losses. The effect of the friction and acceleration losses were estimated to be less than 5 % of total pressure loss in the CCTF tests.[12] The void fractions from TRAC were calculated by averaging with a weight of cell length to match the elevation for measured results.

The calculated void fraction is higher than the measured one at the lower part of the core. At elevation between 0.61 and 1.83 m, TRAC results show almost constant void fraction of 0.75 regardless of the elevation, while CCTF results show higher void fraction as the elevation. In the upper part of the core (above 2.44 m), the calculated result is nearly equal to unity, while CCTF results show void fraction between 0.8 and 0.95.

Figure 4.1.3 shows calculated void fraction at each cell. In the TRAC-PF1/MOD1 code, a special model, named interface sharpener model, is used when a void fraction at lower cell is less than 0.3 and a void fraction at upper cell is higher than 0.75.[3] If the interface sharpener model is used, the flux terms for mass, momentum and energy transfer

through the cell interface is modified assuming that a dispersed flow is established in the upper part of the cell and that a bubbly flow with void fraction of 0.2 is established in the lower part of the cell. Although the interface sharpener model was used in the system calculation for the CCTF base case test,[4] it seems that the interface sharpener model was not used in this calculation because there is no cell boundary where a void fraction at lower cell is less than 0.3 and a void fraction at upper cell is higher than 0.75.

The accumulated mass in a cell is nearly proportional to $(1-\alpha)$ where α indicates the void fraction. As shown in Fig. 4.1.2, the TRAC−PF1 code predicted higher void fraction in the lower part of the core than measured results. In other words, accumulated mass is underestimated in the lower part of the core. The underestimation of the core mass is caused by the overestimation of the void fraction in the lower part of the core.

Figure 4.1.4 shows water and steam mass flow rates at core outlet. The calculated water mass flow rate shows many spikes. The result shows that the water carry−over occurred intermittently in the TRAC calculation. Figure 4.1.5 shows calculated water and steam mass flow rates and void fraction at the cell next to the core outlet between 100 and 150 s. Each number in Fig. 4.1.4 indicates a timing that the water mass flow rate shows a peak value. When the water mass flow rate shows a peak value, both steam mass flow rate and void fraction show peak values.

4.1.2 Thermal behavior in core

Figure 4.1.6 shows comparisons of clad temperature at various elevations along a high power rod. Although the calculated clad temperatures show several peaks, which are not clear in the measured results, they show fairly good agreement with measured results at various elevations. Figure 4.1.7 shows comparisons of turnaround temperature and time along a high power rod. In the lower part of the core, TRAC results show excellent agreement with measured results. In the upper part of the core, TRAC results show slightly lower turnaround temperature and slightly later turnaround time. Figure 4.1.8 shows a comparison of quench time along a high power rod. TRAC results show good agreement with measured results. The TRAC−PF1 code predicted turnaround time, turnaround temperature and quench time along a high power rod fairly good.

Figure 4.1.9 shows heat transfer coefficient and clad temperature at elevation of 1.83 m along a high power rod. In the TRAC code, the wall heat transfer coefficients h_g and

h_l are defined as follows:

$$q_g = h_g (T_w - T_g), \tag{4.1.1}$$

$$q_l = h_l (T_w - T_l), \tag{4.1.2}$$

where

h_g : wall heat transfer coefficient of vapor side (W/m^2K),
h_l : wall heat transfer coefficient of liquid side (W/m^2K),
q_g : wall heat flux of vapor side (W/m^2),
q_l : wall heat flux of liquid side (W/m^2),
T_g : vapor temperature (K),
T_l : liquid temperature (K),
T_W : wall temperature (K).

On the other hand, the total heat transfer coefficient is evaluated in the CCTF tests:

$$\begin{aligned} q_t &= q_g + q_l \\ &= h (T_w - T_{sat}), \end{aligned} \tag{4.1.3}$$

where

h : wall heat transfer coefficient (W/m^2K),
q_t : total wall heat flux (W/m^2),
T_{sat} : saturation temperature (K).

To compare with measured result, calculated heat transfer coefficients were modified by

$$h_g^* = h_g (T_w - T_g)/(T_w - T_{sat}), \tag{4.1.4}$$

$$h_l^* = h_l (T_w - T_l)/(T_w - T_{sat}). \tag{4.1.5}$$

The TRAC result shown in Fig. 4.1.9 corresponds to ($h_g^* + h_l^*$). The calculated result is higher than the measured one in most of the period before quench occurred. At about 30 and 75 s, the calculated result shows low heat transfer coefficient for about 10 s. In these periods, the void fraction became nearly unity at the cell that covers between 1.525 and 2.135 m, as shown in Fig. 4.1.13. It is supposed that the increase of the void

fraction resulted in the decrease of the heat transfer coefficient and in the increase of the clad surface temperature. Figure 4.1.10 summarizes heat transfer at elevation of 1.83 m in the TRAC calculation. Both steam and water temperatures are not so superheated and the change of heat flux is mainly determined by the change in heat transfer coefficient. The liquid side heat transfer coefficient is decreased at about 30 and 75 s, while the vapor side is not decreased so much. It is considered that the decrease of the heat transfer coefficient at about 30 and 75 s is occurred by the reduction of the heat transfer coefficient of liquid side because of increase of the void fraction at these times.

4.1.3 Discussion on interfacial friction model

In the TRAC calculation, the following features were observed, as described in the previous section:

(1) The void fraction is overestimated at the lower part of the core.

(2) The void fraction shows nearly constant regardless of the elevation at the center part of the core.

(3) The void fraction is nearly equal to unity at the top part of the core.

These void fraction profiles are determined by the interfacial friction model of the TRAC code. Thus, the characteristics of the interfacial friction model of the TRAC code will be discussed in this section. The outline of the interfacial friction model of the TRAC−PF1 code is described in Appendix A.

Because the transient is relatively slow during the reflood, it is assumed that the transient effect can be neglected. It is also assumed that the acceleration loss can be neglected. In such a case, the equations of motion for vapor and liquid can be simplified as follows;

$$\alpha \quad dP/dx = Ci(V_g - V_l)\,|\,V_g - V_l\,| - Cw_g\,V_g\,|\,V_g\,| - \alpha\,\rho_g g, \tag{4.1.6}$$

$$(1-\alpha)dP/dx = Ci(V_g - V_l)\,|\,V_g - V_l\,| - Cw_l\,V_l\,|\,V_l\,| - (1-\alpha)\,\rho_l g, \tag{4.1.7}$$

where

Ci : interfacial friction coefficient (kg/m^4),

Cw_g : wall friction coefficient of vapor side (kg/m^4),

Cw_l : wall friction coefficient of liquid side (kg/m^4),

g : acceleration due to gravity (m/s^2),
P : pressure (Pa),
V_g : vapor velocity (m/s),
V_l : liquid velocity (m/s),
x : coordinate (m),
α : void fraction (-),
ρ_g : vapor density (kg/m^3),
ρ_l : liquid density (kg/m^3).

One can get equations from Eqs. (4.1.6) and (4.1.7), given by

$$dP/dx = -\{\alpha\rho_g+(1-\alpha)\rho_l\} - Cw_g V_g |V_g| - Cw_l V_l |V_l|, \tag{4.1.8}$$

and

$$Ci(V_g-V_l)|V_g-V_l| = \alpha(1-\alpha)(\rho_l-\rho_g)g - Cw_g(1-\alpha)V_g|V_g| + Cw_l\alpha V_l|V_l|. \tag{4.1.9}$$

Equation (4.1.9) is rewritten as follows:

$$Fi = Fg + Fw, \tag{4.1.10}$$

where

$$Fi = Ci(V_g-V_l)|V_g-V_l|, \tag{4.1.11}$$

$$Fg = \alpha(1-\alpha)(\rho_l-\rho_g)g, \tag{4.1.12}$$

$$Fw = -Cw_g(1-\alpha)V_g|V_g| + Cw_l\alpha V_l|V_l|. \tag{4.1.13}$$

Equation (4.1.8) indicates that the pressure gradient is the summation of the static water head and the wall friction loss. Equation (4.1.10) indicates that the interfacial frictional force balances with the summation of the gravity force and the wall friction

force.

The void fraction at steady state was calculated with Eq. (4.1.10) using the interfacial friction model and the wall friction model in the TRAC code. Figure 4.1.11 illustrates the calculated void fraction, Fi, Fg and Fw. Although the wall friction force is included in the evaluation, it is very small compared to the interfacial and gravity forces. The void fraction is determined mainly by the balance between interfacial and gravity forces. The void fraction increases sharply at flow quality between 0 and 0.1. The void fraction is almost constant at flow quality between 0.1 and 0.6. The void fraction increases gradually at flow quality between 0.6 and 1.0.

Figure 4.1.12 shows Fi,Fw and Fg at flow conditions m_g = 1,2,3, and 4 kg/s and m_T = 5 kg/s, where m_g and m_T indicate vapor and total mass flow rates, respectively. In the calculation for Fig. 4.1.12, the void fraction is used as a parameter. The points A_1, A_2, A_3 and A_4 in Fig. 4.1.12, where Fi is equal to (Fw+Fg), are the points where three forces balance at steady state under each flow condition. The interfacial friction force decreases very sharply with void fraction near 0.75 where a flow transition from the churn flow to the annular/dispersed flow is assumed in the TRAC code (see Appendix A). This feature causes the void fraction to be nearly equal to 0.75 regardless of flow quality in the range between 0.1 and 0.6. The tendency that the void fraction at the center part of the core is nearly constant at 0.75 in the TRAC results is caused by the characteristics of the interfacial friction model near the flow transition point from the churn flow to the annular/dispersed flow.

Figure 4.1.13 shows a comparison of evaluated void fractions with the TRAC interfacial friction model, Murao−Iguchi void fraction correlation[13] and EPRI drift−flux correlation[14]. The Murao−Iguchi void fraction correlation has already been confirmed to agree with CCTF result excellently.[12] The TRAC model overestimates void fraction at low quality range. This fact explains the overestimation of the void fraction of the TRAC calculation at lower part of the core where flow quality is low. Figure 4.1.14 suggest that the interfacial frictional force is overestimated at low flow quality where the bubbly/slug flow regimes are used in the TRAC−PF1 code (see Appendix A). It is recommended to review the applicability of the interfacial friction model in the bubbly/slug flow regimes to the analyses of the reflood phenomena in PWR.

As a possible improvement of the TRAC interfacial friction model, the use of the EPRI drift−flux correlation is proposed by Los Alamos National Laboratory. Although the

EPRI drift-flux correlation overestimates the void fraction at the lower quality range slightly, the difference from the Murao-Iguchi void fraction correlation is smaller than the TRAC original model, as shown in Fig. 4.1.14. It is expected that the evaluation error is reduced by the use of the EPRI drift-flux correlation for the core void fraction in the analyses of the CCTF tests.

Another problem observed in the TRAC results is many spikes in water mass flow rate at core exit, as shown in Figs. 4.1.4 and 4.1.5. Figure 4.1.15 shows effect of total mass flow rate on void fraction in the TRAC model. The point, where the void fraction departs from 0.75, moves to the low quality as the total mass flow rate increases. In the flow quality range around 0.5, a small change in the total mass flow rate can cause a big change in the void fraction. It is supposed that the spiky water mass flow rate transient is caused by the strong dependency of the void fraction on the total mass flow rate. In the transient calculation, the total mass flow rate fluctuates. Once the total or water mass flow rate is increased, the void fraction in a cell is also increased as shown in Fig. 4.1.14. This means that the accumulated mass in the cell should be carried out of the cell. Then, the carried water to the adjacent cell causes the total or water mass flow rate to be increased at the adjacent cell. In such a way, the increase in the total or water mass flow rate propagates cell to cell. The effect of the increase in the total or water mass flow rate is amplified in the upper cell because the increase in the lower cell is added cell by cell. Such a behavior seems to be generated by the characteristics of the interfacial friction model near the flow transition point from the churn flow to the annular/dispersed flow. If an interfacial friction model that predicts void fraction insensitive to the total mass flow rate, spikes in water mass flow rates may be mitigated. It is recommended to review the interfacial friction model near the flow transition point from the churn flow to the annular/dispersed flow for the mitigation of spikes in water mass flow rate transients.

4.1.4 Discussion on wall heat transfer model

The TRAC-PF1 code predicted turnaround time, turnaround temperature and quench time along a high power rod fairly good, as shown in Figs. 4.1.6 through 4.1.8. In this section, it will be discussed why such a good agreement is attained with the TRAC-PF1 code in the prediction of clad temperature transients.

In the TRAC-PF1 code, various correlations are used to calculate wall heat transfer

coefficients along heater rods.[3] The outline of the wall heat transfer model of the TRAC-PF1 code is described in Appendix A.

In the analyses of the CCTF and SCTF tests with the TRAC-PF1 code, the most important wall heat transfer regime was the film boiling regime to evaluate the core cooling rate before heater rods were quenched. The TRAC-PF1 code calculated the minimum film-boiling temperature T_{min} at first to determine the wall heat transfer regime with Eq. (A.23) in Appendix A. T_{min} was calculated to be about 610 K under typical condition in the analyses of the CCTF and SCTF tests. The clad or wall temperature was higher than 610 K before heater rods were quenched in the CCTF and SCTF tests except the CCTF best-estimate test. Thus, the film boiling regime was selected in most of the CCTF and SCTF test analyses although the film boiling was not selected in the analyses of the CCTF best-estimate test because of low initial clad temperature. The discussion for the CCTF best-estimate test with low initial clad temperature will be presented in section 4.4 separately and discussions for the other CCTF and SCTF tests will be presented in the followings.

In the film boiling regime, the TRAC-PF1 code calculates wall heat transfer coefficients of liquid and vapor sides with correlations shown in Appendix A as Eqs. (A.27) through (A.41). In the correlations, hydraulic parameters such as void fraction α, liquid and vapor velocities, are used. Although the TRAC-PF1 code predicted clad temperature transients fairly good, it failed to predict the void fraction with good agreement in quantity. This fact suggests a problem of the wall heat transfer model of the TRAC-PF1 code that the good agreement in the clad temperature transients is attained as a result of the compensation of errors in the void fraction calculation by errors in the wall heat transfer calculation.

In order to confirm the problem in the wall heat transfer model of the TRAC-PF1 code, an evaluation was made. In the evaluation, wall heat transfer coefficients were calculated using measured data of void fraction, fluid and wall temperatures, liquid and vapor velocities in order to assess the wall heat transfer model separately. The physical properties of fluid and wall were calculated with the subroutines that was used in the TRAC calculation.

Figure 4.1.15 shows a comparison of wall heat transfer coefficients among measured and evaluated results with the TRAC-PF1 model and the Murao-Sugimoto correlation. The Murao-Sugimoto correlation[15] is given by

$$h = h_{con} + h_{rad}, \tag{4.1.14}$$

where

$$h_{con} = 0.94\{(k_g^3 \rho_g \rho_l h_{fg} g)/(L_q \mu_g (T_w - T_{sat})\}^{1/4}(1-\alpha)^{1/2}, \tag{4.1.15}$$

$$h_{rad} = \sigma_{SB}\, \varepsilon\, (1-\alpha)^{1/2}(T_w^4 - T_{sat}^4)/(T_w - T_{sat}), \tag{4.1.16}$$

g : acceleration due to gravity, (m/s^2)
h_{fg} : latent heat for evaporation, (J/kg)
k_g : thermal conductivity of vapor, (J/(Kms))
L_q : distance from quench front, (m)
T_{sat} : saturation temperature, (K)
T_w : wall temperature, (K)
α : void fraction,
ε : wall emissivity,
μ_g : viscosity, (kg/(ms))
ρ_l : liquid density, (kg/m^3)
ρ_g : vapor density, (kg/m^3)
σ_{SB} : Stefan-Boltzmann constant, ($J/(m^2K^4s)$).

The calculated result with the TRAC-PF1 model is about three times of the measured one. It is necessary to improve the wall heat transfer model in the film boiling regime as well as the hydraulic model.

The Murao-Sugimoto correlation gives excellent agreement with the measured one. One of the major differences between the TRAC-PF1 model and the Murao-Sugimoto correlation is the characteristic length used in the convection term. The Murao-Sugimoto correlation uses the distance from the quench front L_q, while the TRAC-PF1 model uses the wave length λ given by Eq. (A.30) in Appendix A. Figure 4.1.15 suggests that the dependence on the distance from the quench front should be considered in the film-boiling heat transfer model during the reflood in a PWR LOCA.

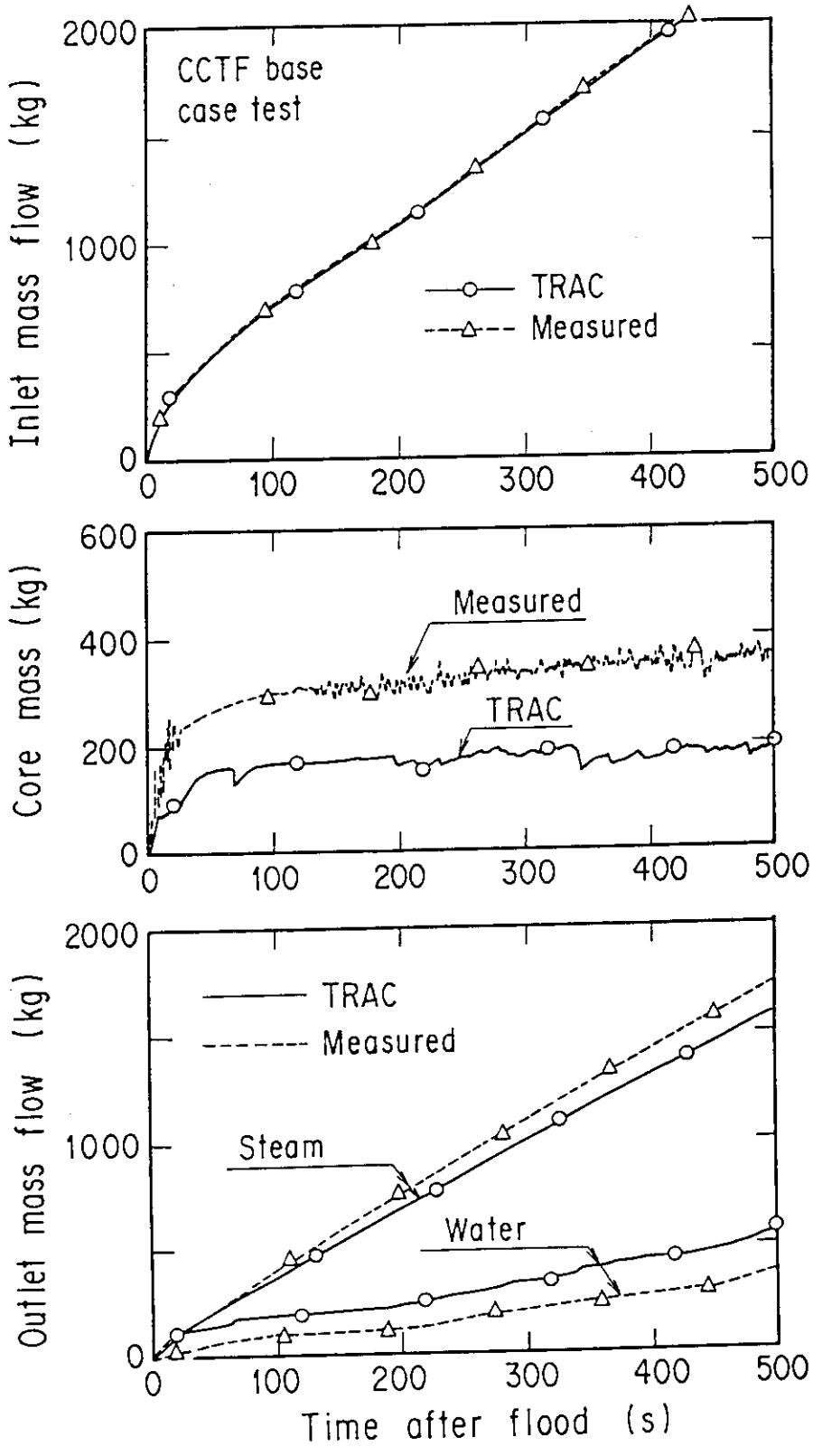

Fig. 4.1.1 Overall mass balance at core in CCTF base case test

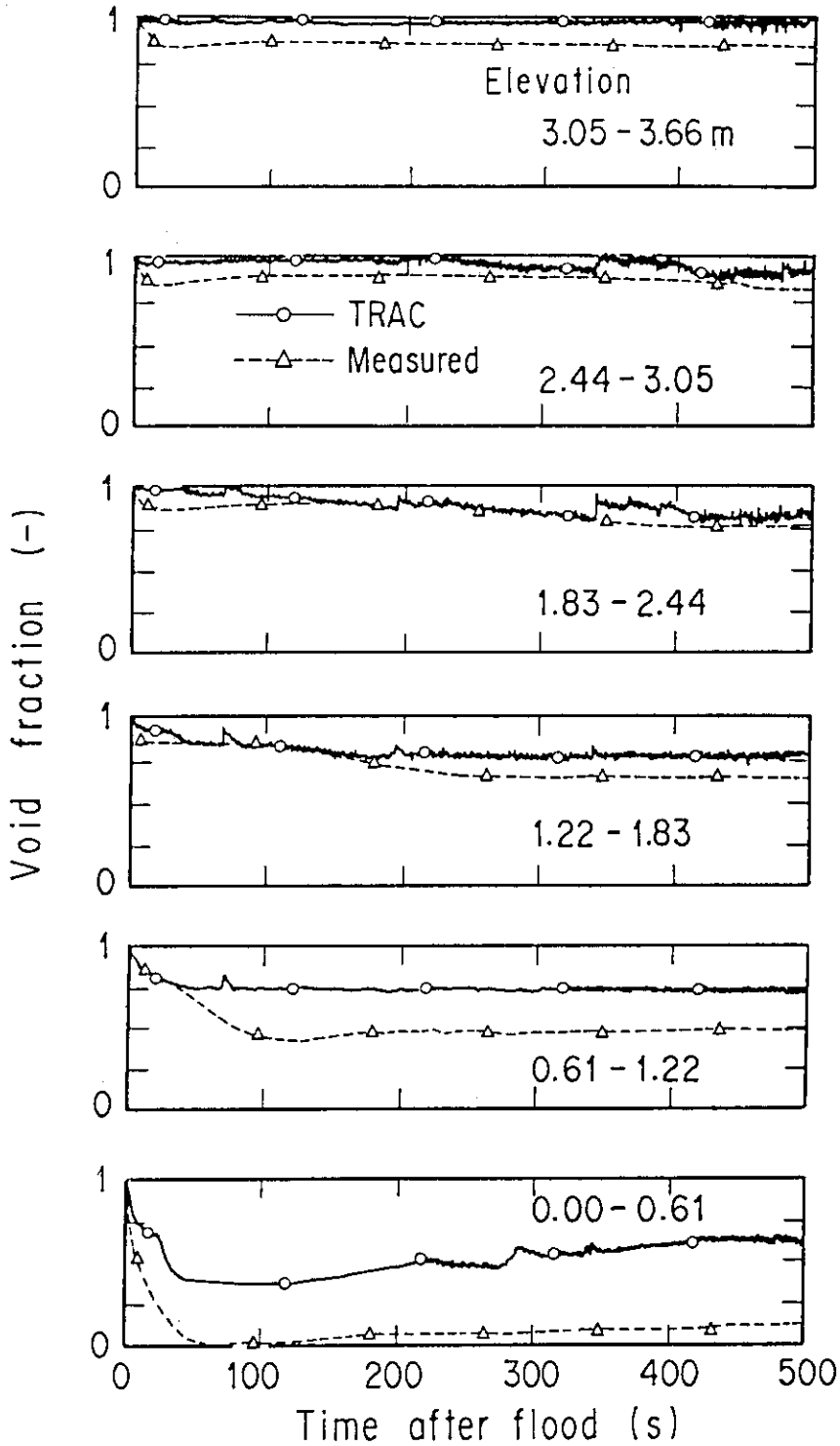

Fig. 4.1.2 Core void fractions in CCTF base case test

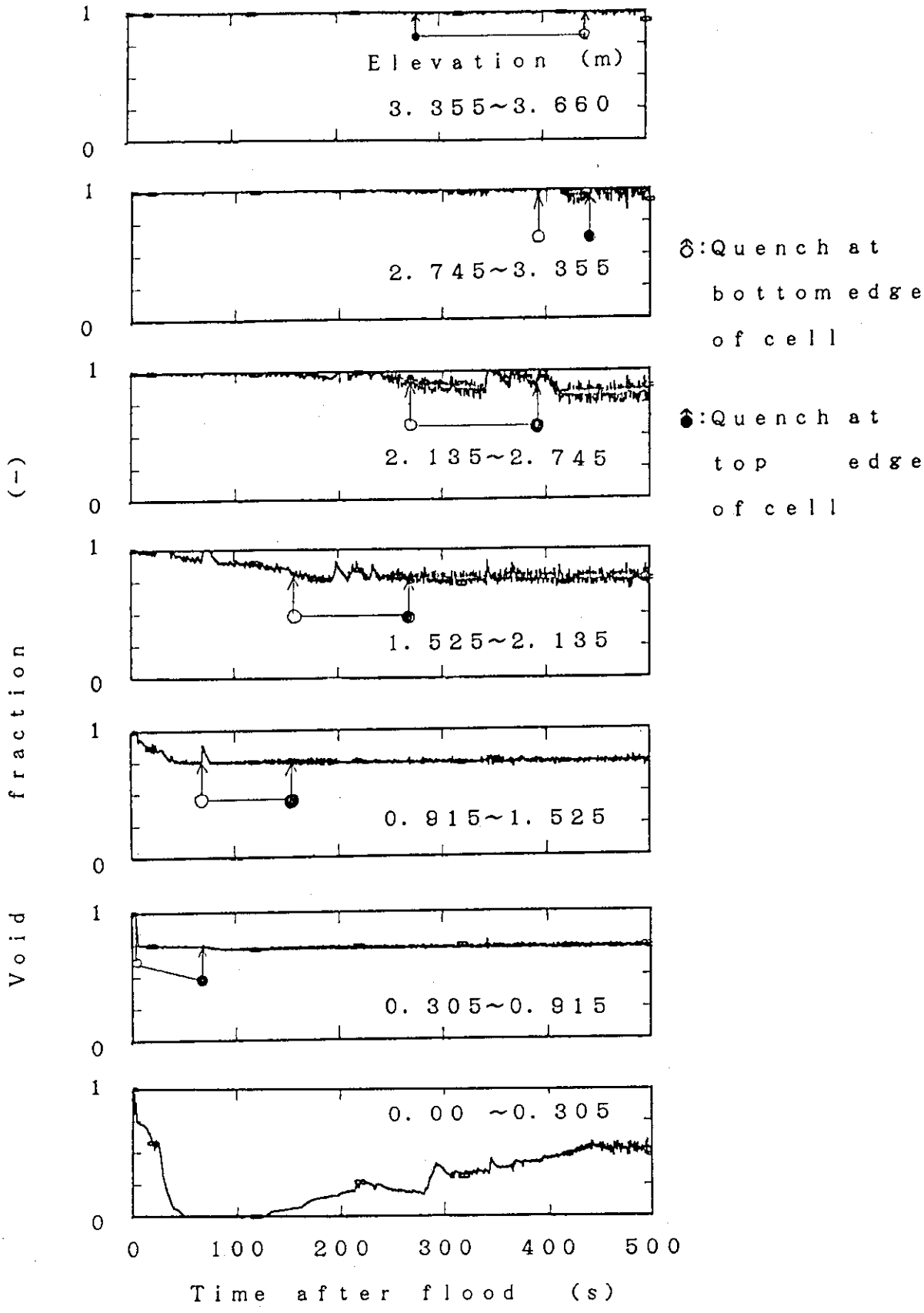

Fig. 4.1.3 Calculated core void fractions in CCTF base case test

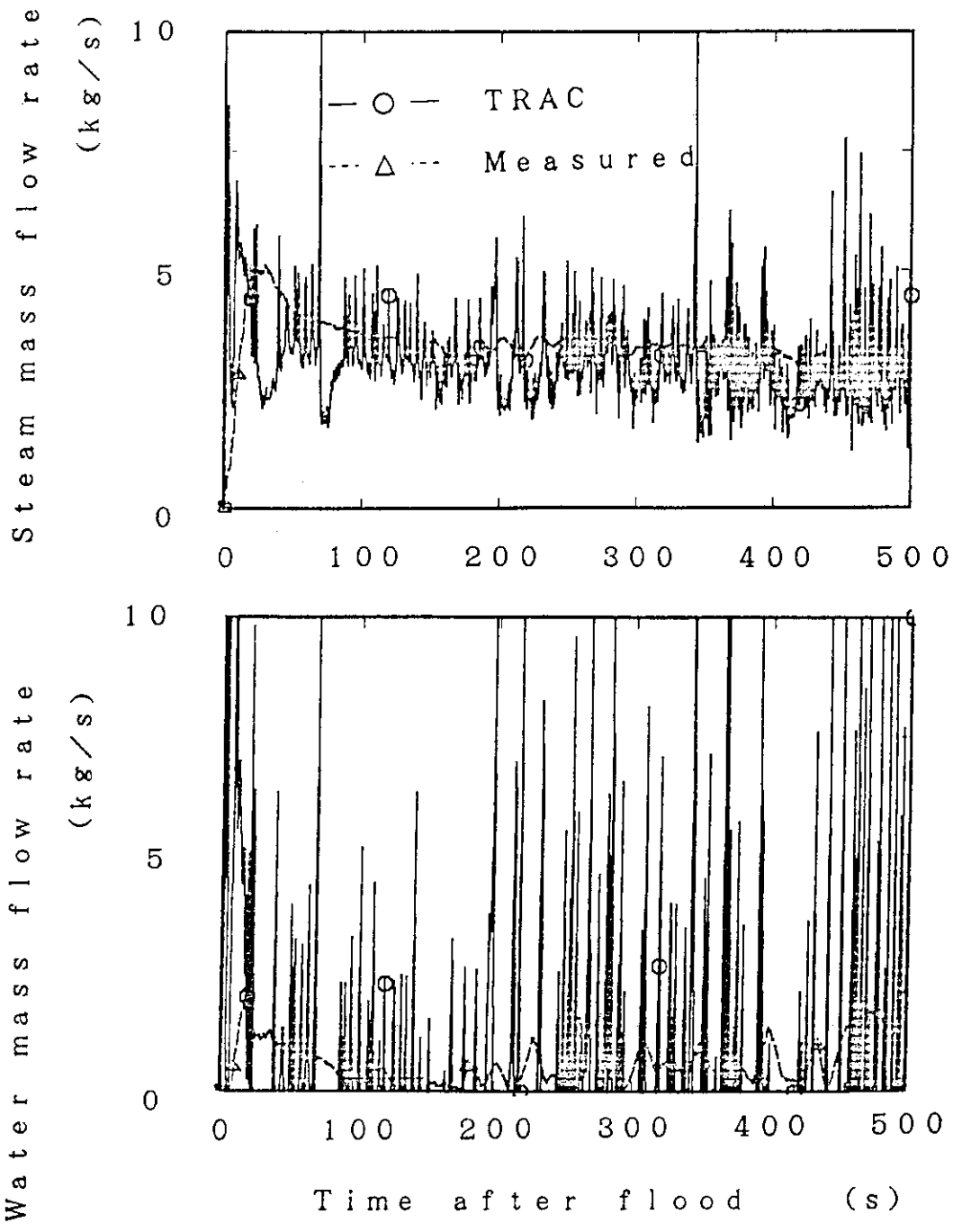

Fig. 4.1.4 Water and steam mass flow rates at core outlet in CCTF base case test

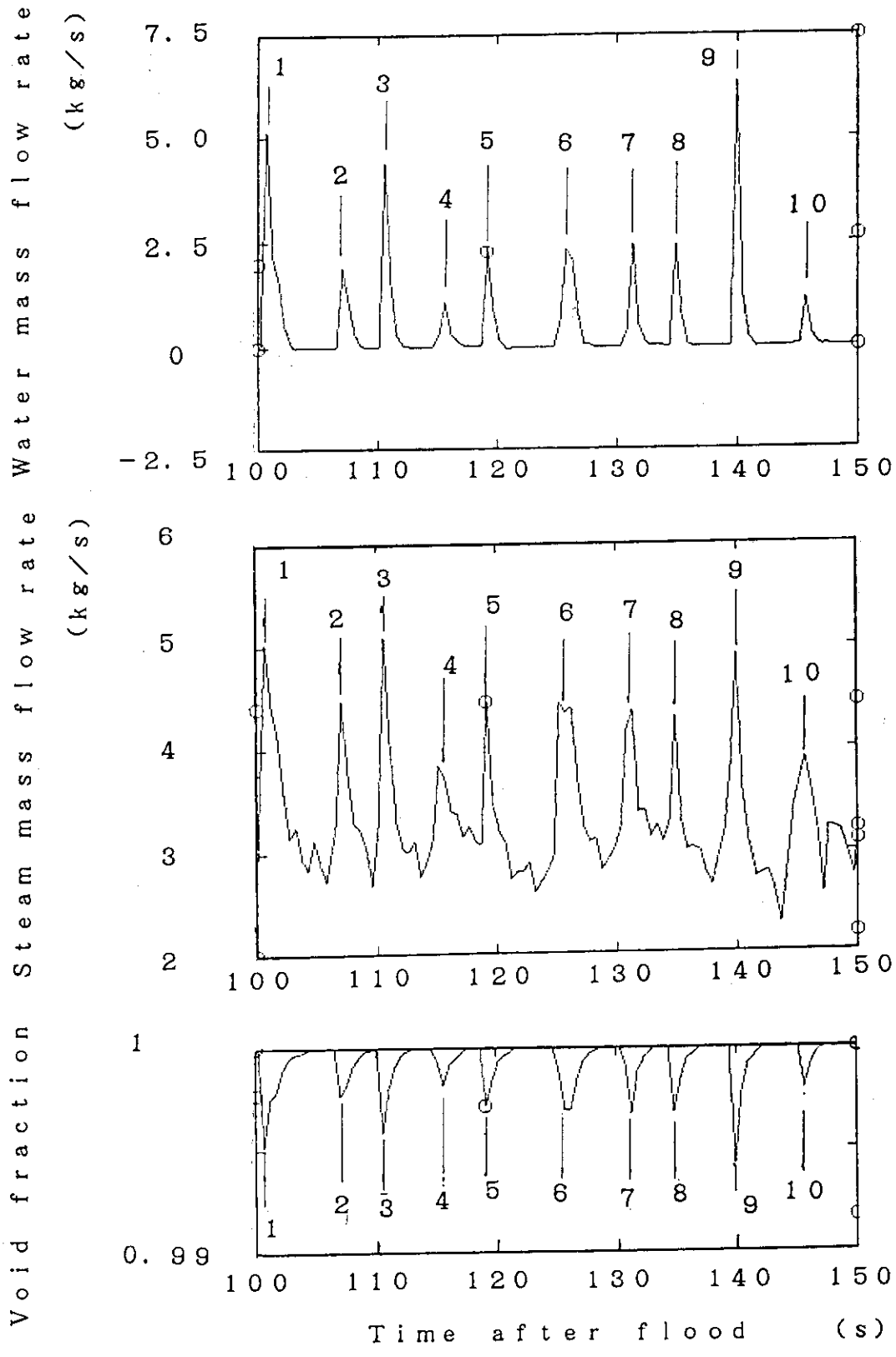

Fig. 4.1.5 Calculated steam and water mass flow rates and void fraction at core outlet in CCTF base case test

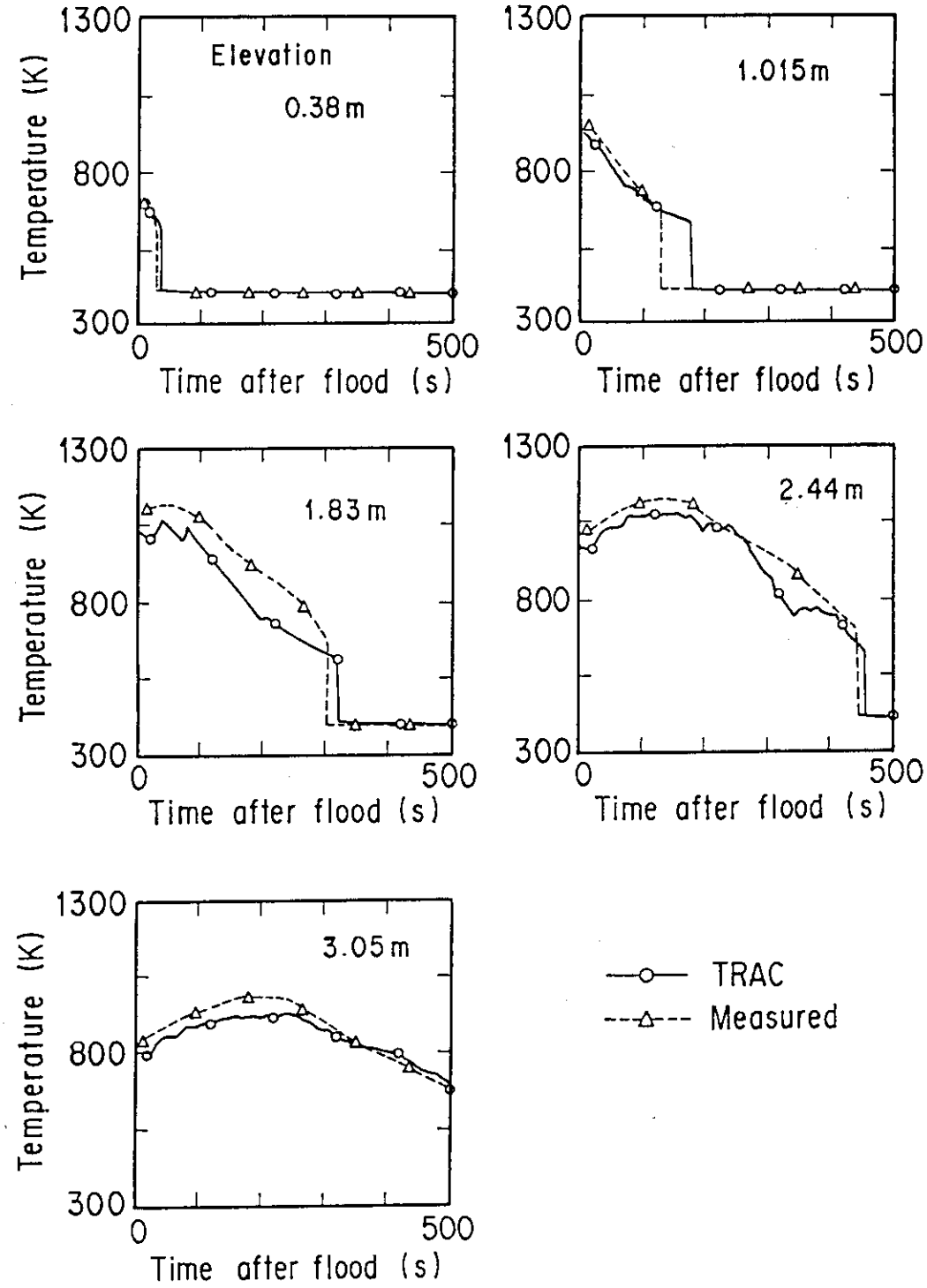

Fig. 4.1.6 Clad temperature along a high power rod in CCTF base case test

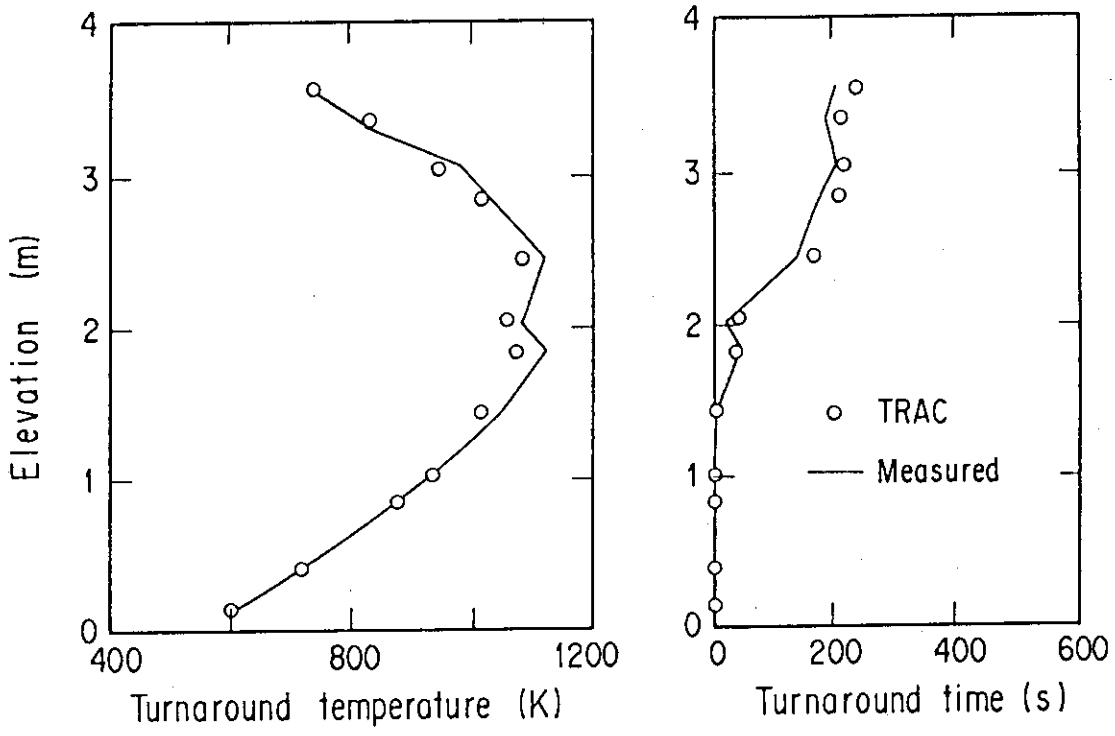

Fig. 4.1.7 Turnaround temperature and turnaround time along a high power rod in CCTF base case test

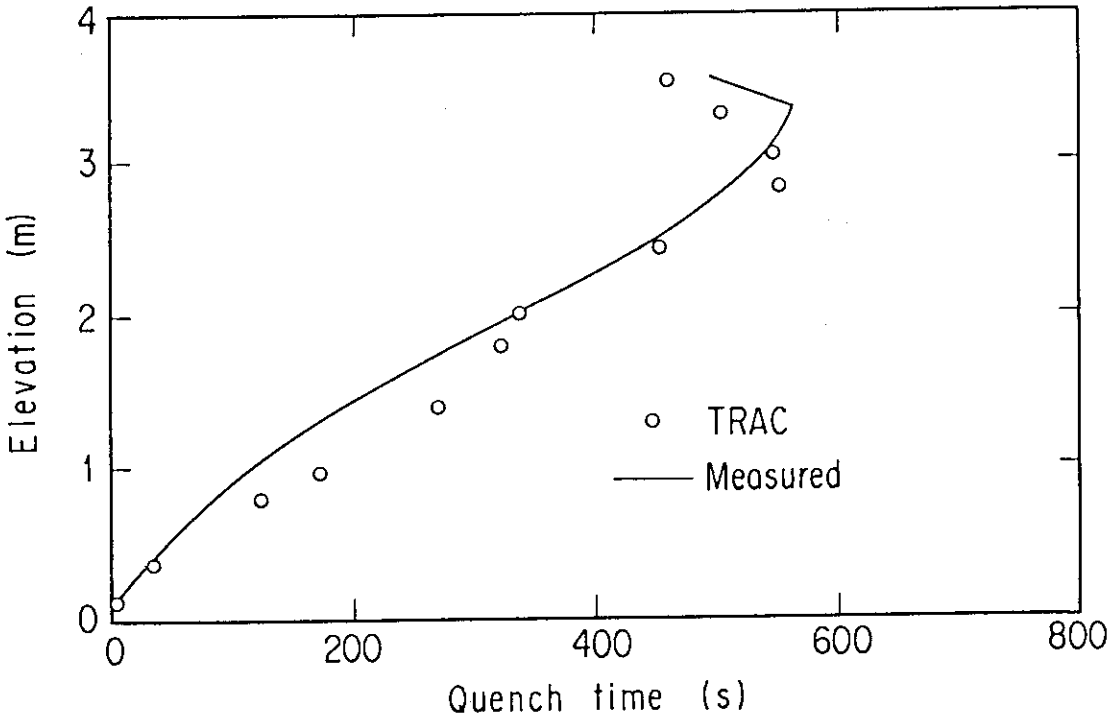

Fig. 4.1.8 Quench envelope along a high power rod in CCTF base case test

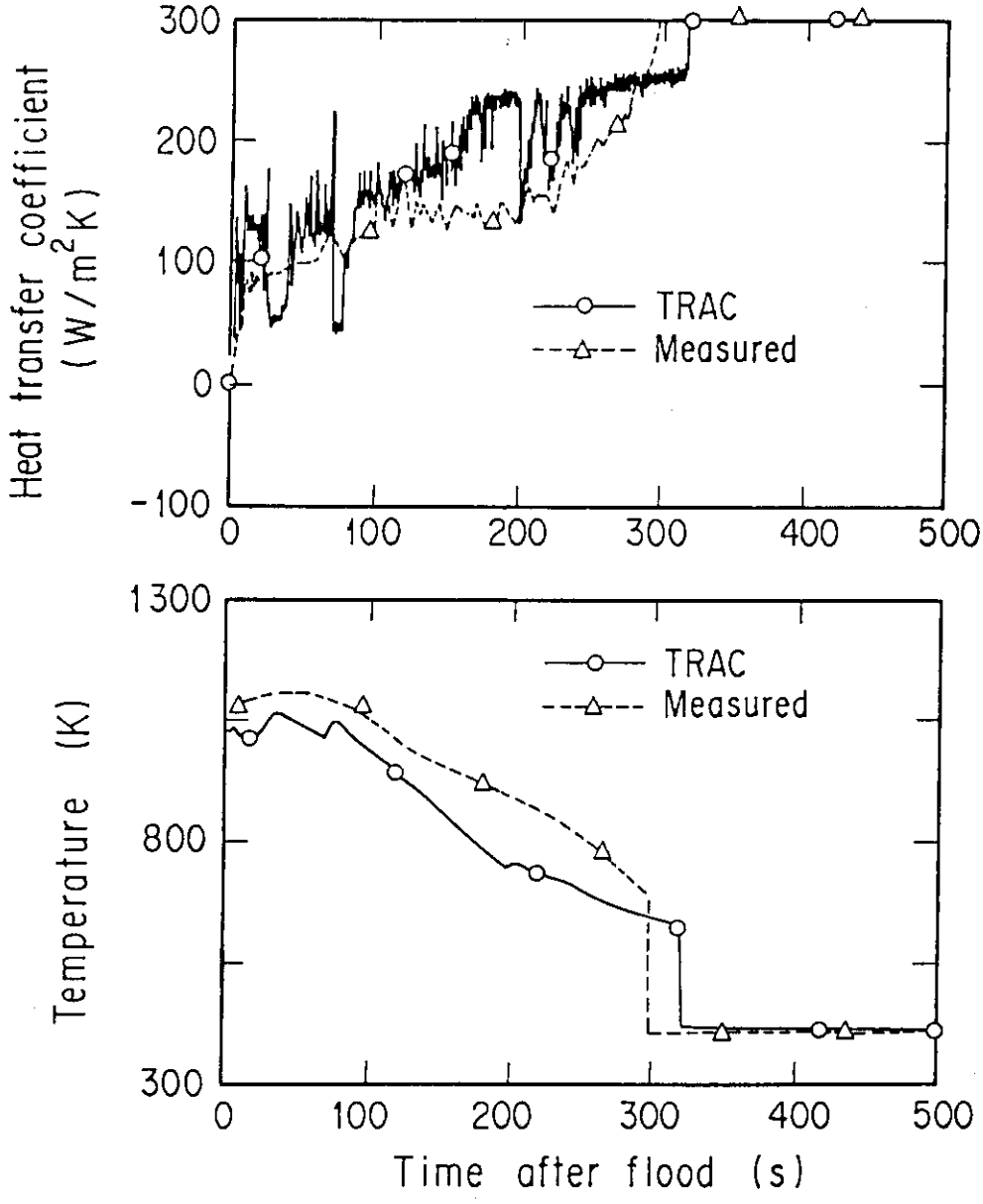

Fig. 4.1.9 Clad temperature and heat transfer coefficient at elevation of 1.83 m along a high power rod in CCTF base case test

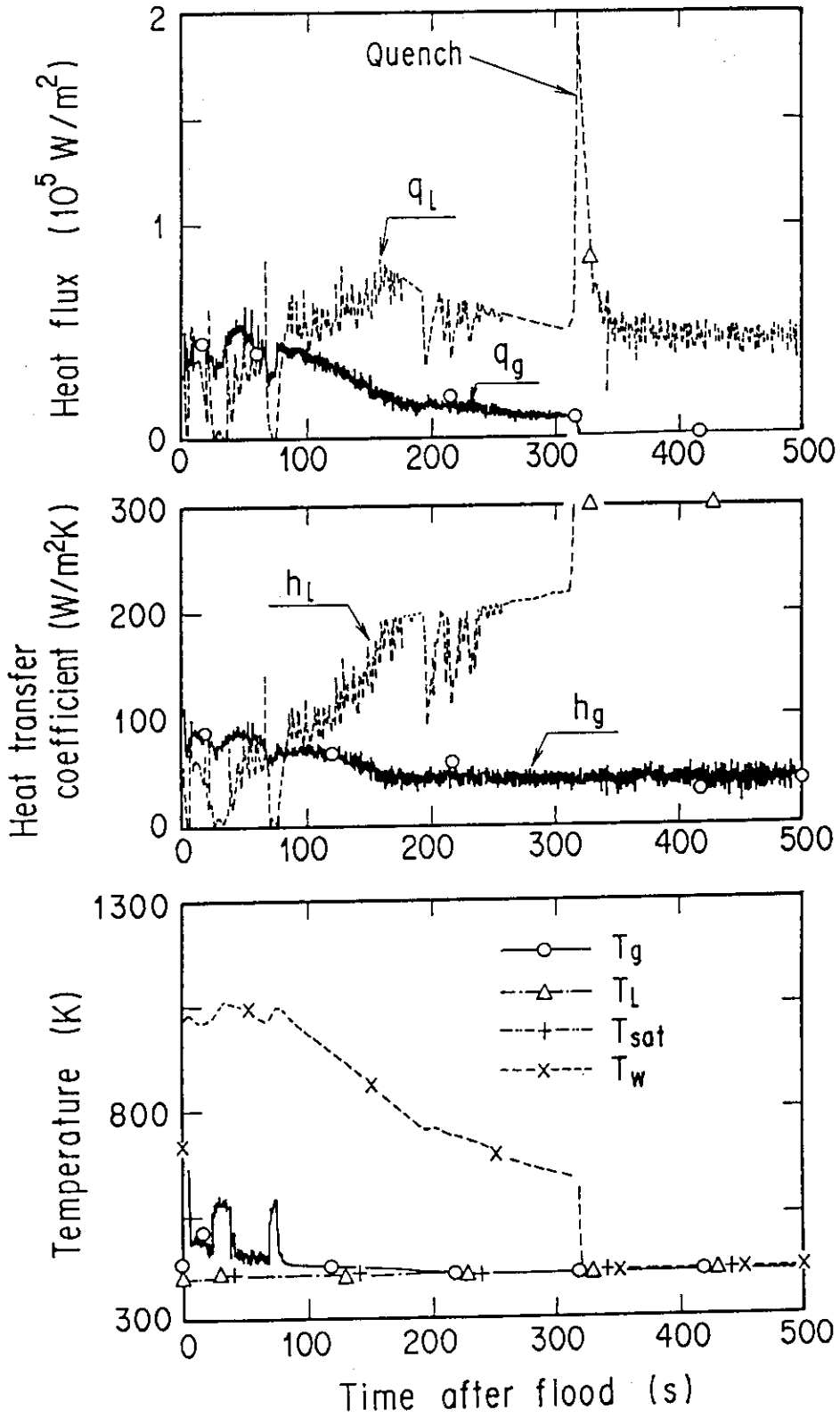

Fig. 4.1.10 Calculated heat transfer at elevation of 1.83 m along a high power rod in CCTF base case test

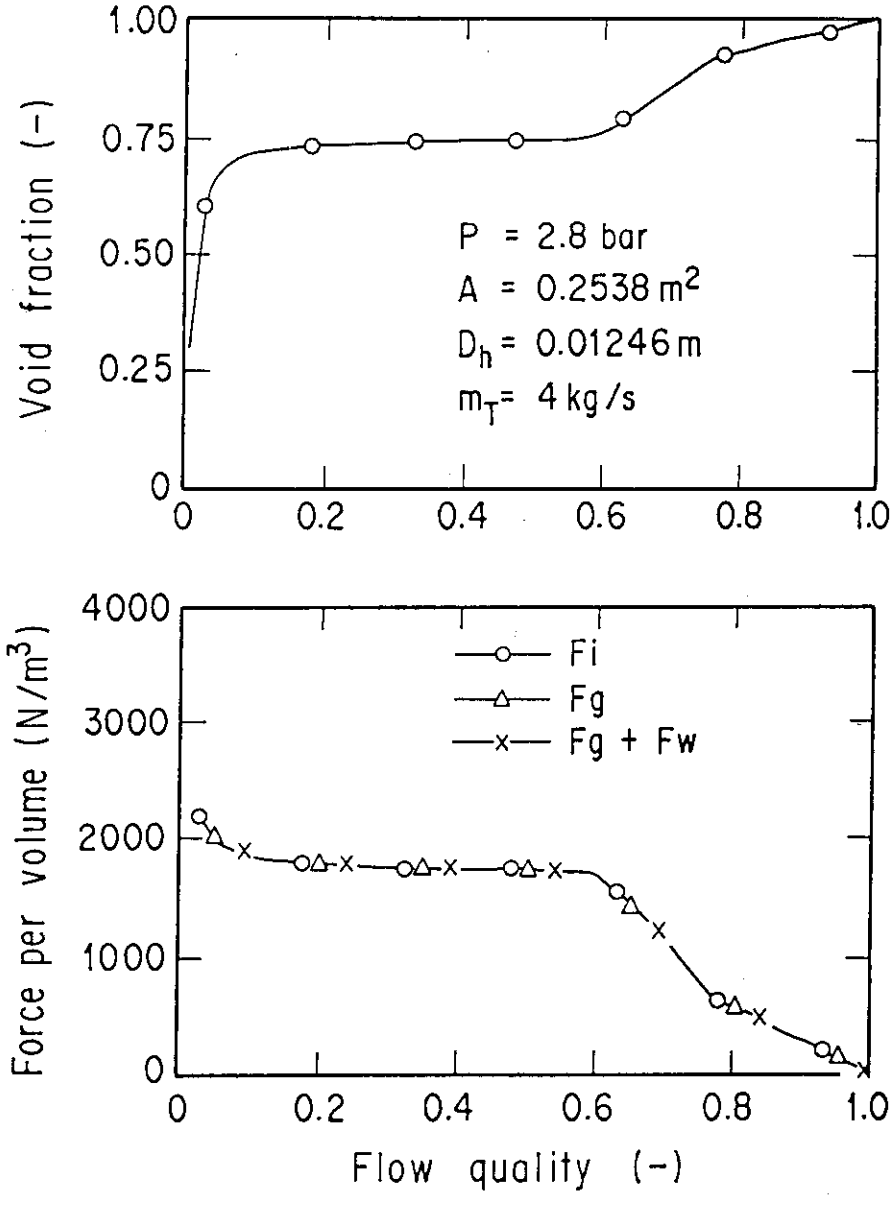

Fig. 4.1.11 Effect of flow quality on void fraction at steady state with TRAC interfacial friction model

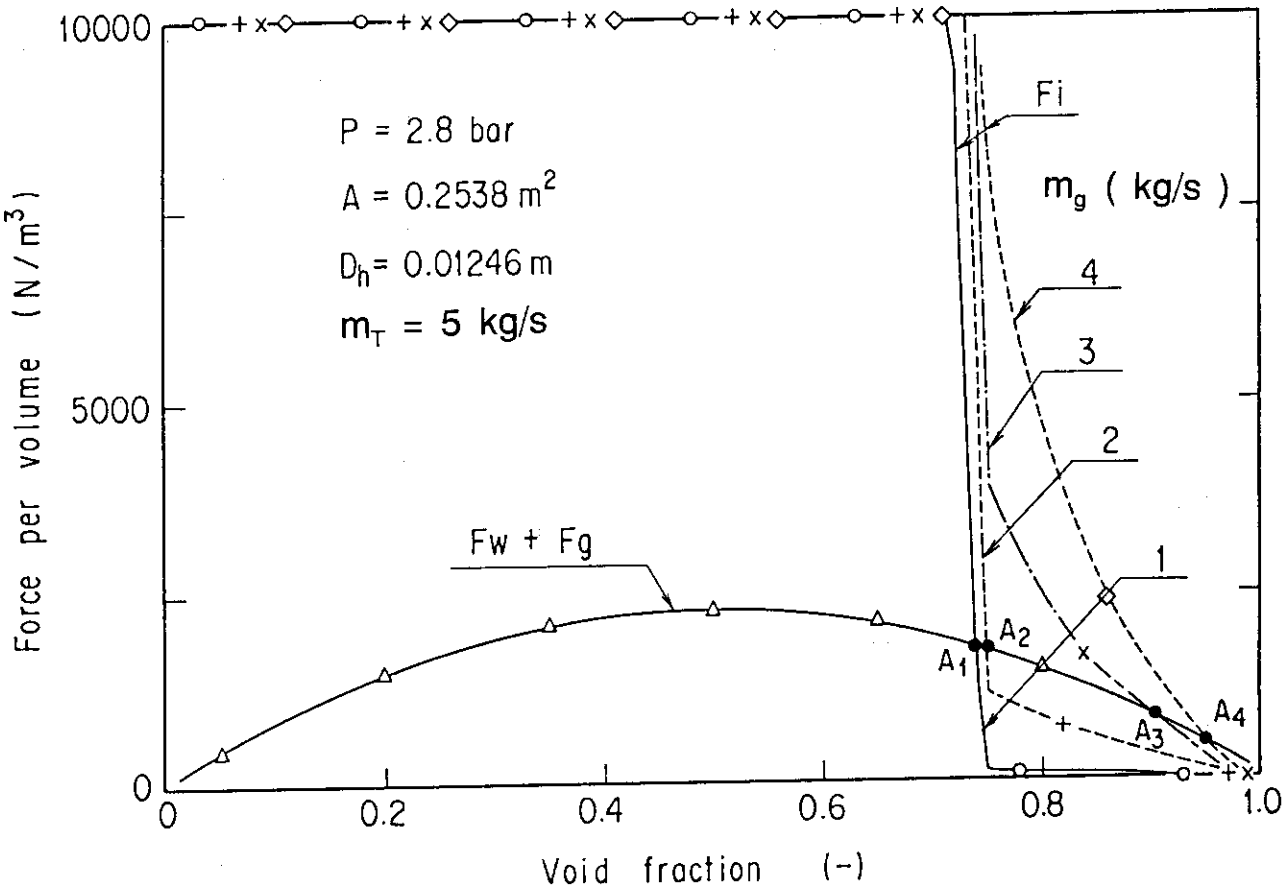

Fig. 4.1.12 Interfacial friction, wall friction and gravity forces in TRAC model

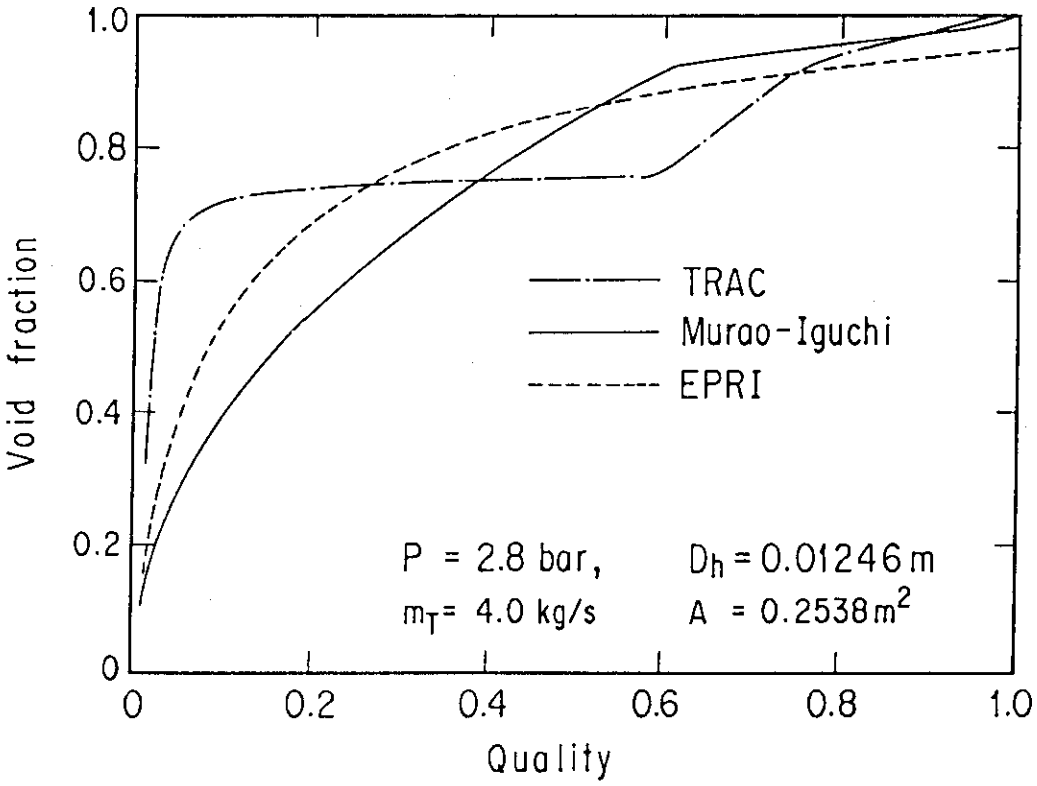

Fig. 4.1.13 Core void fraction

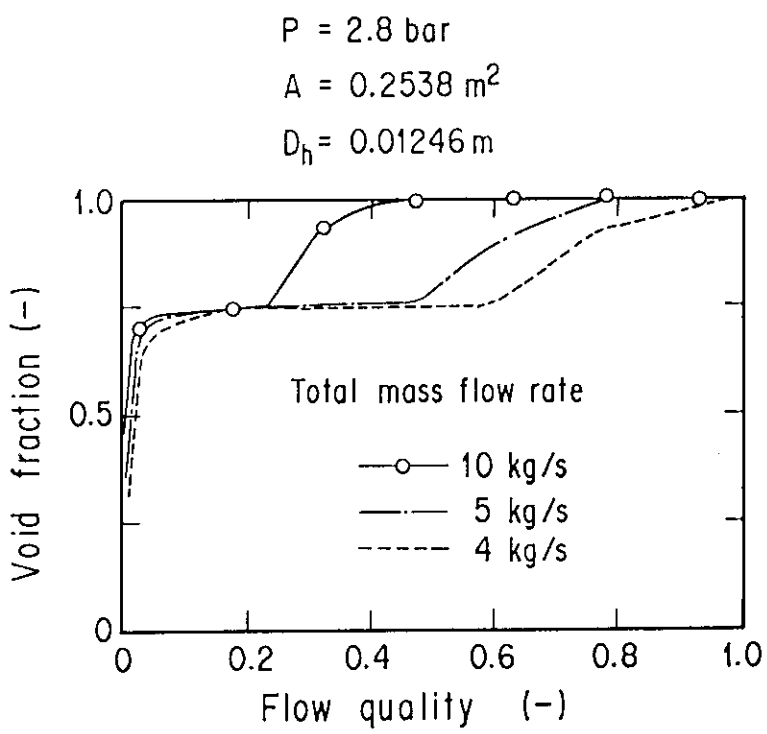

Fig. 4.1.14 Effect of total mass flow rate on void fraction at steady state with TRAC interfacial friction model

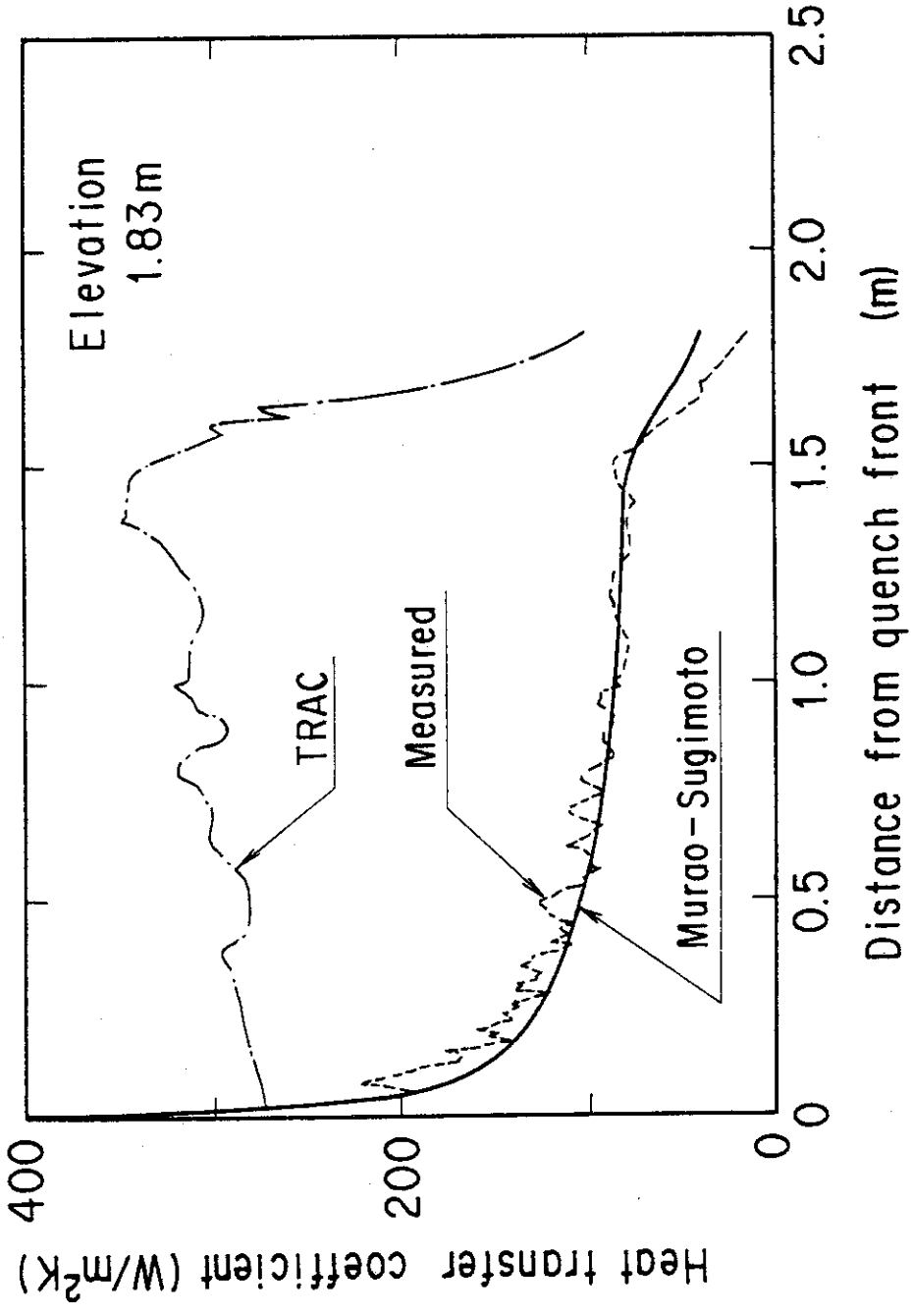

Fig. 4.1.15 Comparison of wall heat transfer coefficient between measured and calculated results

4.2 Assessment for CCTF pressure effect tests

In this section, the predictive capability of the TRAC code for the system pressure effect will be discussed through comparisons between CCTF low and high pressure tests.

4.2.1 Comparison of boundary condition

Figures 4.2.1 through 4.2.6 show comparisons of boundary conditions. In the low and high pressure tests, the containment pressure was kept constant at 0.15 and 0.42 MPa, respectively. The pressures at upper plenum are about 0.22 MPa and 0.45 MPa during tests in low and high pressure tests, respectively, as shown in Fig. 4.2.1. The core power is the same between these two tests, as shown in Fig. 4.2.2. Although the ECC injection conditions were the same between low and high pressure tests, the core inlet mass flow rate was higher in the high pressure test than in the low pressure test, as shown in Figs. 4.2.3 and 4.2.4. The core inlet fluid temperature is higher in the high pressure test than in the low pressure test although the core inlet subcooling is slightly lower in the high pressure test than in the low pressure test, as shown in Figs. 4.2.5 and 4.2.6.

4.2.2 Pressure effect on core hydraulic behavior

Figures 4.2.7 through 4.2.10 show system pressure effect on overall mass balance at core. In CCTF test results, the following tendencies can be observed:

(1) The core inlet mass flow increases as system pressure increases.
(2) The core mass increases as system pressure increases.
(3) The steam mass flow at core outlet increases as system pressure increases.
(4) The water mass flow at core outlet increases as system pressure increases.

For the core inlet mass flow rate, an excellent agreement was obtained because the core inlet mass flow rate was one of input data in these TRAC calculations.

For the core mass, the calculated core mass increases with system pressure in TRAC calculations as observed in CCTF test results. The TRAC code predicted well the system pressure effect on the core mass qualitatively. However, the calculated core mass is about half of measured result in both low and high pressure tests quantitatively. Figure 4.2.8 suggests a problem for a water accumulation model in the TRAC code as mentioned for the CCTF base case test.

For steam and water mass flows at core outlet, the TRAC code predicted well the system pressure effect on these mass flows. In the low pressure test, the steam mass flow was underpredicted and the water mass flow was overpredicted by the TRAC code as in the calculation of the CCTF base case test. In the high pressure test, good agreement with measured results was obtained by the TRAC code.

Figure 4.2.11 shows comparisons of void fraction at various elevations in core. The void fraction is overestimated at the lower part of the core. The void fraction shows nearly constant regardless of elevation at the center part of the core. The void fraction is nearly equal to unity in the upper part of the core before it goes down to 0.75. These tendencies are similar to those observed in the analysis of the CCTF base case test.

These comparisons can be summarized as follows:

(1) The TRAC code predicted system pressure effect on overall mass balance through core qualitatively under the condition where the core inlet mass flow rate and inlet fluid temperature are specified as input data.

(2) The core mass was underestimated in both low and high pressure tests as in the base case test which was performed with a containment pressure of 0.20 MPa. The water accumulation model should be reviewed at pressure range including 0.15 through 0.42 MPa.

4.2.3 Pressure effect on core thermal behavior

Figure 4.2.12 shows clad temperature at elevation of 1.83 m along a high power rod in low and high pressure tests. The high pressure resulted in low turnaround temperature and fast quench in both CCTF tests and TRAC calculations. Figure 4.2.13 shows heat transfer coefficient at elevation of 1.83 m along a high power rod. The high pressure resulted in the high heat transfer coefficient in both CCTF tests and TRAC calculations. The TRAC calculations show low heat transfer coefficient at about 150 s in the high pressure test or at about 250 s in the low pressure test. As shown in Fig. 4.2.11, the void fraction is increased in the TRAC calculation when these low heat transfer coefficients are predicted. Figure 4.2.14 shows a comparison of quench envelope along a high power rod in low and high pressure tests. The effect of the system pressure on the quench front propagation was predicted well by the TRAC code. The TRAC code predicted well the system pressure effect on the core cooling behavior.

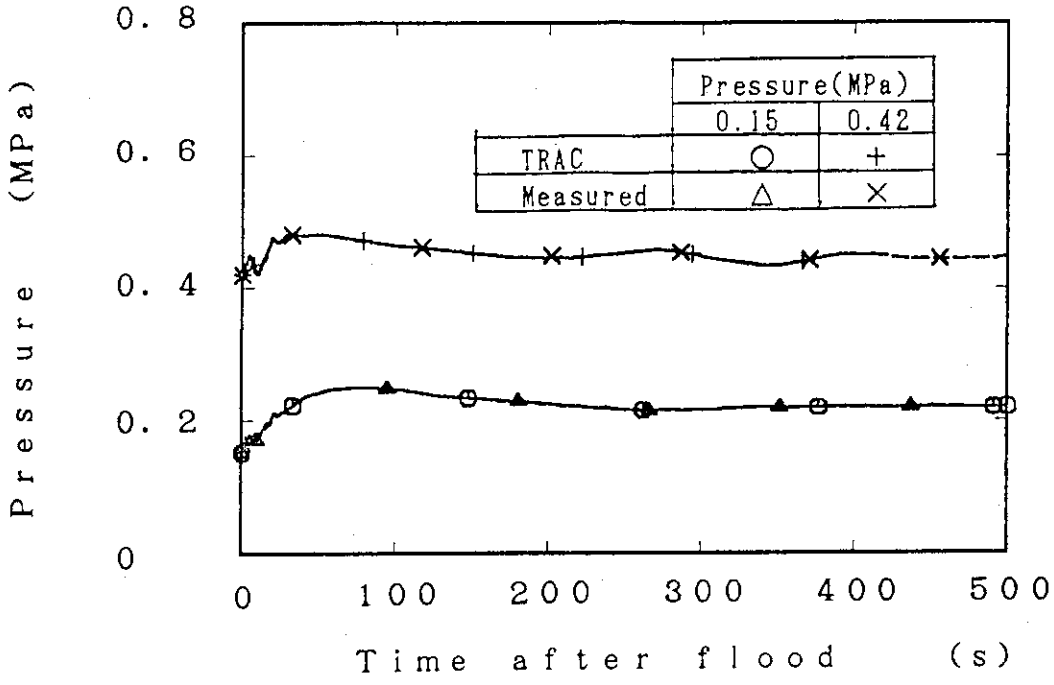

Fig. 4.2.1 Comparison of core outlet pressure between low and high pressure tests

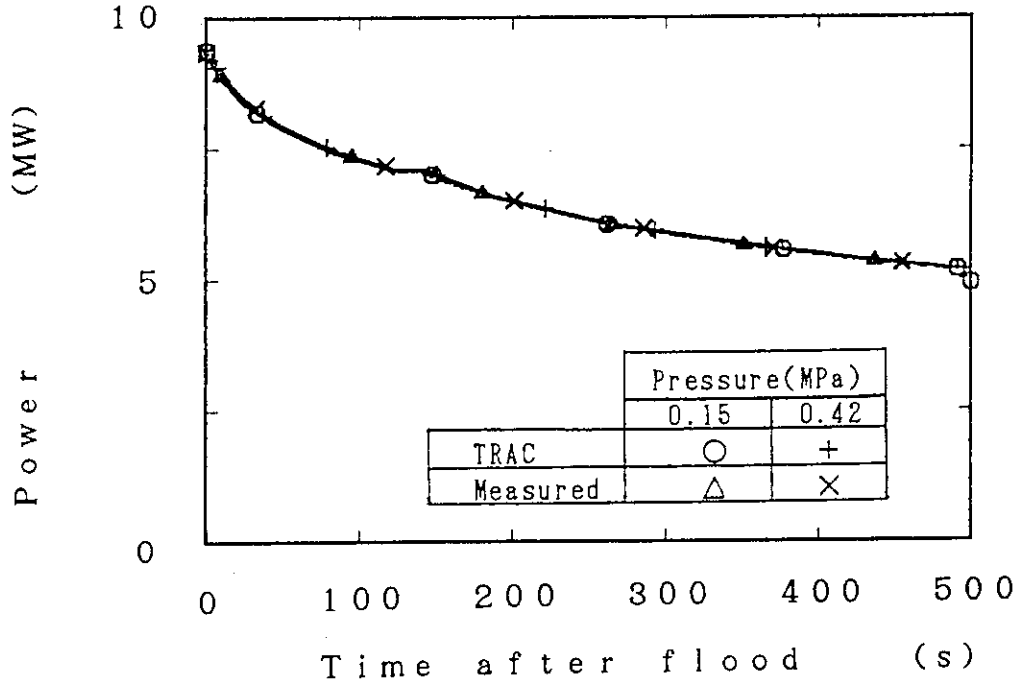

Fig. 4.2.2 Comparison of core power between low and high pressure tests

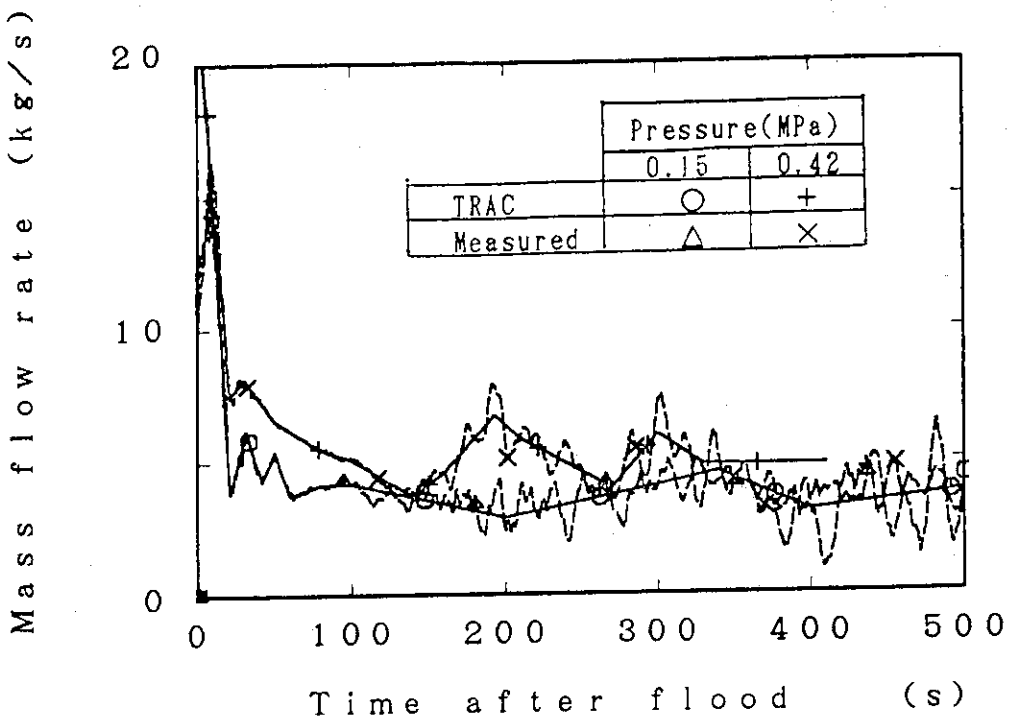

Fig. 4.2.3 Comparison of core inlet mass flow rate between low and high pressure tests

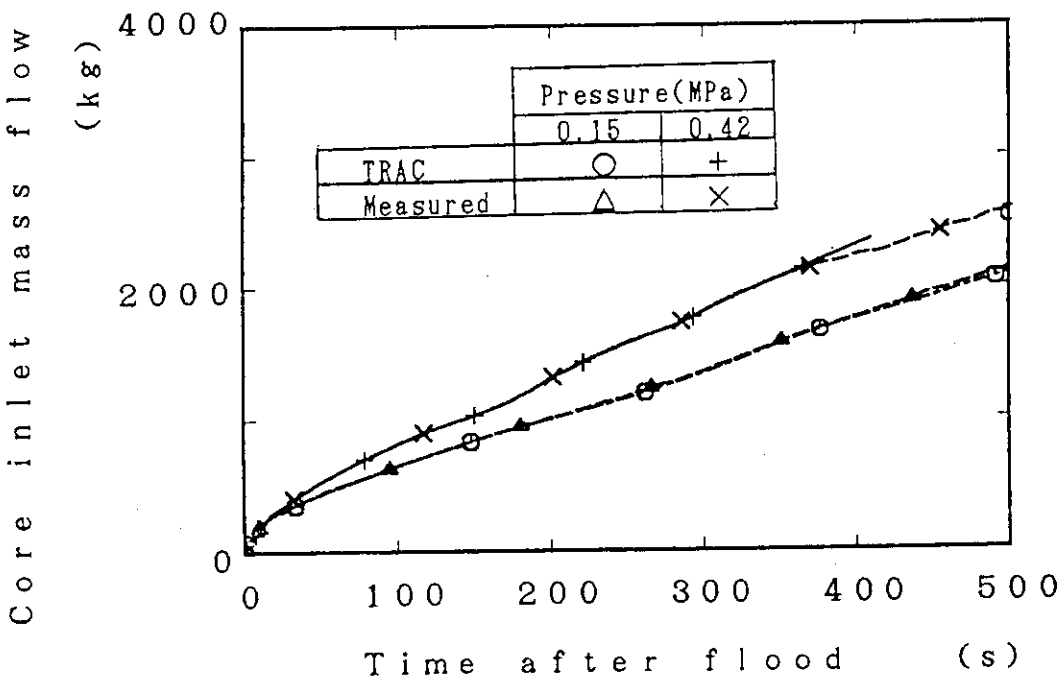

Fig. 4.2.4 Comparison of core inlet mass flow between low and high pressure tests

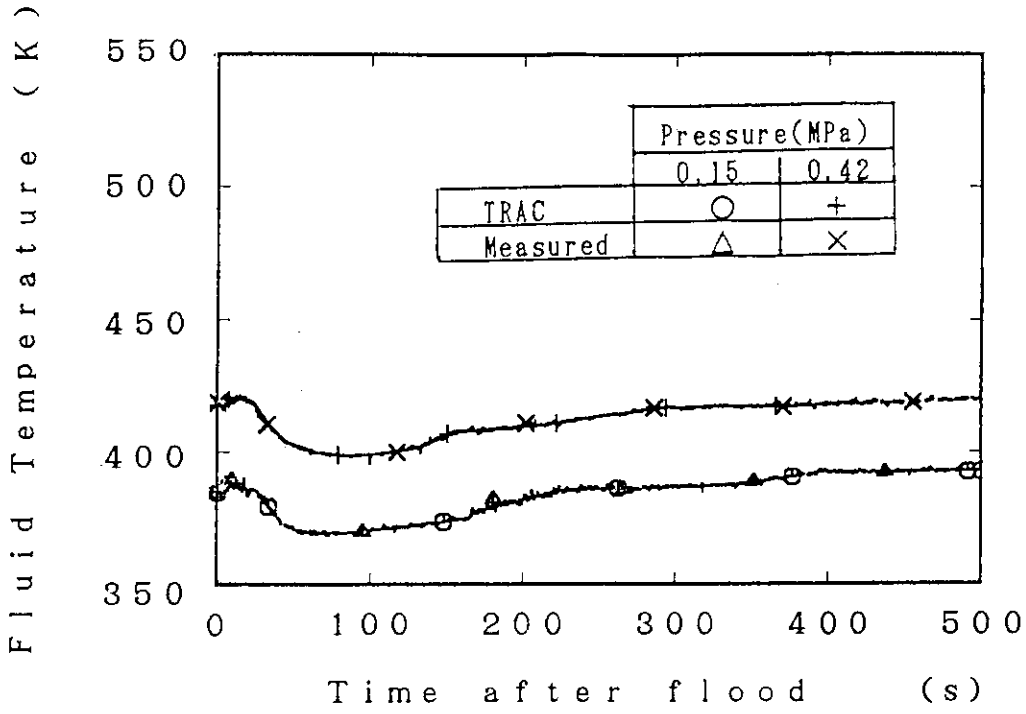

Fig. 4.2.5 Comparison of core inlet fluid temperature between low and high pressure tests

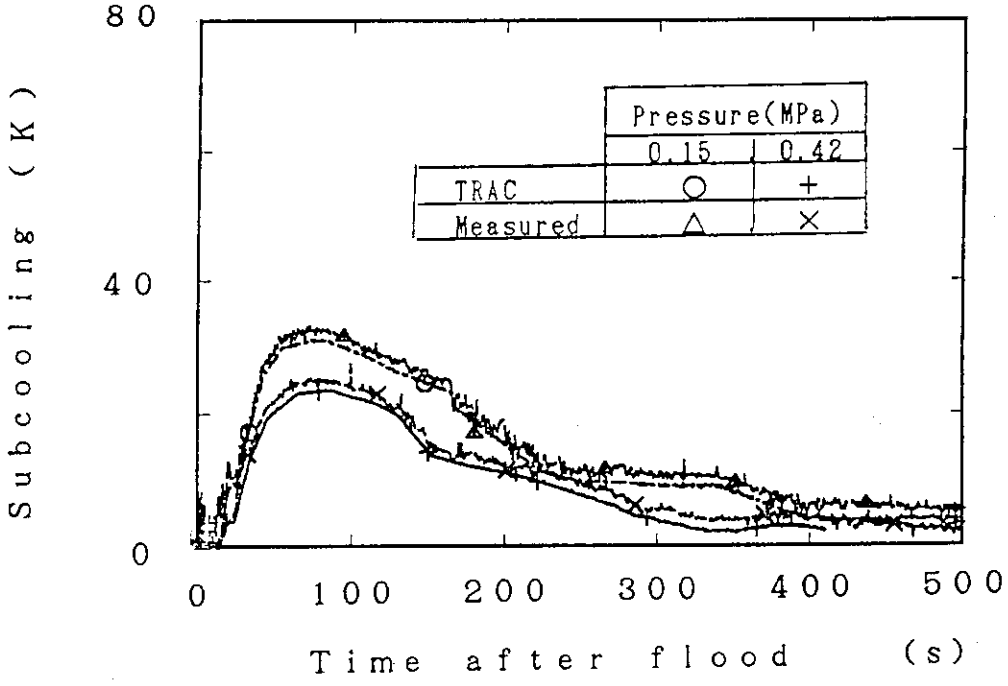

Fig. 4.2.6 Comparison of core inlet subcooling between low and high pressure tests

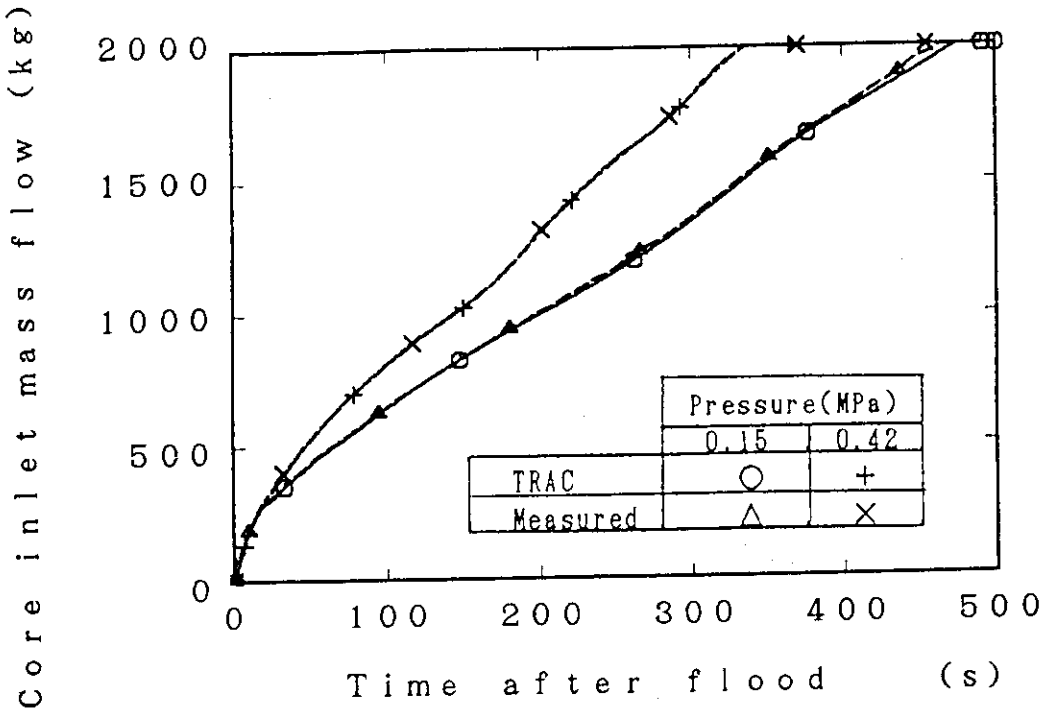

Fig. 4.2.7 Effect of system pressure on core inlet mass flow

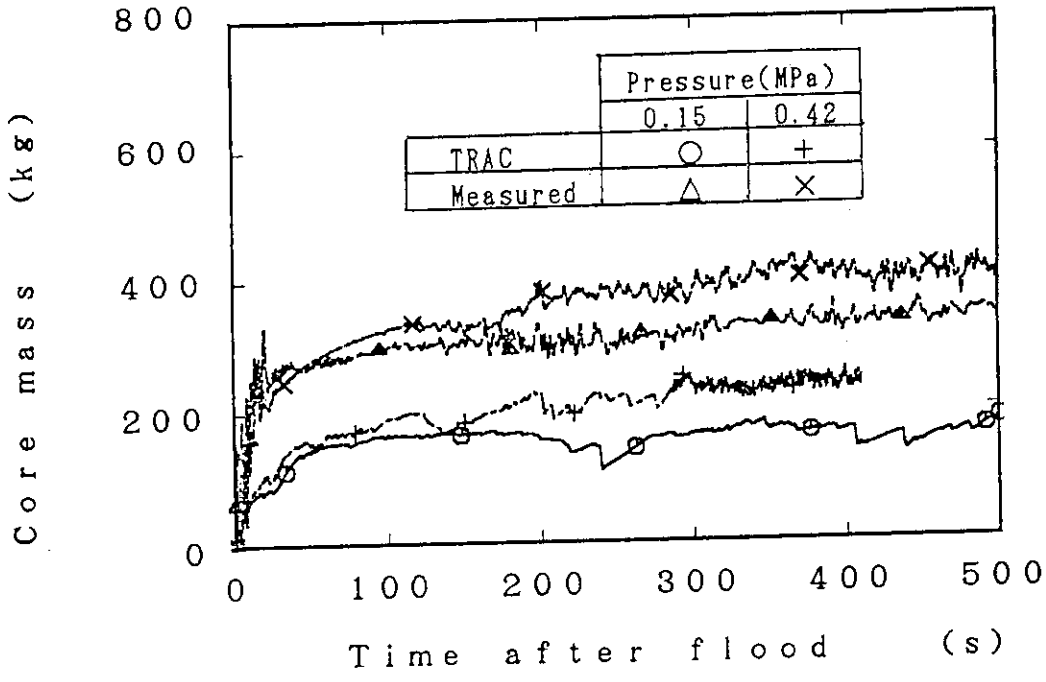

Fig. 4.2.8 Effect of system pressure on core mass

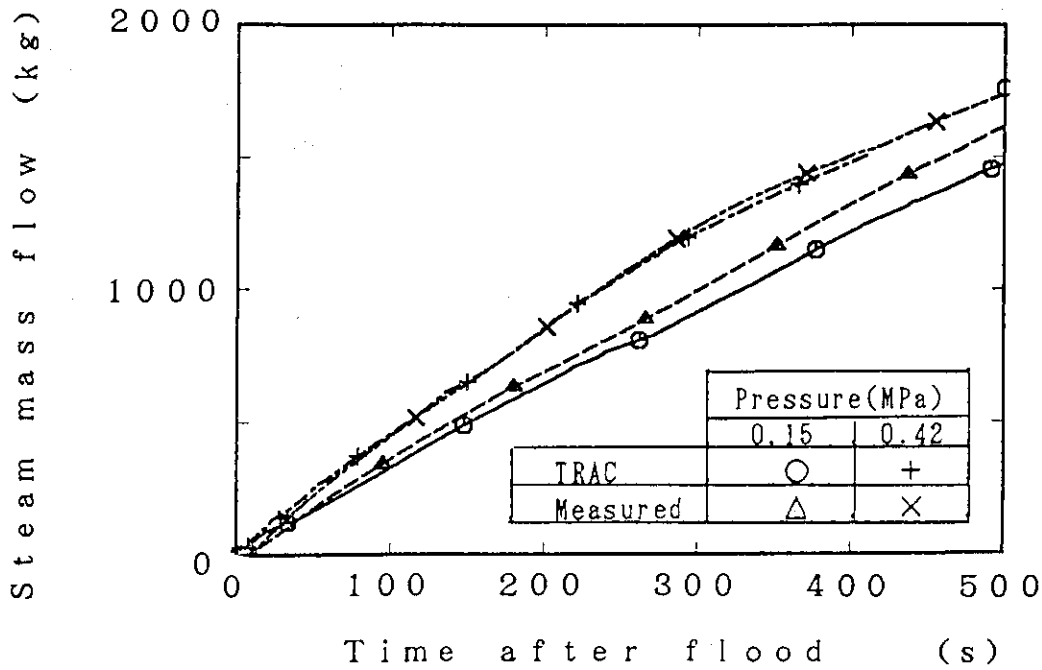

Fig. 4.2.9 Effect of system pressure on steam mass flow at core outlet

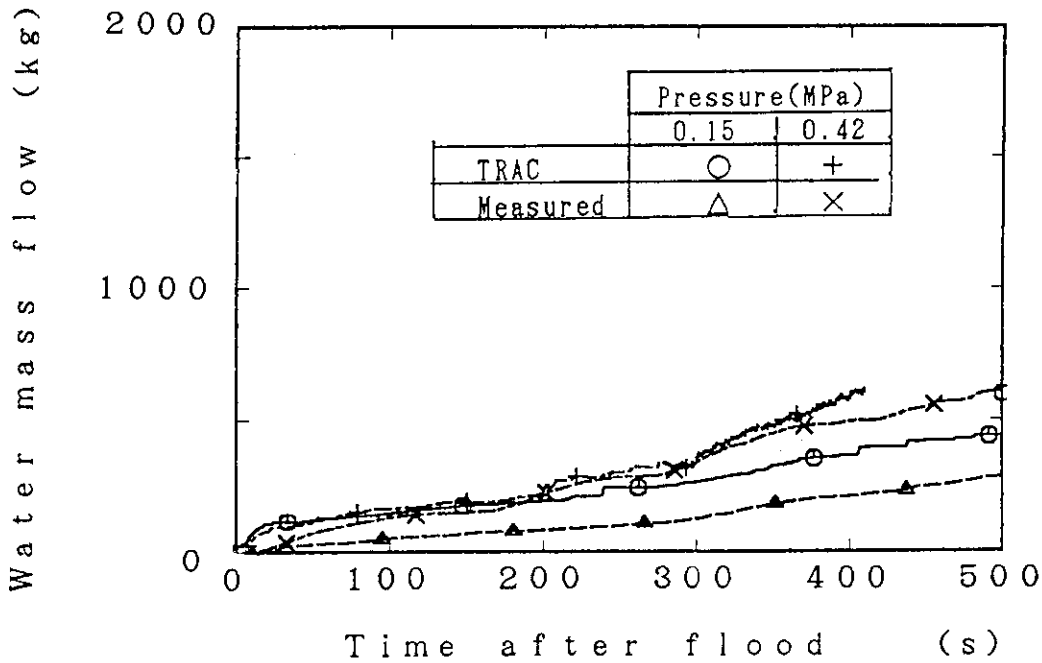

Fig. 4.2.10 Effect of system pressure on water mass flow rate at core outlet

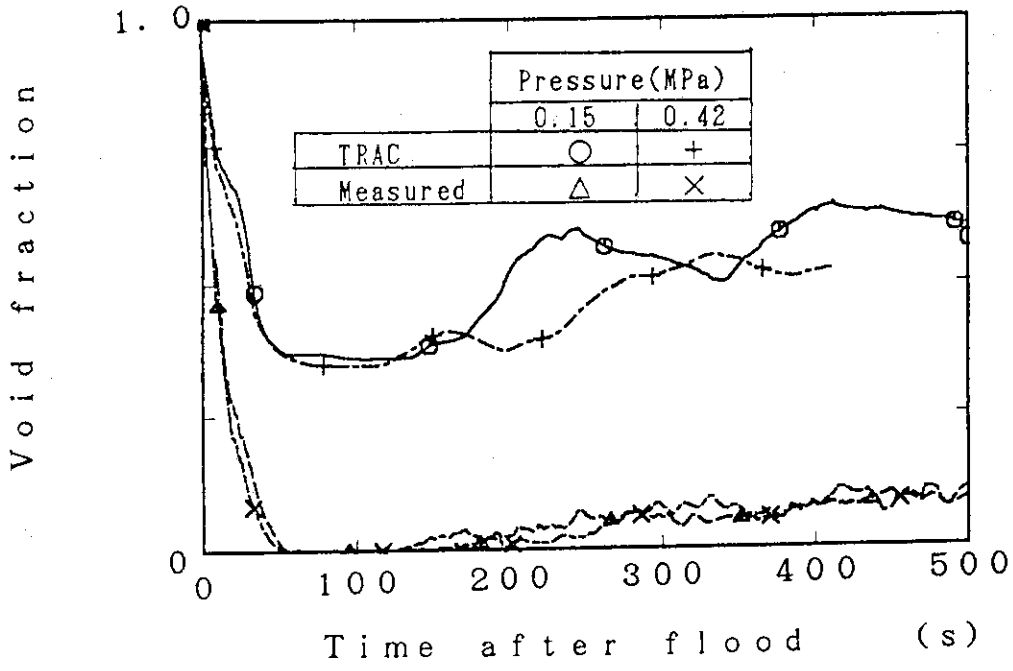

(a) Between 0.00 and 0.61 m

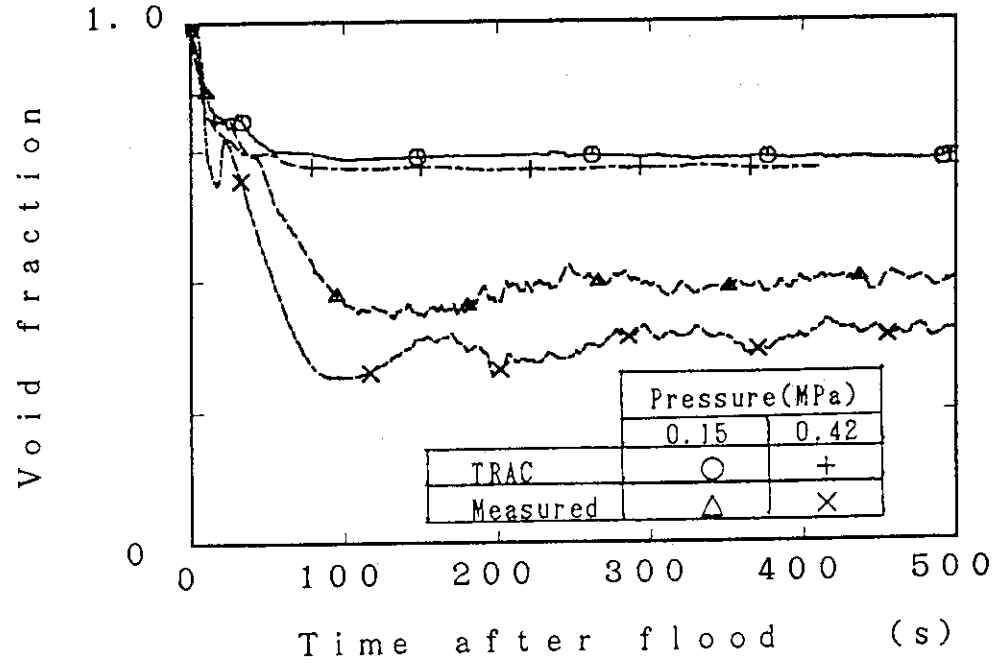

(b) Between 0.61 and 1.22 m

Fig. 4.2.11 Effect of system pressure on void fractions in core

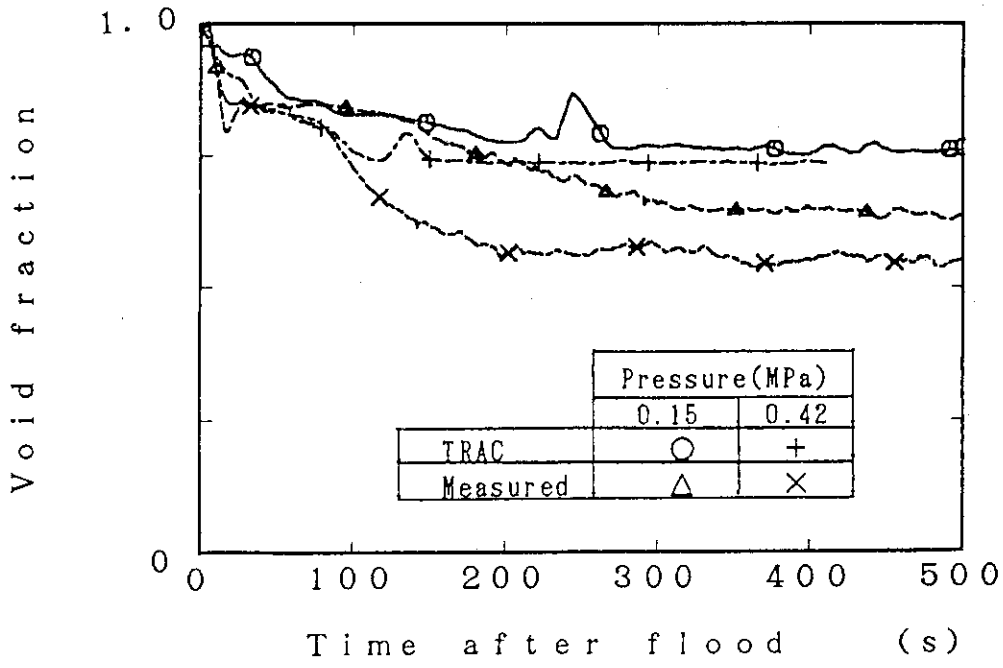

(c) Between 1.22 and 1.83 m

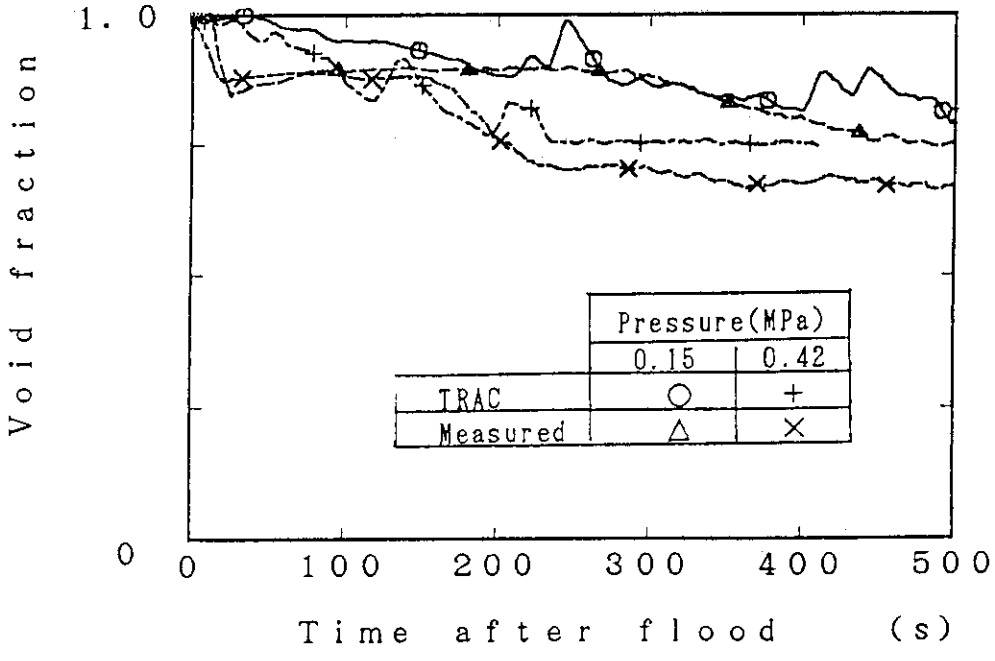

(d) Between 1.83 and 2.44 m

Fig. 4.2.11 (Cont'd)

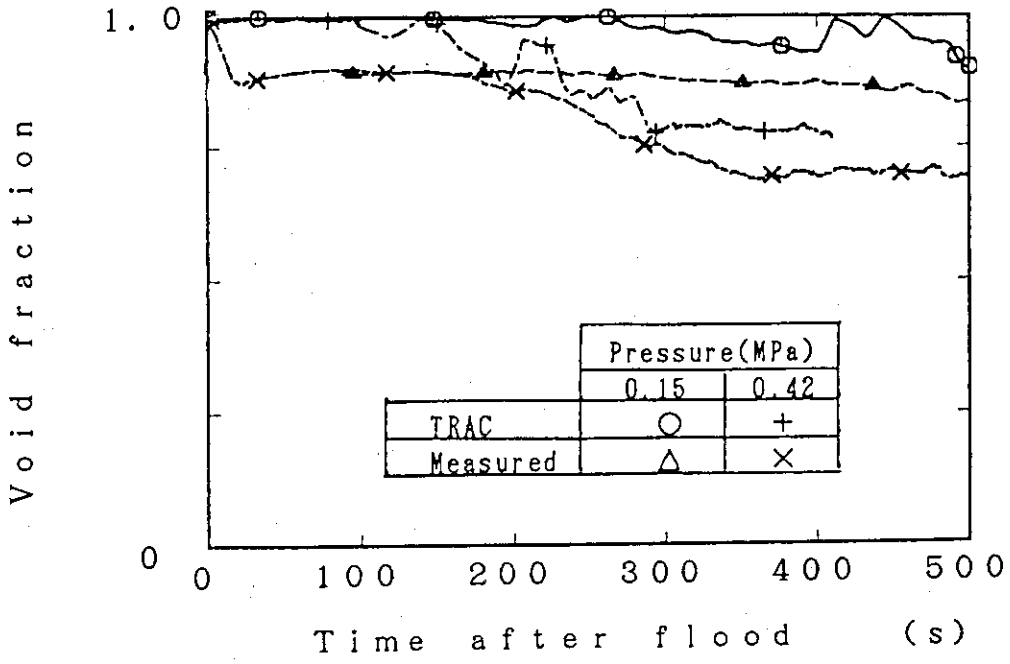

(e) Between 2.44 and 3.05 m

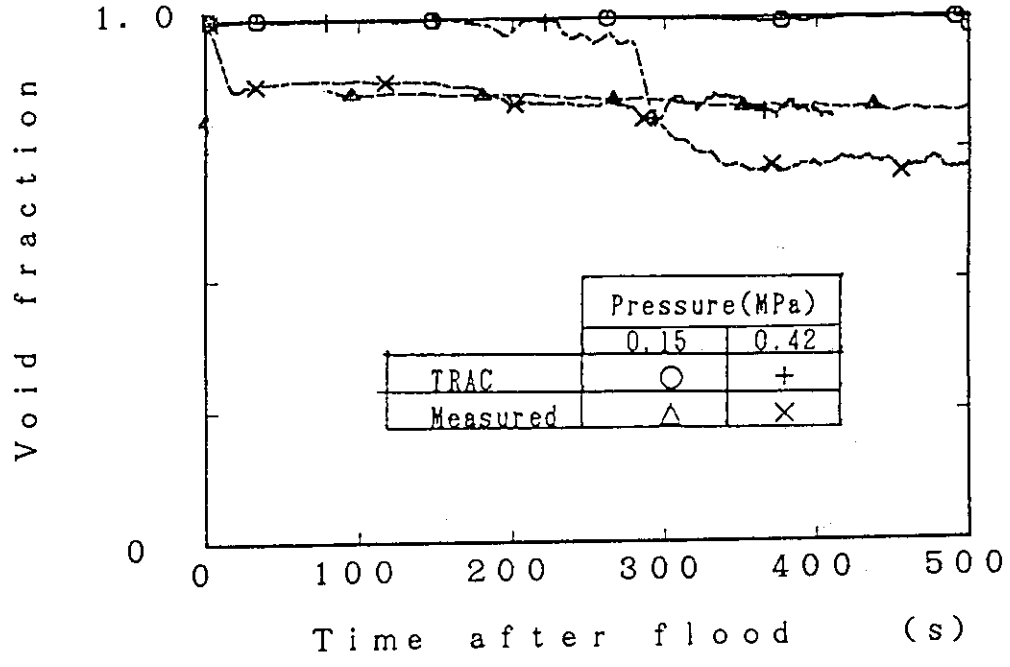

(f) Between 3.05 and 3.66 m

Fig. 4.2.11 (Cont'd)

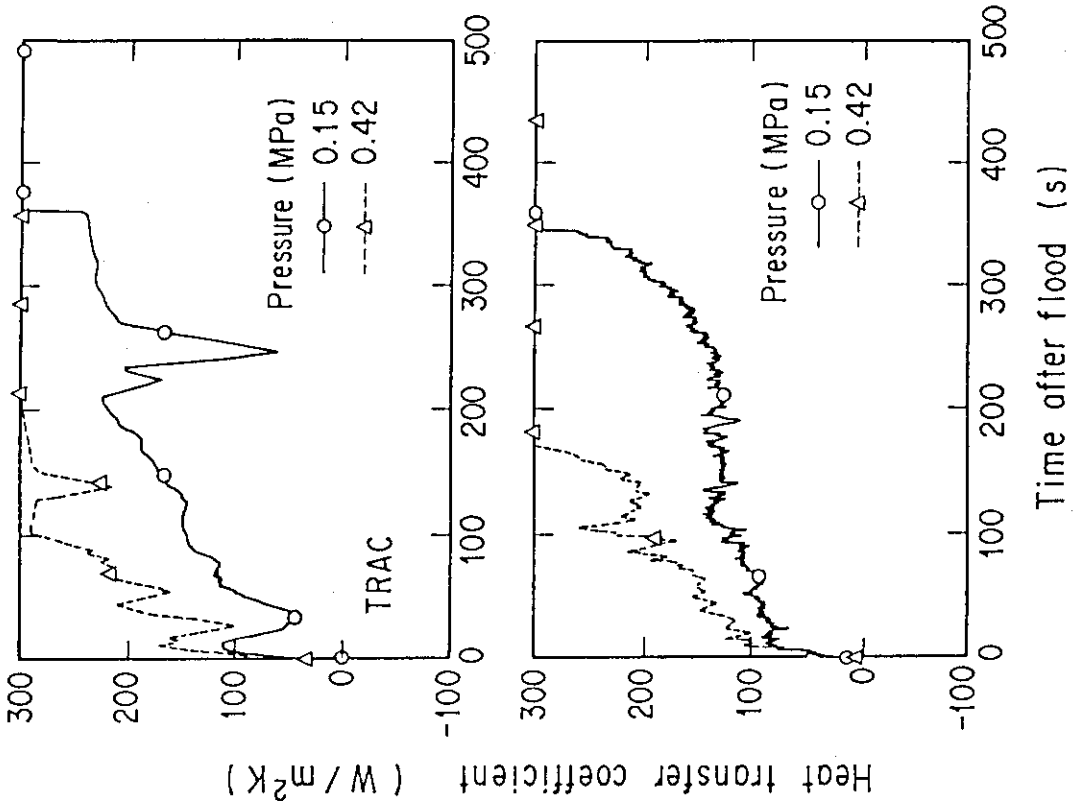

Fig. 4.2.13 Effect of system pressure on heat transfer coefficient at elevation of 1.83 m along a high power rod

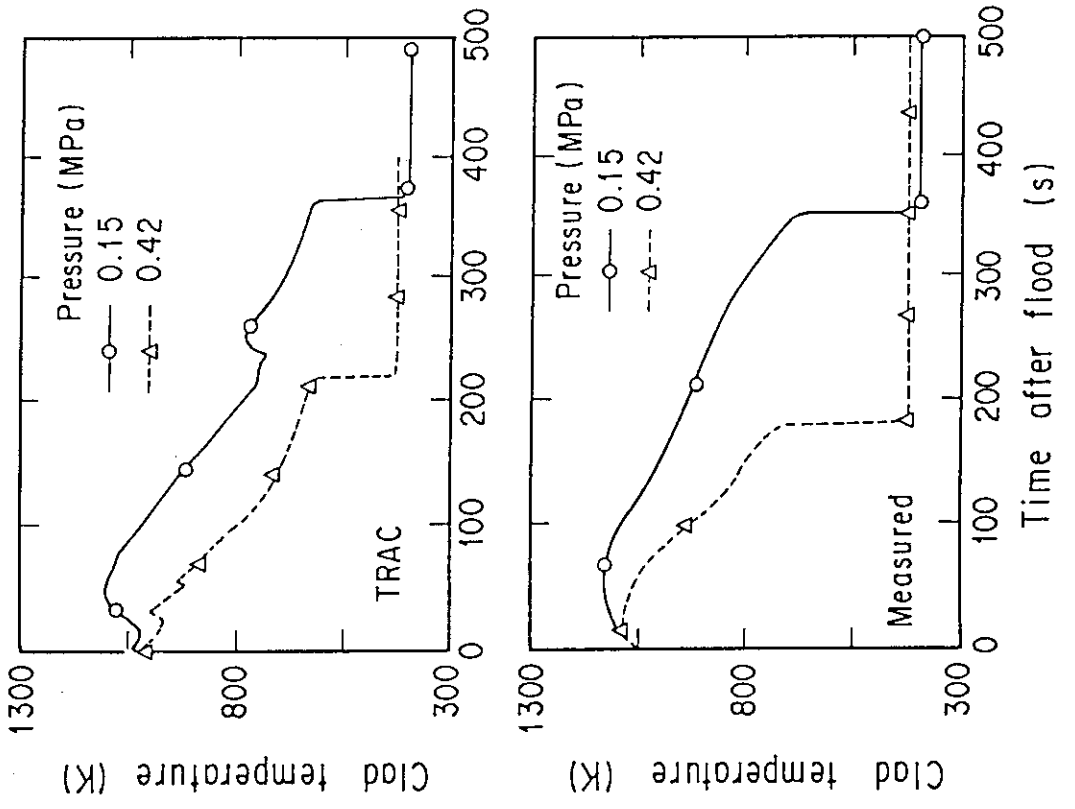

Fig. 4.2.12 Effect of system pressure on clad temperature at elevation of 1.83 m along a high power rod

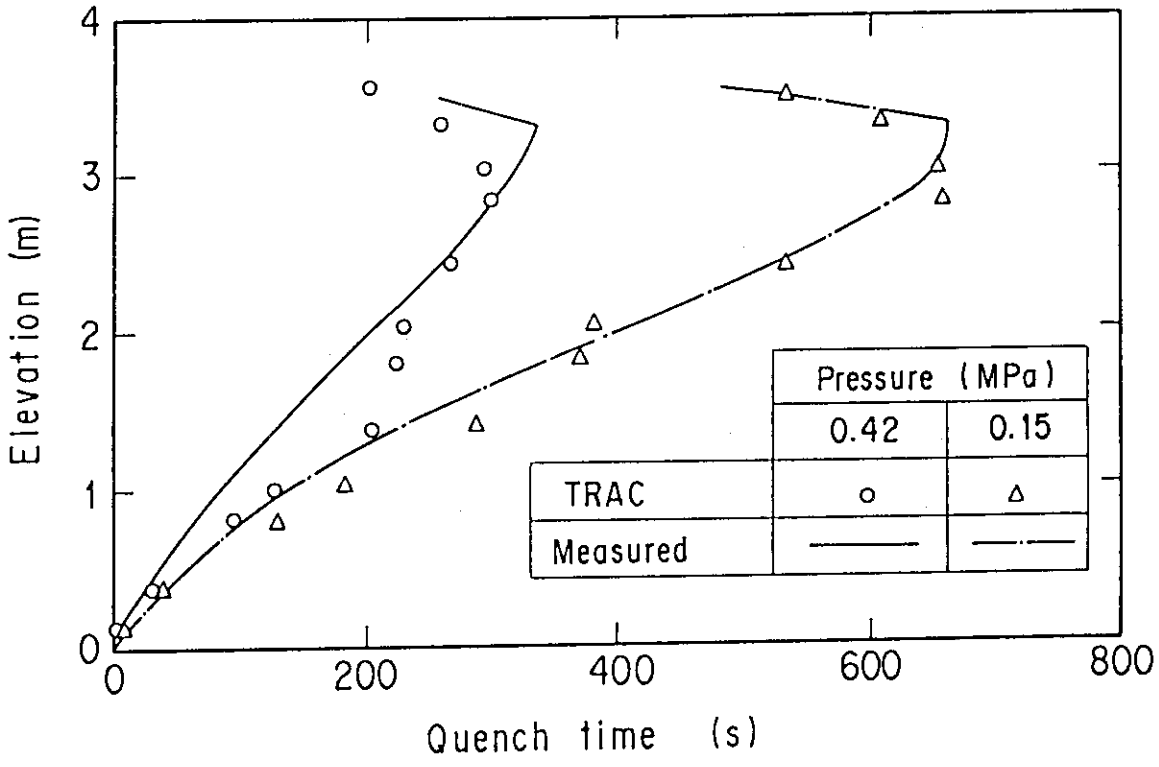

Fig. 4.2.14 Effect of system pressure on quench front propagation along a high power rod

4.3 Assessment for CCTF power level effect tests

In this section, the predictive capability of the TRAC code for the power level effect will be discussed through comparisons between the CCTF low power test and the CCTF base case test.

4.3.1 Comparisons of boundary conditions

Figures 4.3.1 through 4.3.6 show comparisons of boundary conditions. The CCTF low power test was performed under the same test conditions as the CCTF base case test except the core power. The total power is 7.12 MW in the low power test at the reflood initiation and it is 9.35 MW in the CCTF base case test. These total powers correspond to core average linear powers of 1.067 kW/m and 1.40 kW/m, respectively. The power decay curve type is (ANS x 1.0 + 1.1 x Actinide(40 s after scram)) in the low power test, while it is (ANS x 1.2 + 1.1 x Actinide (30 s after scram)) in the base case test. The total power in the low power test is about 76 % of the power in the base case test, as shown in Fig. 4.3.1.

Although the containment pressure was set at 0.20 MPa in both tests, the core outlet pressure of the CCTF base case test is slightly higher than that of the CCTF low power test, as shown in Fig. 4.3.2. The core inlet mass flow rate and core inlet mass flow of the low power test are slightly higher than those of the base case test, as shown in Figs. 4.3.3 and 4.3.4. The core inlet fluid temperature is almost the same between both tests, as shown in Fig. 4.3.5. The core inlet subcooling of the low power test is slightly lower than that of the base case test, as shown in Fig. 4.3.6.

4.3.2 Power level effect on core hydraulic behavior

Figures 4.3.7 through 4.3.10 show power level effect on overall mass balance at core. In the CCTF tests, following tendencies can be observed:

(1) The core inlet mass flow decreases slightly as the core power increases in the later period of the reflood.

(2) The core mass decreases slightly as the core power increases.

(3) The steam mass flow at core outlet increases as the core power increases.

(4) The water mass flow at core outlet decreases as the core power increases.

For the core inlet mass flow, an excellent agreement was obtained because the core inlet mass flow rate was one of input data in these TRAC calculations.

For the core mass, the calculated core mass decreased with the core power as observed in CCTF test results. The TRAC code predicted the core power level effect on the core mass qualitatively. However, the calculated core mass is only about a half of the measured result in the CCTF low power test as observed in the base case test. Figure 4.3.8 shows that a problem of the water accumulation model in the TRAC code is a common problem to a lower power level.

For steam and water mass flows at core outlet, the TRAC code predicted qualitatively the effect of the core power level on these mass flows. In the low power test, the steam mass flow at core outlet is slightly underestimated and the water mass flow at core outlet is slightly overpredicted, as in the analysis of the CCTF base case test.

Figure 4.3.11 shows comparisons of void fractions at various elevations in core. In the low power test, the void fraction is overestimated in the lower part of the core and it is nearly constant regardless of the elevation in the center part of the core as observed for the CCTF base case test. The void fraction is nearly equal to unity in the upper part of the core before the quench front reach the cell as observed for the CCTF base case test.

These comparisons show that the TRAC code predicted qualitatively the effect of the core power level on the overall mass balance through the core and that the core mass was underpredicted even in the low power case in quantity.

4.3.3 Power level effect on core thermal behavior

Figure 4.3.12 shows clad temperature at elevation of 1.83 m along a high power rod in the low power and the base case tests. The low power level resulted in low turnaround temperature and fast quench propagation in both CCTF test and TRAC calculation. The low power level resulted in the high heat transfer coefficient as shown in Fig. 4.3.13 in CCTF test and TRAC calculation. Figure 4.3.14 shows a comparison of quench envelope along a high power rod between the low power test and the base case test. The effect of the core power level on the quench front propagation is predicted excellently by the TRAC code. The TRAC code predicted excellently the core power level effect on clad temperature histories.

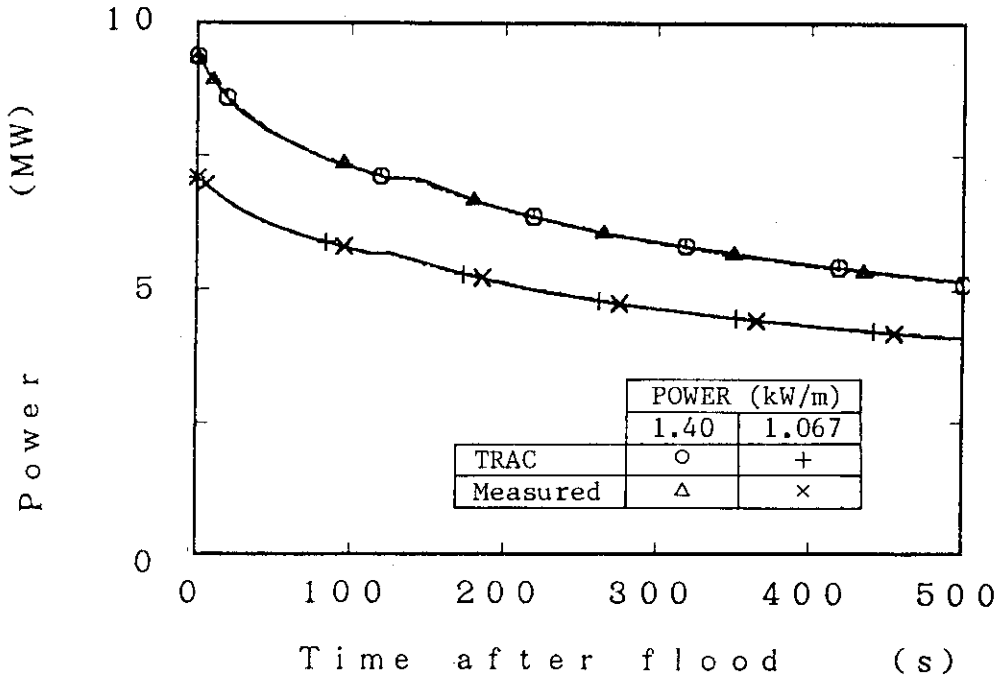

Fig. 4.3.1 Comparison of core power between low and high power tests

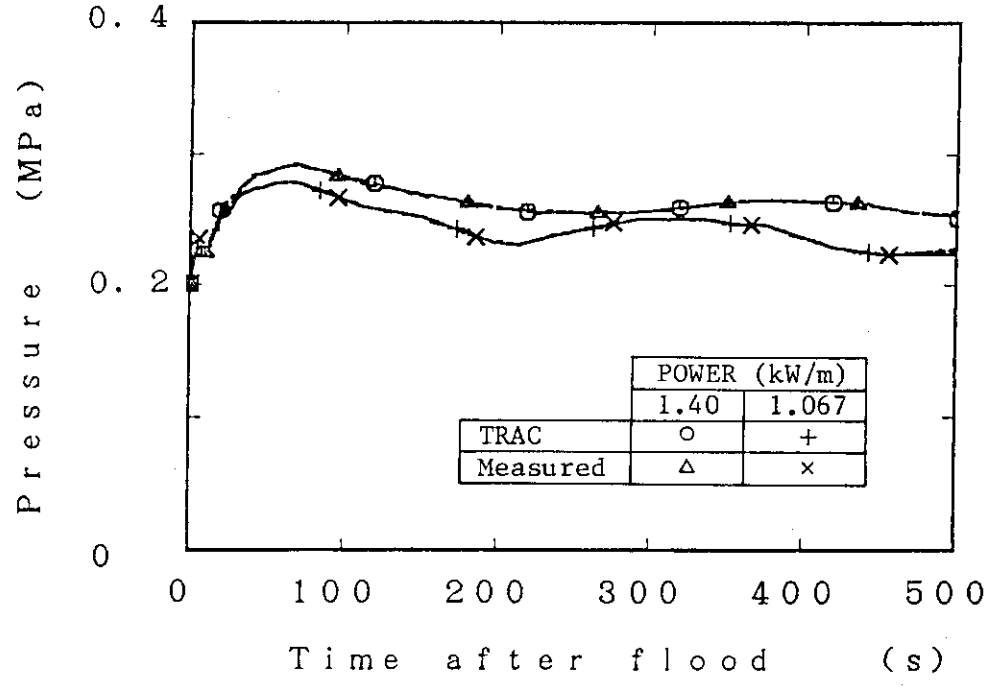

Fig. 4.3.2 Comparison of core outlet pressure between low and high power tests

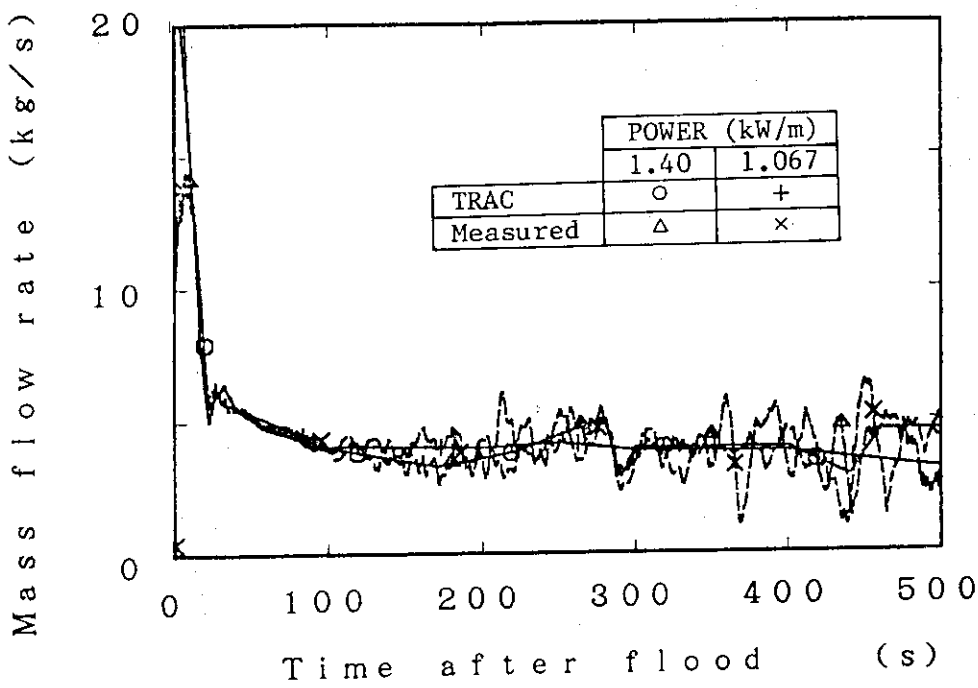

Fig. 4.3.3 Comparison of core inlet mass flow rate between low and high power tests

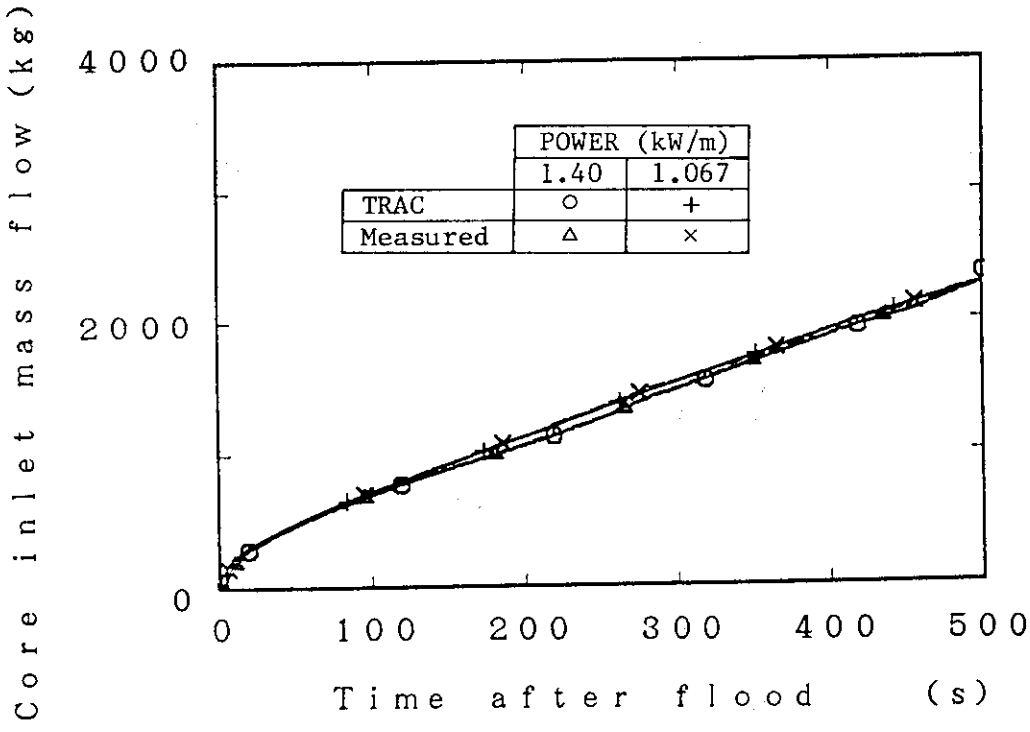

Fig. 4.3.4 Comparison of core inlet mass flow between low and high power tests

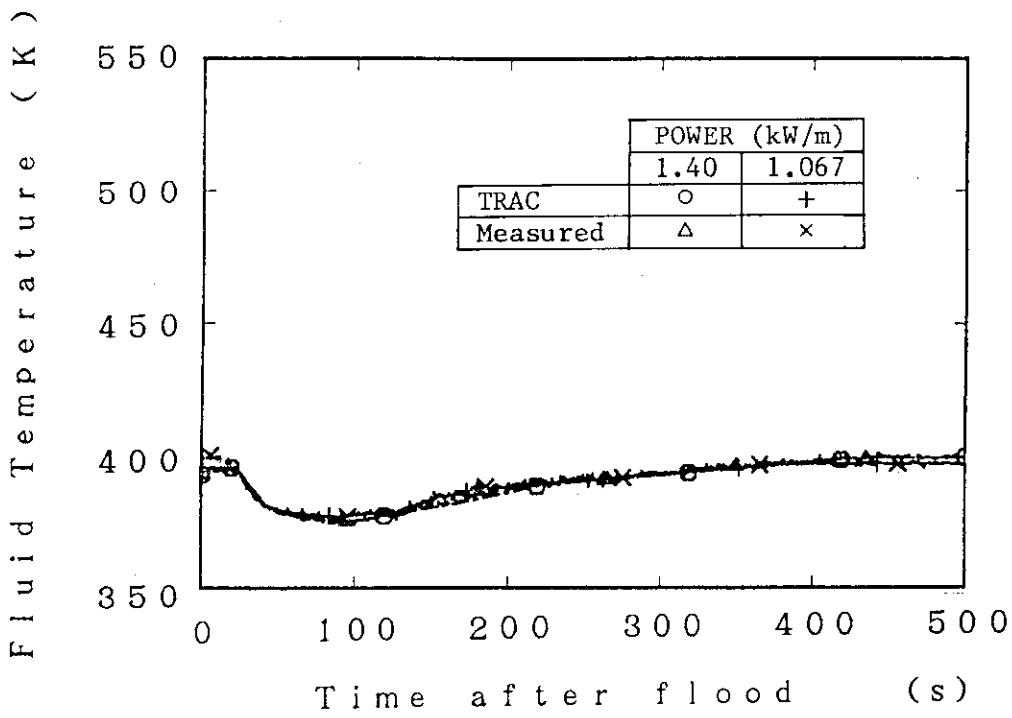

Fig. 4.3.5 Comparison of core inlet fluid temperature between low and high power tests

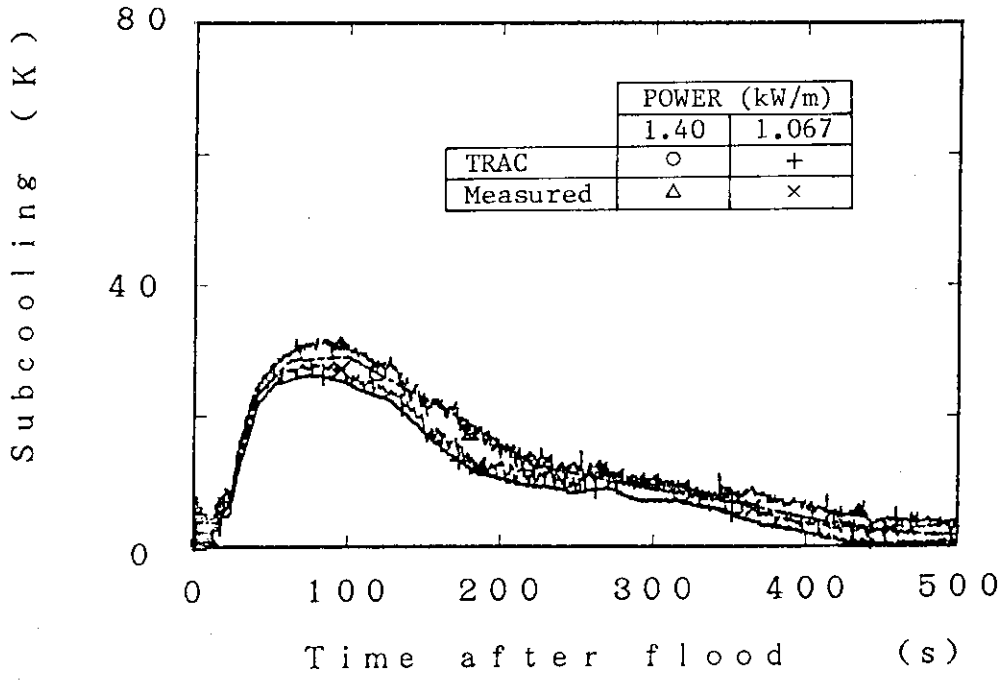

Fig. 4.3.6 Comparison of core inlet subcooling between low and high power tests

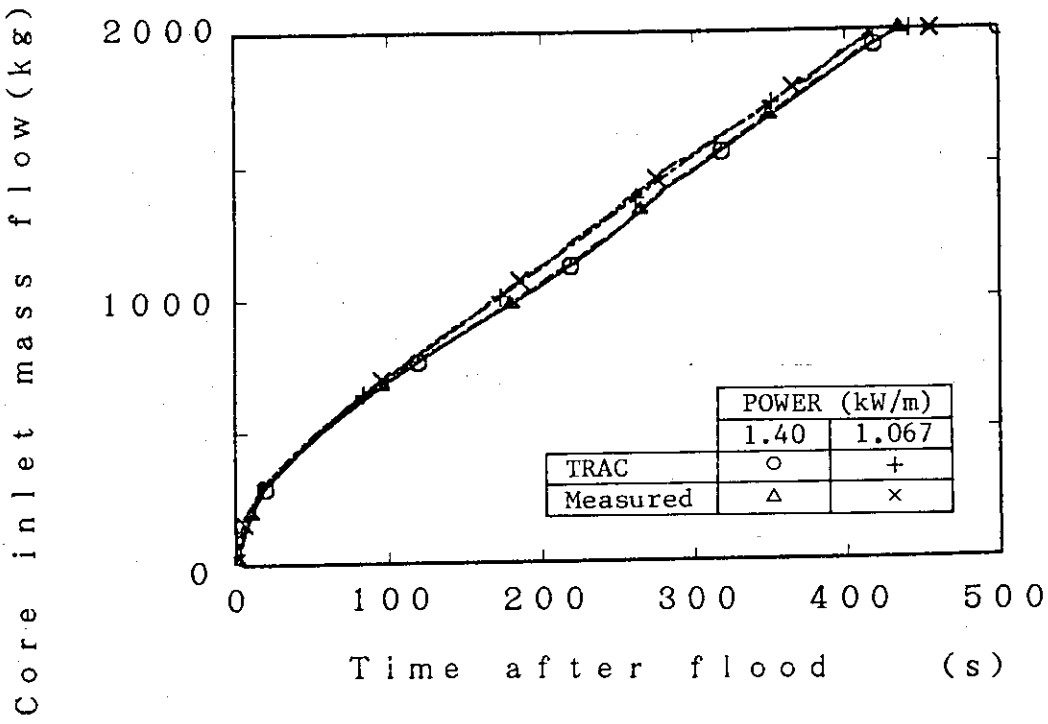

Fig. 4.3.7 Effect of power level on core inlet mass flow

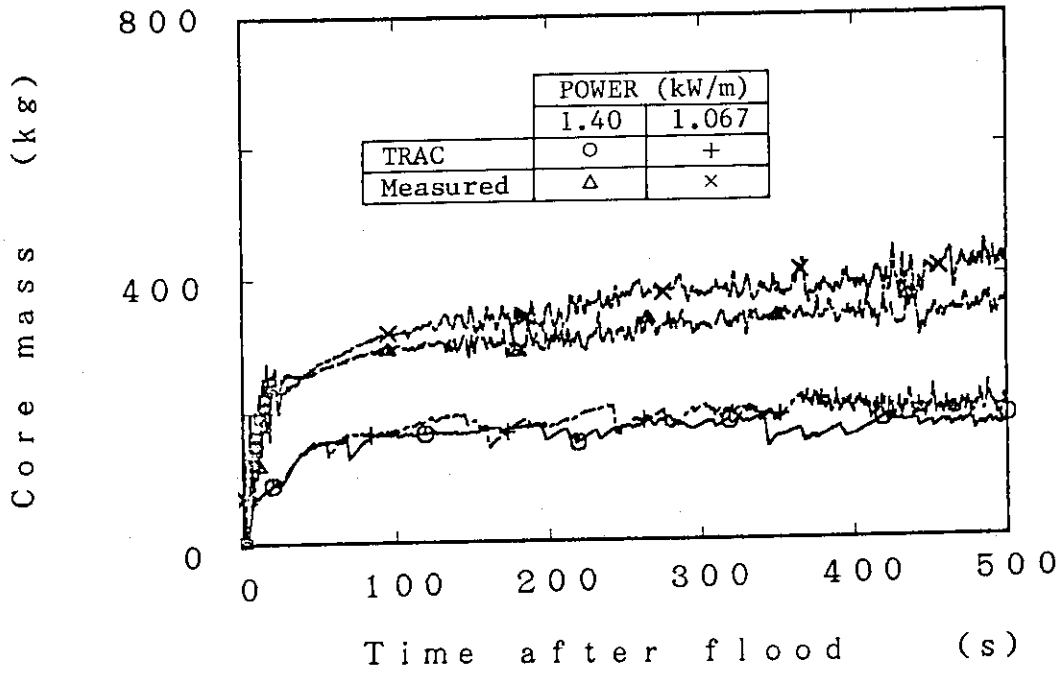

Fig. 4.3.8 Effect of power level on core mass

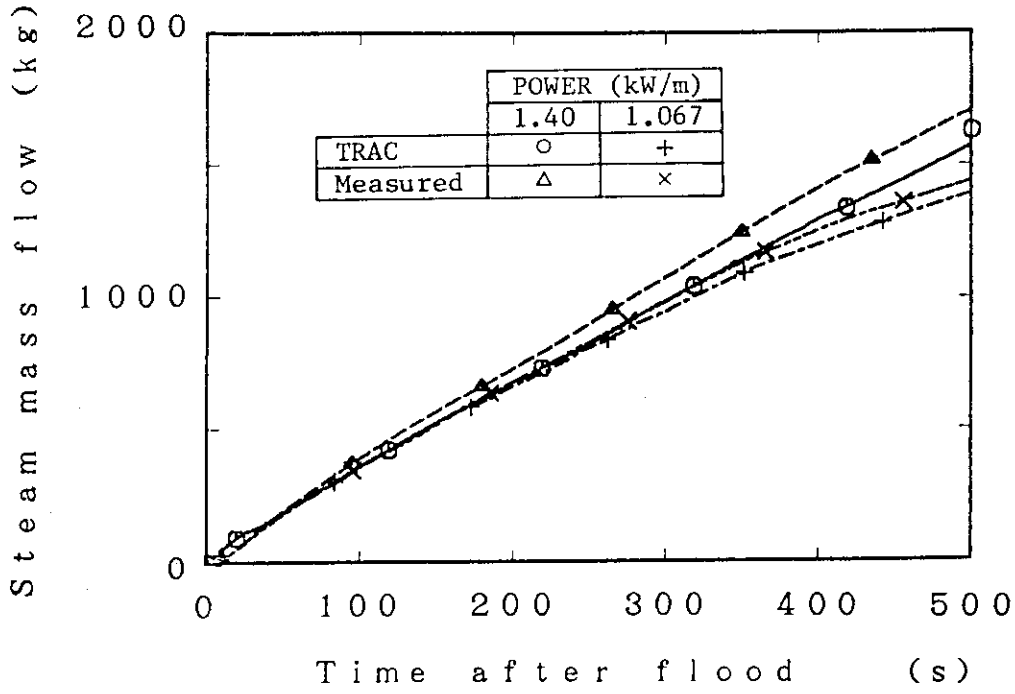

Fig. 4.3.9 Effect of power level on steam mass flow at core outlet

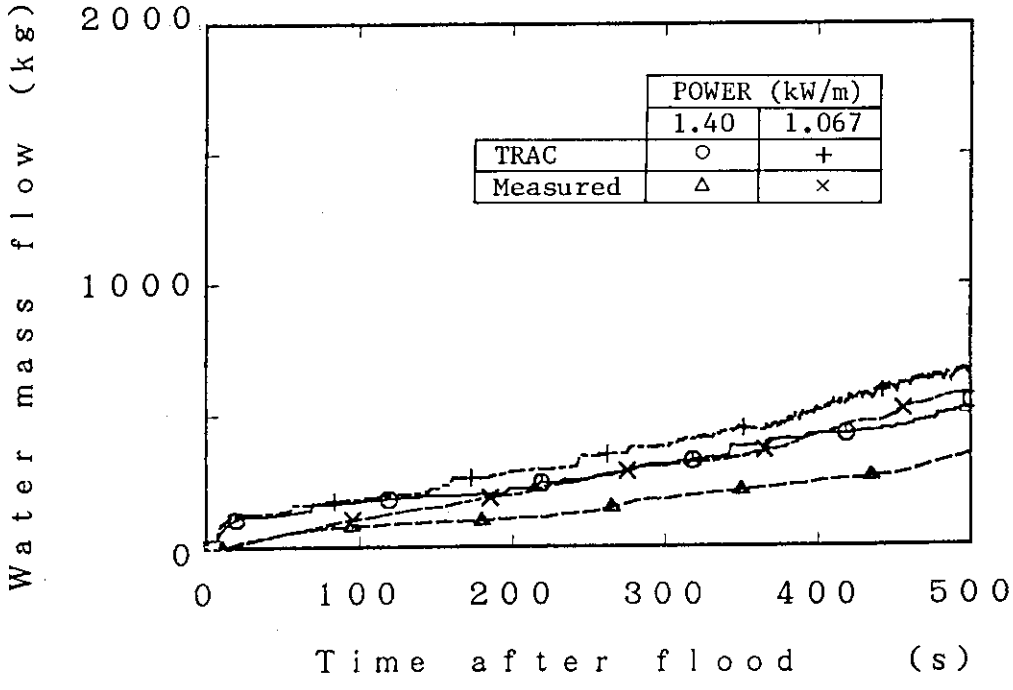

Fig. 4.3.10 Effect of power level on water mass flow at core outlet

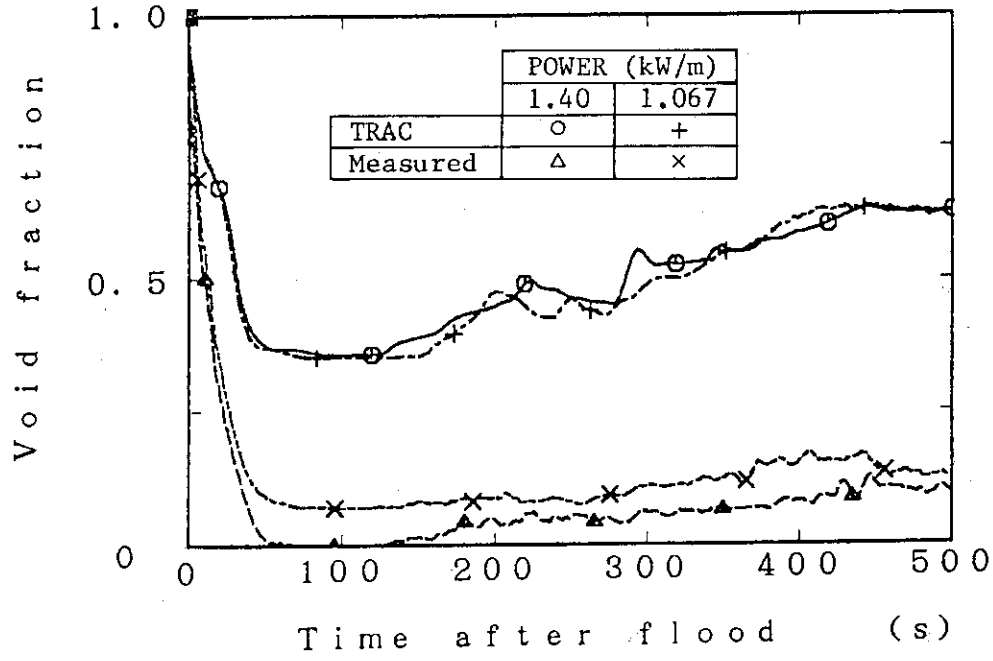

(a) Between 0.00 and 0.61 m

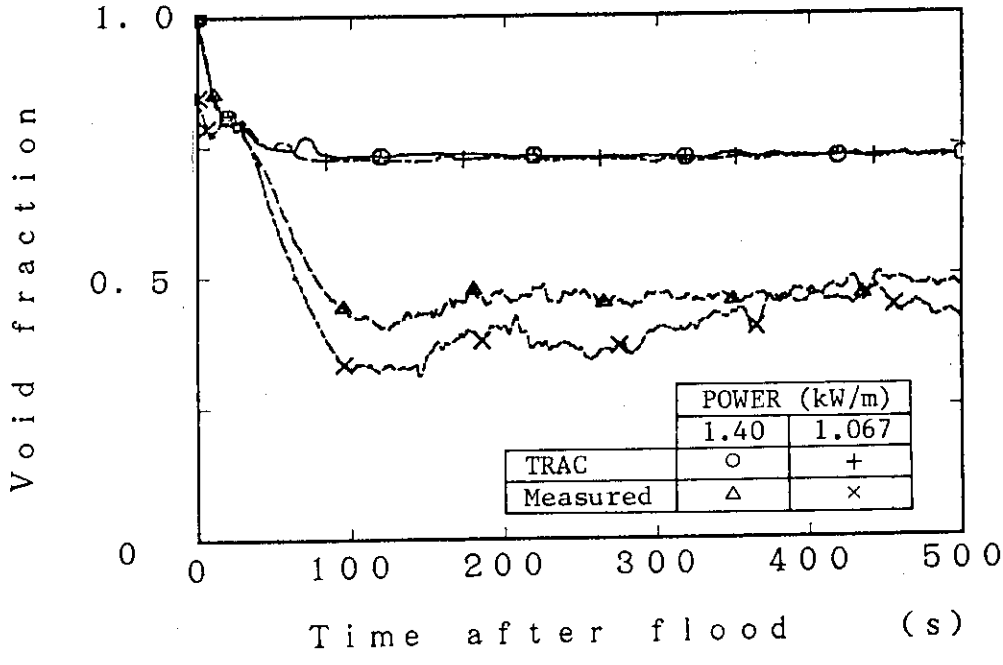

(b) Between 0.61 and 1.22 m

Fig. 4.3.11 Effect of power level on void fractions in core

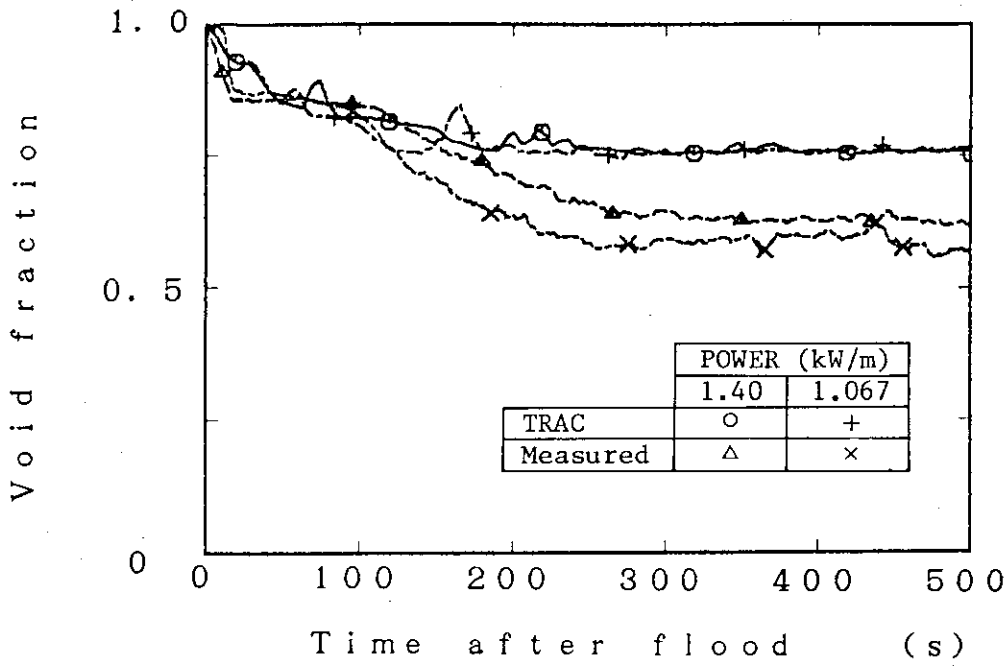

(c) Between 1. 22 and 1. 83 m

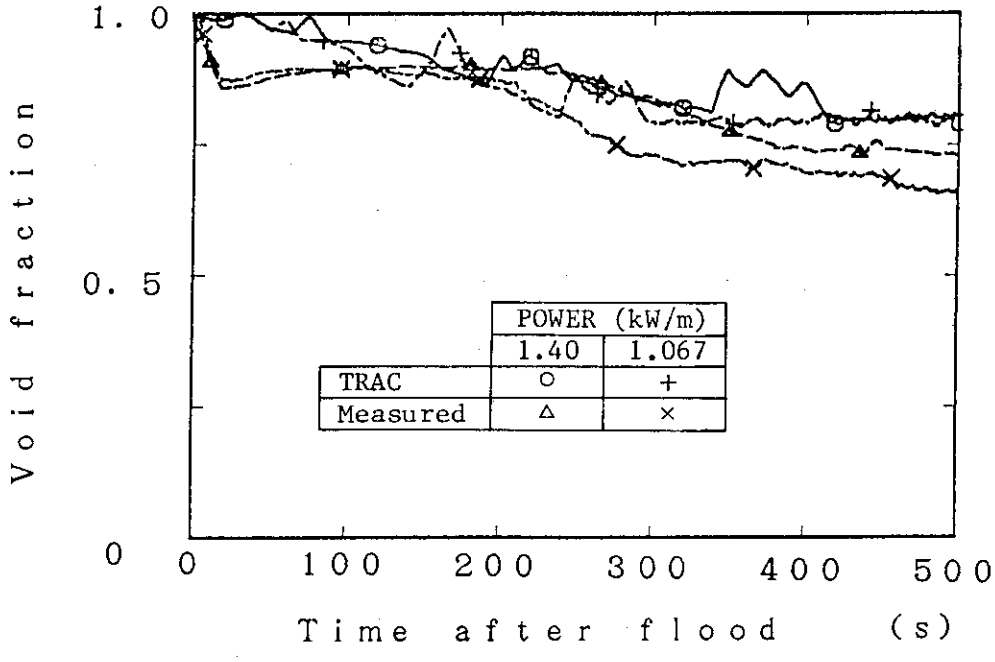

(d) Between 1. 83 and 2. 44 m

Fig. 4.3.11 (Cont'd)

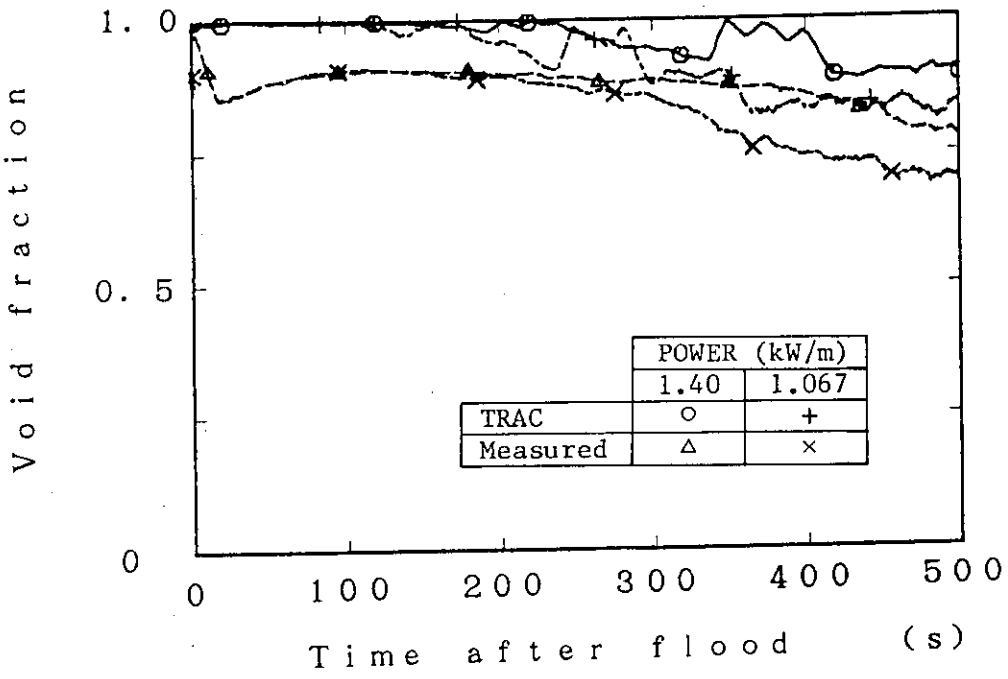

(e) Between 2.44 and 3.05 m

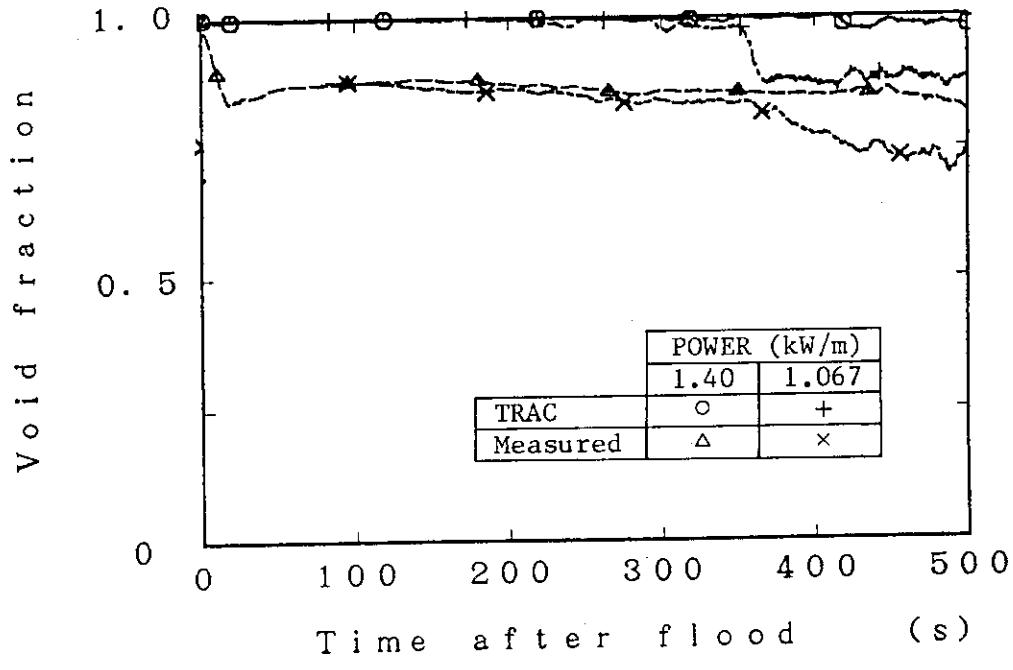

(f) Between 3.05 and 3.66 m

Fig. 4.3.11 (Cont'd)

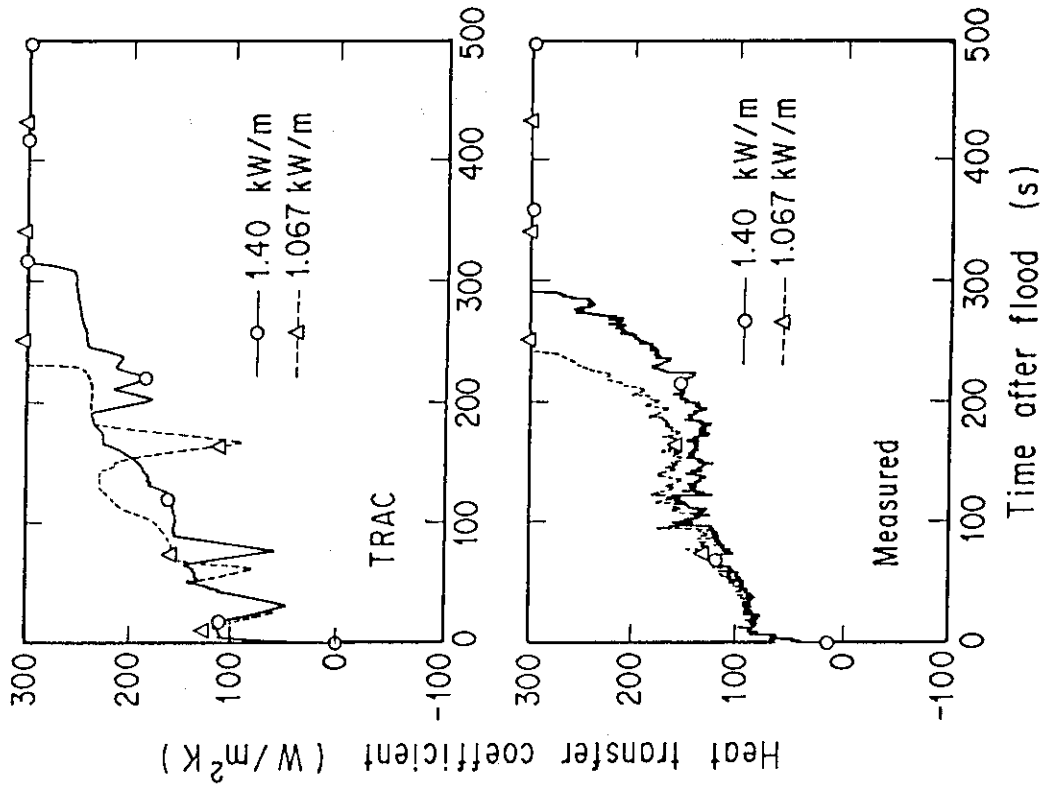

Fig. 4.3.13 Effect of power level on heat transfer coefficient at elevation of 1.83 m along a high power rod

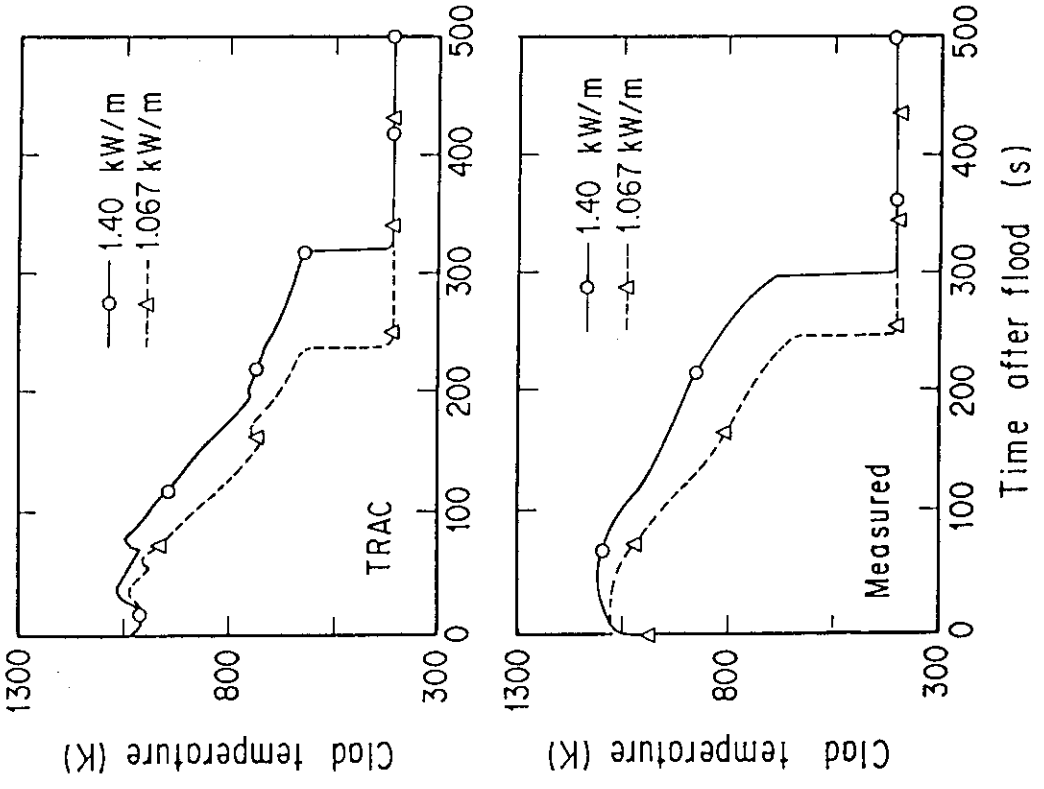

Fig. 4.3.12 Effect of power level on clad temperature at elevation of 1.83 m along a high power rod

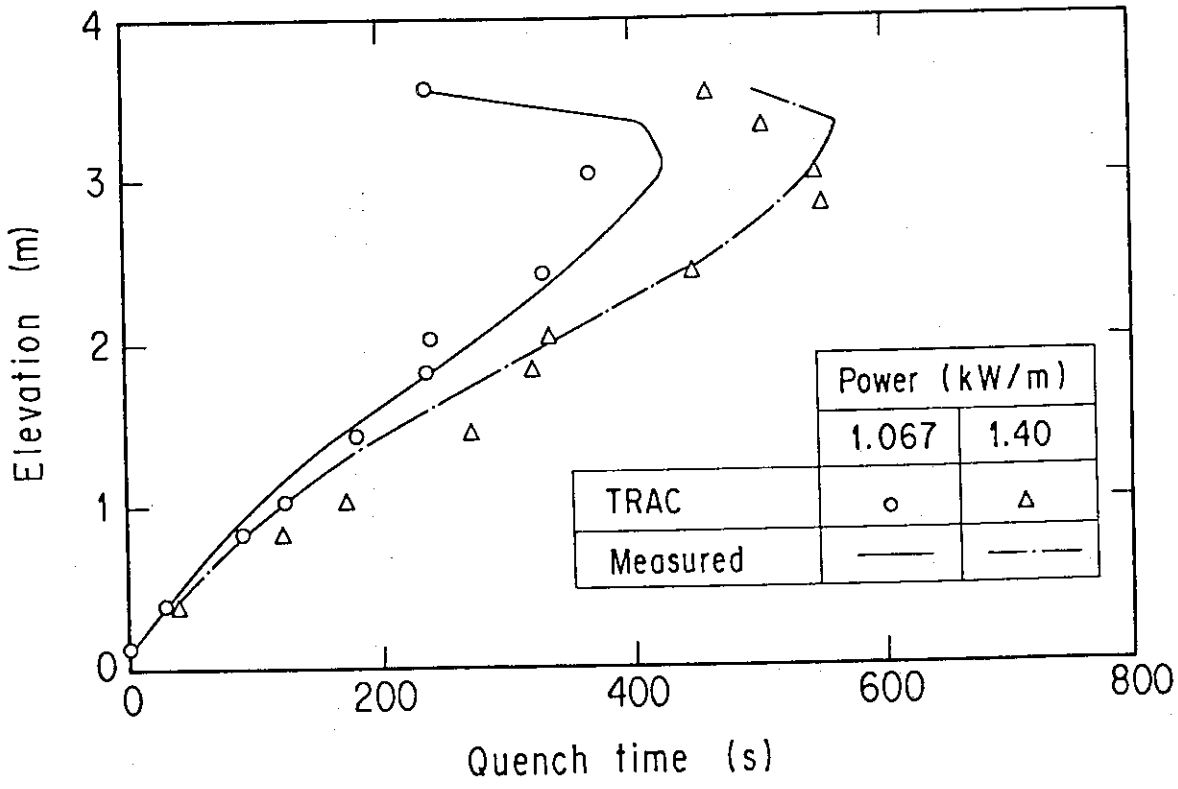

Fig. 4.3.14 Effect of power level on quench front propagation along a high power rod

4.4 Assessment for CCTF best estimate test

Figure 4.4.1 shows a core power history in the CCTF best-estimate test. Figure 4.4.2 shows core outlet pressure in the CCTF best-estimate test. The best-estimate test was performed at lower power level and higher system pressure than the CCTF base case test.

Figure 4.4.3 shows the core inlet mass flow rate in the CCTF best-estimate test. In the CCTF best-estimate test, oscillatory core inlet mass flow rate was observed due to the system effect.[9] In the TRAC calculation, the core inlet mass flow rate and core inlet fluid temperature were specified by a FILL component with measured results. However, the calculated fluid temperature was higher than measured result when the core inlet mass flow rate is negative, as shown in Fig. 4.4.4. When the core inlet mass flow rate is negative, the fluid temperature at the core inlet is determined by the fluid temperature at the bottom part of the core not by the fluid temperature specified by the FILL component.

Another important boundary condition of the CCTF best-estimate test is clad temperatures at reflood initiation. The peak clad temperature at reflood initiation is about 600 K in the CCTF best-estimate test, as shown in Fig. 4.4.5. At the pressure of 0.3 MPa, the transition temperature between the transition boiling regime and the film boiling regime was calculated to be 610 K with the correlation used in the TRAC code (see Eq. (A.23) in Appendix A). The peak clad temperature at reflood initiation is lower than the transition temperature from the film boiling regime to the transition boiling in the TRAC calculation.

Figure 4.4.6 shows core mass in the CCTF best-estimate test. The calculated core mass is lower by about 150 kg than measured result. Figure 4.4.7 show void fractions at various elevations of the core. The void fraction in the lower part of the core is overpredicted by the TRAC code. The constant void fraction about 0.75 is frequently calculated in the center part of the core. These results in the CCTF best-estimate test are similar to those in the CCTF base case test although the flow conditions are quite different.

Figure 4.4.8 shows comparisons of clad temperatures for the CCTF best-estimate test between measured and calculated results. Quick quench was calculated by the TRAC code at various elevations compared to measured results. Figure 4.4.9 illustrates heat transfer regimes in the TRAC calculation. The transition boiling or the nucleate boiling regimes

are selected in the TRAC calculation at various elevations. Thus, high heat transfer coefficients was calculated and caused quick quench at various elevations in the TRAC calculation.

Figure 4.4.10 illustrates boiling curve and quench behavior. For the boiling transition from film boiling to transition boiling, two limit temperatures are well known; one is homogeneous nucleation temperature and the other is minimum film boiling temperature. In the TRAC code, only the homogeneous nucleation temperature is modeled as a transition temperature between the film boiling and the transition boiling. The transition temperature was calculated to be about 610 K with the correlation in the TRAC code. Because of low clad temperature in the CCTF best estimate test, the quick quench was calculated by the TRAC code. On the other hand, low heat transfer coefficient was observed in the CCTF test for about 100 s as shown in Fig. 4.4.8. The clad temperature at reflood initiation of the CCTF best-estimate test is considered to be between the homogeneous nucleation and the minimum film boiling temperature as illustrated point B in Fig. 4.4.10. It is recommended to model two transition temperatures for boiling transition between film boiling and transition boiling regimes.

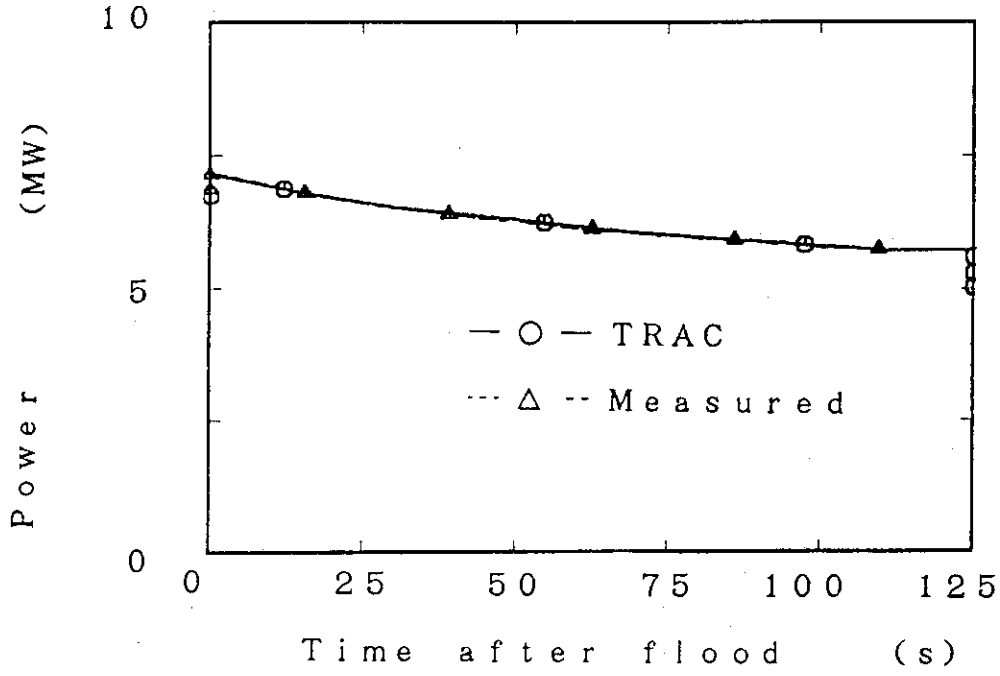

Fig. 4.4.1 Core power in CCTF best estimate test

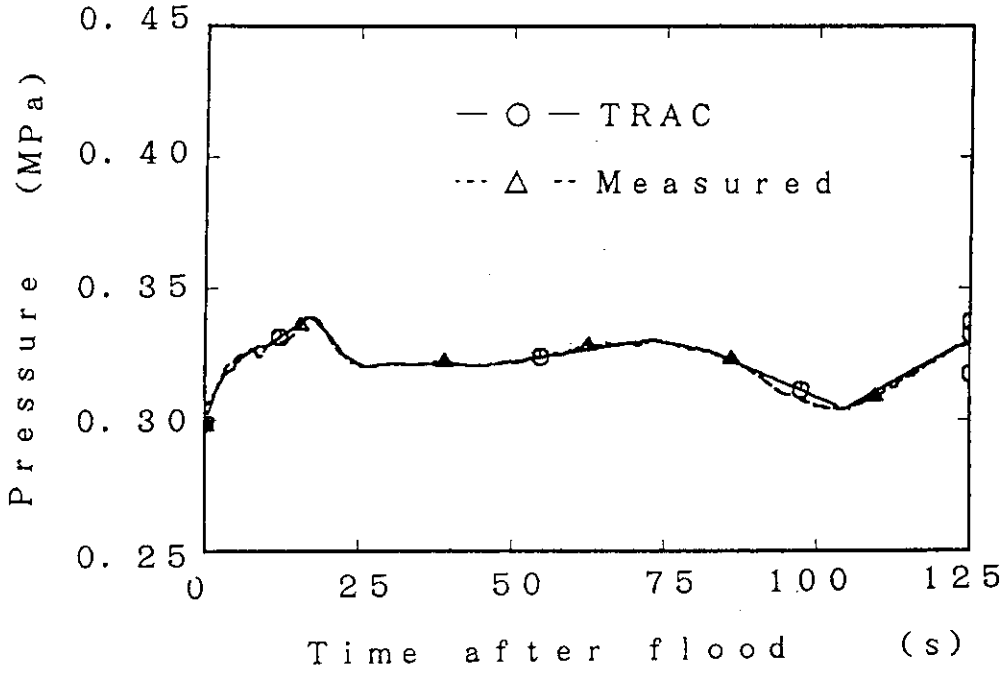

Fig. 4.4.2 Core outlet pressure in CCTF best estimate test

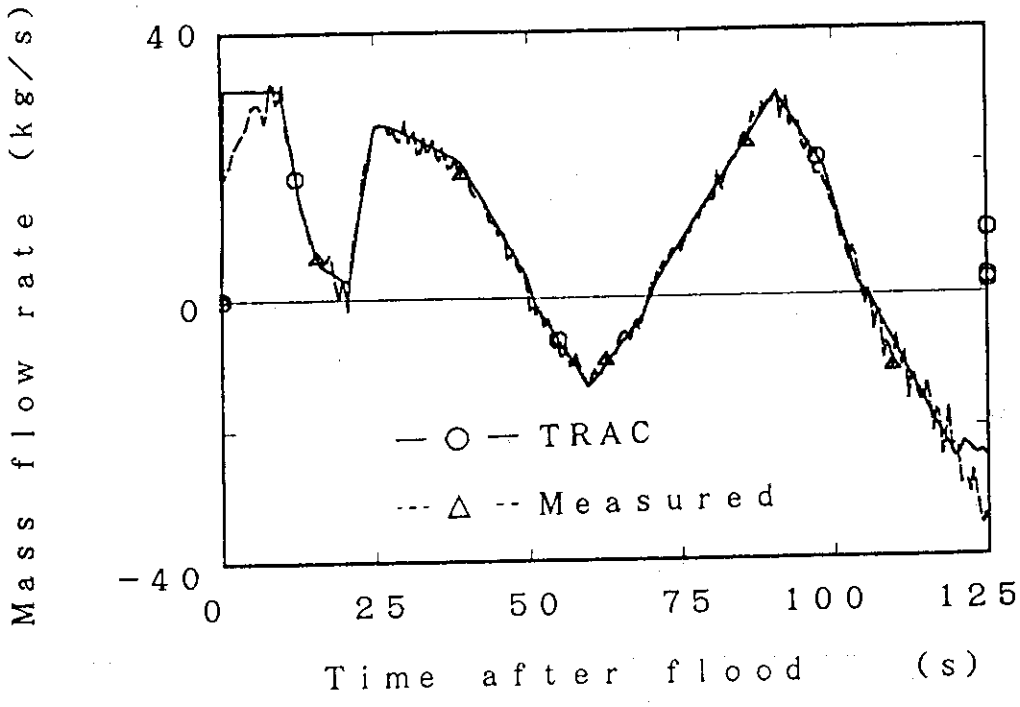

Fig. 4.4.3 Core inlet mass flow rate in CCTF best estimate test

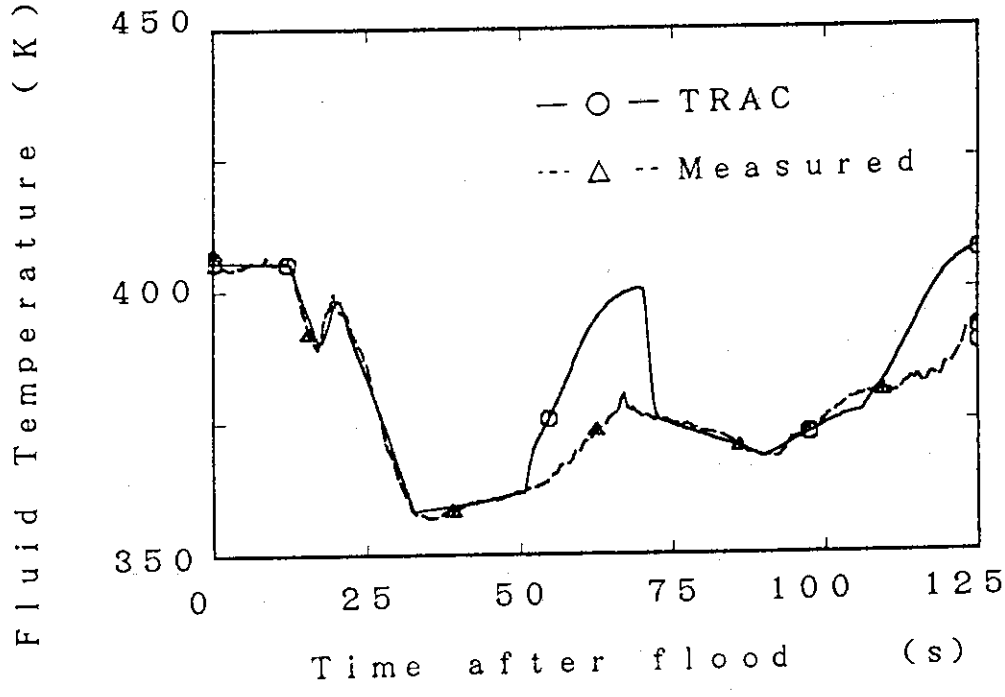

Fig. 4.4.4 Core inlet fluid temperature in CCTF best estimate test

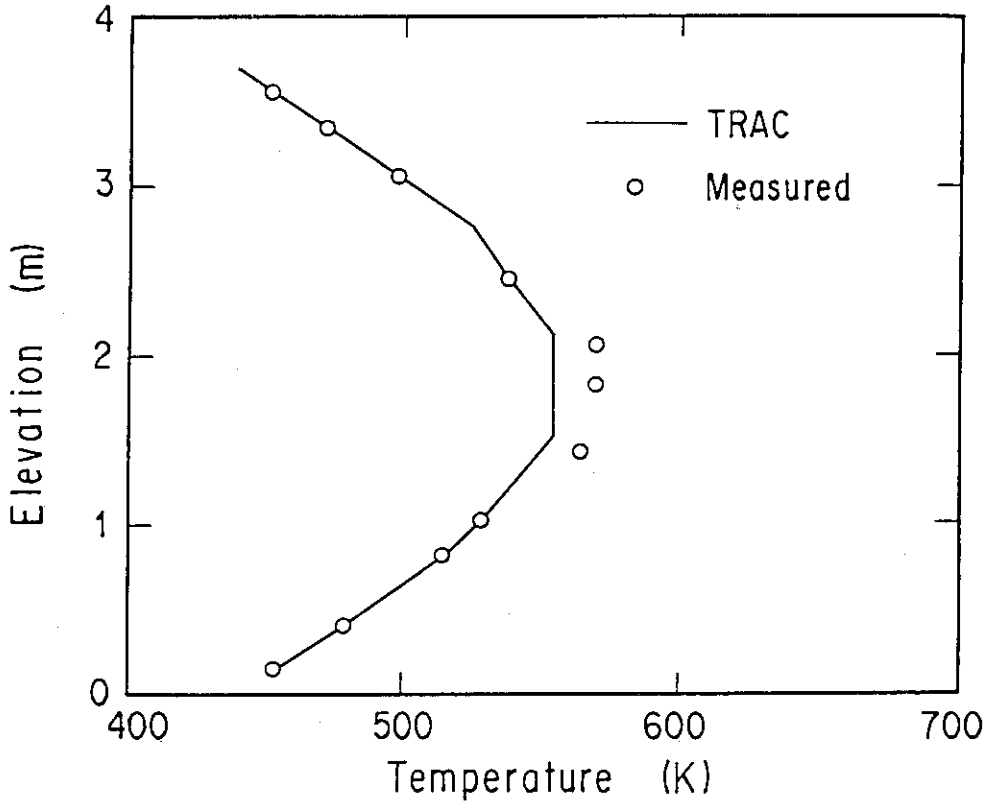

Fig. 4.4.5 Initial clad temperature in CCTF best estimate test

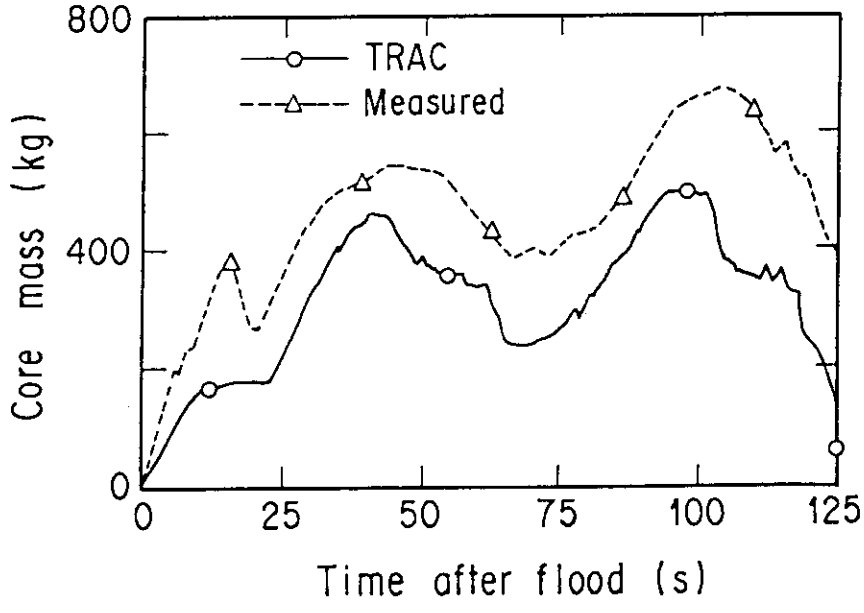

Fig. 4.4.6 Core mass in CCTF best estimate test

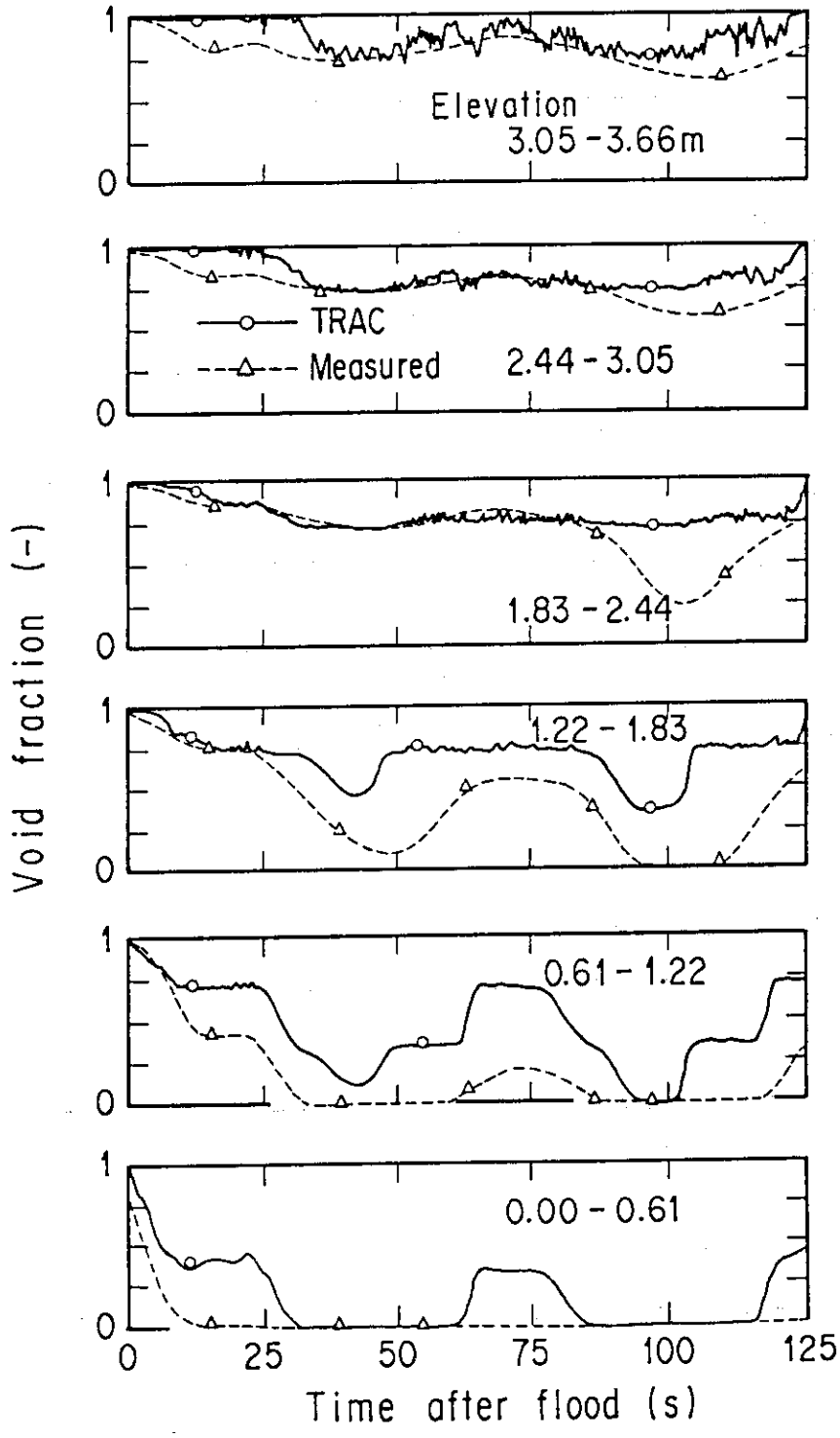

Fig. 4.4.7 Void fractions in core of CCTF best estimate test

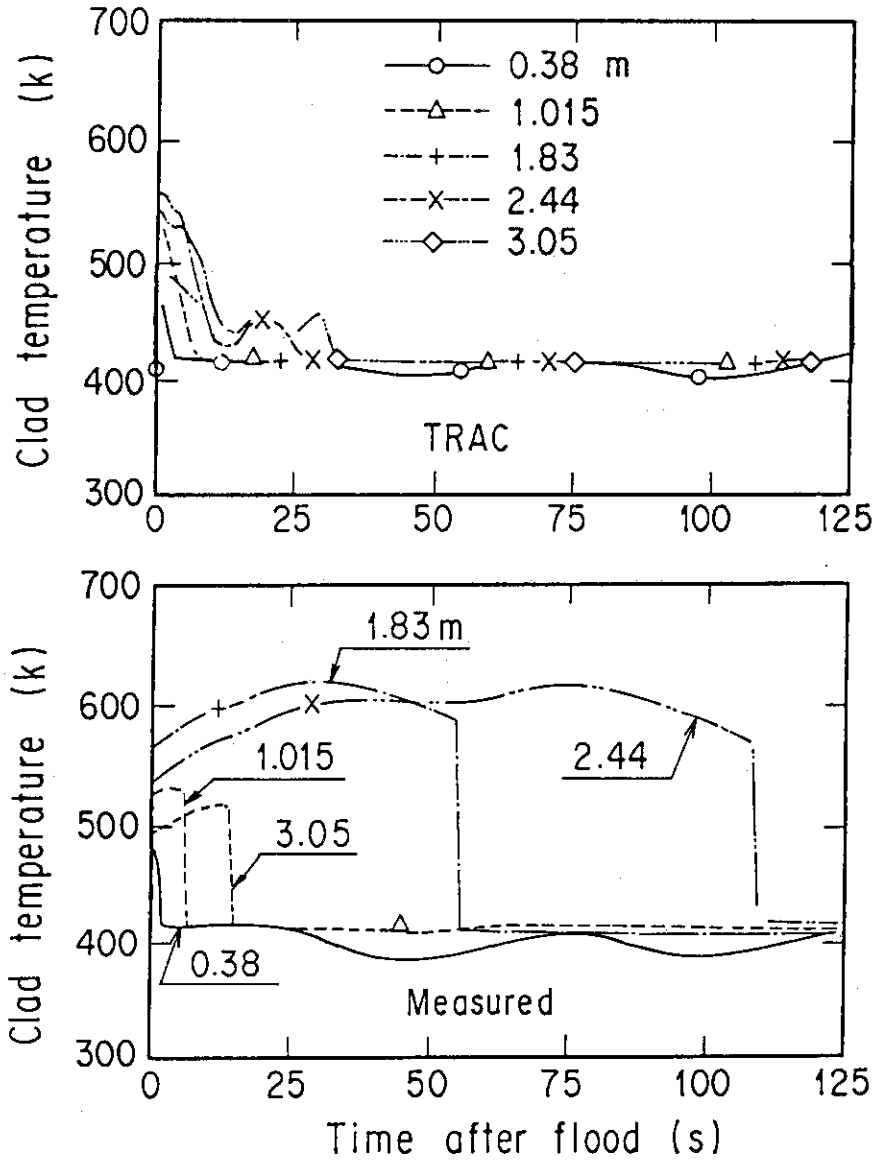

Fig. 4.4.8 Clad temperature in CCTF best estimate test

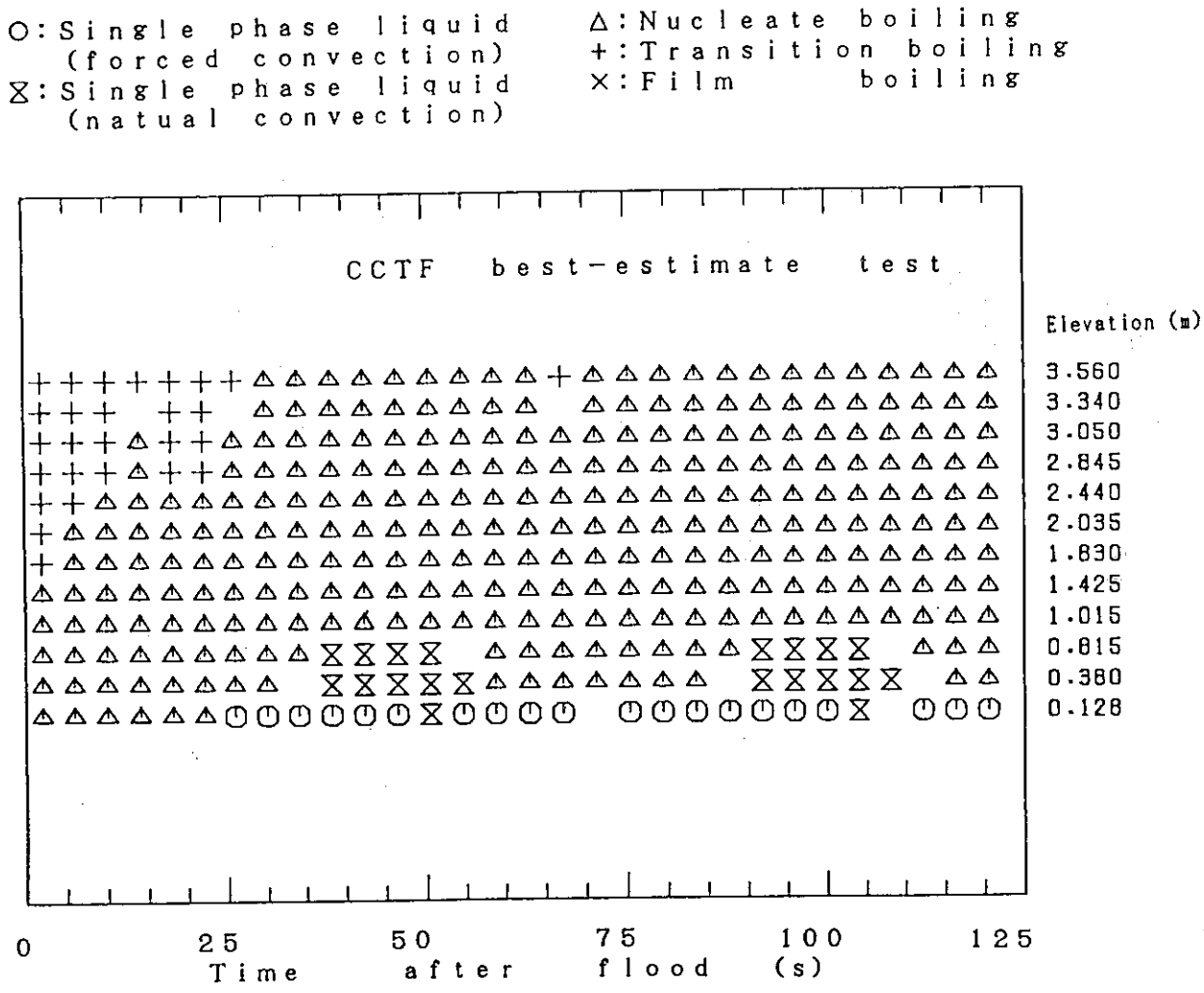

Fig. 4.4.9 Wall heat transfer regime along a heater rod in CCTF best estimate test

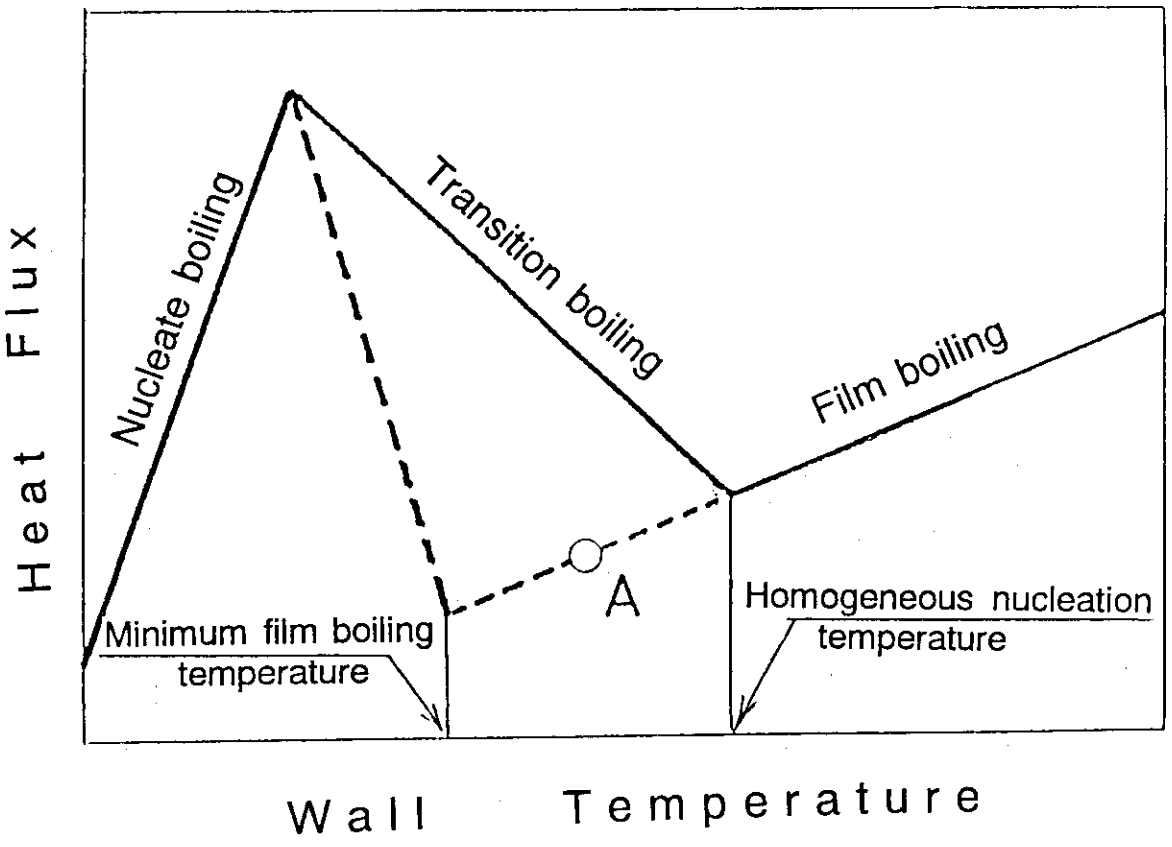

Fig. 4.4.10 Boiling curve and quench behavior

4.5 Assessment for SCTF flat power test

Figure 4.5.1 shows the core power history in the SCTF flat power test. Figure 4.5.2 shows the core outlet pressure in the SCTF flat power test. The SCTF flat power test was performed at the same power level and pressure as the CCTF low power test. Figures 4.5.3 and 4.5.4 show the core inlet mass flow rate and fluid temperature in the SCTF flat power test. The core inlet mass flow rate of the SCTF flat power test is slightly higher than that of the CCTF low power test.

Figure 4.5.5 shows comparisons of core void fractions at various elevations in the SCTF flat power test. The test results were inferred to differential pressure data assuming no friction and acceleration losses. The void fractions from the TRAC calculation were calculated by averaging with a weight of cell length to match the elevation for measured results.

The calculated void fraction is higher than the measured one at the lower part of the core(below 1.365 m). At elevation between 0.70 and 1.365 m, TRAC result shows almost constant void fraction after 20 s. In the center part and the top part of the core(above 1.365 m), TRAC results tend to approach the void fraction of 0.75 with time. In the top part of the core(between 2.695 and 3.235 m), the void fraction drops to about 0.90 right after the reflood initiation in the measured result, while it is almost unity in the TRAC calculation by about 200 s. Although the core configuration of the SCTF is different from that of the CCTF, similar differences between measured and calculated results were observed.

Figure 4.5.6 shows clad temperature at elevation of 1.905 m in the SCTF flat power test. The TRAC result shows slightly lower turnaround temperature and faster quench time than the measured result. The TRAC code predicted higher heat transfer coefficient than the measured result as shown in Fig. 4.5.7. Then, the TRAC code predicted faster quench propagation than the measured result as shown in Fig. 4.5.8.

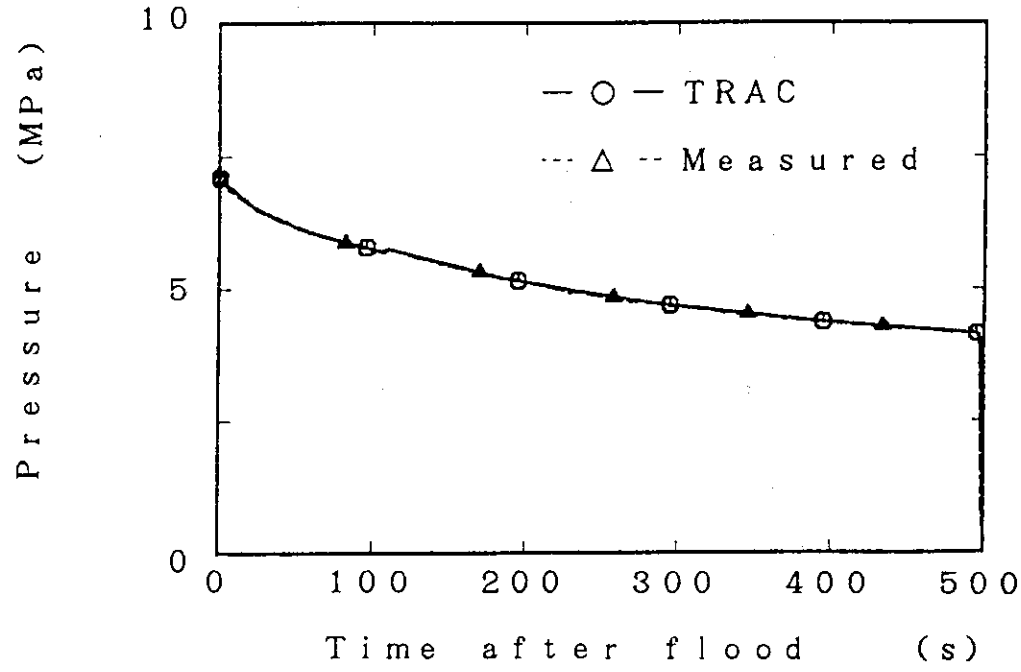

Fig. 4.5.1 Core power in SCTF flat power test

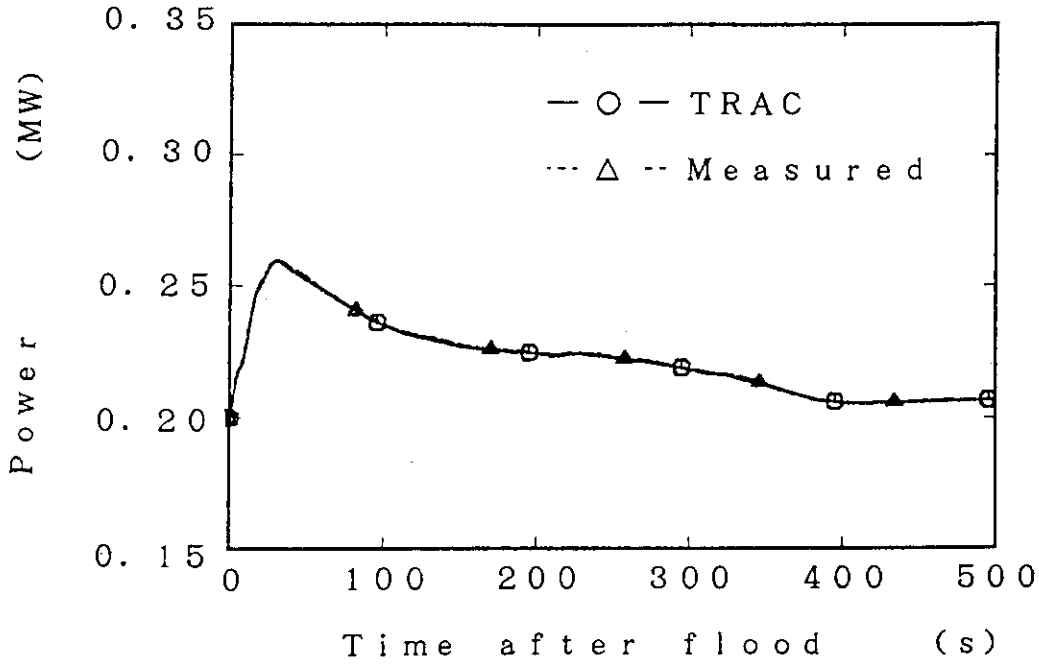

Fig. 4.5.2 Core outlet pressure in SCTF flat power test

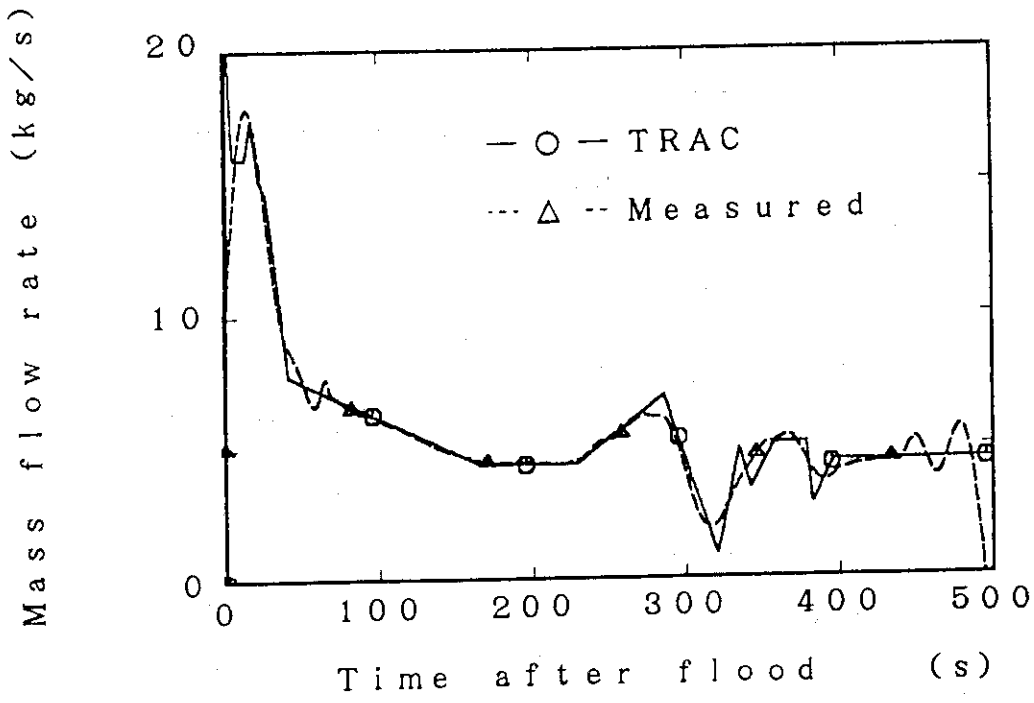

Fig. 4.5.3 Core inlet mass flow rate in SCTF flat power test

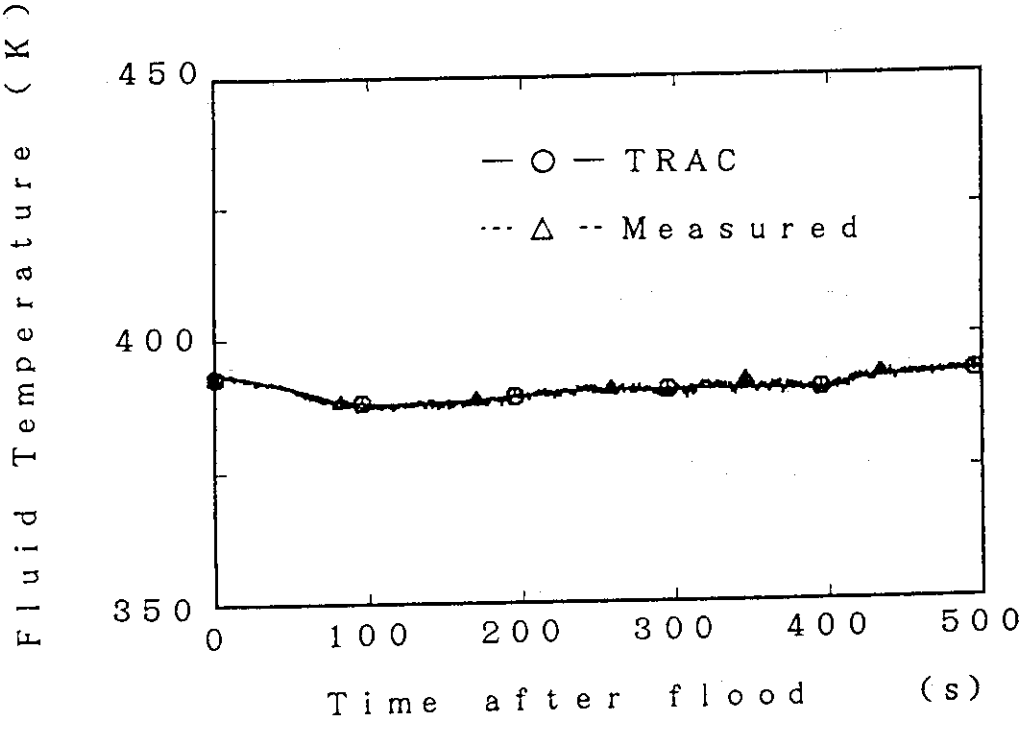

Fig. 4.5.4 Core inlet fluid temperature in SCTF flat power test

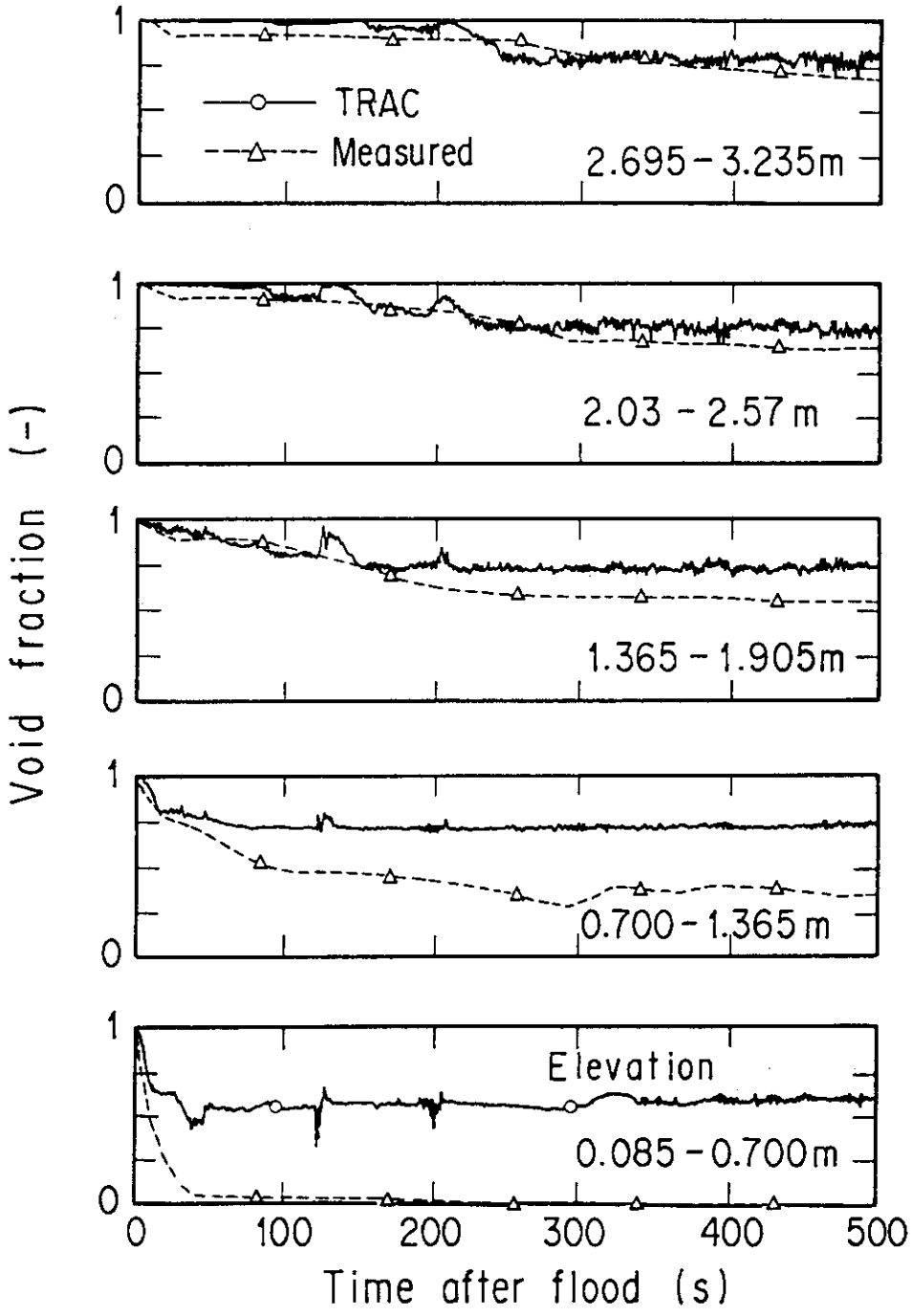

Fig. 4.5.5 Void fractions in core of SCTF flat power test

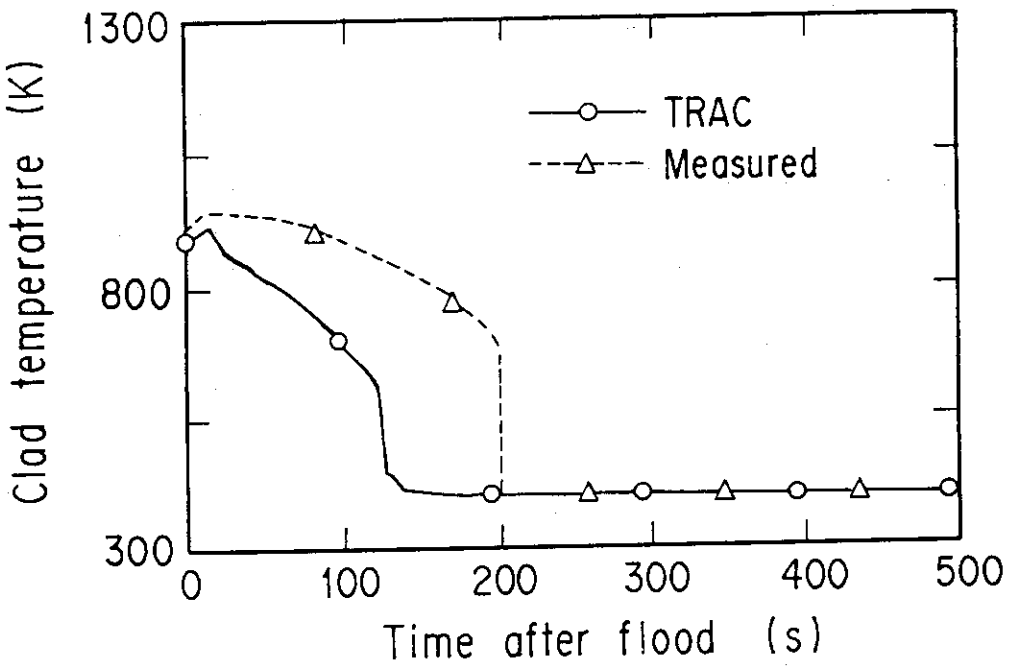

Fig. 4.5.6 Clad temperature at elevation of 1.905 m in SCTF flat power test

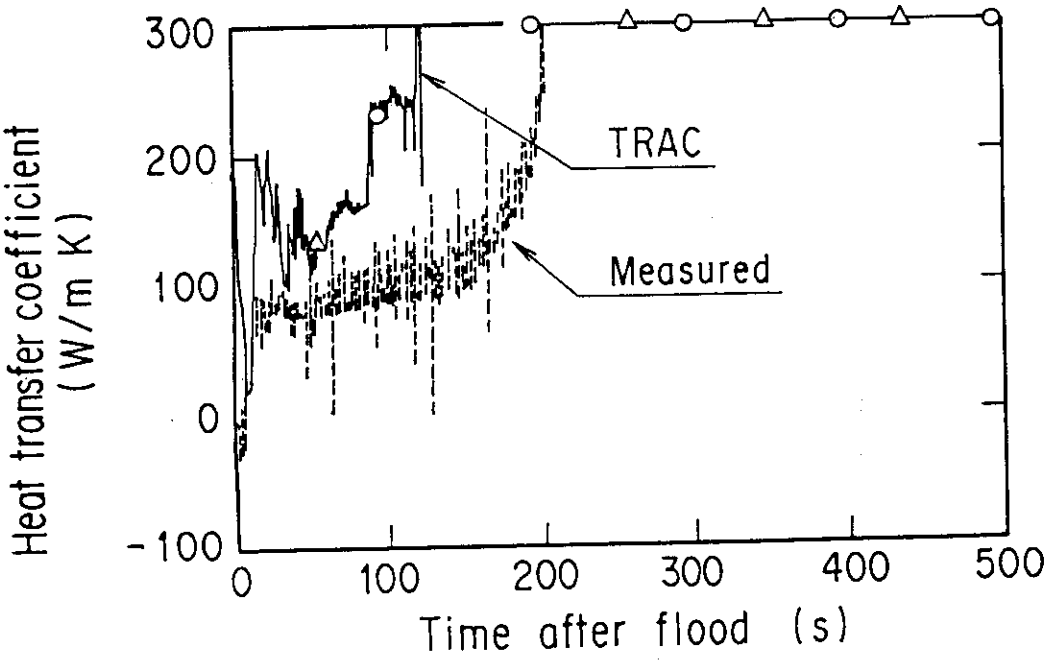

Fig. 4.5.7 Heat transfer coefficient at elevation of 1.905 m in SCTF flat power test

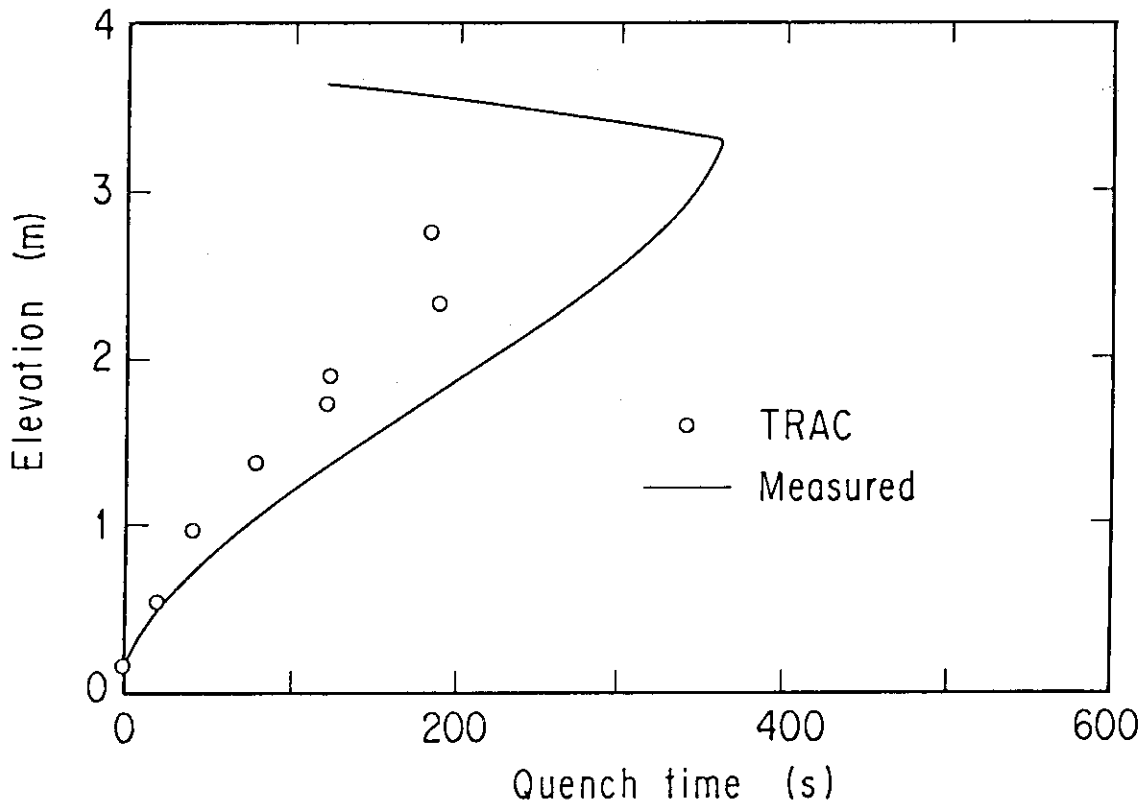

Fig. 4.5.8 Quench envelope in SCTF flat power test

4.6 Run statistics

Table 4.6.1 summarizes run statistics of this assessment study. All calculations were performed with the FACOM M-780 computer at JAERI. The plots of time step size and total CPU time are included in Appendix A.

Table 4.6.1 Run statistics

Test name	Transient time (s) RT	Total CPU time (s) CPU	Total time step No. ST	CPU/RT (-)	CPU/ST (ms)	RT/ST (ms)
CCTF base case test	700.2	3843.6	44306	5.46	86.8	15.80
CCTF high pressure test	500.2	1678.6	20419	3.36	82.2	24.50
CCTF low pressure test	800.0	4897.7	57600	6.12	85.0	13.89
CCTF low power test	700.0	3161.3	37804	4.52	83.6	18.52
CCTF best estimate test	300.0	358.8	12631	1.196	28.4	23.80
SCTF flat power test	700.0	1032.4	29362	1.475	35.2	23.80

5 Conclusions and Recommendations

Post test calculations for six selected CCTF and SCTF tests were performed to assess the core thermal hydraulic models of the TRAC-PF1 code for reflood phenomena in a PWR LOCA. Major results from the present study can be summarized as follows:

The TRAC-PF1 code predicted void fraction and core mass showed poor agreement with measured results in all six selected tests. The TRAC-PF1 code predicted many spikes in water mass flow rates inside the core, which was not significant in the CCTF and SCTF tests. These discrepancies from measured results were mainly caused by the problems in the interfacial friction model of the code. It is recommended to improve the interfacial friction model in the bubbly/slug flow regimes and in the vicinity of the flow transition point from the churn flow to the annular/dispersed flow regimes in order to improve the accuracy of the void fraction prediction in the lower part of the core and stabilize the calculation of the water mass flow rate inside the core.

The TRAC-PF1 code predicted well turnaround time, turnaround temperature and quench time including parameter effect of system pressure and core power level. However, good agreement in clad temperature transients with the TRAC-PF1 code was obtained due to the compensation of errors in hydraulic and wall-heat-transfer models. It is recommended to improve the wall heat transfer model in the film boiling regime including the dependency of the wall heat transfer coefficient on the distance from the quench front.

The TRAC-PF1 code over-predicted core cooling rate in the CCTF best-estimate test, which was performed with low initial clad temperature. The over-prediction of the core cooling rate in the CCTF best-estimate test was caused by the error in the boiling transition at low initial clad temperature from the film boiling to the transition boiling regimes. It is recommended to improve the criteria for the boiling transition at low initial clad temperature.

Acknowledgments

The authors wish to express their thanks the members of the CCTF and SCTF analysis group, Drs. H. Adachi, M. Sobajima, J. Sugimoto, T.Iwamura and Y. Abe and Messrs. T. Iguchi and T. Okubo for valuable discussions.

5 Conclusions and Recommendations

Post test calculations for six selected CCTF and SCTF tests were performed to assess the core thermal hydraulic models of the TRAC-PF1 code for reflood phenomena in a PWR LOCA. Major results from the present study can be summarized as follows:

The TRAC-PF1 code predicted void fraction and core mass showed poor agreement with measured results in all six selected tests. The TRAC-PF1 code predicted many spikes in water mass flow rates inside the core, which was not significant in the CCTF and SCTF tests. These discrepancies from measured results were mainly caused by the problems in the interfacial friction model of the code. It is recommended to improve the interfacial friction model in the bubbly/slug flow regimes and in the vicinity of the flow transition point from the churn flow to the annular/dispersed flow regimes in order to improve the accuracy of the void fraction prediction in the lower part of the core and stabilize the calculation of the water mass flow rate inside the core.

The TRAC-PF1 code predicted well turnaround time, turnaround temperature and quench time including parameter effect of system pressure and core power level. However, good agreement in clad temperature transients with the TRAC-PF1 code was obtained due to the compensation of errors in hydraulic and wall-heat-transfer models. It is recommended to improve the wall heat transfer model in the film boiling regime including the dependency of the wall heat transfer coefficient on the distance from the quench front.

The TRAC-PF1 code over-predicted core cooling rate in the CCTF best-estimate test, which was performed with low initial clad temperature. The over-prediction of the core cooling rate in the CCTF best-estimate test was caused by the error in the boiling transition at low initial clad temperature from the film boiling to the transition boiling regimes. It is recommended to improve the criteria for the boiling transition at low initial clad temperature.

Acknowledgments

The authors wish to express their thanks the members of the CCTF and SCTF analysis group, Drs. H. Adachi, M. Sobajima, J. Sugimoto, T.Iwamura and Y. Abe and Messrs. T. Iguchi and T. Okubo for valuable discussions.

References

(1) USNRC:"Guidelines and Procedure for the International Code Assessment and Applications Program," NUREG-1271 April (1987).

(2) Hirano,K.,Murao,Y.:J. At. Energy Soc. Japan, 22(10), 681(1980),(in Japanese).

(3) Los Alamos National Laboratory:"TRAC-PF1/MOD1:An Advanced Best-Estimate Computer Program for Pressurized Water Reactor Thermal-Hydraulic Analysis," NUREG/CR-3858 LA-10157-MS, July (1986).

(4) Kikuta,M. et al.:"Assessment of TRAC-PF1/MOD1 code for Cylindrical Core Test Facility Base Case Test C2-4," to be published as JAERI-M report.

(5) Ohnuki,A. et al.:"Assessment of TRAC-PF1/MOD1 code for thermal hydraulic behavior including two-dimensional behavior in pressure vessel during reflood in Slab Core Test Facility," to be published as JAERI-M report.

(6) Okubo,T.,et al.:"Evaluation Report on CCTF Core-II Reflood Test C2-4 (Run 62) - Investigation of Reproducibility -,", JAERI-M 85-026, (1986).

(7) Akimoto,H., et al.:"System Pressure Effect on System and Core Cooling Behavior during Reflood Phase of PWR LOCA," J. Nucl. Sci. Technol., 24(4) 276-288,(1987).

(8) Iguchi,T., Murao,Y.:"Effect of Decay Heat Level on Reflood Phenomena during PWR-LOCA," ibid. 24(10) 821-831, (1987).

(9) Murao,Y., et al.:"Status of CCTF/SCTF Test Programs," Twelfth Water Reactor Safety Information Meeting, NUREG/CP-0058 Vol. 2, 342-372, (1985).

(10) Iwamura,T., et al.:"Quantitative Evaluation of Heat Transfer Enhancement due to Radial Power Distribution during Reflood Phase of PWR-LOCA," J. Nucl. Sci. Technol., 26(4) 428-440, (1989).

(11) Iguchi,T., et al.:"Assessment of Core Radial Power Profile Effect Model for REFLA Code by Using CCTF Data," ibid., 25(1) 45-55, (1988).

(12) Akimoto,H. et al.:"Core Radial Power Profile Effect on System and Core Cooling Behavior during Reflood Phase of PWR LOCA," ibid., 22(7) 538-550, (1985).

(13) Murao,Y.,Iguchi,T.:"Experimental Modeling of Core Hydrodynamics during Reflood Phase of LOCA," ibid., 19(8), 613-627, (1982).

(14) Chexal,B.,Lellouche,G.:"A Full-Range Drift-Flux Correlation for Vertical Flows," EPRI NP-3989-SR, June (1985).

(15) Murao,Y. and Sugimoto,J.:"Correlation of Heat Transfer Coefficient for Saturated Film Boiling during Reflood Phase Prior to Quenching," J. Nucl.Sci. Technol., 18(4), 275-284, (1981).

Appendix A

Outline of interfacial friction model and wall heat transfer model of TRAC-PF1 Code

In the TRAC-PF1/MOD1 code, various correlations are used to calculate the interfacial and wall friction forces and interfacial and wall heat transfer rates to close basic equations based on the two fluid model of the two-phase flow. These correlations are called constitutive equations. The details of constitutive equations are described in the references (A-1) and (A-2) published at Los Alamos National Laboratory(LANL). The constitutive equations were studied at JAERI based on the source listing of the TRAC-PF1/MOD1 code. The investigated results are summarized in reference (A-3). Because it is too much to describe the details of the constitutive equations of the TRAC-PF1 code, only the outline of the interfacial friction model and wall heat transfer model in the transition and film boiling regimes will be described briefly.

A.1 Outline of Interfacial Friction Model of TRAC-PF1 Code

In the analysis of the CCTF and SCTF tests, a vertical flow without application of the interfacial sharpener model was realized with mass velocity less than 200 kg/m^2s at the core part. In the description, shown below, several simplification will be made focussing on the correlations used in the analysis of the CCTF and SCTF tests.

Figure A.1 shows the flow pattern map assumed in the TRAC-PF1/MOD1 code. Bubbly, Slug and annular/dispersed flows are assumed as the basic flow patterns of the two-phase flow. The bubbly flow is assumed when void fraction is less than 0.3. The slug flow is assumed when void fraction is between 0.3 and 0.5. The annular/dispersed flow is assumed when void fraction is higher than 0.75. Interpolation between slug and annular/dispersed flows is made when void fraction is between 0.5 and 0.75. The region where void fraction is between 0.5 and 0.75 is called as a churn flow in this appendix. As the first step, the flow pattern of the two-phase flow is determined by the flow pattern map shown in Fig. A.1. Then, the interfacial friction force Fi is calculated with correlations specified for each flow pattern.

A.1.1 Correlations for bubbly and slug flows

Figure A.2 illustrates flow pattern assumed for bubbly and slug flows in the TRAC-PF1 code. The bubbly and slug flows are described by the combination of large bubbles with diameter of D_h(hydraulic diameter of flow path) and small bubbles with diameter of D_b. The interfacial friction force per unit volume is evaluated by

$$Fi = Ci(V_g - V_l)\,|\,V_g - V_l\,| = 3C_b\,\alpha\,\rho_l(V_g - V_l)\,|\,V_g - V_l\,|\,/4D_{bave}. \tag{A.1}$$

Equation (A.1) can be derived by multiplying number density of bubble $N_b(=6\alpha/\pi D_b^3)$ with interfacial friction force acting to a spherical bubble $Fi^*(=C_b\pi D_b^2\rho_l(V_g-V_l)^2)$.

The drag coefficient for a bubble C_b is calculated by

$$C_b = \begin{cases} 240, & (Re_b \leqq 0.1031) \\ 24(1 + 0.15Re_b^{0.687})/Re_b, & (0.1031 \leqq Re_b < 989) \\ 0.44, & (Reb \leqq 989) \end{cases} \tag{A.2}$$

where

$$Re_b = \rho_l\,|\,V_g - V_l\,|\,D_{bave}/\mu_l. \tag{A.3}$$

The average bubble diameter D_{bave} is calculated by

$$D_{bave} = We_b(1 - X_{slug})/\rho_l\,|\,V_g - V_l\,|^2 + D_h X_{slug}, \tag{A.4}$$

where

$$X_{slug} = 3X_s^2 - 2X_s^3, \tag{A.5}$$

$$X_s = \begin{cases} 4 - 0.25, & (\,G \leqq 2000\,) \\ 4(\alpha - 0.25)\exp\{-(G-2000)/700\}, & (\,G \leqq 2000\,) \end{cases} \tag{A.6}$$

$$We_b = 7.5. \tag{A.7}$$

A.1.2 Correlations for annular/dispersed flow

Figure A.3 illustrates flow pattern assumed for the annular/dispersed flow in the TRAC-PF1 code. The liquid phase is separated into droplets and liquid film on the wall.

The interfacial friction force per unit volume is evaluated by

$$Fi = Ci\,\rho_g(V_g-V_l)\,|\,V_g-V_l\,|\,/2 \tag{A.8}$$

where

$$Ci = Ci_d E + Ci_{an}(1-E). \tag{A.9}$$

The interfacial friction coefficient of droplet is given by

$$Ci_d = 3C_d(1-\alpha)/2D_d, \tag{A.10}$$

where

$$C_d = \begin{cases} 240, & (Re_d \leqq 0.1031) \\ 24(1+0.15Re_d^{0.687})/Re_d, & (0.1031 < Re_d < 989) \\ 0.44, & (989 \leqq Re_d) \end{cases} \tag{A.11}$$

$$Re_d = \rho_g\,|\,V_g-V_l\,|\,D_d/\mu_g. \tag{A.12}$$

The droplet diameter D_d is calculated by

$$D_d = We_d\,\sigma/\rho_g(V_g-V_l)^2, \quad We_d = 4.0. \tag{A.13}$$

The interfacial friction coefficient of liquid film contribution is evaluated by

$$Ci_{an} = 0.02\,\{1 + 75(1-\alpha)(1-E)\}\,/D_h. \tag{A.14}$$

The fraction of droplet in the liquid phase E is calculated by

$$E = \max\,(A,B), \tag{A.15}$$

where

$$A = 1 - \exp\,\{\,0.50(V_E-V_g)/V_E\,\}, \tag{A.16}$$

$$V_E = 2.33\{(\rho_l - \rho_g)We_d/\rho_g^2\}^{1/4}, \tag{A.17}$$

$$B = 7.75 \times 10^{-7}\ We_e(Re_l We_e)^{1/4}, \tag{A.18}$$

$$We_e = \rho_g(\sigma\ |\ V_g\ |)2D_h(\rho_l - \rho_g)/\sigma, \tag{A.19}$$

$$Re_l = \rho_l(1-\alpha)\ |\ V_l\ |\ D_h/\mu_l. \tag{A.20}$$

A.1.3 Correlation for churn flow

The interfacial friction force for the churn flow is calculated by interpolating the interfacial friction force Fi_1 by correlations for bubbly and slug flows and interfacial friction force Fi_2 by correlations for annular/dispersed flow, that is,

$$Fi = (1-w)Fi_1 + wFi_2, \tag{A.21}$$

where

$$w = (4\alpha-2)^2(7-8\alpha). \tag{A.22}$$

A.2 Outline of Wall Heat Transfer Model of TRAC-PF1 Code

In the TRAC-PF1/MOD1 code, various correlations are used to calculate wall heat transfer coefficients. As the wall heat transfer regimes, eight regimes, listed below, are assumed:

(1) forced convection to single-phase liquid,
(2) nucleate boiling,
(3) transition boiling,
(4) film boiling,
(5) convection to single phase vapor,
(6) convection to two-phase mixture,
(7) condensation, and
(8) liquid natural convection.

At first, the wall heat transfer regime is determined through comparison among wall, fluid and saturation temperature, void fraction, etc. Then, wall heat transfer coefficients of vapor and liquid sides are calculated with correlations in each regimes.

In the analyses of the CCTF and SCTF tests, the most important wall heat transfer regime was the film boiling regime to evaluate the core cooling rate before heater rod was quenched. In the following, only the selection logic for the film boiling regime and the correlations used in the film boiling regime will be described briefly.

A.2.1 Condition for selection of film boiling regime

Figure A.4 shows a portion of the boiling curve assumed in the TRAC-PF1/MOD1 code. The single-phase vapor and condensation regimes are not shown in this figure. The film boiling regime is selected when the wall temperature T_w is higher than the minimum film-boiling temperature T_{min}.

The minimum film boiling temperature is calculated by

$$T_{min} = T_{nh} + (T_{nh}+T_l)R^{0.5}, \tag{A.23}$$

where

$$R = (k\rho Cp)_l/(k\rho cp)_w. \tag{A.24}$$

In above equations subscript l indicates liquid properties and subscript w indicates wall properties. T_{nh} is the homogeneous-nucleation temperature and calculated by

$$T_{nh} = 705.44 - 4.722\text{x}10^{-2}(DP) + 2.3907\text{x}10^{-5}(DP)^2 - 5.8193\text{x}10^{-9}(DP)^3, \tag{A.25}$$

where

$$(DP) = 3203.6 - P. \tag{A.26}$$

The pressure P is in psia units, and T_{nh} is in degree Fahrenheit.

A.2.2 Correlations in film boiling regime

In the film-boiling heat transfer regime, radiative and dispersed-flow heat transfers occur between the wall surface and the liquid. Convective heat transfer occurs between the wall surface and the vapor.

Liquid side heat transfer coefficient

The liquid side heat transfer coefficient h_l is given by

$$h_l = (h_r + h_{fbb})(T_w - T_{sat})/(T_w - T_l) + h_{df}, \tag{A.27}$$

where h_r is the radiative heat transfer coefficient, and h_{fbb} is the heat transfer coefficient due to convection, and h_{df} is the heat transfer coefficient for the dispersed flow.

The radiative heat transfer coefficient h_r is given by

$$h_r = (1-\alpha)\sigma_{SB}\,\varepsilon\,(T_w^4-T_{sat}^4)/(T_w-T_{sat}), \tag{A.28}$$

where σ_{SB} is the Stefan-Boltzmann constant(=5.6697x10^{-8}) and ε is the wall emissivity.

The convective heat transfer coefficient h_{fbb} is given by

$$h_{fbb} = \begin{cases} h_{fbb0}, & (\alpha<0.5) \\ h_{fbbo}(3-2X_1)X_1^2, & (0.5<\alpha<0.75) \\ 0. & (0.75<\alpha) \end{cases} \tag{A.29}$$

h_{fbb0} is the heat transfer coefficient by Bromley and given by

$$h_{fbb0} = 0.62\ [\ \{\rho_g k_g^3(\rho_l-\rho_g)h_{fg}'g\}\ /\ \{\mu_g(T_w-T_{sat})\lambda\}\ ]^{1/4}, \tag{A.30}$$

where

$$\lambda = 2\pi\{\sigma/g(\rho_l-\rho_g)\}^{0.5}, \tag{A.31}$$

$$h_{fg}' = h_{fg} + 0.5Cp_g(T_g-T_{sat}). \tag{A.32}$$

X_1 is the parameter for the interpolation and given by

$$X_1 = (0.75-\alpha)/0.25. \tag{A.33}$$

The heat transfer coefficient for the dispersed flow h_{df} is calculated by

$$h_{df} = \begin{cases} 0, & (\alpha<0.5) \\ \min(h_{df0},h_{fbb0})(3-2X_1)X_1^2, & (0.5<\alpha<0.75) \\ \min(h_{df0},h_{fbb0}), & (0.75<\alpha) \end{cases} \tag{A.34}$$

where

$$h_{df0} = 0.2552\ \{(1-\alpha)E\}^{0.667}B^{0.25}(T_w-T_{sat})/(T_w-T_l), \tag{A.35}$$

$$B = g\rho_l\rho_g h_{fg}'k_l^3/\mid T_w-T_{sat}\mid \mu_g D_{drop}, \tag{A.36}$$

$$D_{drop} = We\,\sigma/\rho_g(V_g-V_l)^2,\ We=4.0. \tag{A.37}$$

The fraction of droplet in liquid phase E is calculated by Eq. (A.15) and X_1 is calculated by Eq. (A.33).

Vapor side heat transfer coefficient

The vapor side heat transfer coefficient h_g is calculated by

$$h_g = \max(h_{gnc},h_{gDR}), \tag{A.38}$$

where

$$h_{gnc} = 0.13\ k_g\{(\rho_g^2 g\mid T_w-T_g\mid)/\mu_g^2T_g\}^{0.333}Pr_g^{0.333}, \tag{A.39}$$

$$h_{gDR} = (k_g/D_h)\ \mathrm{x}\ 0.023Re_{TP}^{0.8}Pr_g^{0.4}, \tag{A.40}$$

$$Pr_g = Cp_g\mu_g/k_g,\ Re_{TP}=\rho_g\{\mid V_g\mid\alpha + \mid V_l\mid(1-\alpha)\}D_h/\mu_g. \tag{A.41}$$

References

(A-1) Los Alamos National Laboratory:"TRAC-PF1/MOD1:An Advanced Best-Estimate Computer Program for Pressurized Water Reactor Thermal-Hydraulic Analysis," NUREG/CR-3858 LA-10157-MS R4, July (1986).

(A-2) Los Alamos National Laboratory:"TRAC-PF1/MOD1 Correlations and Models," NUREG/CR-5069 LA-11208-MS, December (1988).

(A-3) Akimoto,H., et al.:"MINI-TRAC Code: A Driver Program for Assessment of Constitutive Equations of Two-Fluid Model," JAERI-M 91-086, May (1991), (in Japanese).

Nomenclature

Cp	:	Specific heat at constant pressure, (J/(kgK))
D_h	:	Hydraulic diameter, (m)
g	:	Acceleration due to gravity, (m/s^2)
G	:	Mass velocity, (kg/m^2s)
h_{fg}	:	Latent heat for evaporation, (J/kg)
k_g	:	Thermal conductivity, (J/(Ksm))
T	:	Temperature, (K)
V	:	Velocity, (m/s)
α	:	Void fraction
μ	:	Viscosity, (kg/ms)
ρ	:	Density, (kg/m^3)
σ	:	Surface tension, (N/m)

Subscript

g	:	Vapor
l	:	Liquid
sat	:	Saturation
w	:	Wall

Appendix B Selected Results

(1) CCTF Base Case Test (Run 62)

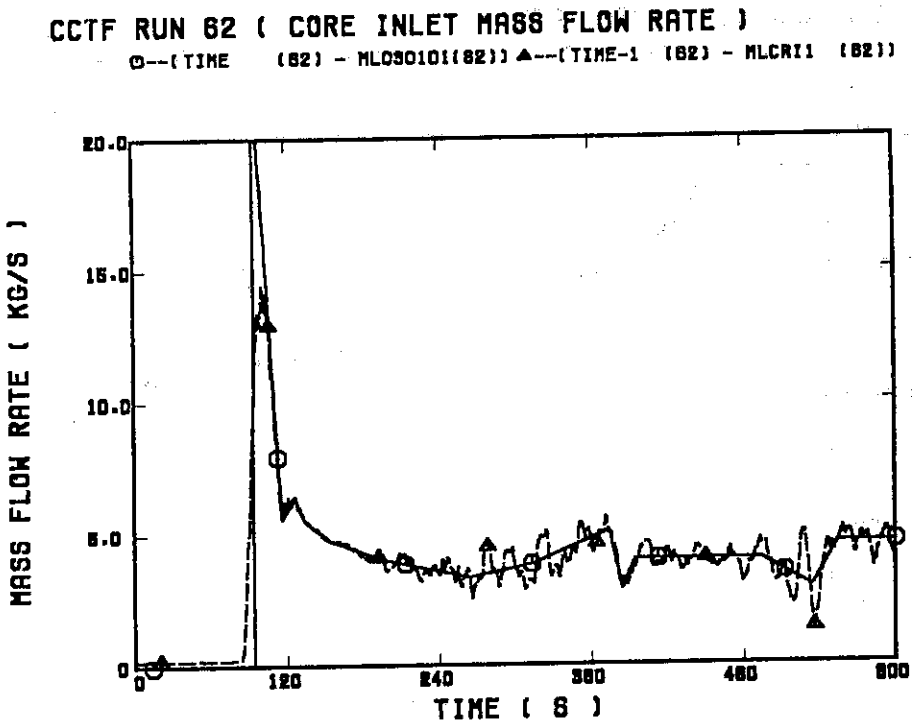

Fig. B.1.1 Core inlet mass flow rate (input)

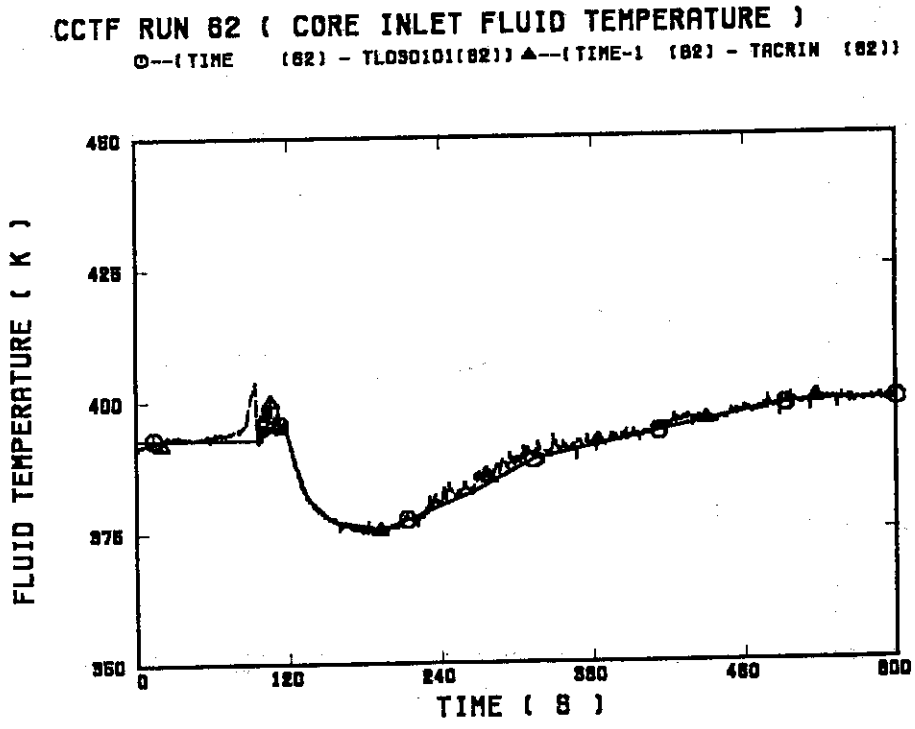

Fig. B.1.2 Core inlet fluid temperature (input)

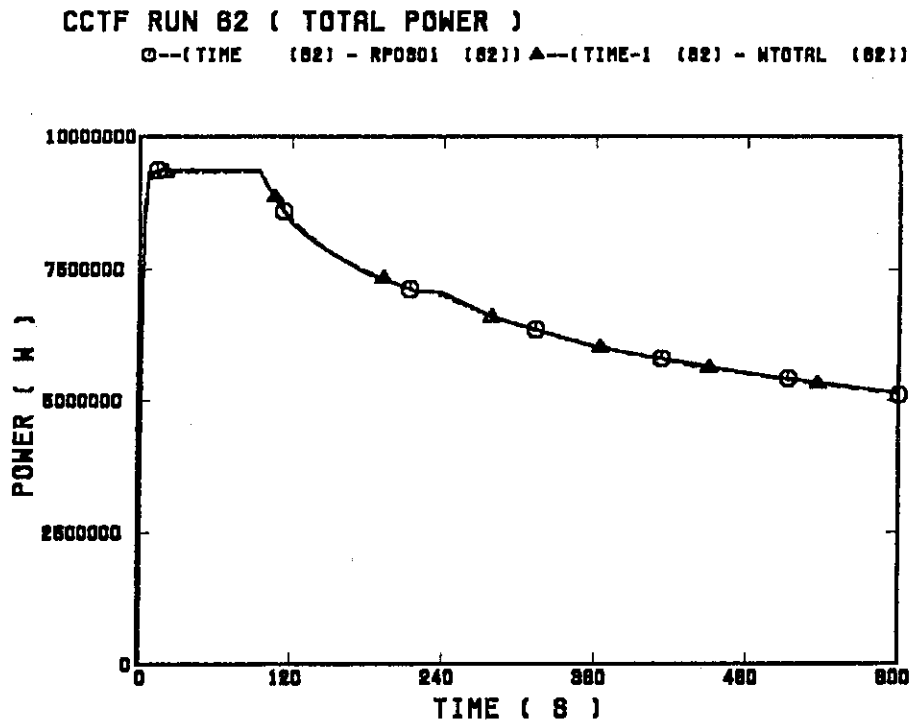

Fig. B.1.3 Total power supplied to core (input)

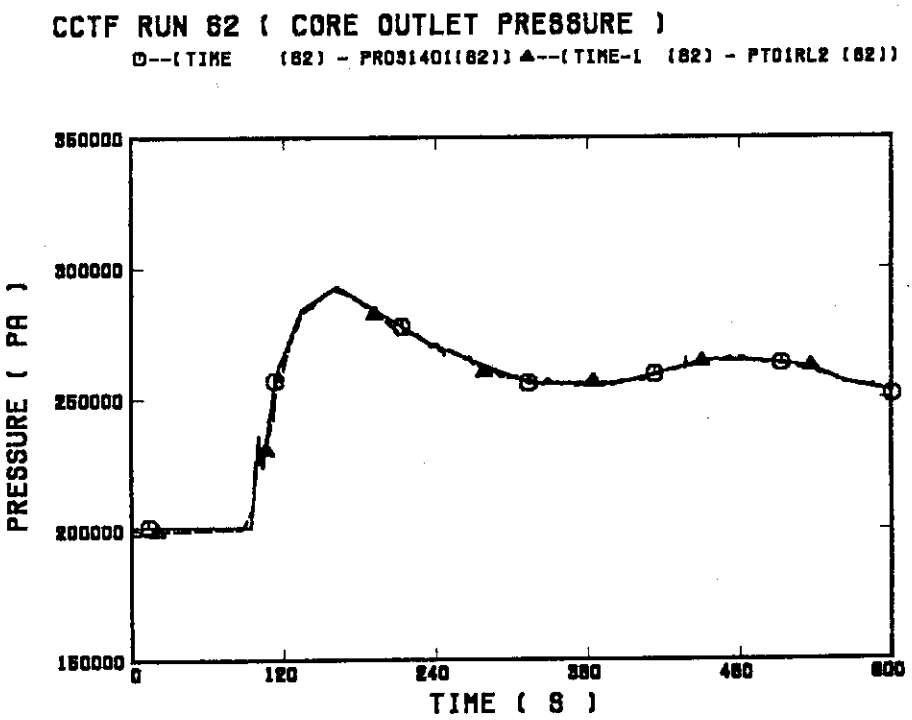

Fig. B.1.4 Core outlet pressure (input)

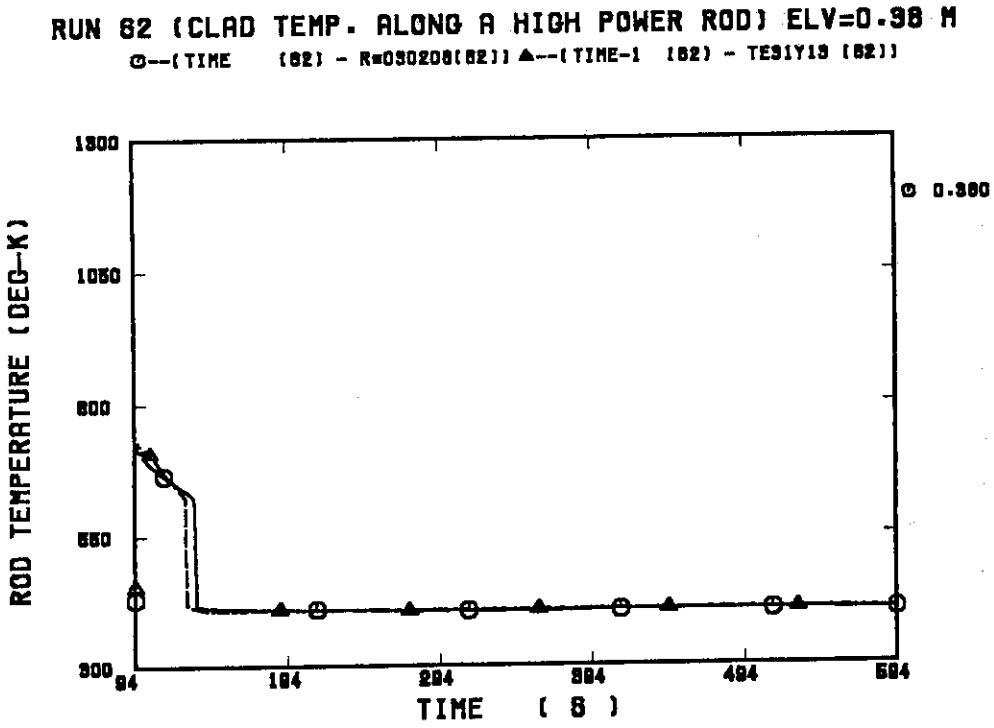

Fig. B.1.5 Clad temperature at elevation of 0.38 m along a high power rod

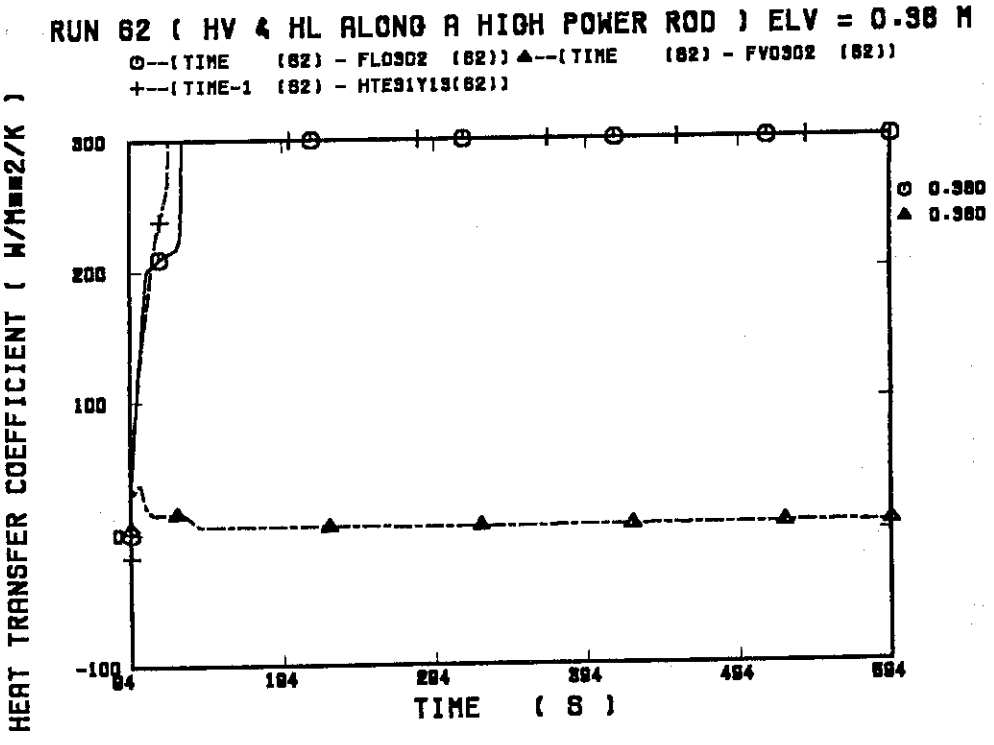

Fig. B.1.6 Heat transfer coefficient at elevation of 0.38 m along a high power rod

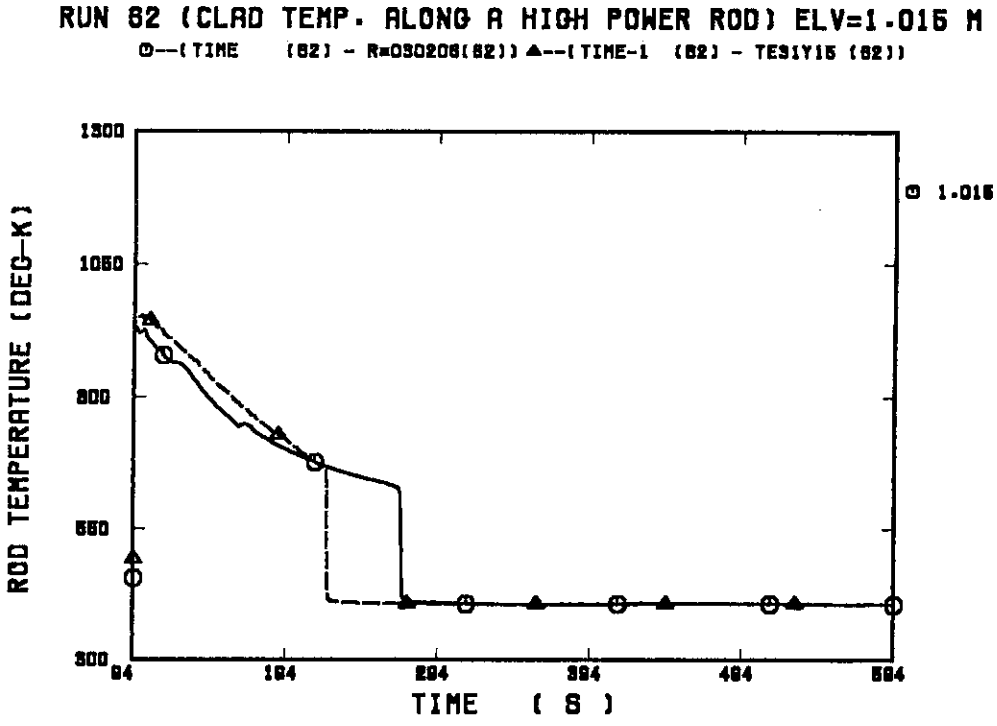

Fig. B.1.7 Clad temperature at elevation of 1.015 m along a high power rod

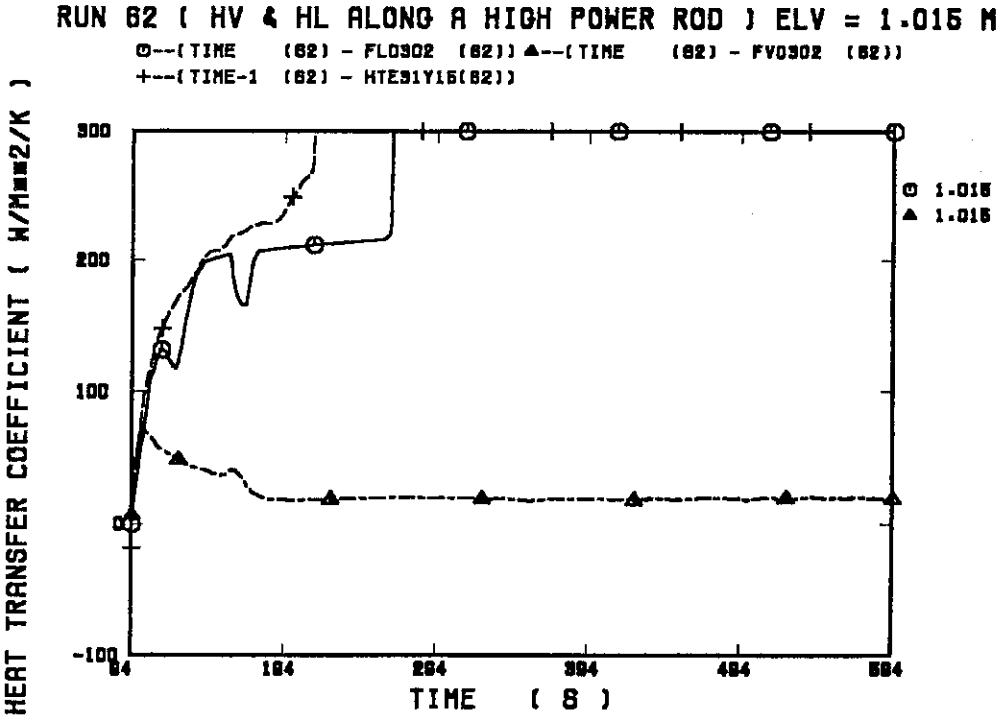

Fig. B.1.8 Heat transfer coefficient at elevation of 1.015 m along a high power rod

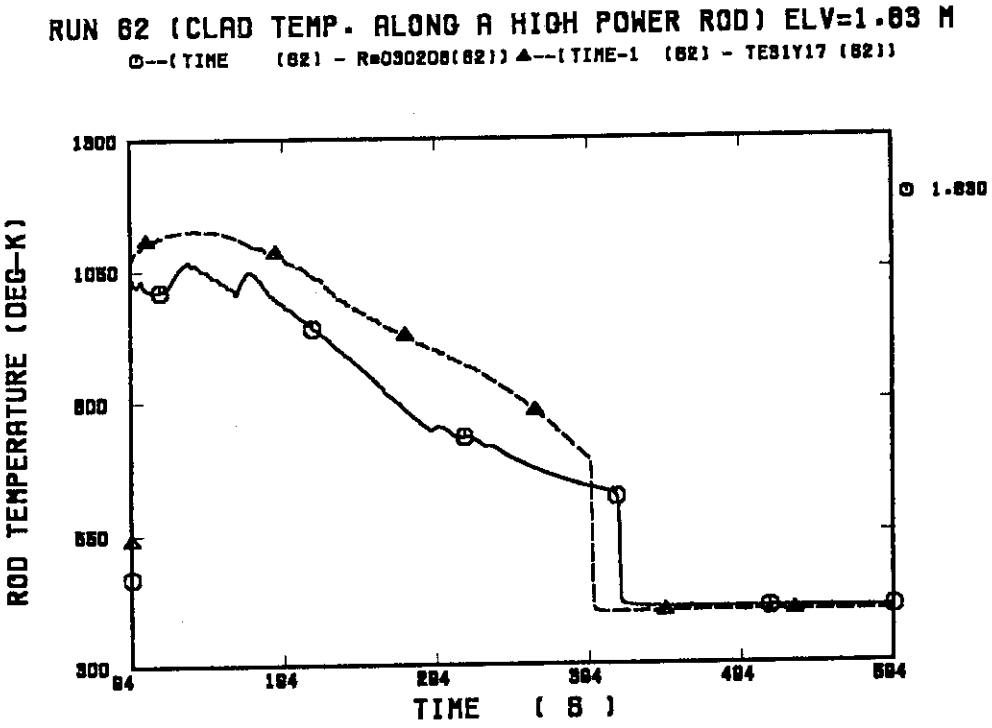

Fig. B.1.9 Clad temperature at elevation of 1.83 m along a high power rod

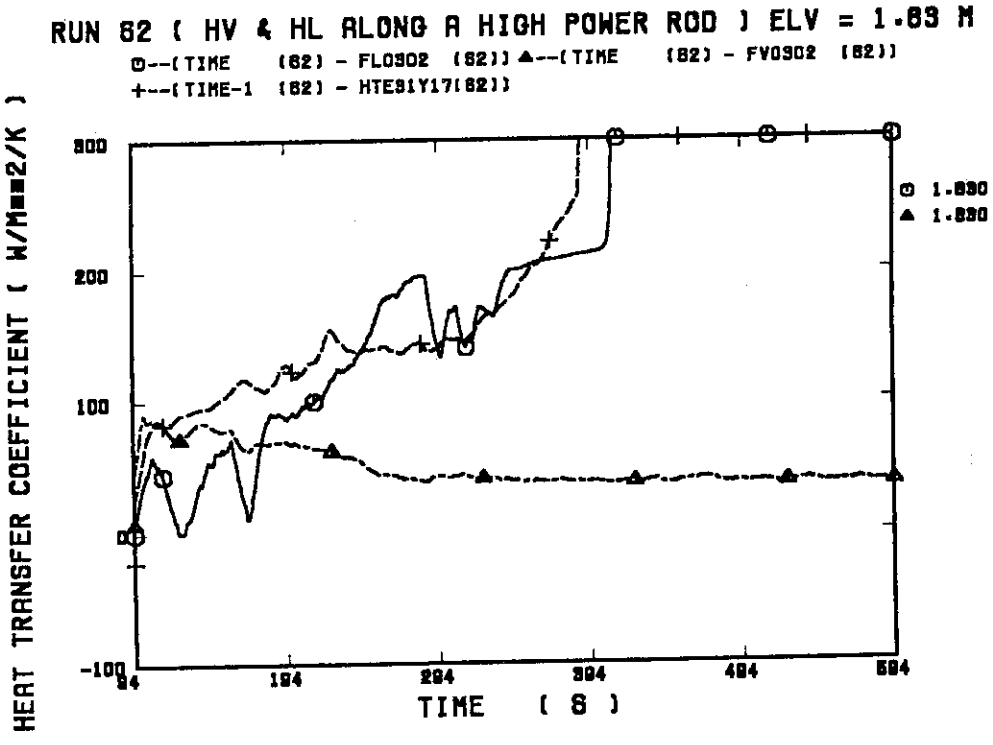

Fig. B.1.10 Heat transfer coefficient at elevation of 1.83 m along a high power rod

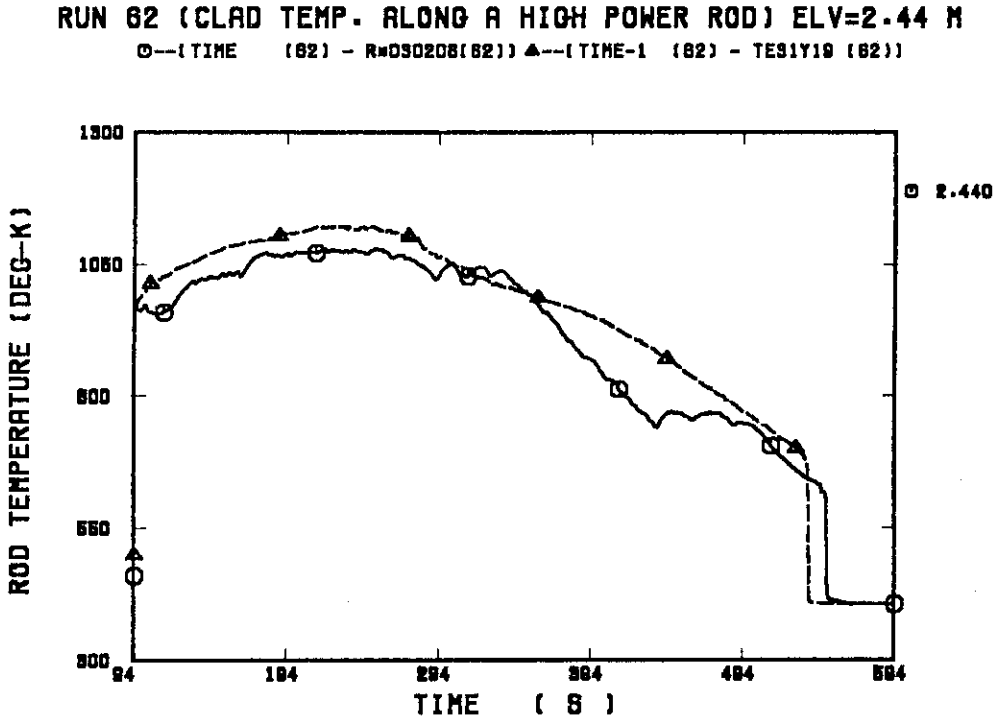

Fig. B.1.11 Clad temperature at elevation of 2.44 m along a high power rod

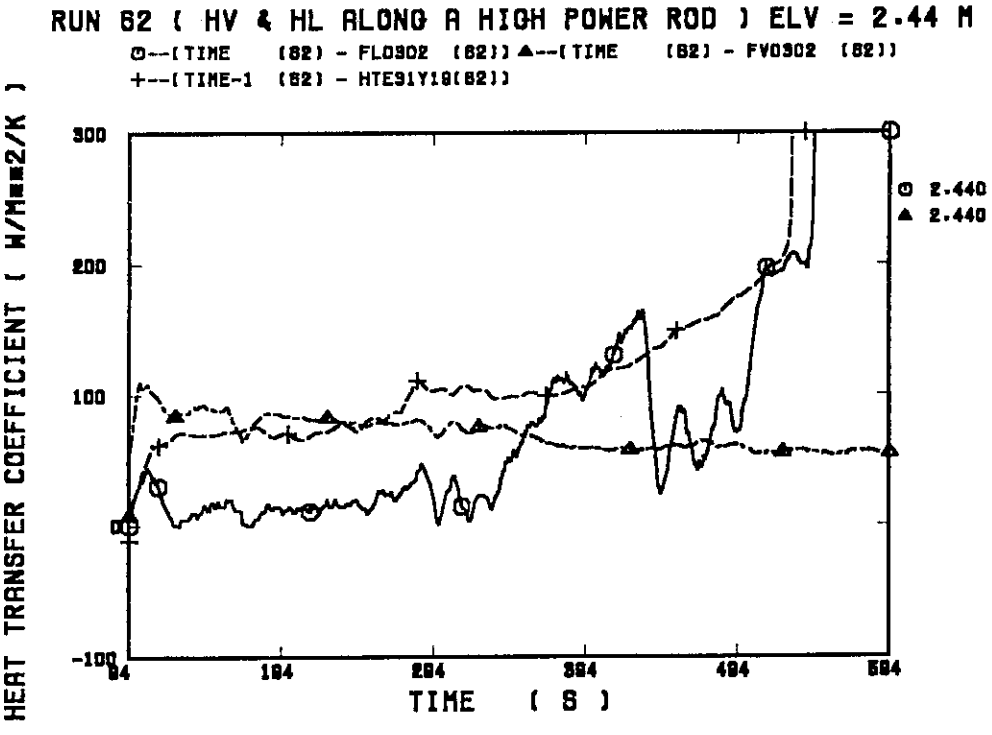

Fig. B.1.12 Heat transfer coefficient at elevation of 2.44 m along a high power rod

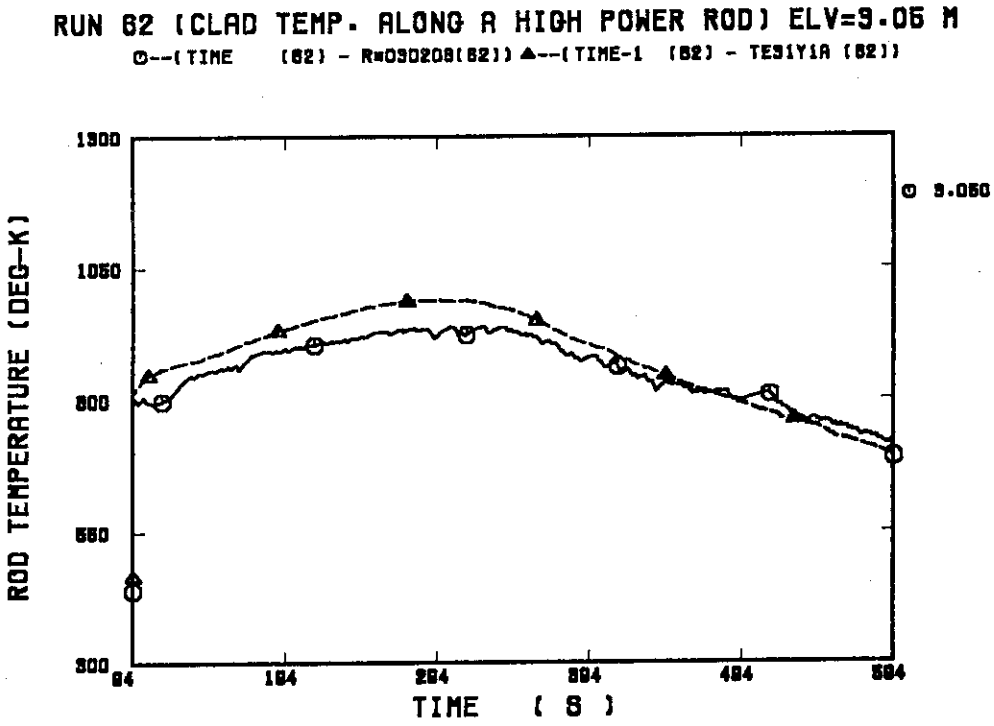

Fig. B.1.13 Clad temperature at elevation of 3.05 m along a high power rod

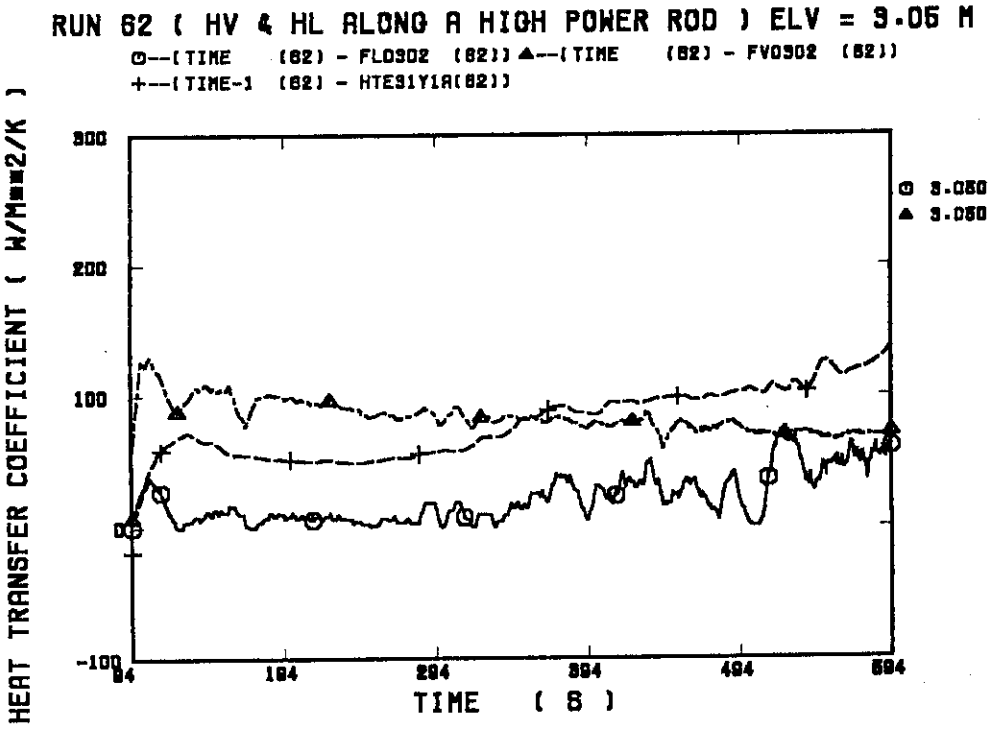

Fig. B.1.14 Heat transfer coefficient at elevation of 3.05 m along a high power rod

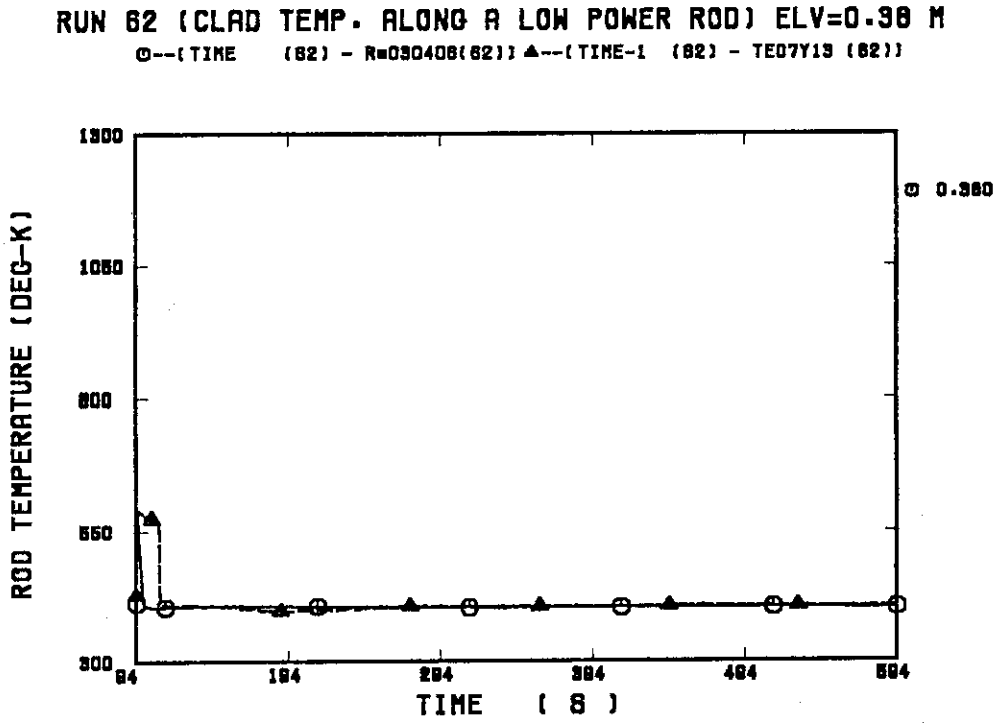

Fig. B.1.15 Clad temperature at elevation of 0.38 m along a low power rod

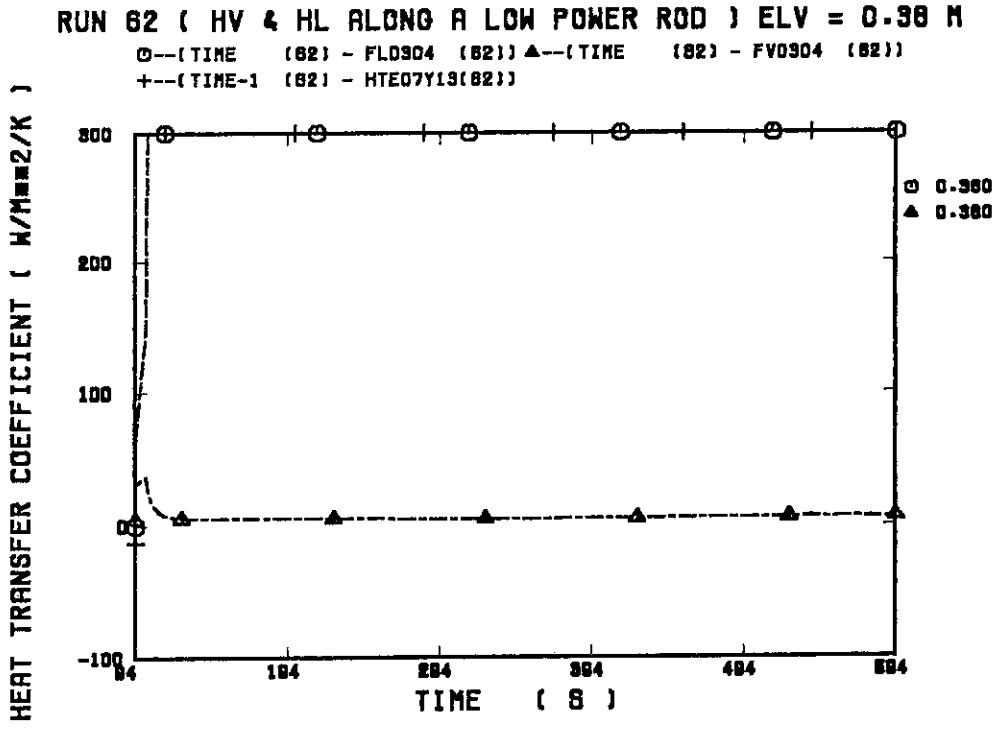

Fig. B.1.16 Heat transfer coefficient at elevation of 0.38 m along a low power rod

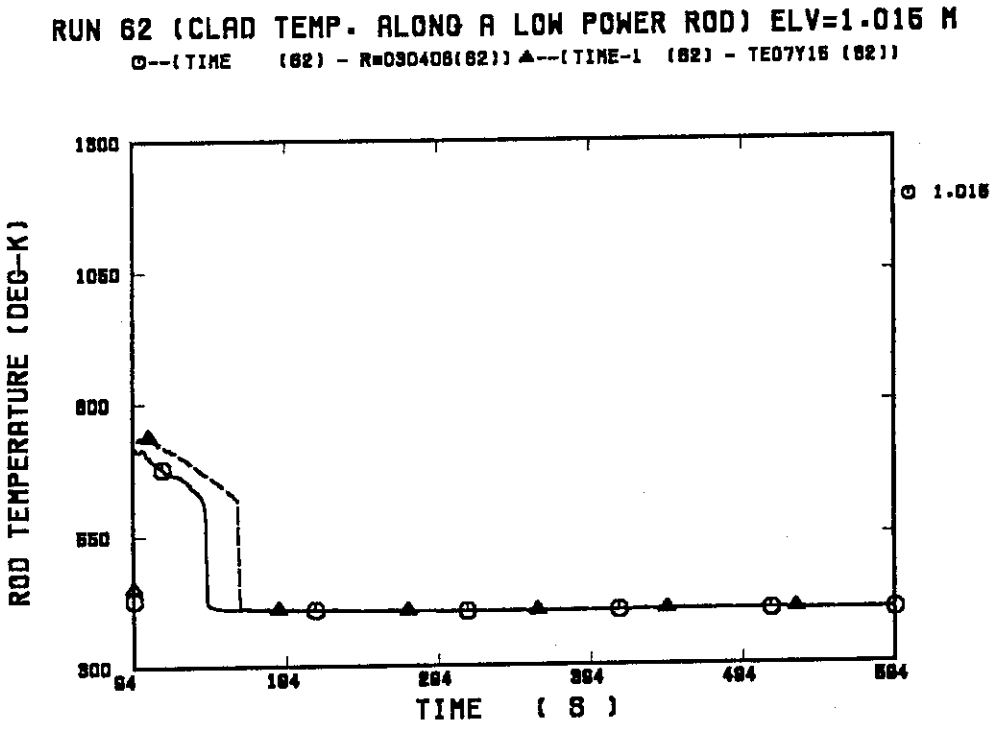

Fig. B.1.17 Clad temperature at elevation of 1.015 m along a low power rod

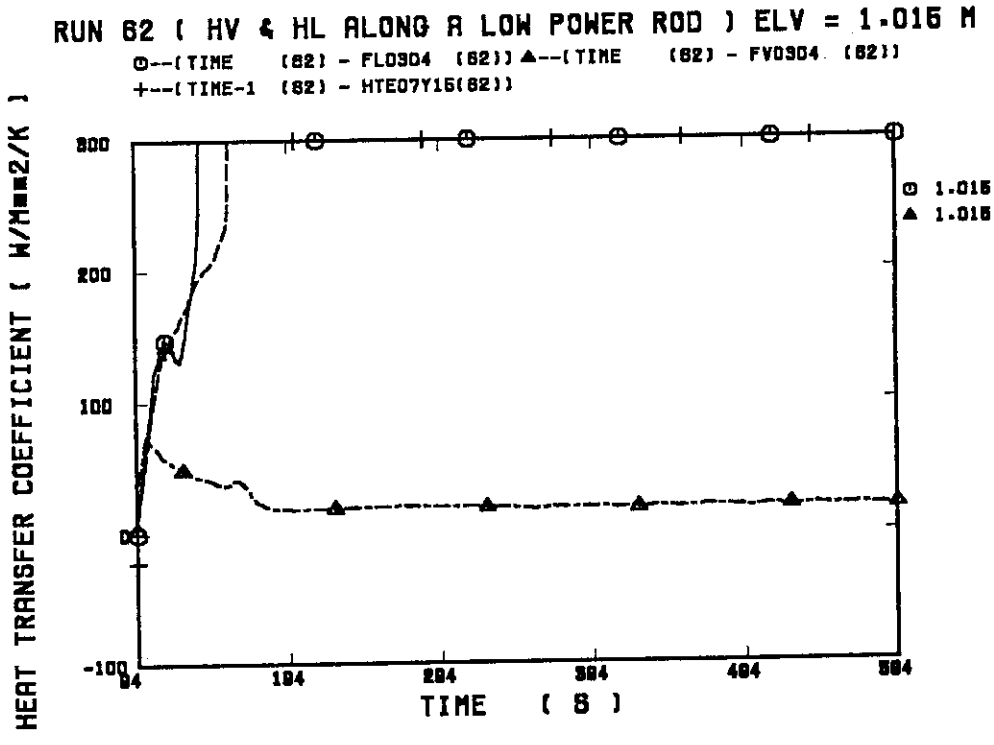

Fig. B.1.18 Heat transfer coefficient at elevation of 1.015 m along a low power rod

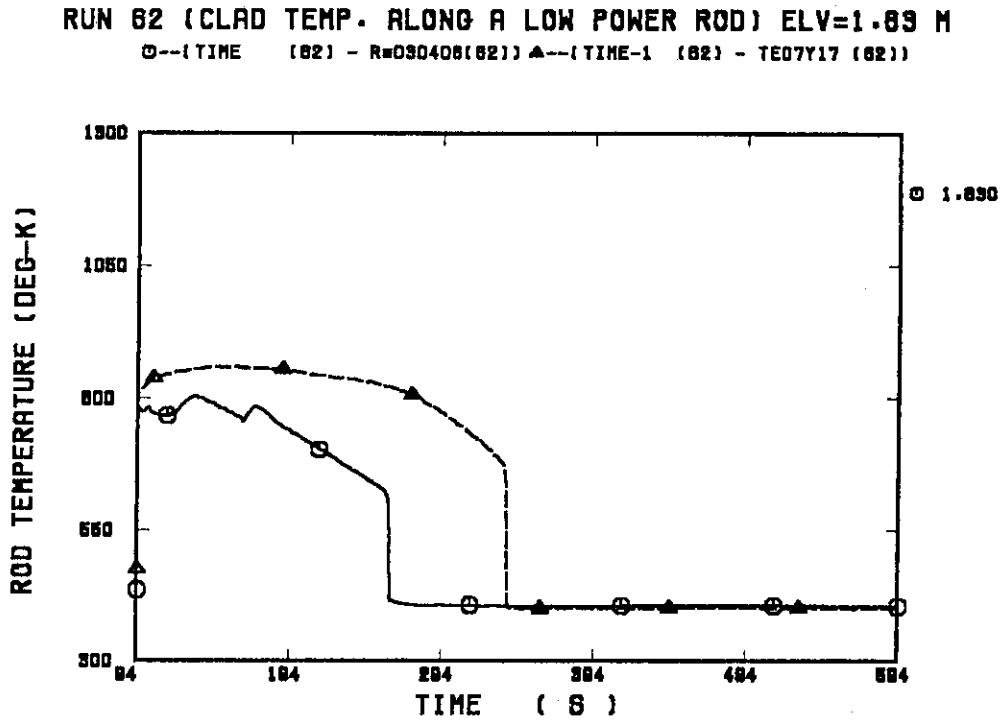

Fig. B.1.19 Clad temperature at elevation of 1.83 m along a low power rod

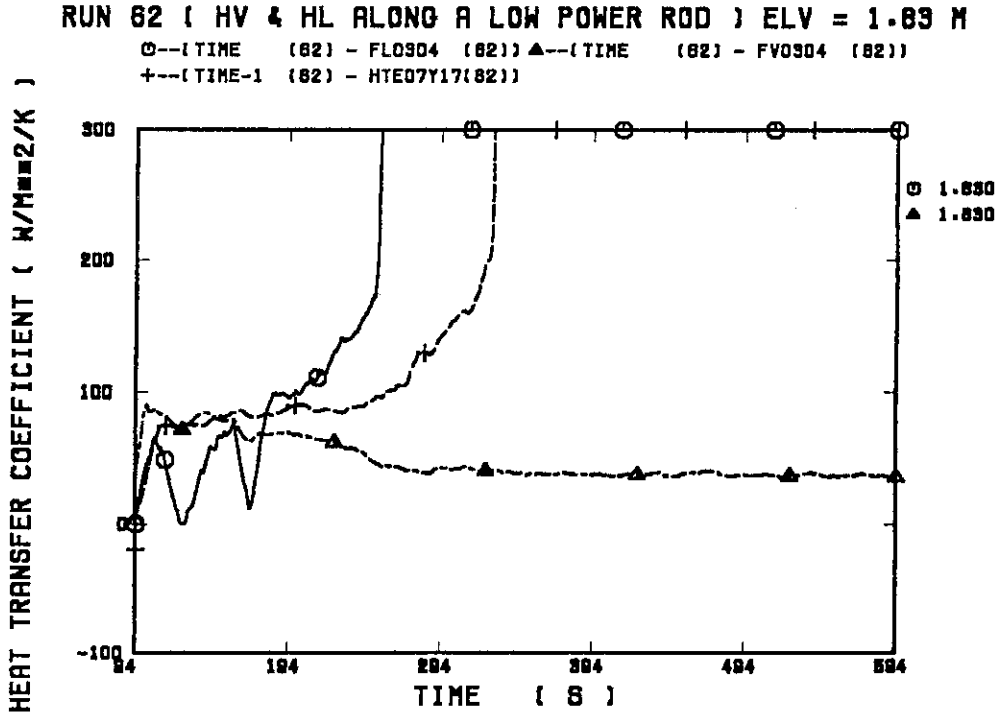

Fig. B.1.20 Heat transfer coefficient at elevation of 1.83 m along a low power rod

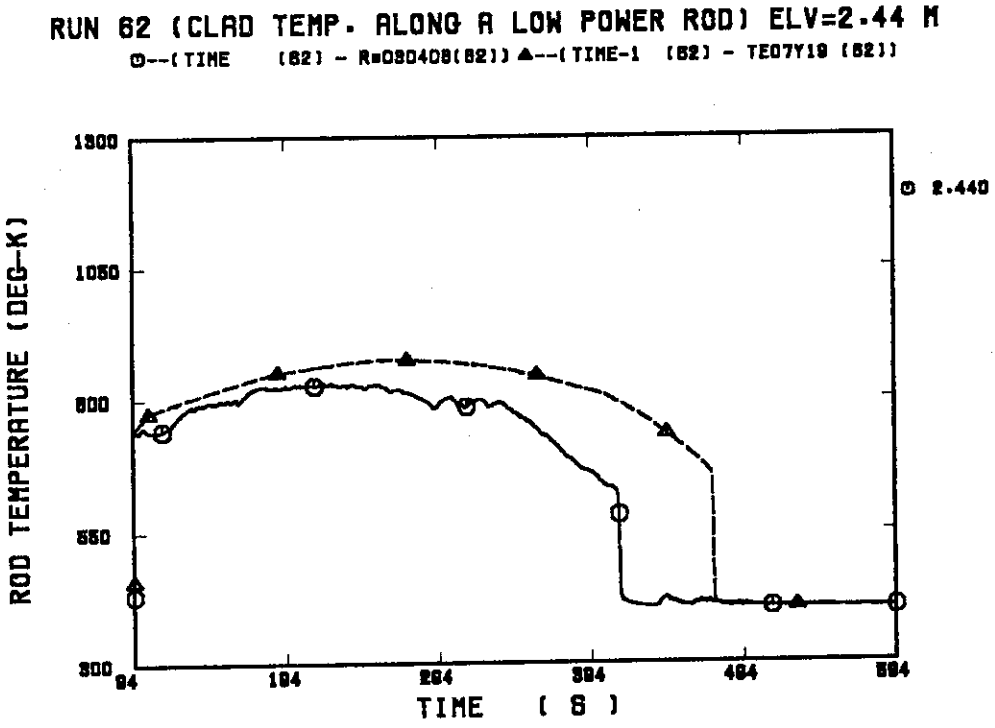

Fig. B.1.21 Clad temperature at elevation of 2.44 m along a low power rod

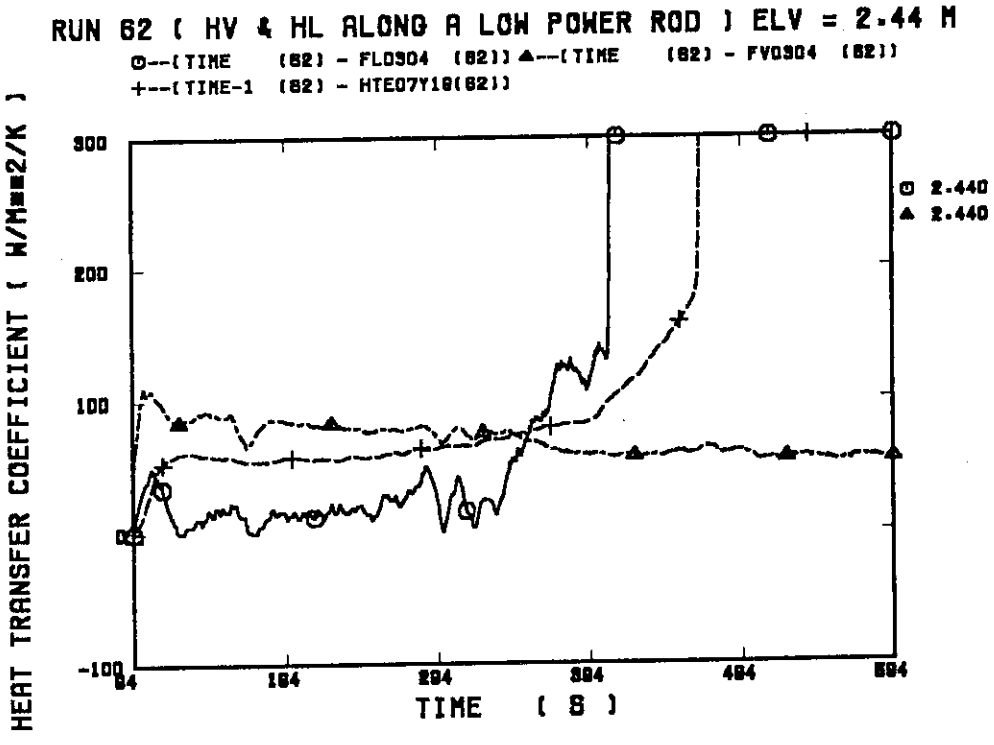

Fig. B.1.22 Heat transfer coefficient at elevation of 2.44 m along a low power rod

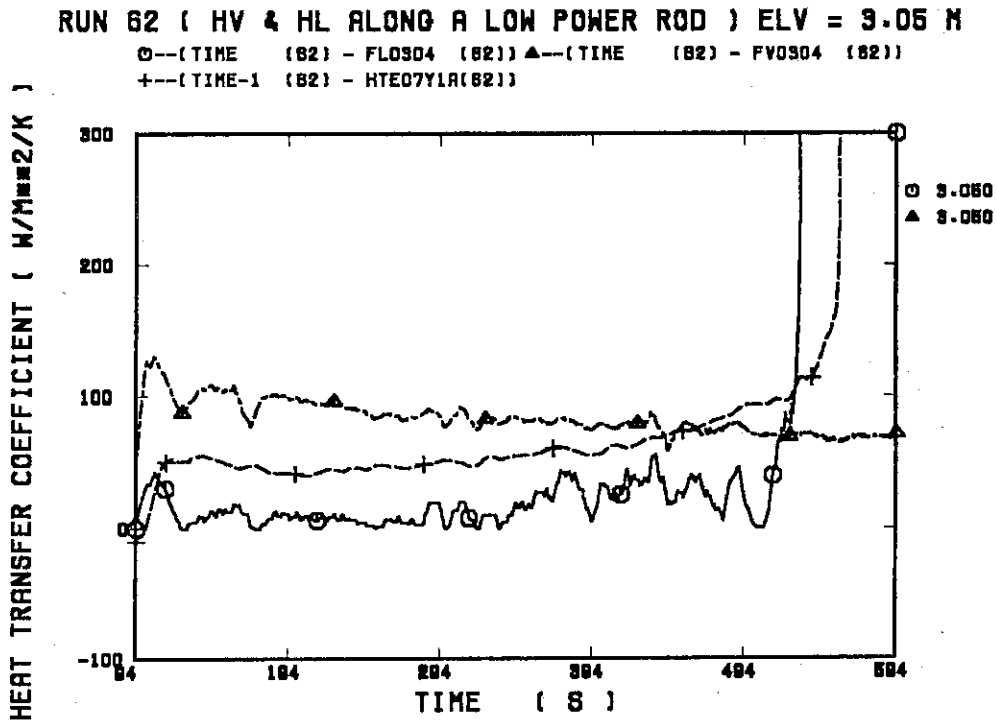

Fig. B.1.23 Clad temperature at elevation of 3.05 m along a low power rod

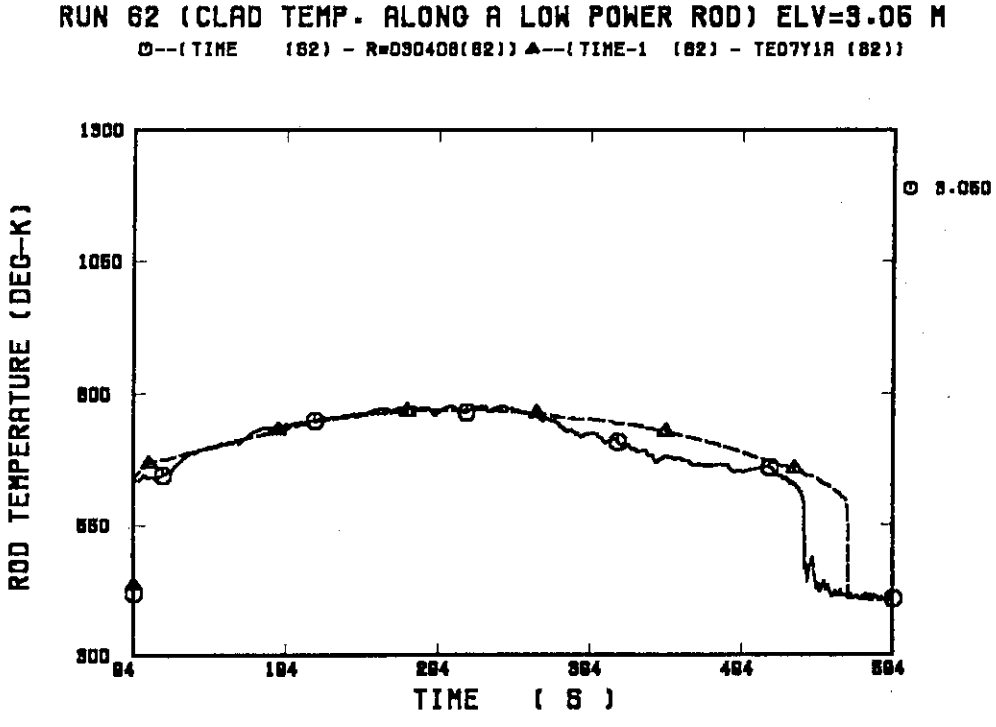

Fig. B.1.24 Heat transfer coefficient at elevation of 3.05 m along a low power rod

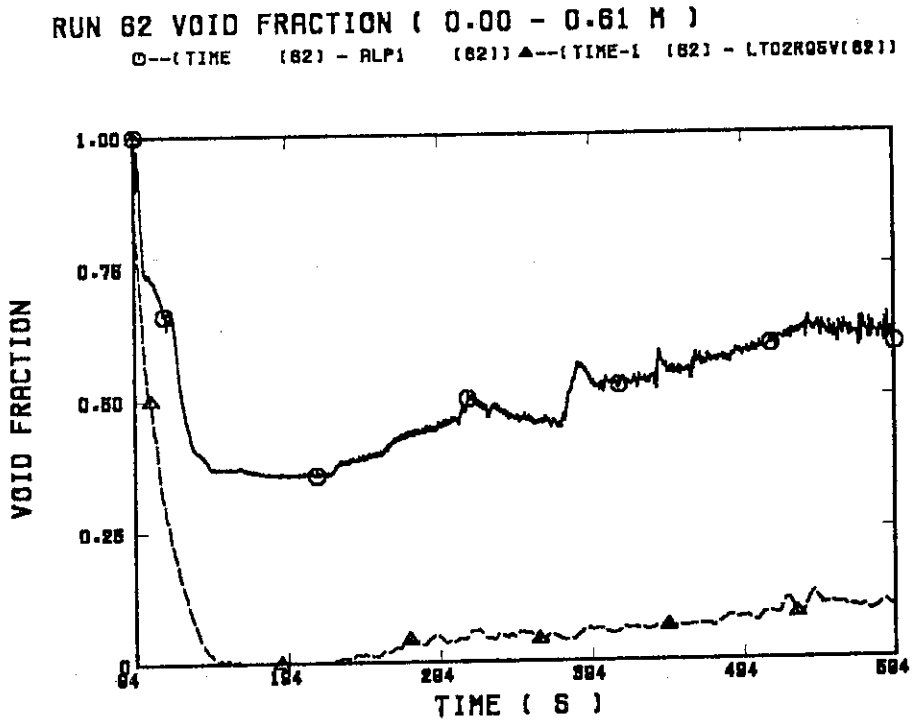

Fig. B.1.25 Average void fraction between 0.00 and 0.61 m

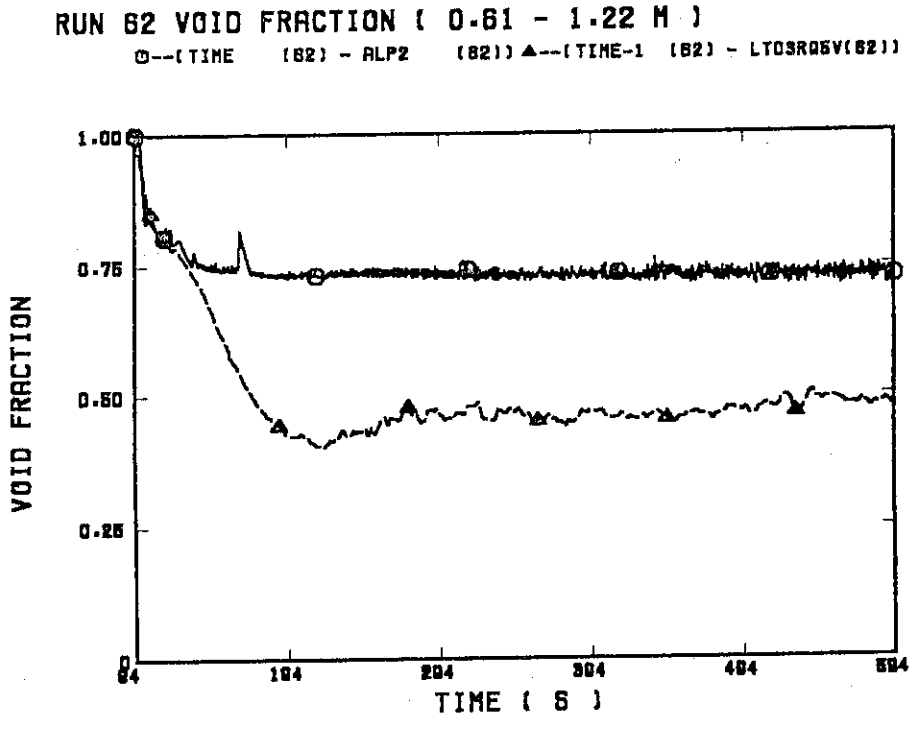

Fig. B.1.26 Average void fraction between 0.61 and 1.22 m

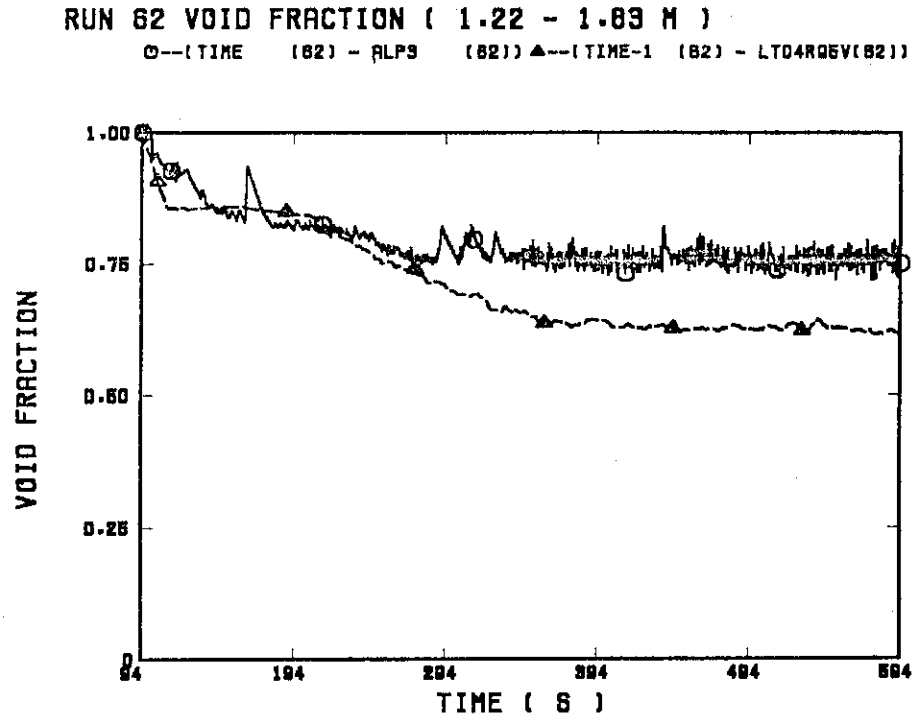

Fig. B.1.27 Average void fraction between 1.22 and 1.83 m

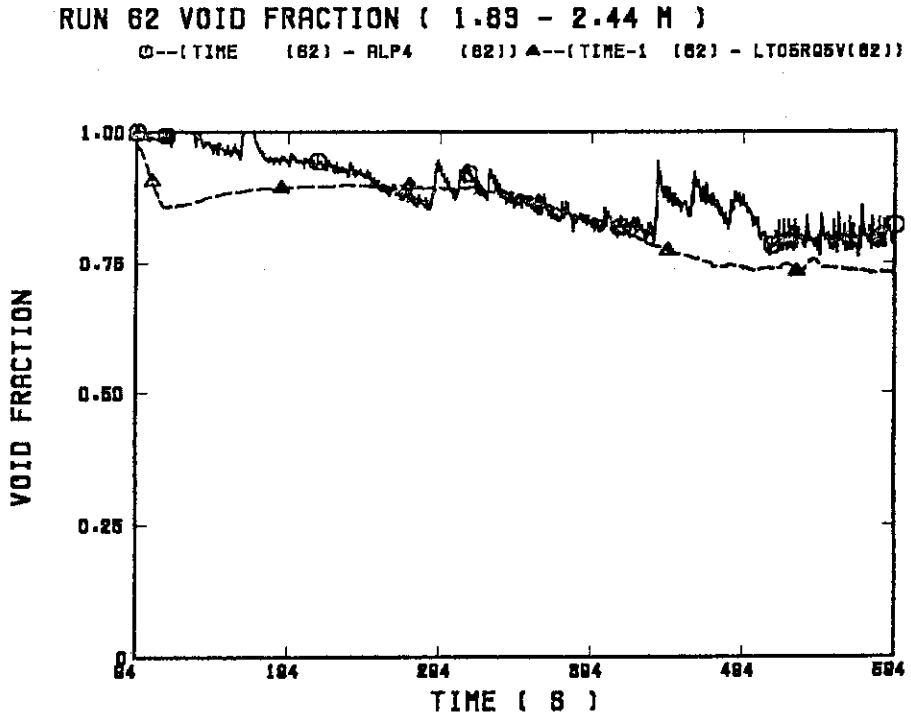

Fig. B.1.28 Average void fraction between 1.83 and 2.44 m

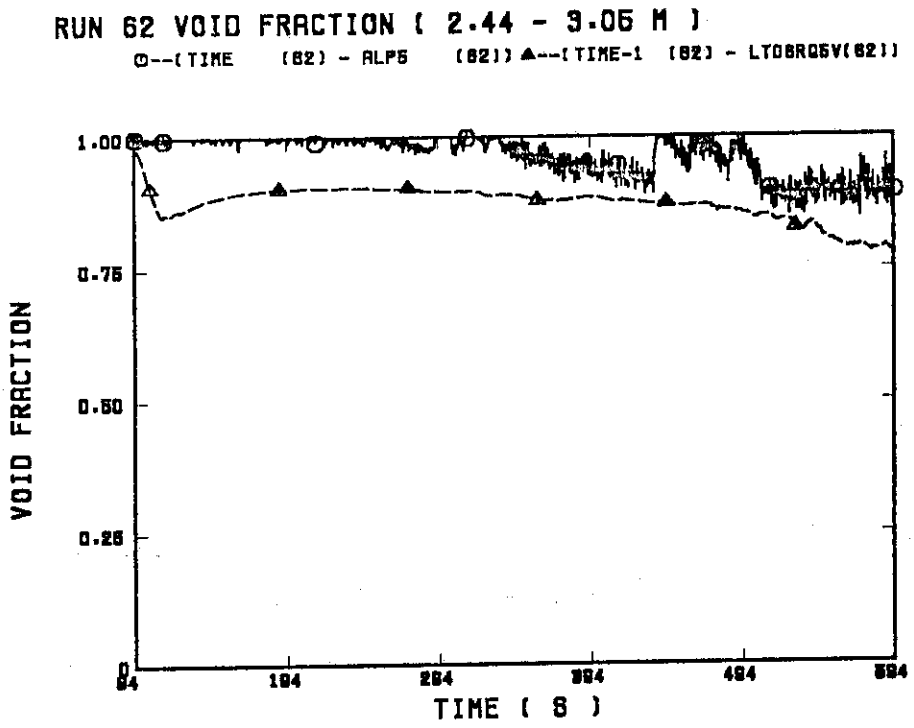

Fig. B.1.29 Average void fraction between 2.44 and 3.05 m

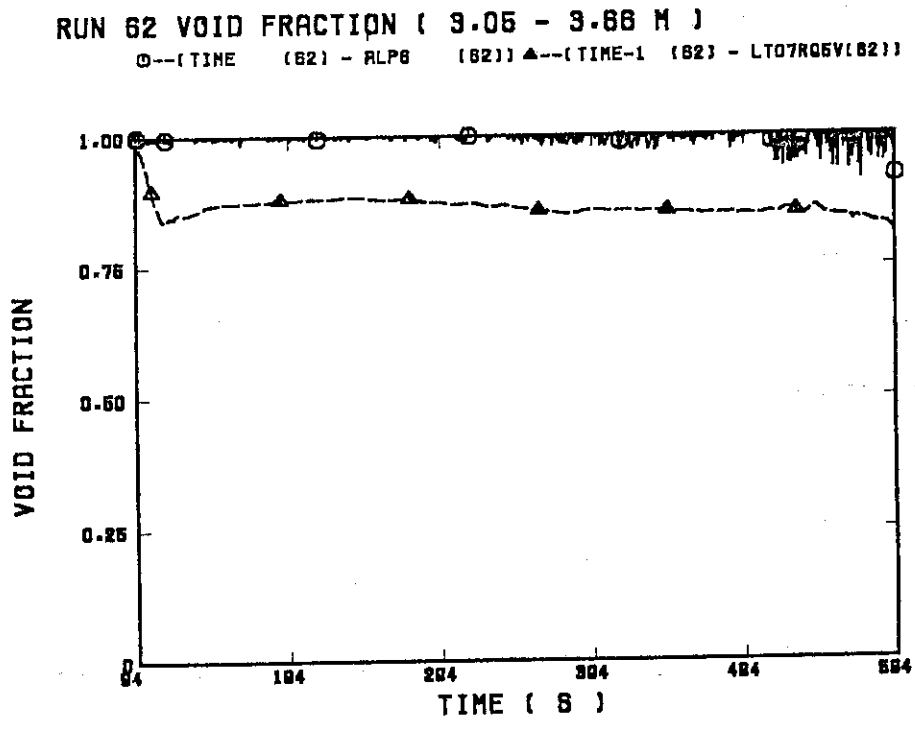

Fig. B.1.30 Average void fraction between 3.05 and 3.66 m

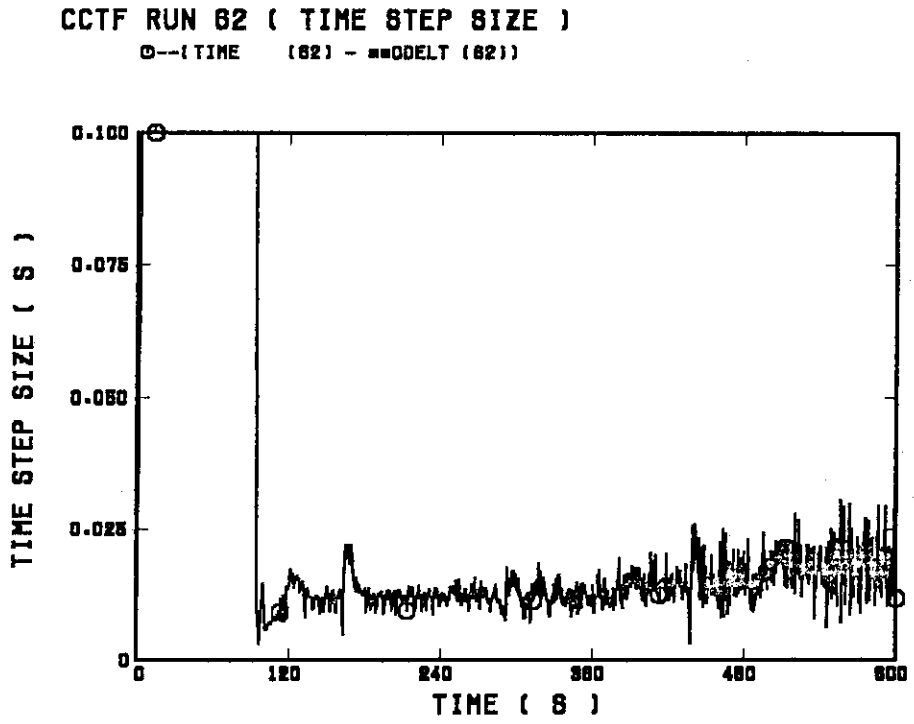

Fig. B.1.31 Time step size

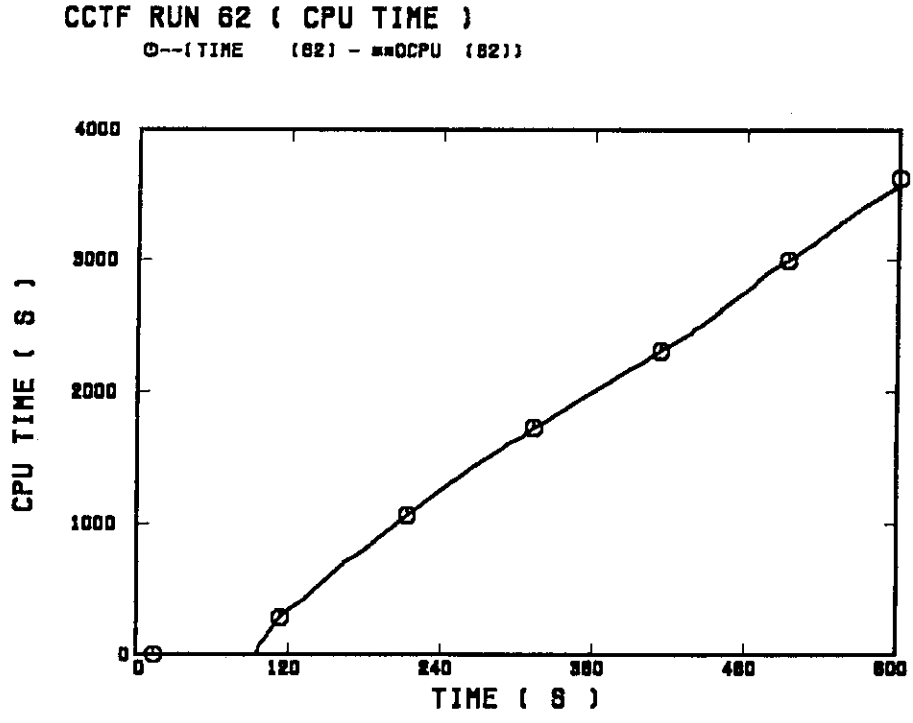

Fig. B.1.32 CPU time

(2) CCTF High Pressure Test (Run 55)

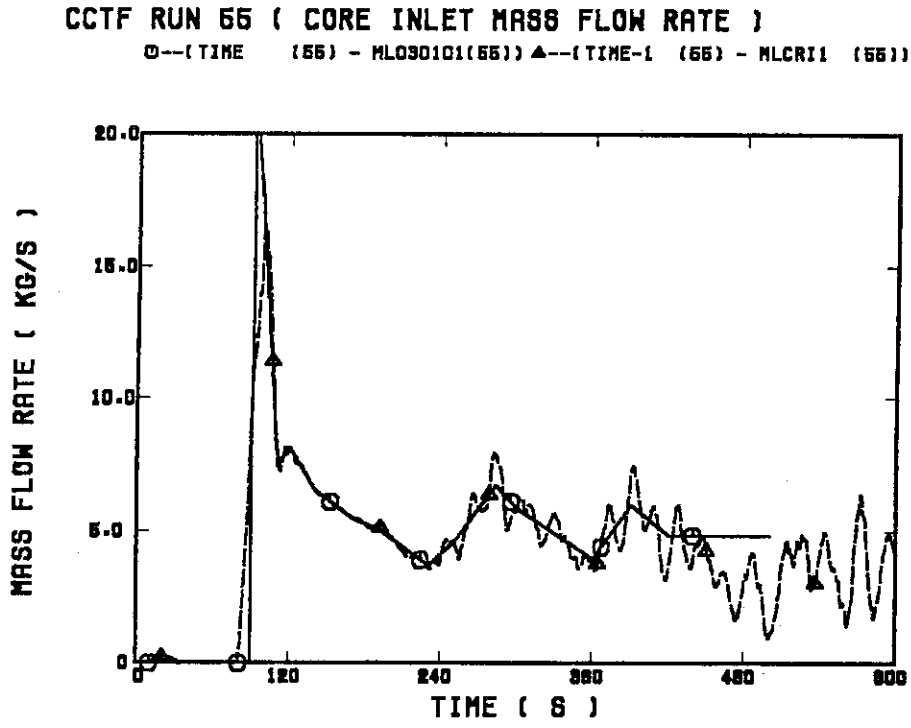

Fig. B.2.1 Core inlet mass flow rate (input)

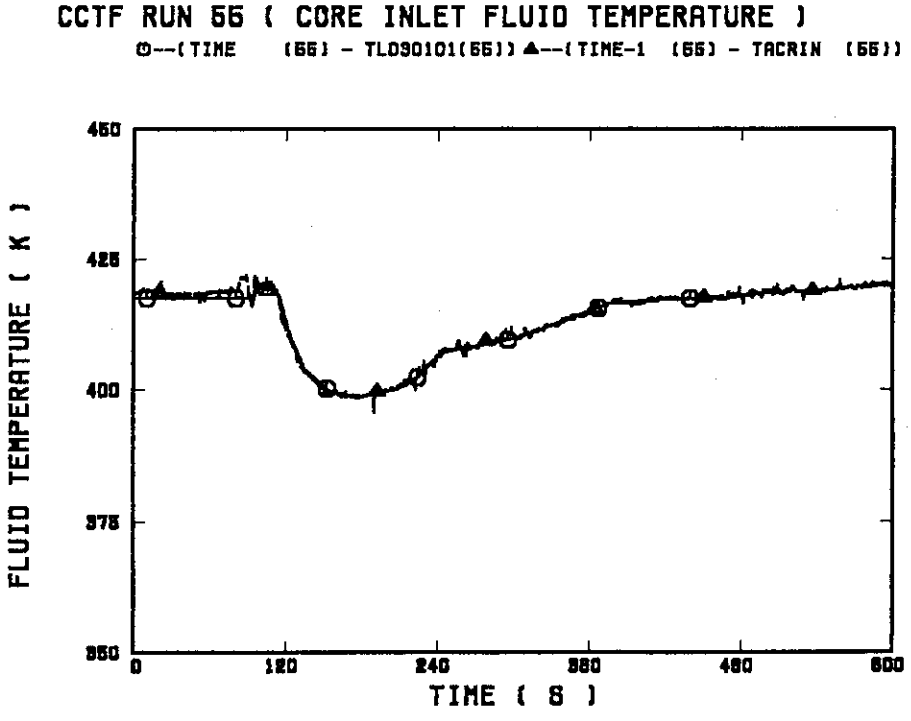

Fig. B.2.2 Core inlet fluid temperature (input)

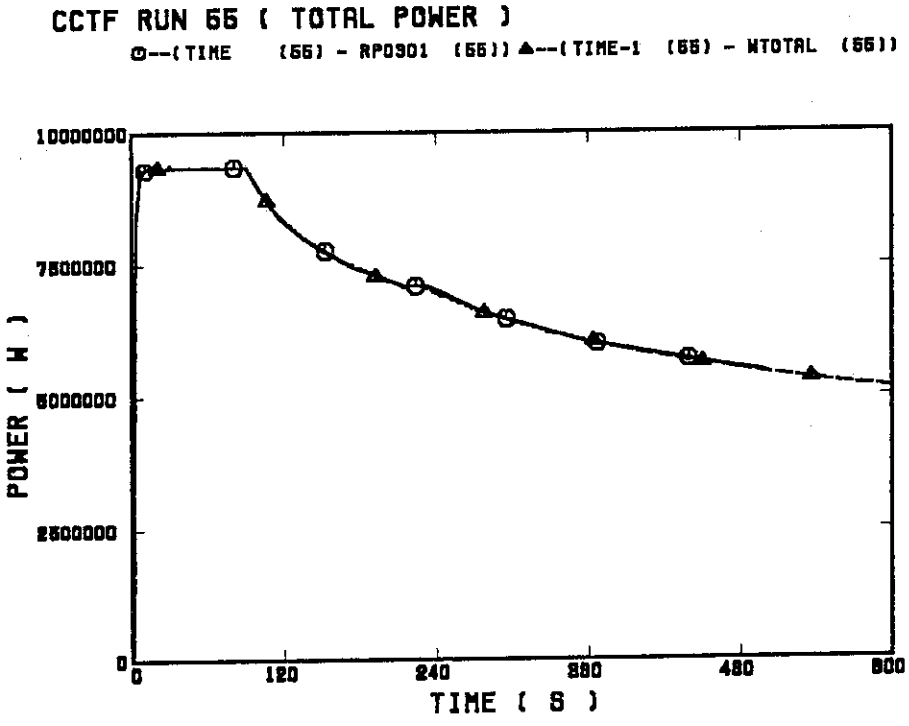

Fig. B.2.3 Total power supplied to core (input)

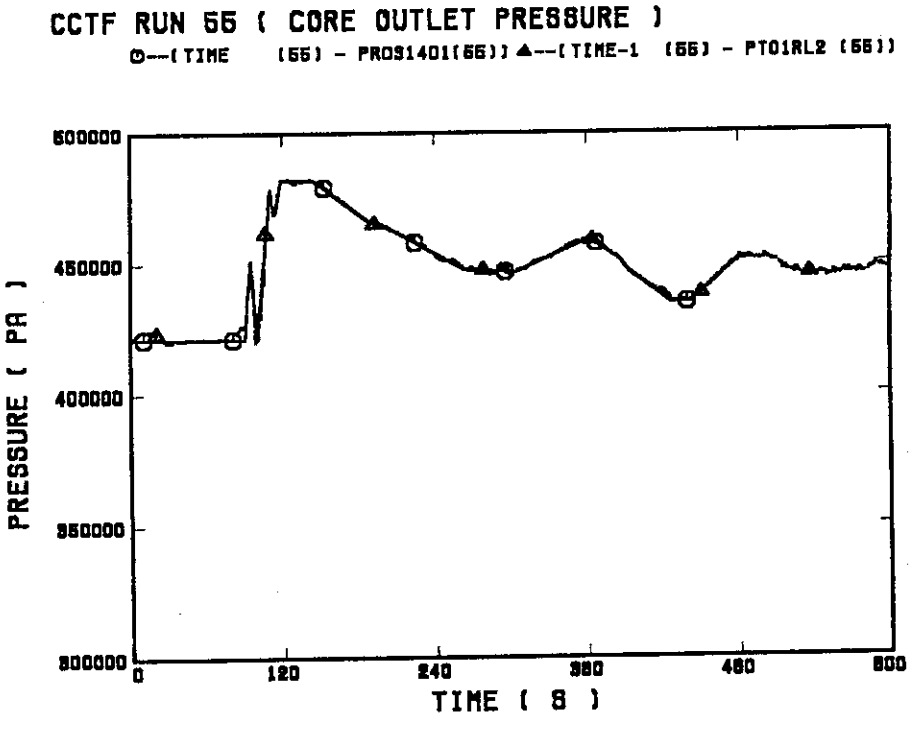

Fig. B.2.4 Core outlet pressure (input)

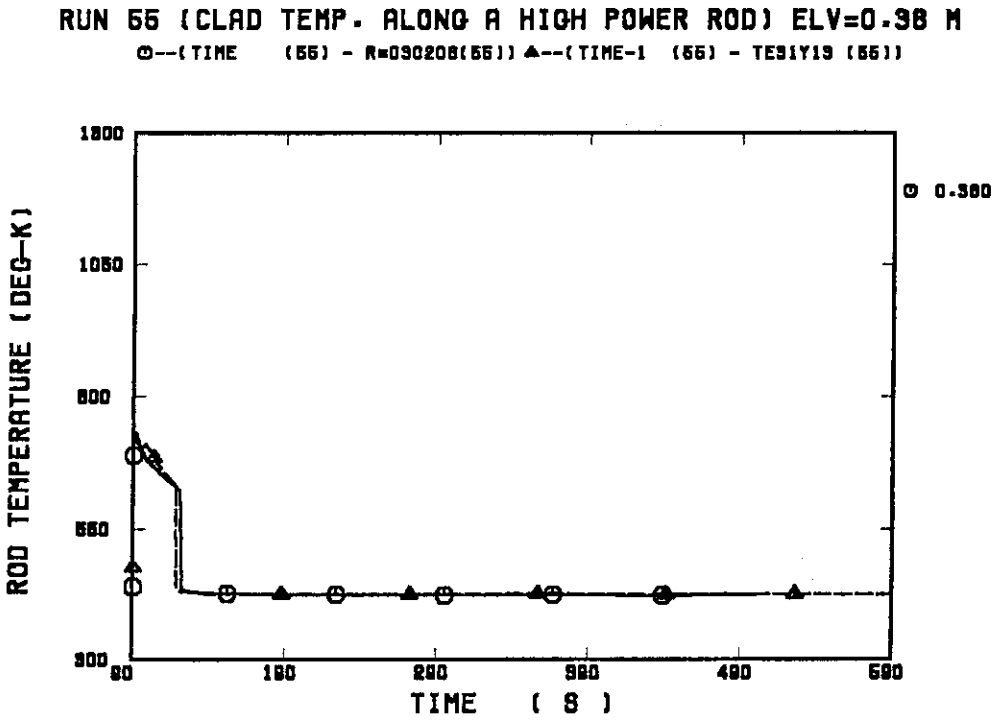

Fig. B.2.5 Clad temperature at elevation of 0.38 m along a high power rod

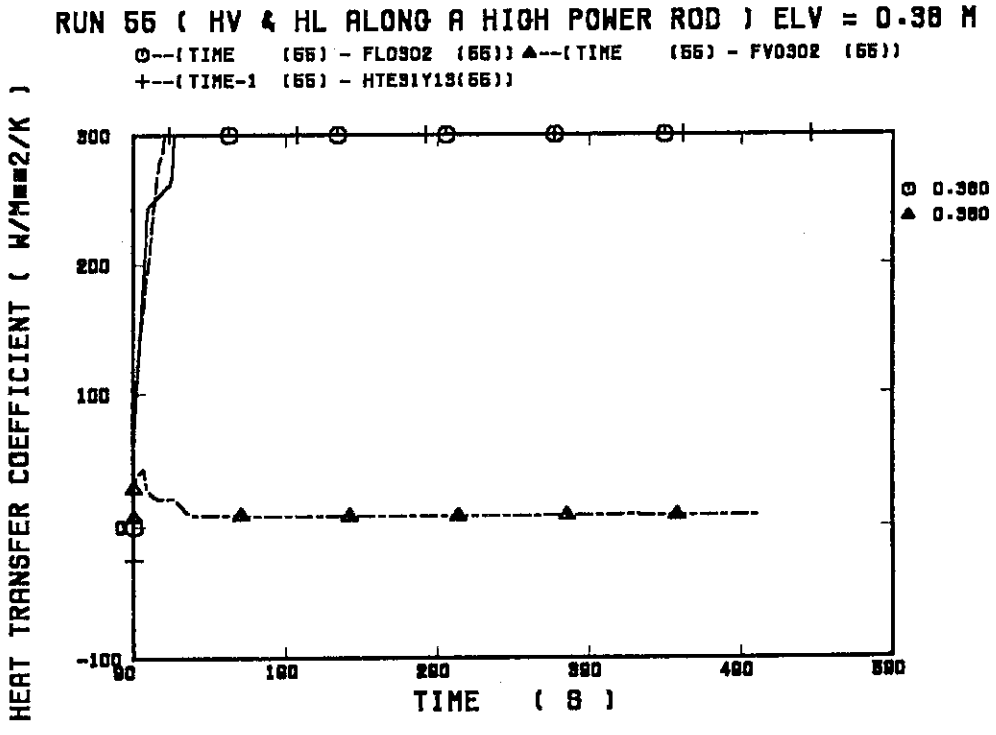

Fig. B.2.6 Heat transfer coefficient at elevation of 0.38 m along a high power rod

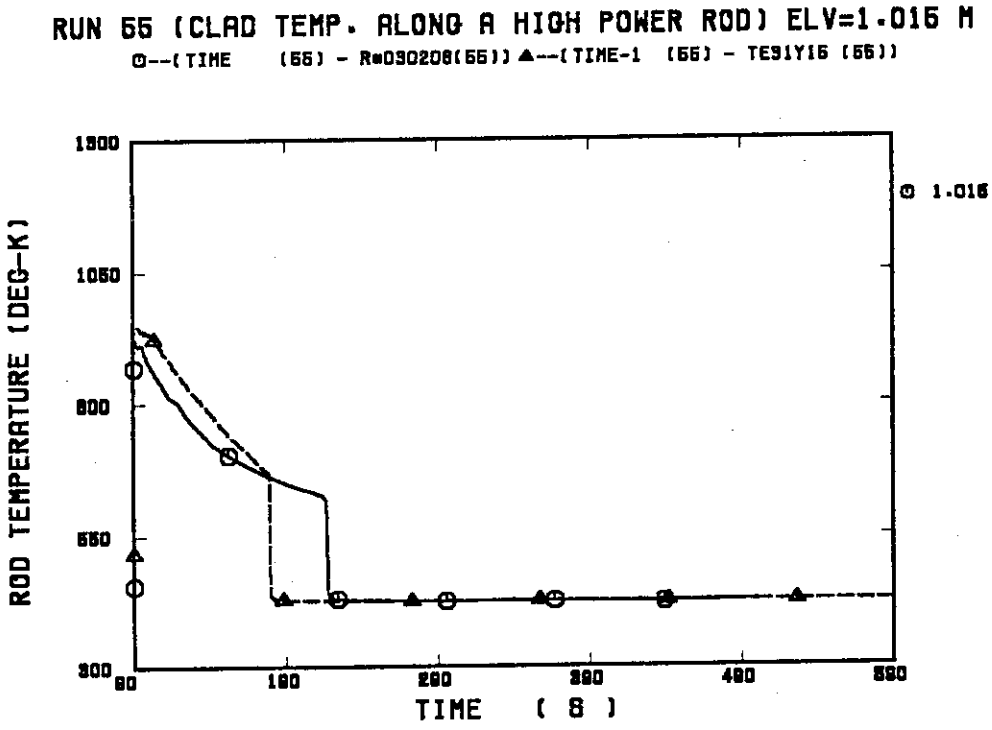

Fig. B.2.7 Clad temperature at elevation of 1.015 m along a high power rod

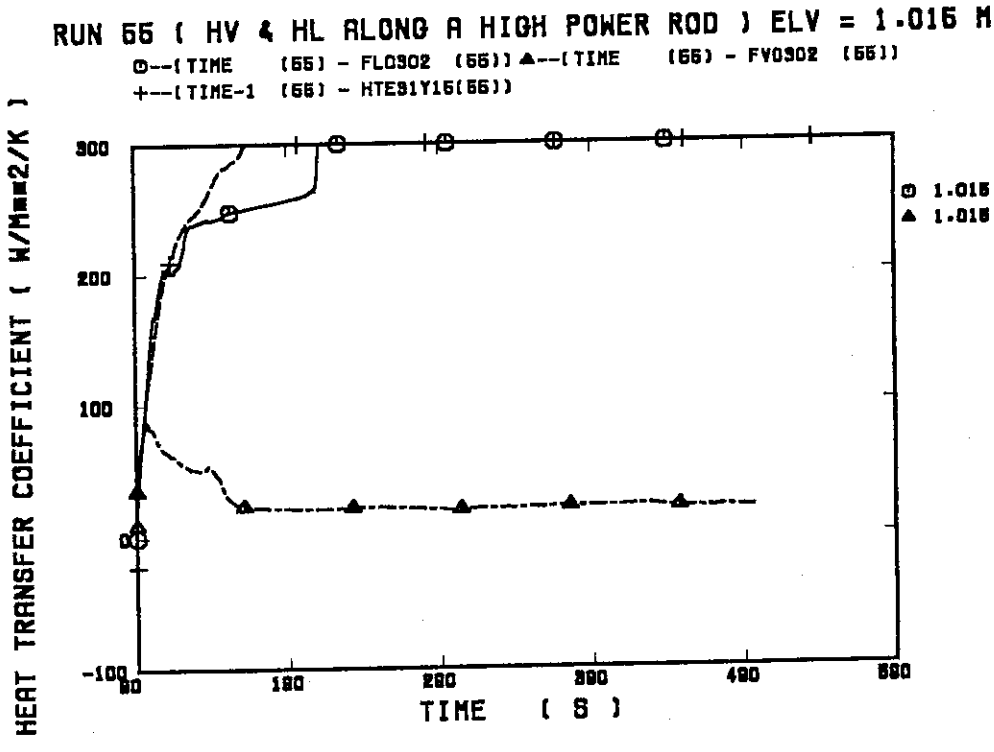

Fig. B.2.8 Heat transfer coefficient at elevation of 1.015 m along a high power rod

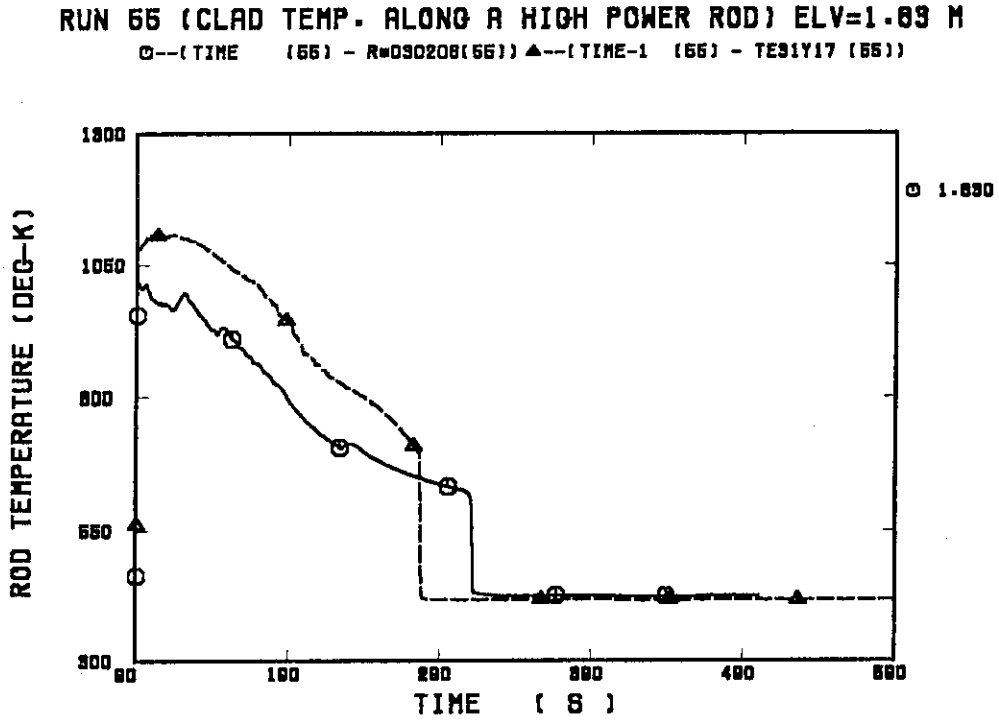

Fig. B.2.9 Clad temperature at elevation of 1.83 m along a high power rod

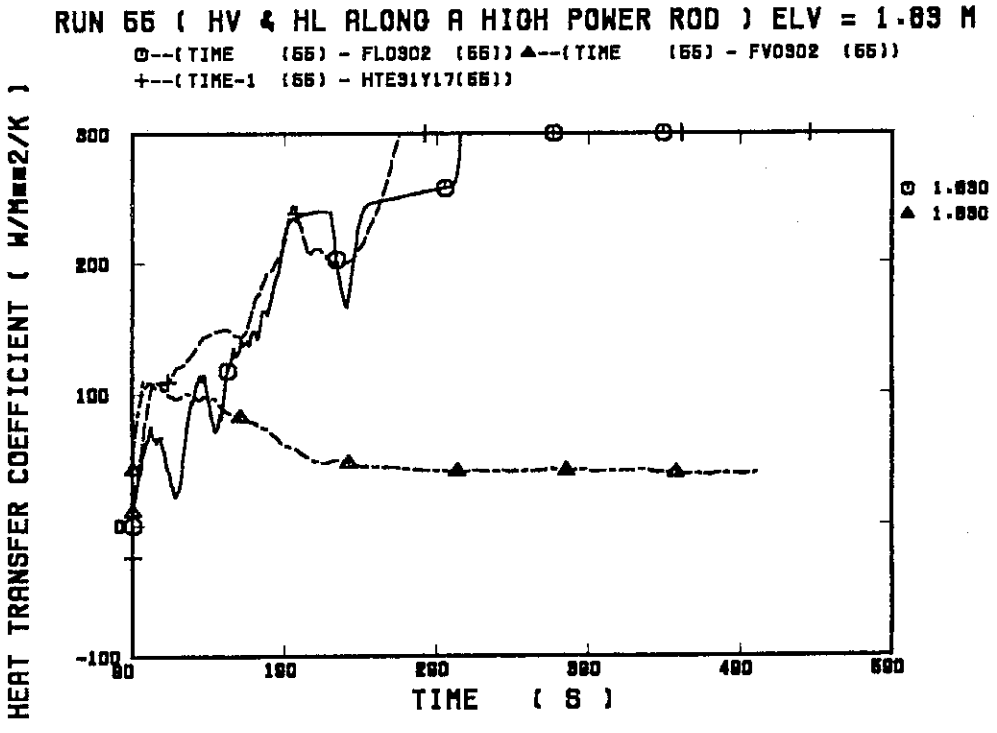

Fig. B.2.10 Heat transfer coefficient at elevation of 1.83 m along a high power rod

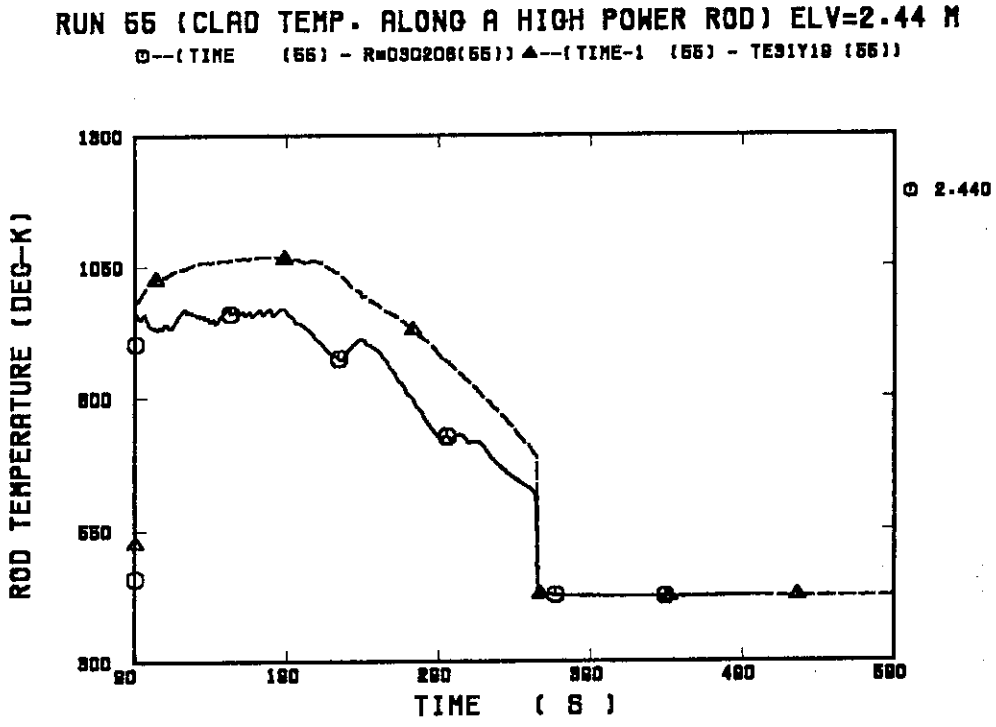

Fig. B.2.11 Clad temperature at elevation of 2.44 m along a high power rod

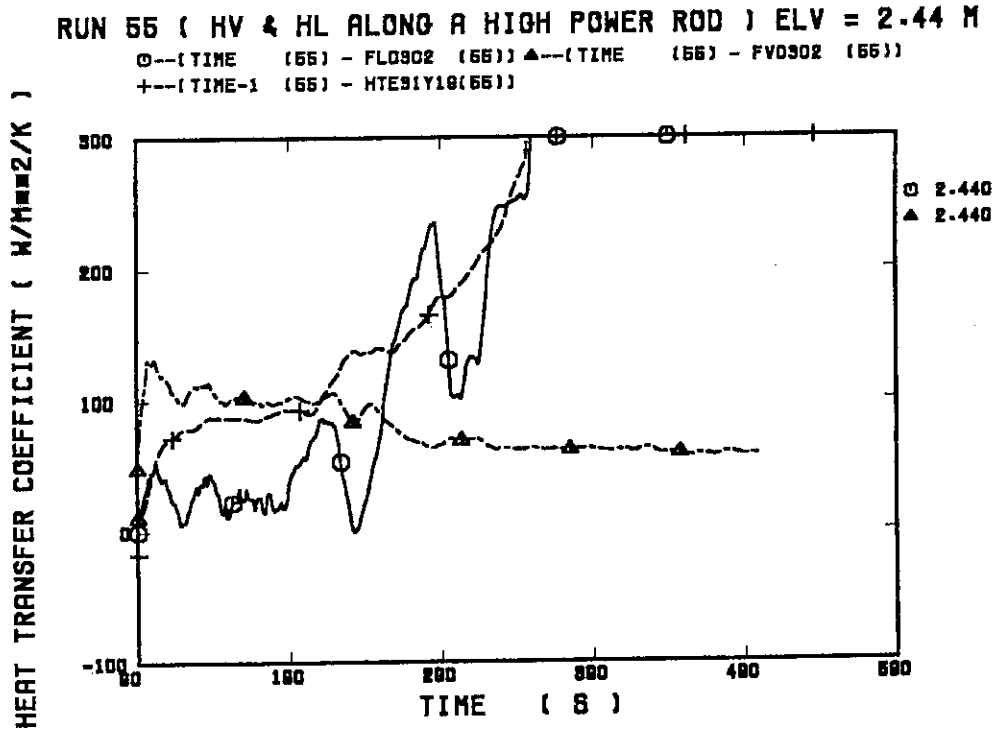

Fig. B.2.12 Heat transfer coefficient at elevation of 2.44 m along a high power rod

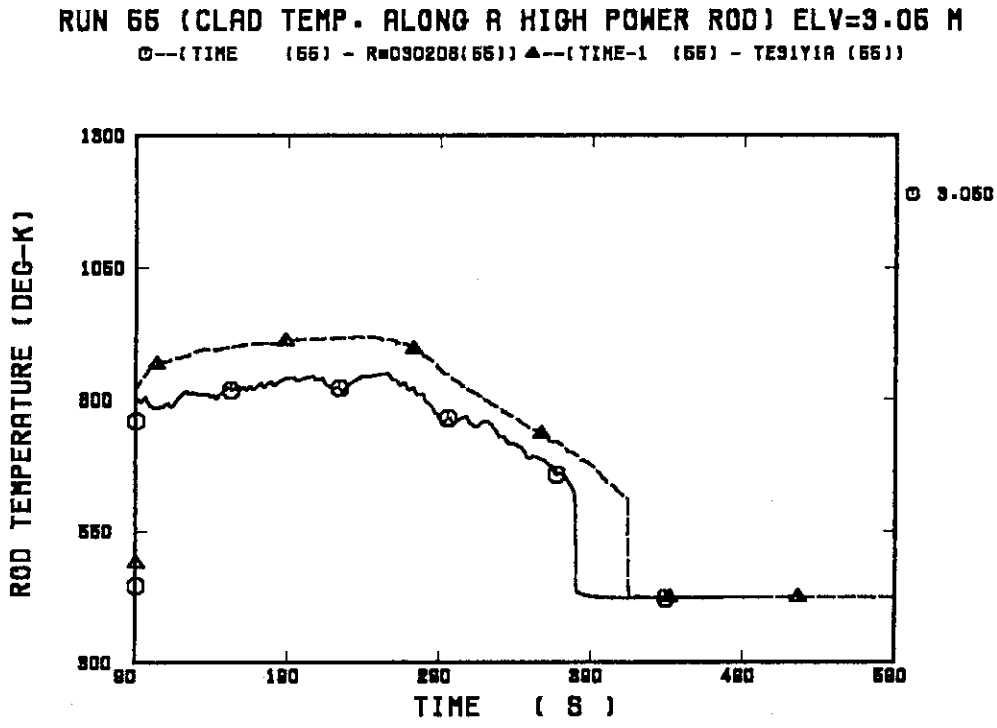

Fig. B.2.13 Clad temperature at elevation of 3.05 m along a high power rod

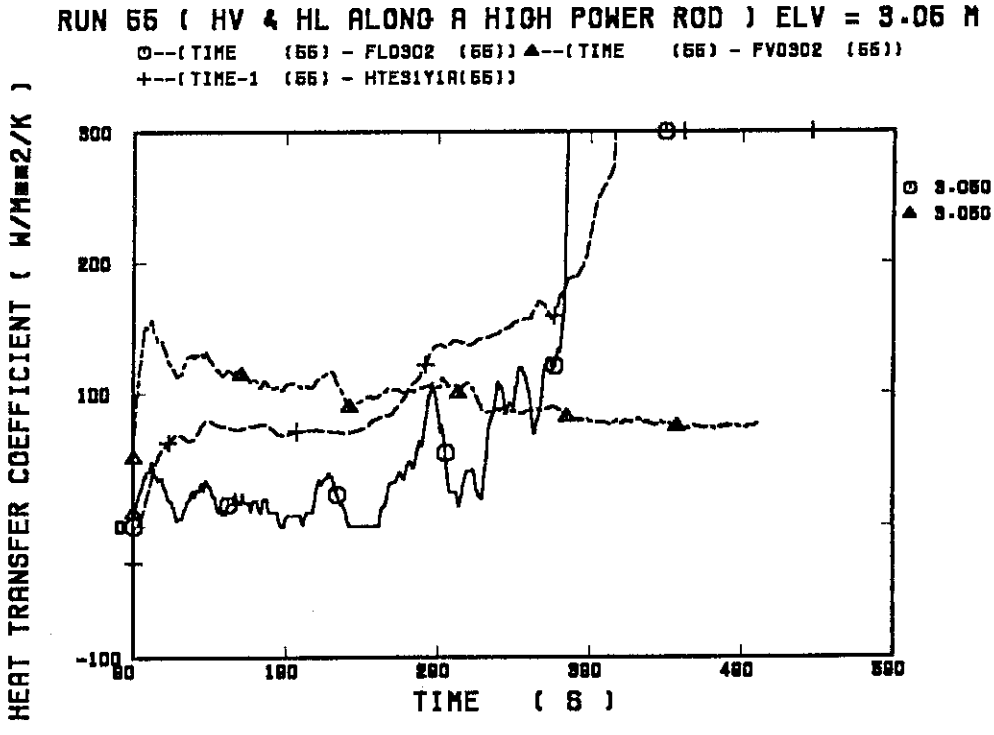

Fig. B.2.14 Heat transfer coefficient at elevation of 3.05 m along a high power rod

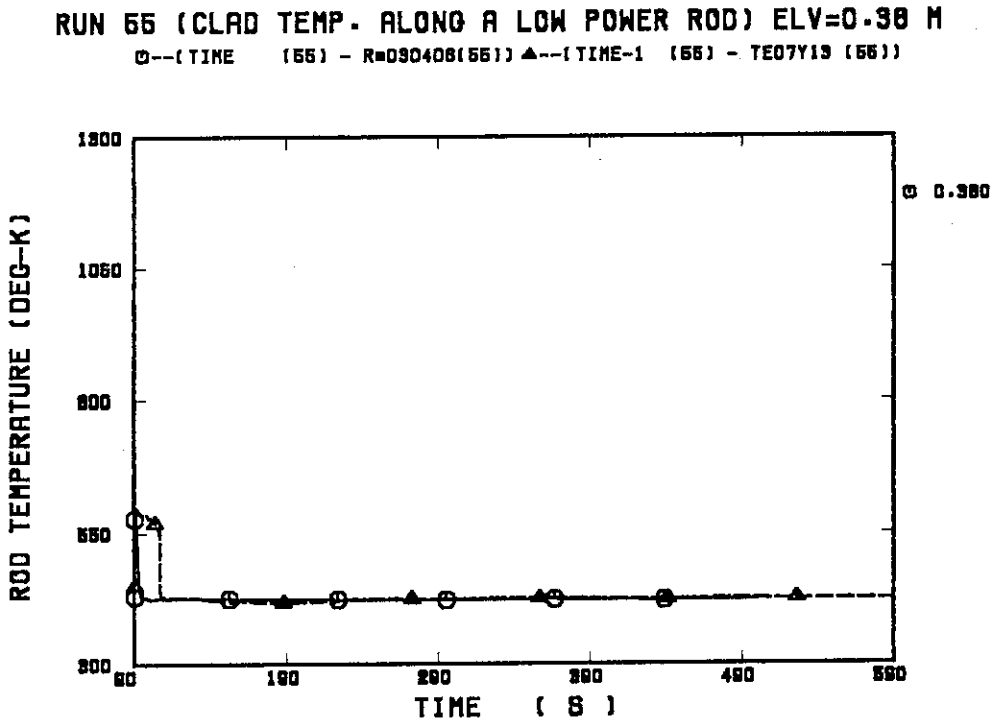

Fig. B.2.15 Clad temperature at elevation of 0.38 m along a low power rod

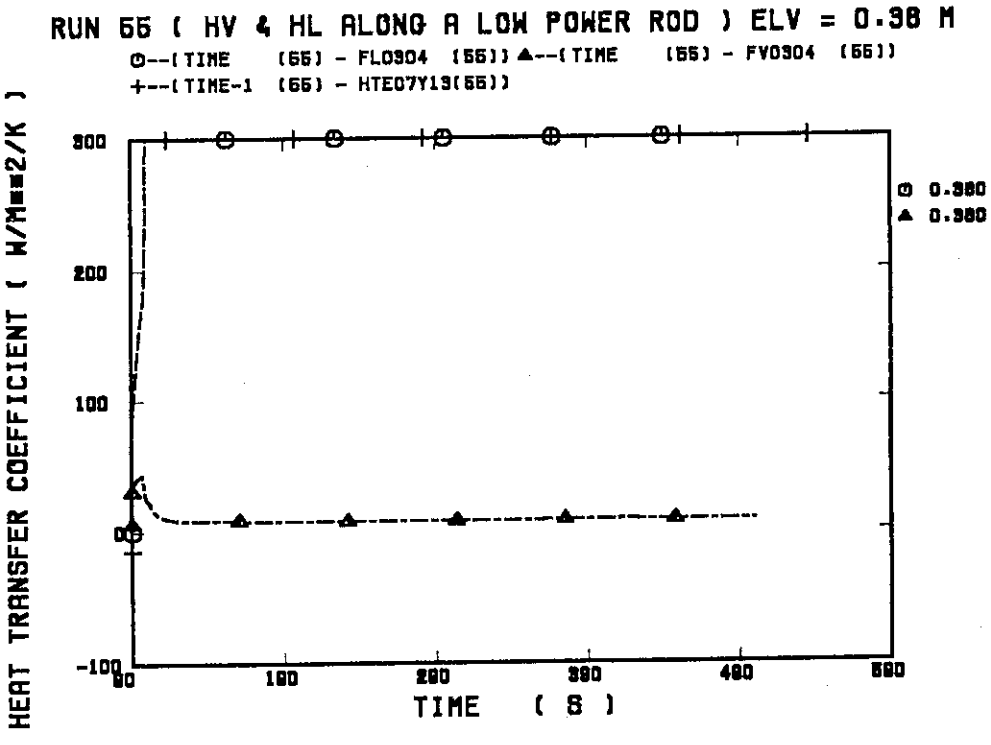

Fig. B.2.16 Heat transfer coefficient at elevation of 0.38 m along a low power rod

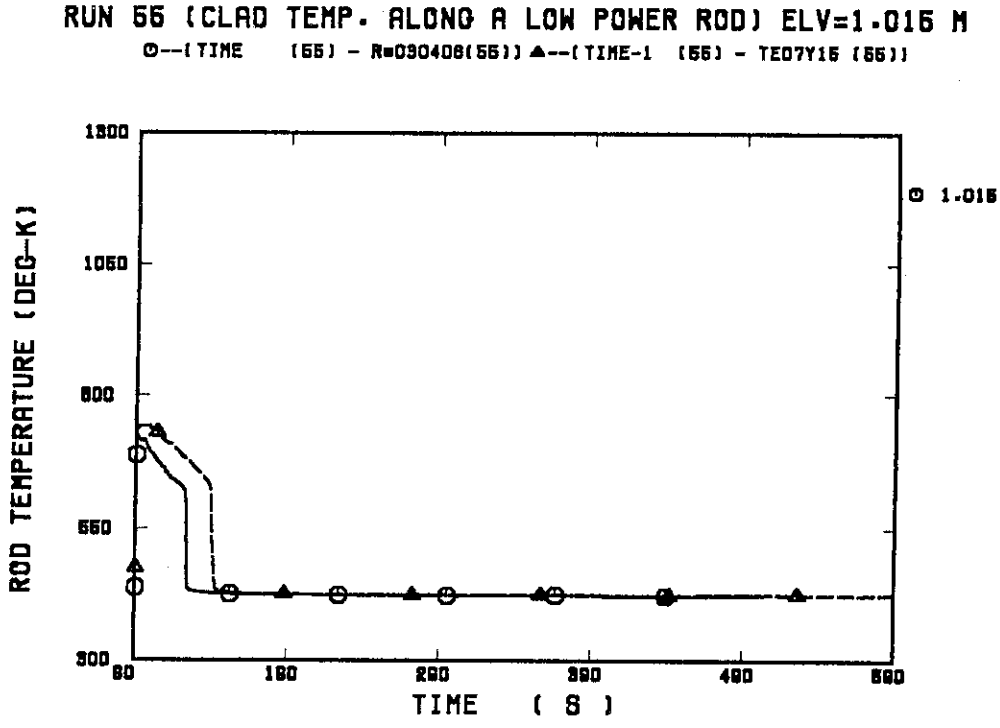

Fig. B.2.17 Clad temperature at elevation of 1.015 m along a low power rod

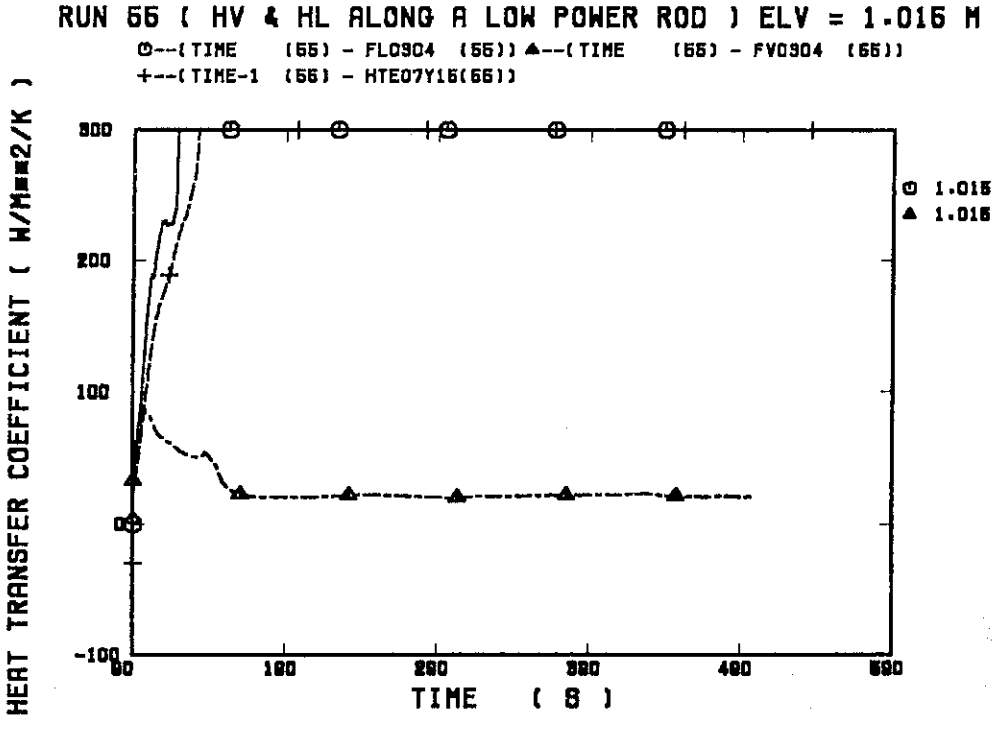

Fig. B.2.18 Heat transfer coefficient at elevation of 1.015 m along a low power rod

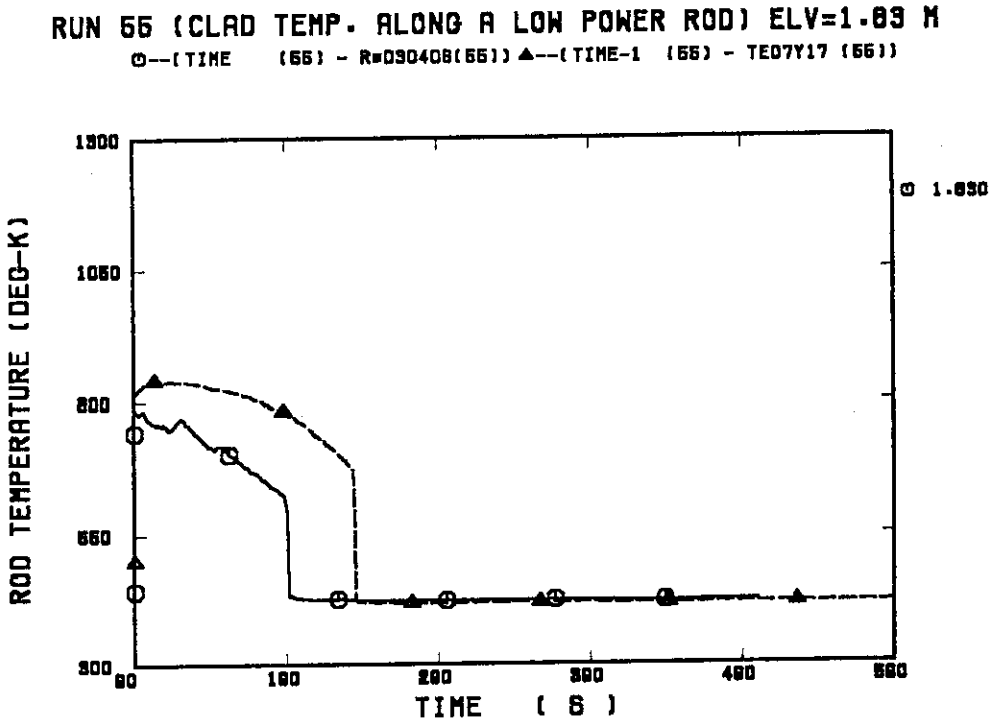

Fig. B.2.19 Clad temperature at elevation of 1.83 m along a low power rod

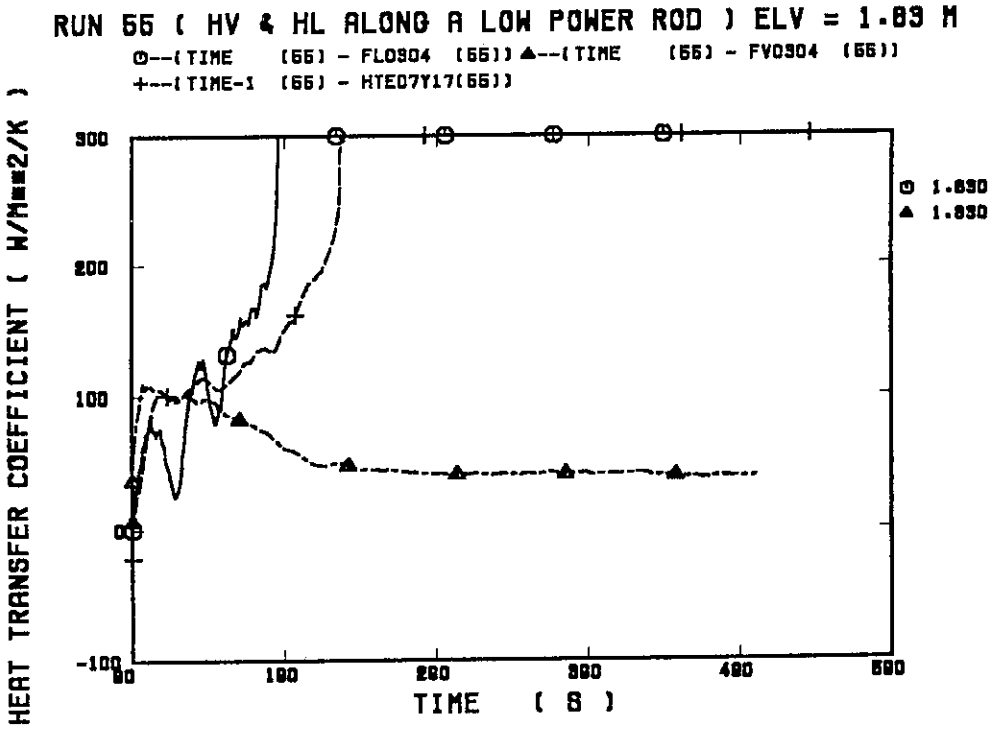

Fig. B.2.20 Heat transfer coefficient at elevation of 1.83 m along a low power rod

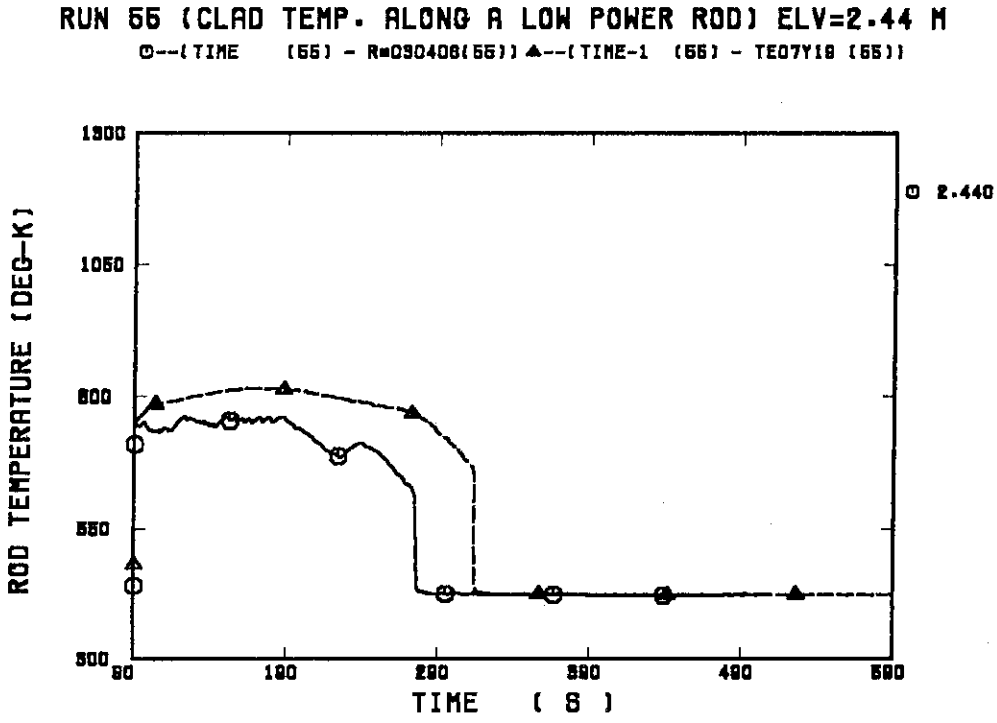

Fig. B.2.21 Clad temperature at elevation of 2.44 m along a low power rod

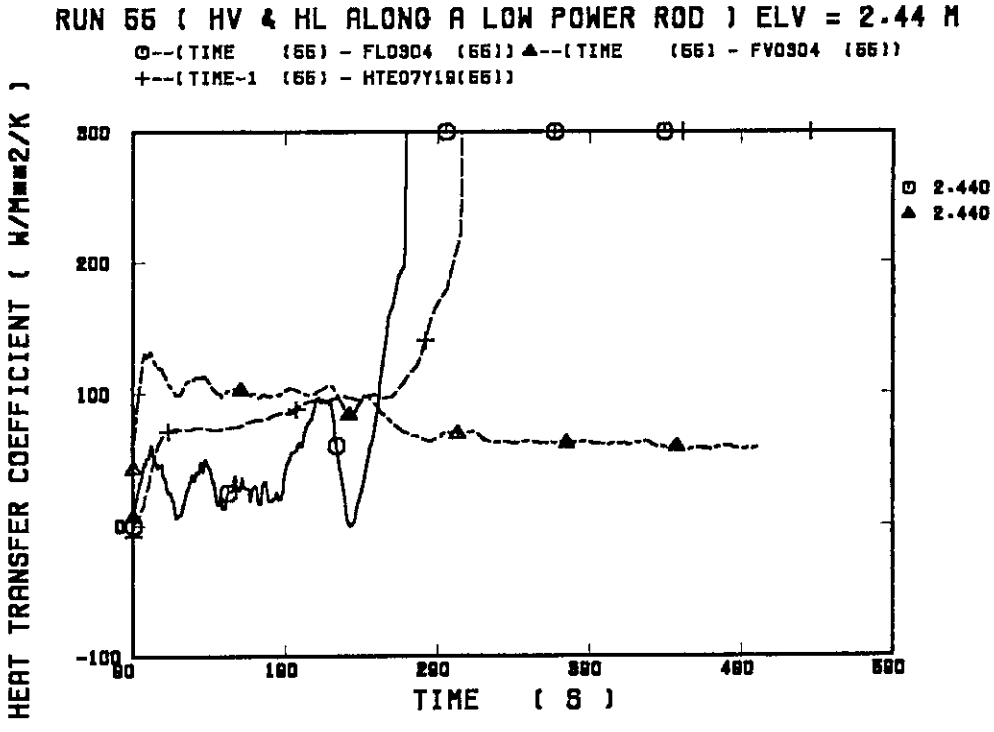

Fig. B.2.22 Heat transfer coefficient at elevation of 2.44 m along a low power rod

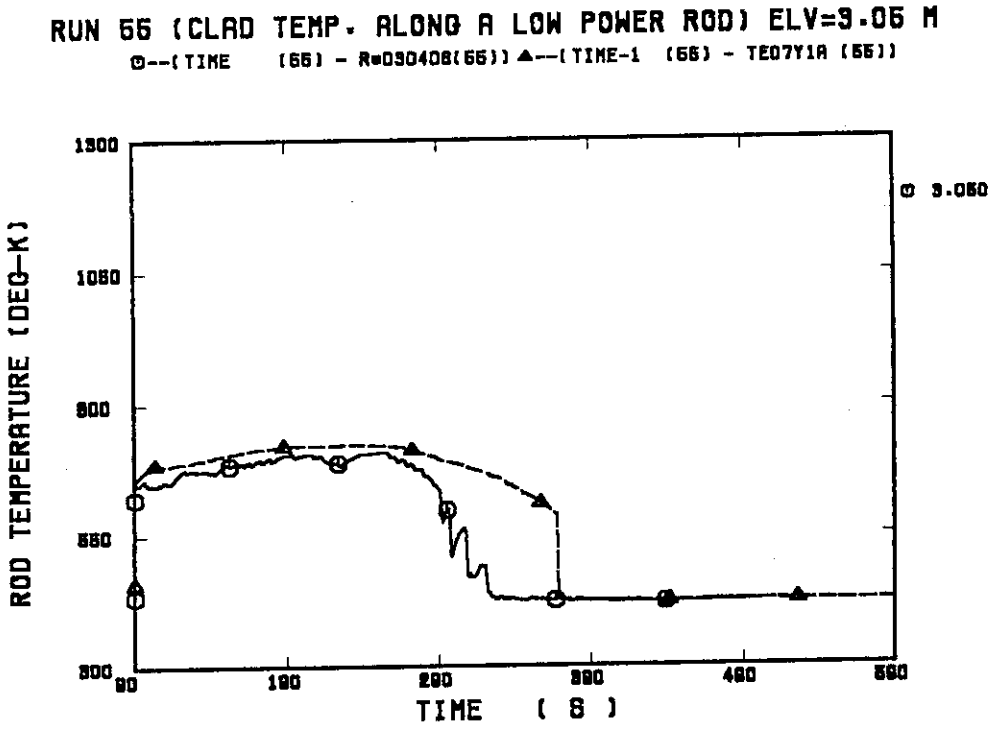

Fig. B.2.23 Clad temperature at elevation of 3.05 m along a low power rod

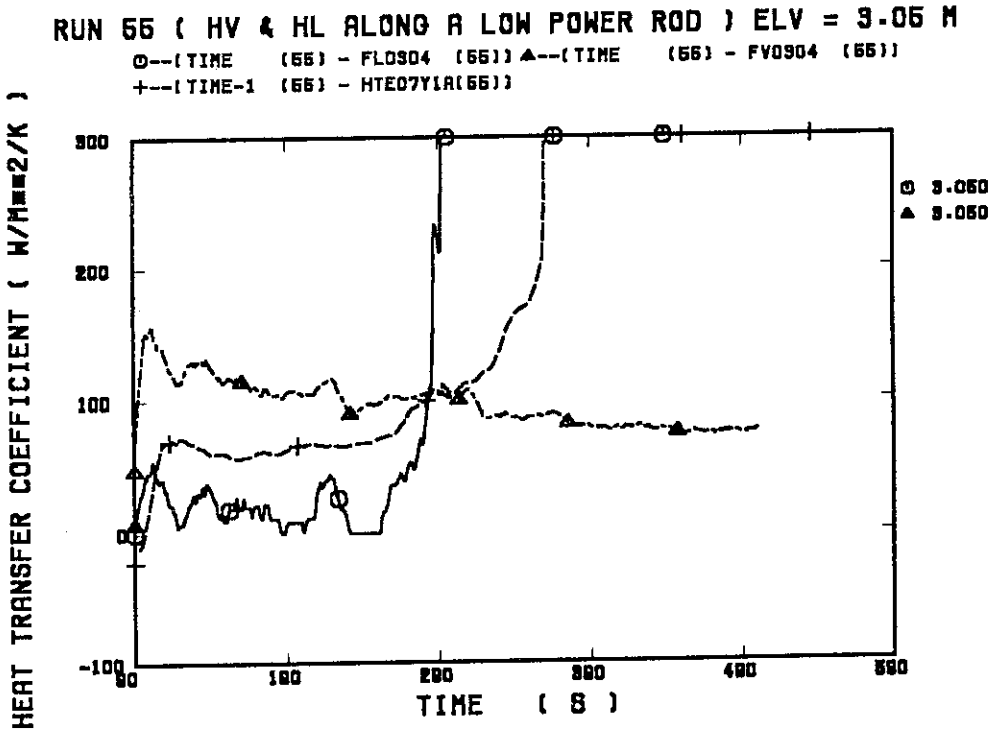

Fig. B.2.24 Heat transfer coefficient at elevation of 3.05 m along a low power rod

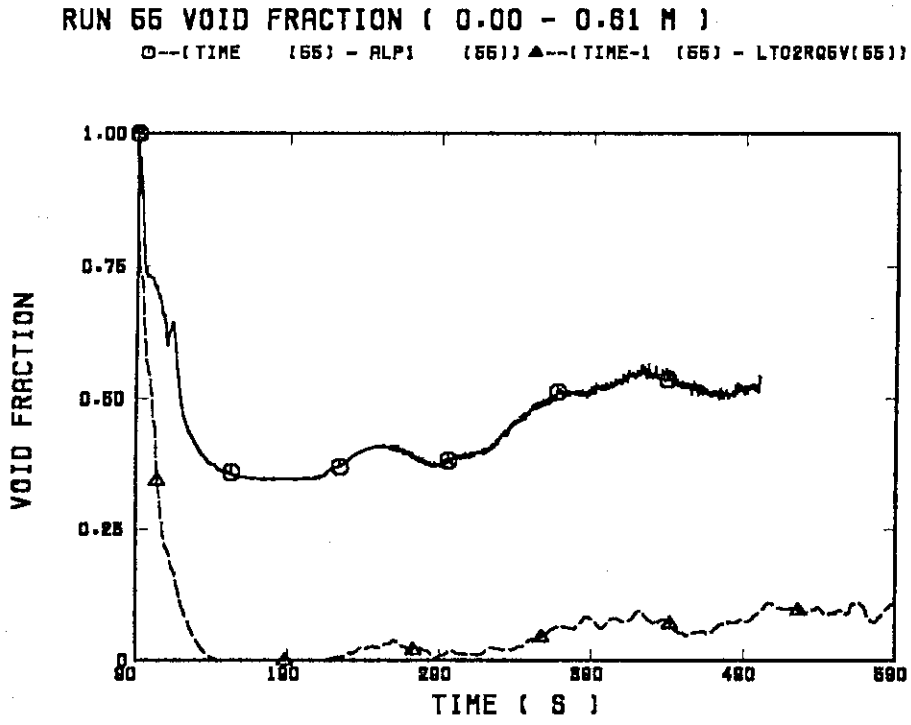

Fig. B.2.25 Average void fraction between 0.00 and 0.61 m

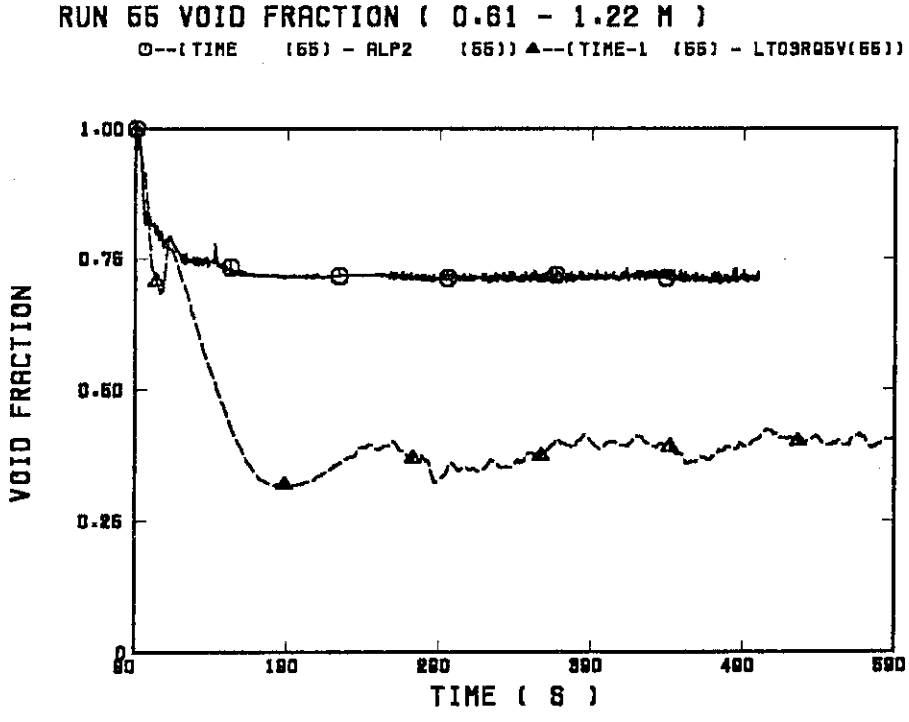

Fig. B.2.26 Average void fraction between 0.61 and 1.22 m

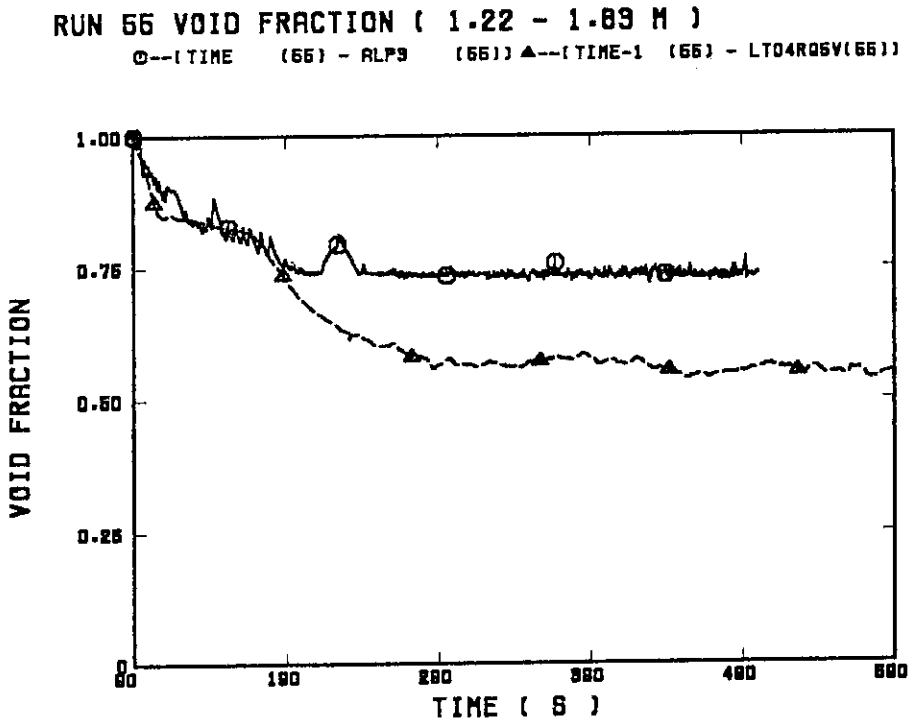

Fig. B.2.27 Average void fraction between 1.22 and 1.83 m

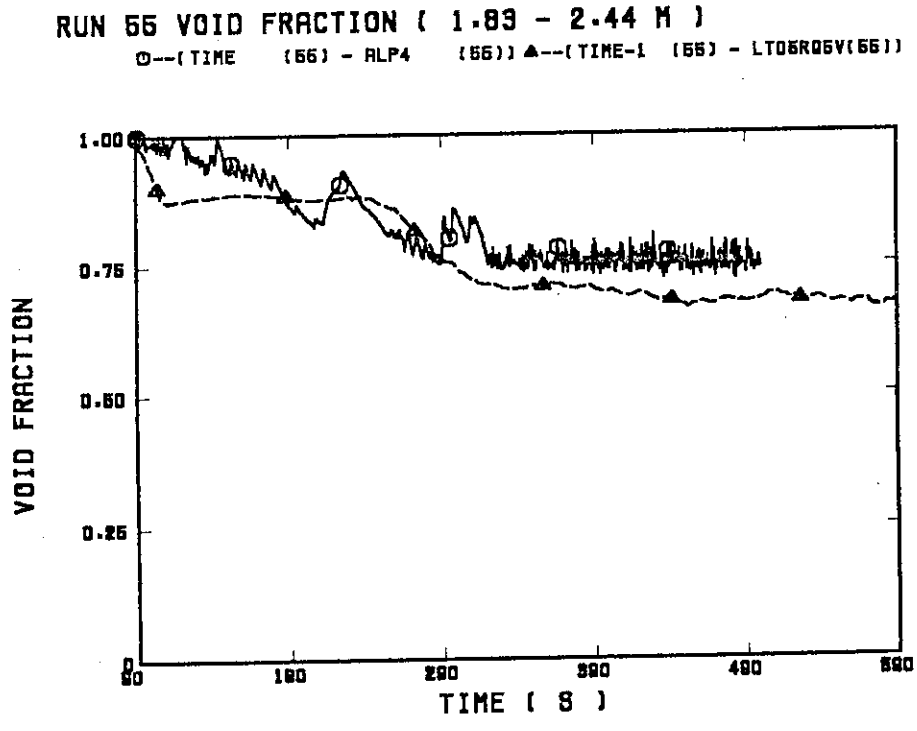

Fig. B.2.28 Average void fraction between 1.83 and 2.44 m

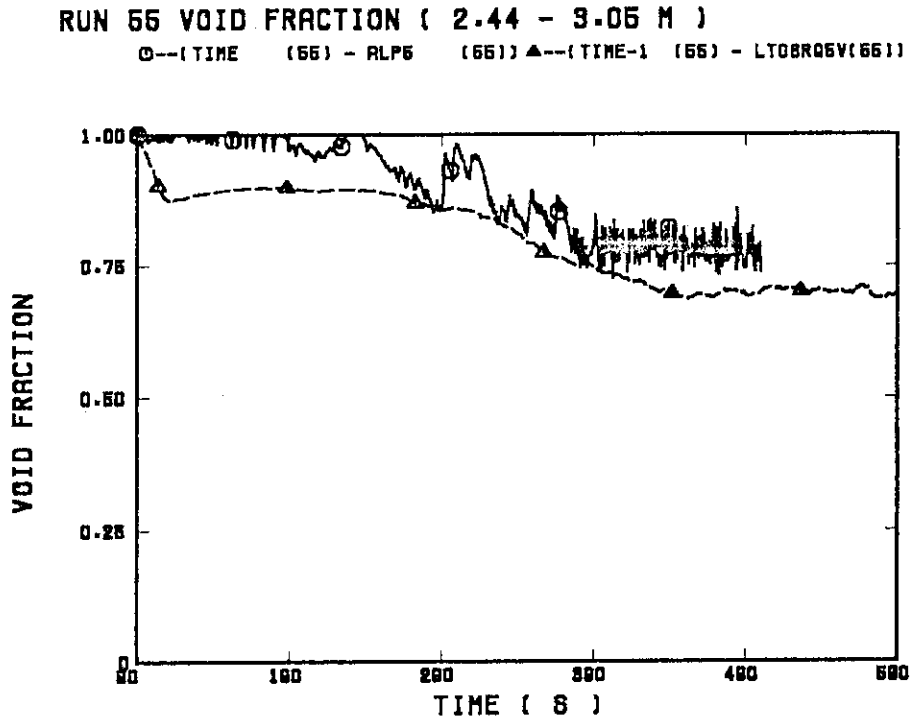

Fig. B.2.29 Average void fraction between 2.44 and 3.05 m

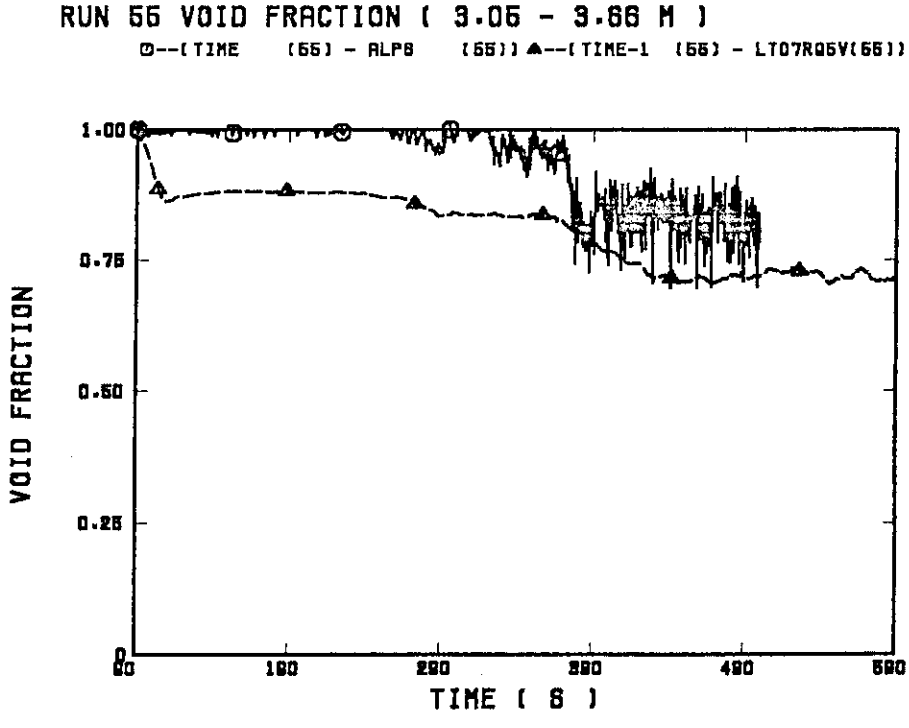

Fig. B.2.30 Average void fraction between 3.05 and 3.66 m

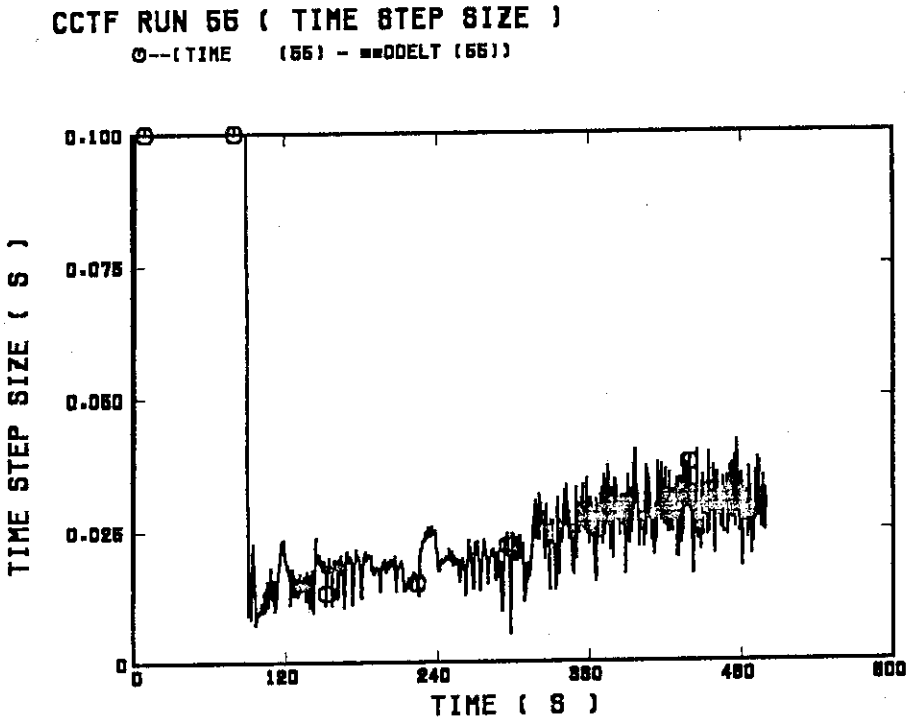

Fig. B.2.31 Time step size

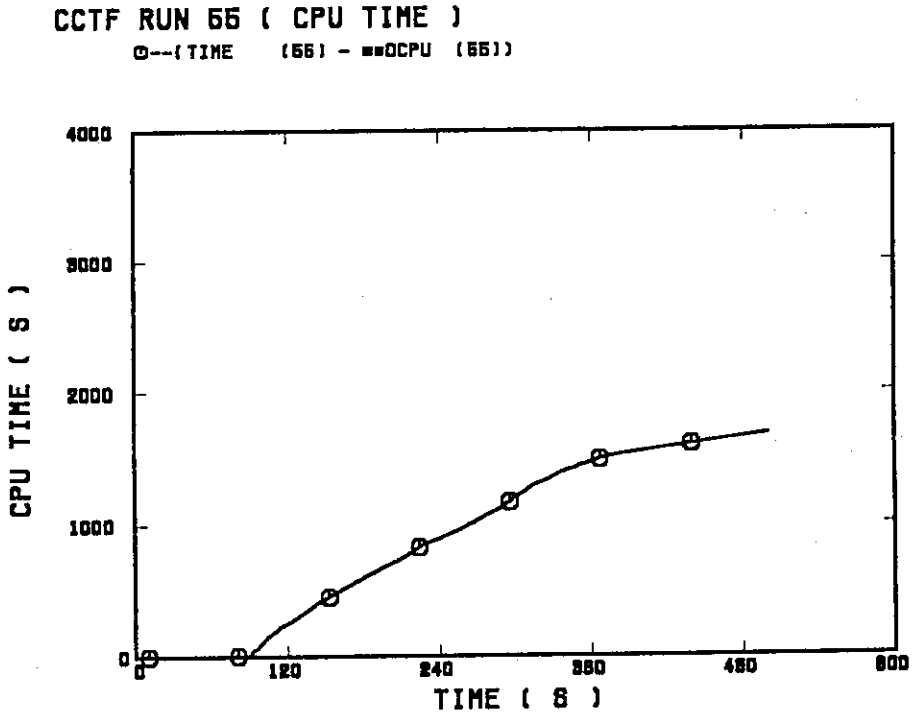

Fig. B.2.32 CPU time

(3) CCTF Low Pressure Test (Run 67)

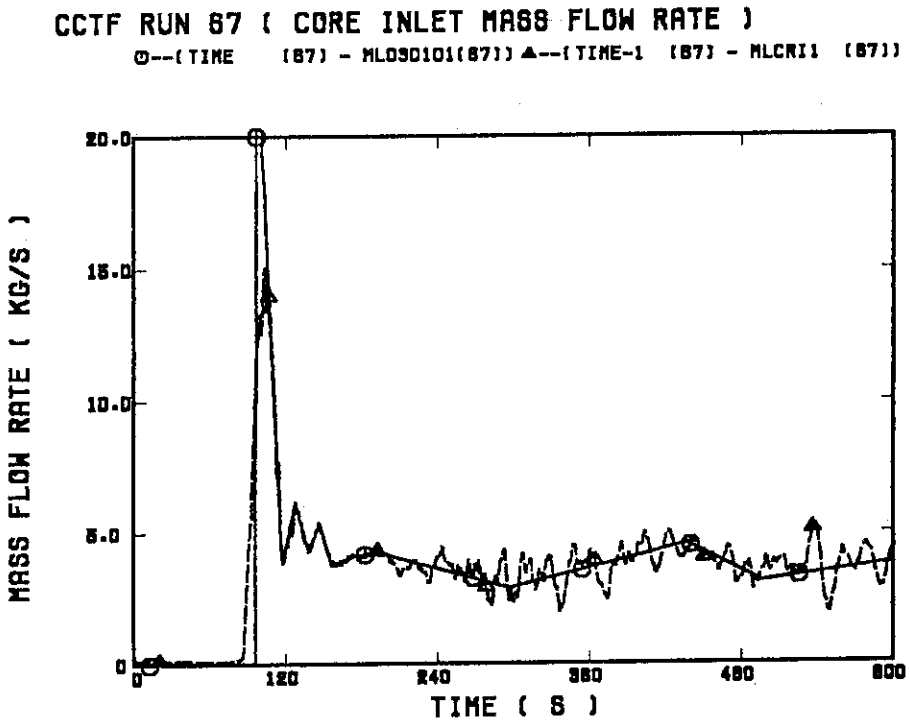

Fig. B.3.1 Core inlet mass flow rate (input)

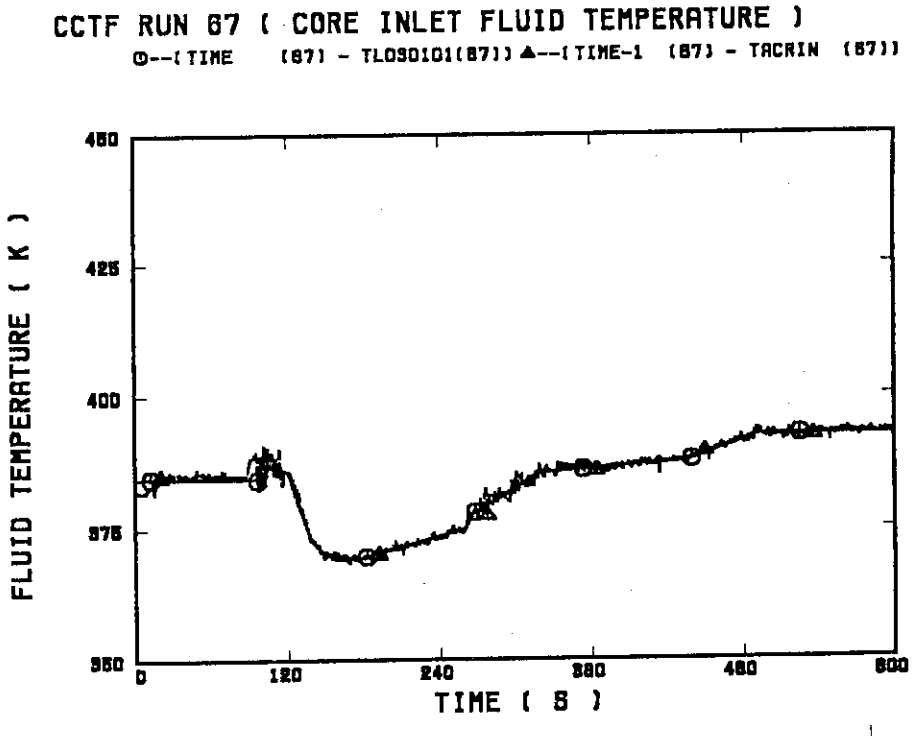

Fig. B.3.2 Core inlet fluid temperature (input)

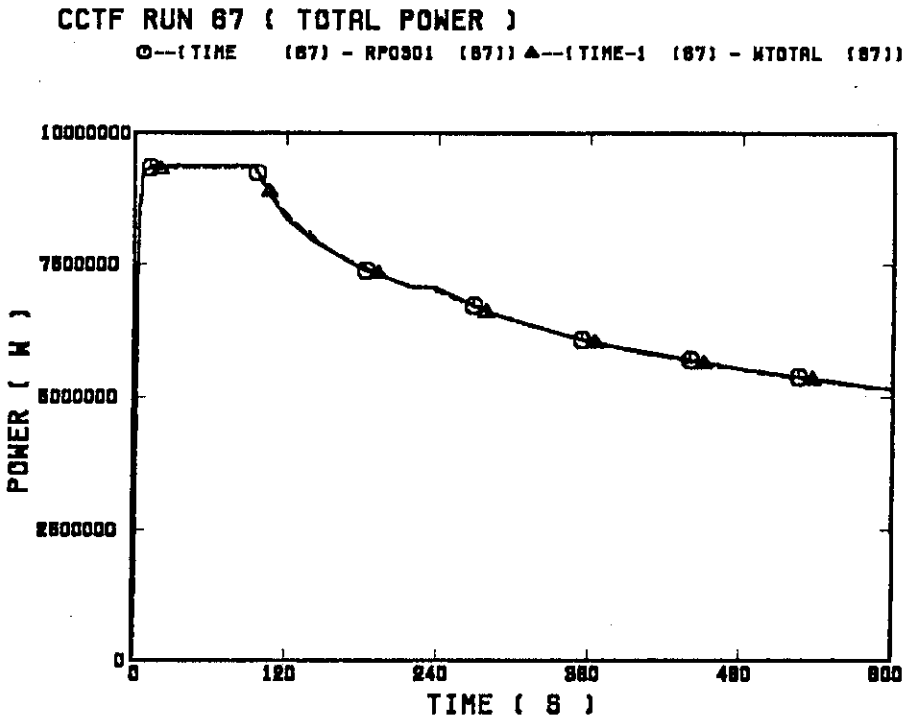

Fig. B.3.3 Total power supplied to core (input)

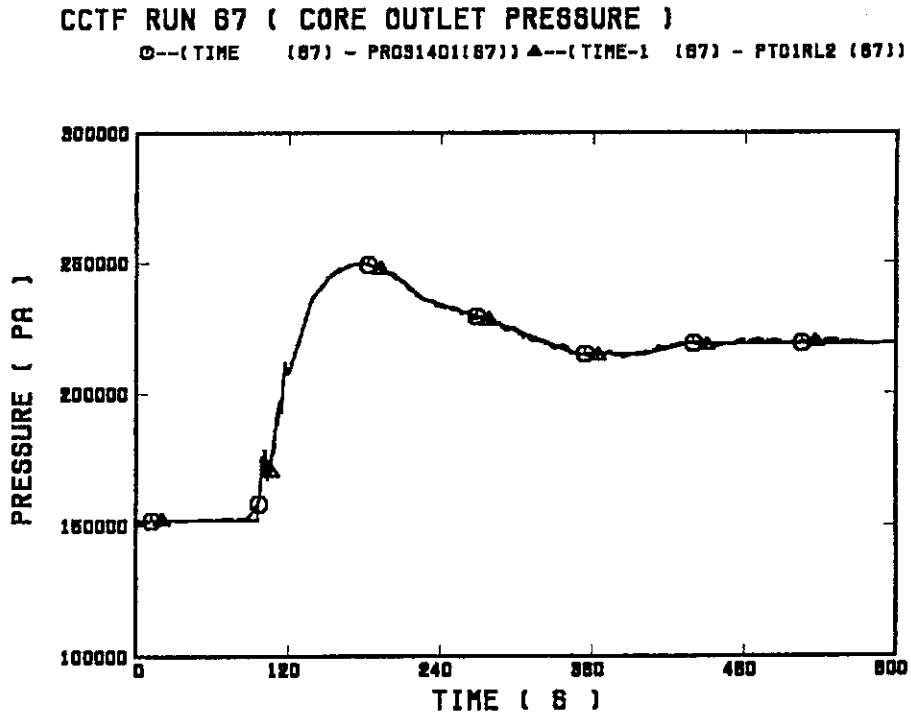

Fig. B.3.4 Core outlet pressure (input)

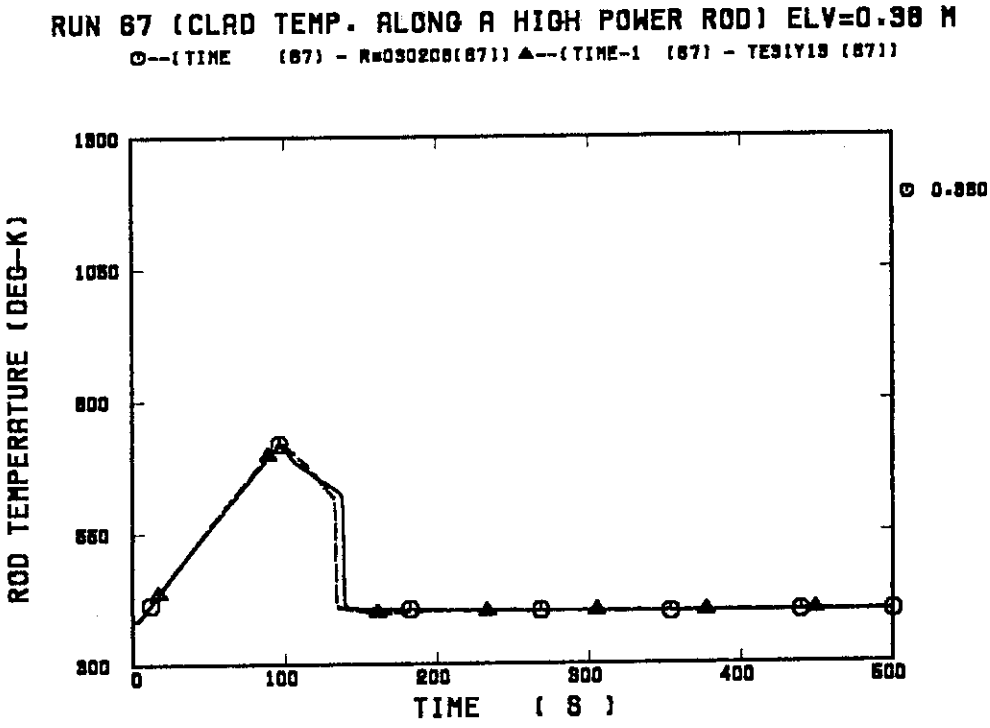

Fig. B.3.5 Clad temperature at elevation of 0.38 m along a high power rod

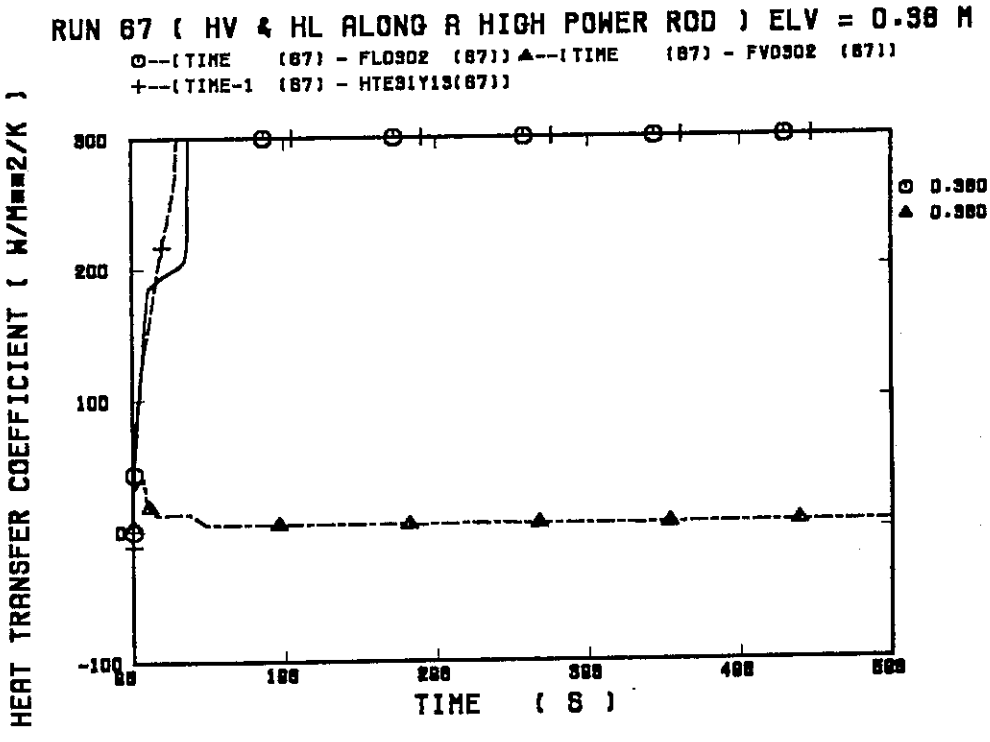

Fig. B.3.6 Heat transfer coefficient at elevation of 0.38 m along a high power rod

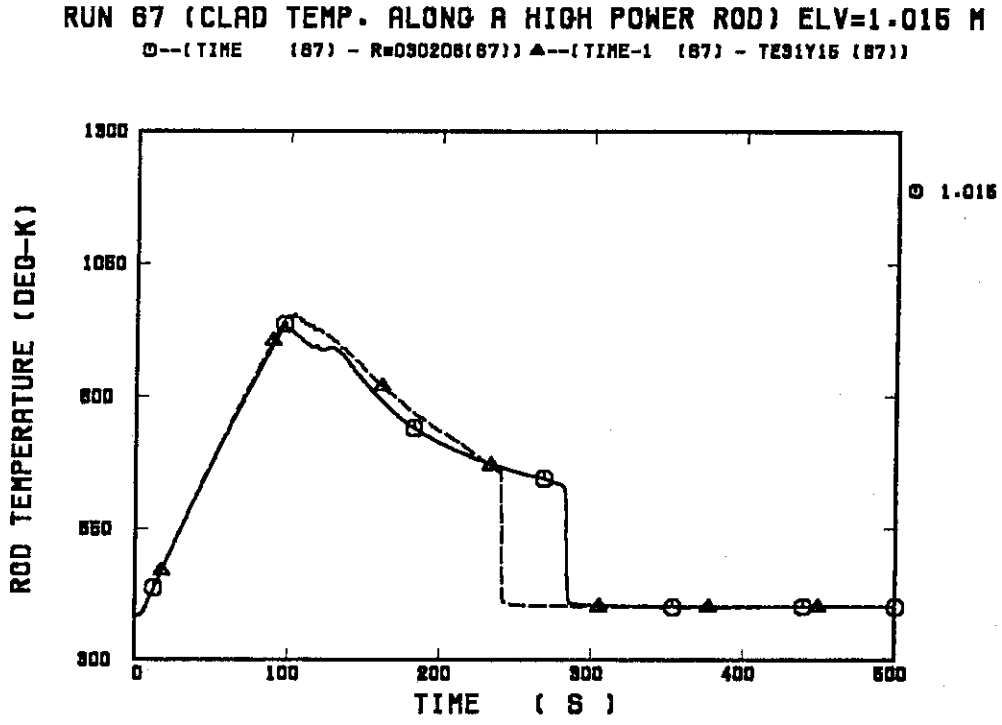

Fig. B.3.7 Clad temperature at elevation of 1.015 m along a high power rod

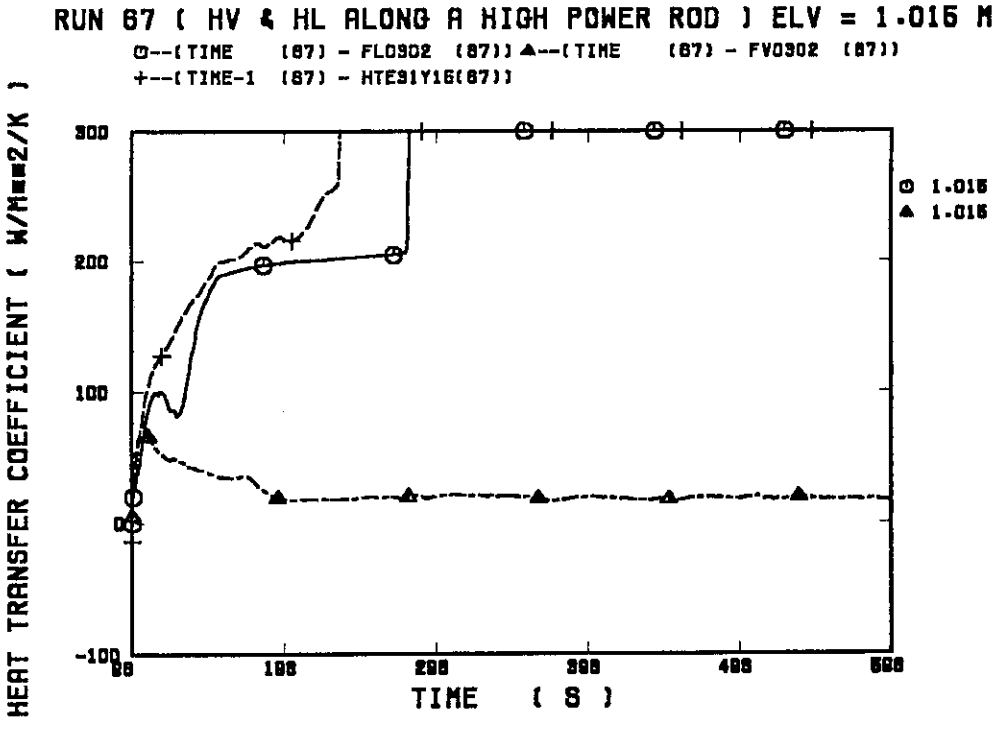

Fig. B.3.8 Heat transfer coefficient at elevation of 1.015 m along a high power rod

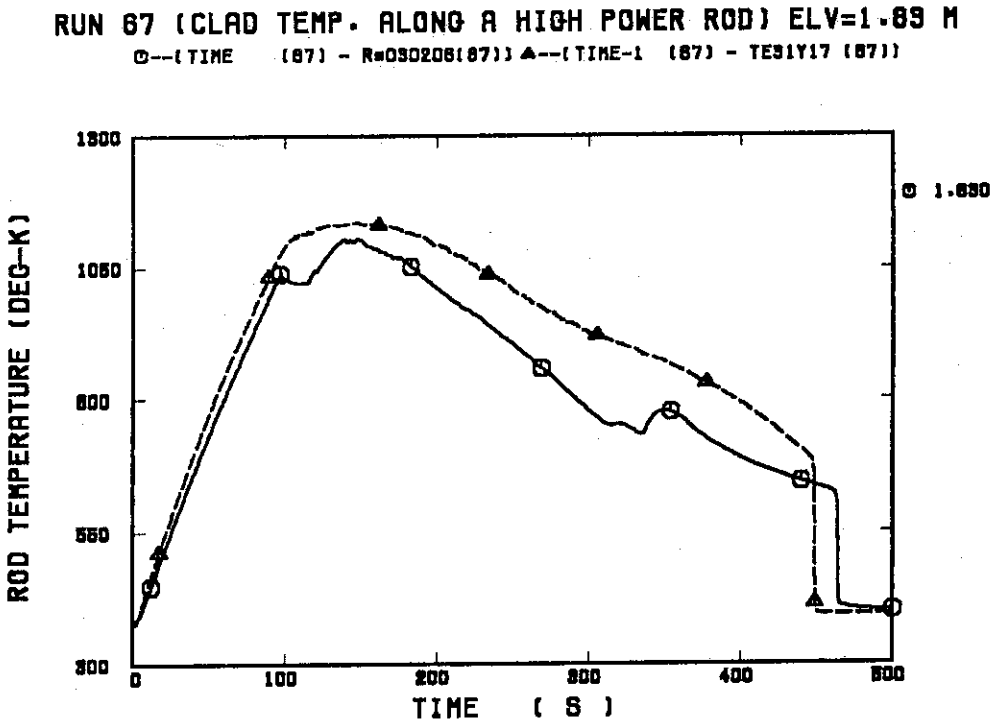

Fig. B.3.9 Clad temperature at elevation of 1.83 m along a high power rod

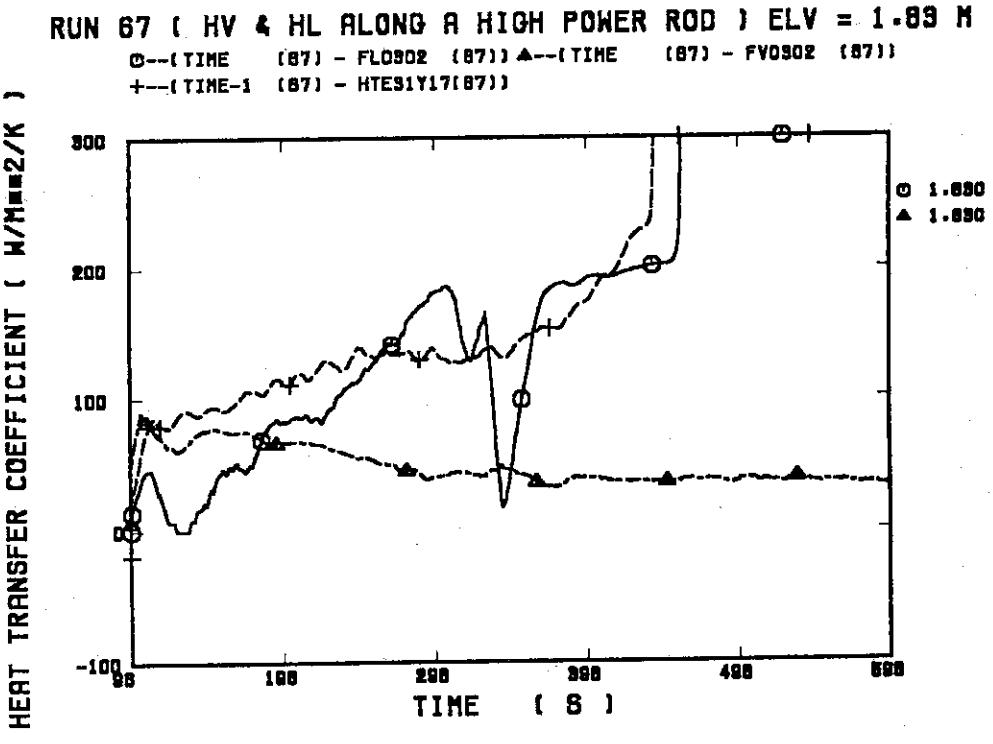

Fig. B.3.10 Heat transfer coefficient at elevation of 1.83 m along a high power rod

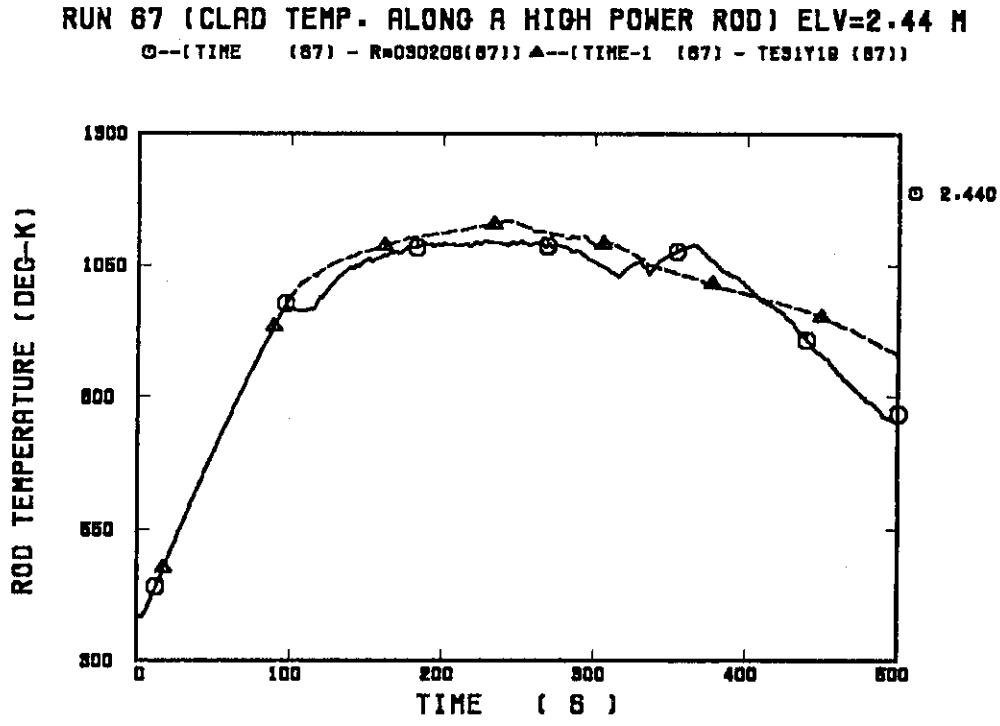

Fig. B.3.11 Clad temperature at elevation of 2.44 m along a high power rod

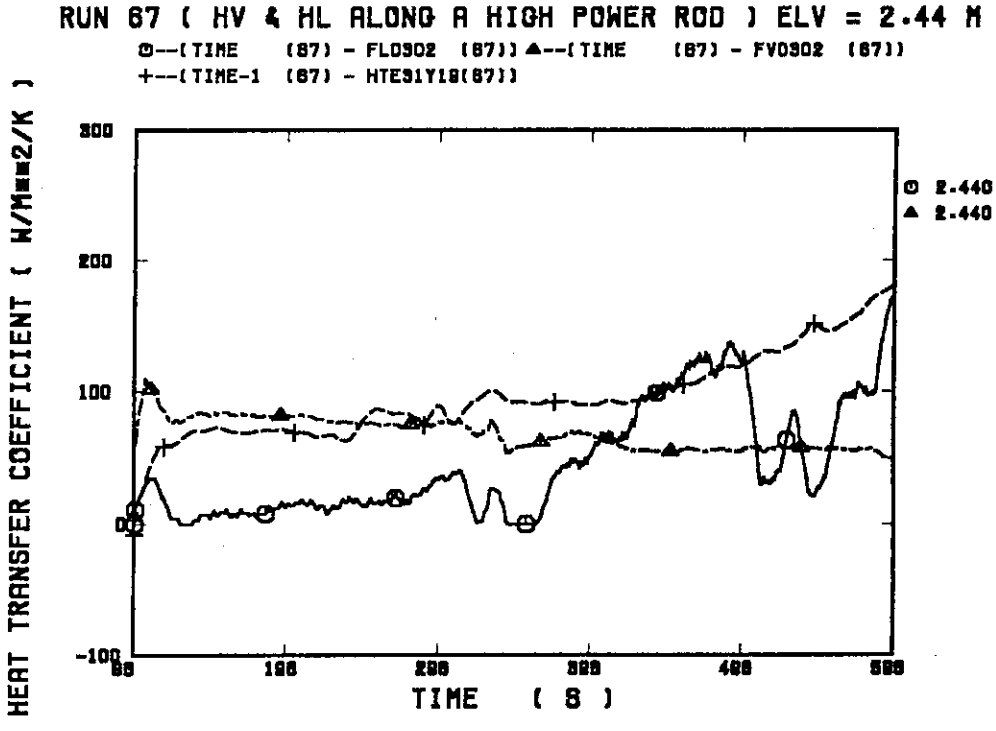

Fig. B.3.12 Heat transfer coefficient at elevation of 2.44 m along a high power rod

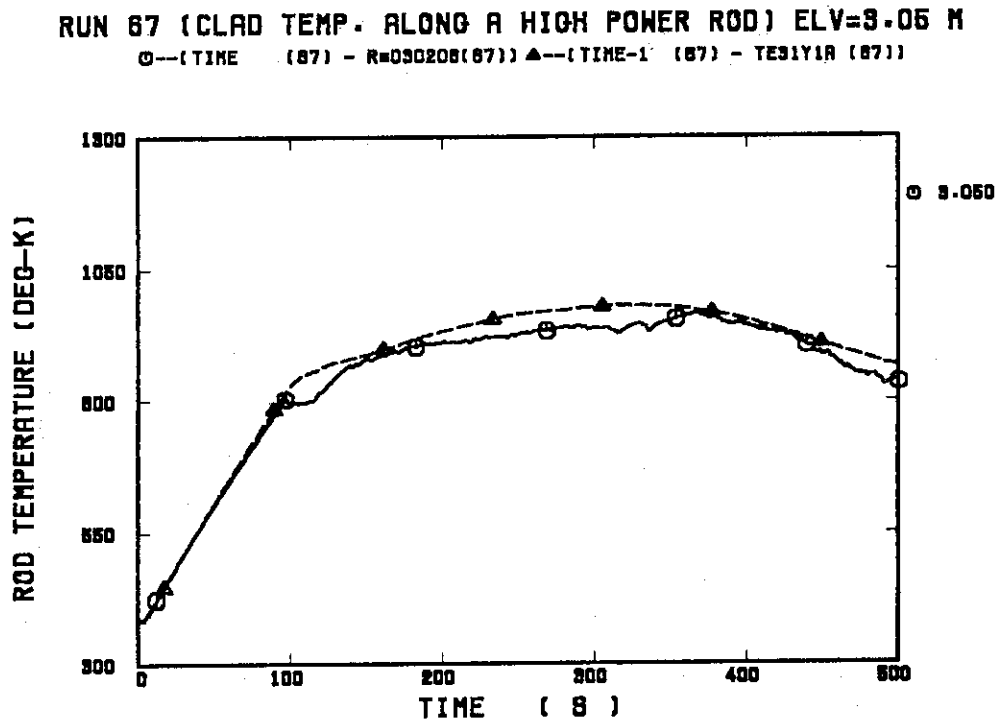

Fig. B.3.13 Clad temperature at elevation of 3.05 m along a high power rod

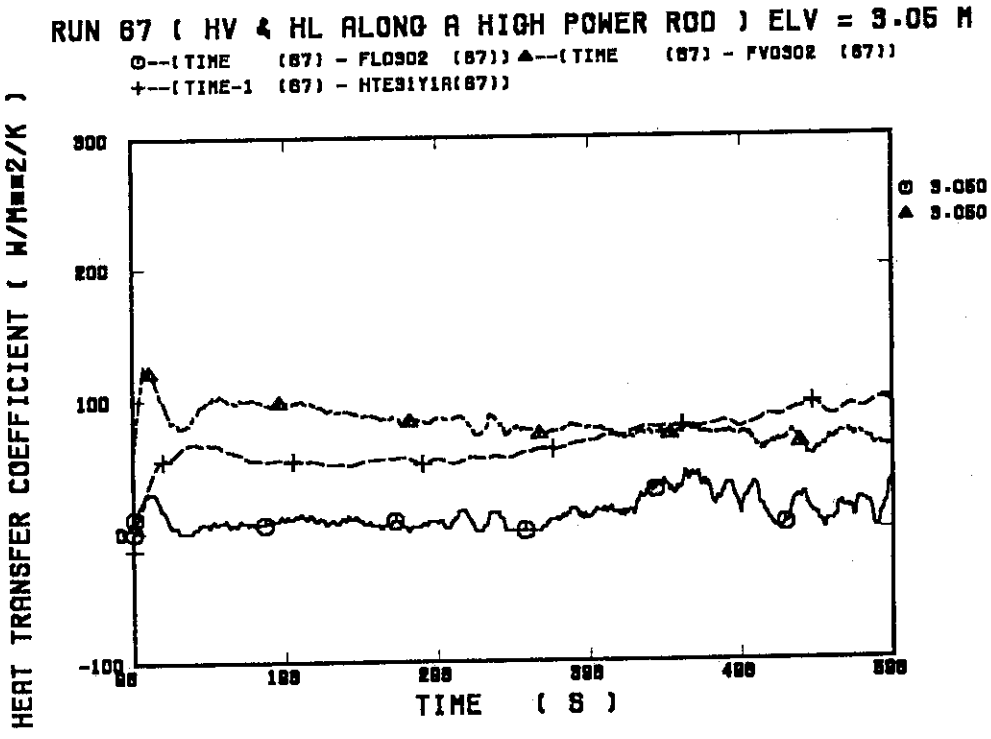

Fig. B.3.14 Heat transfer coefficient at elevation of 3.05 m along a high power rod

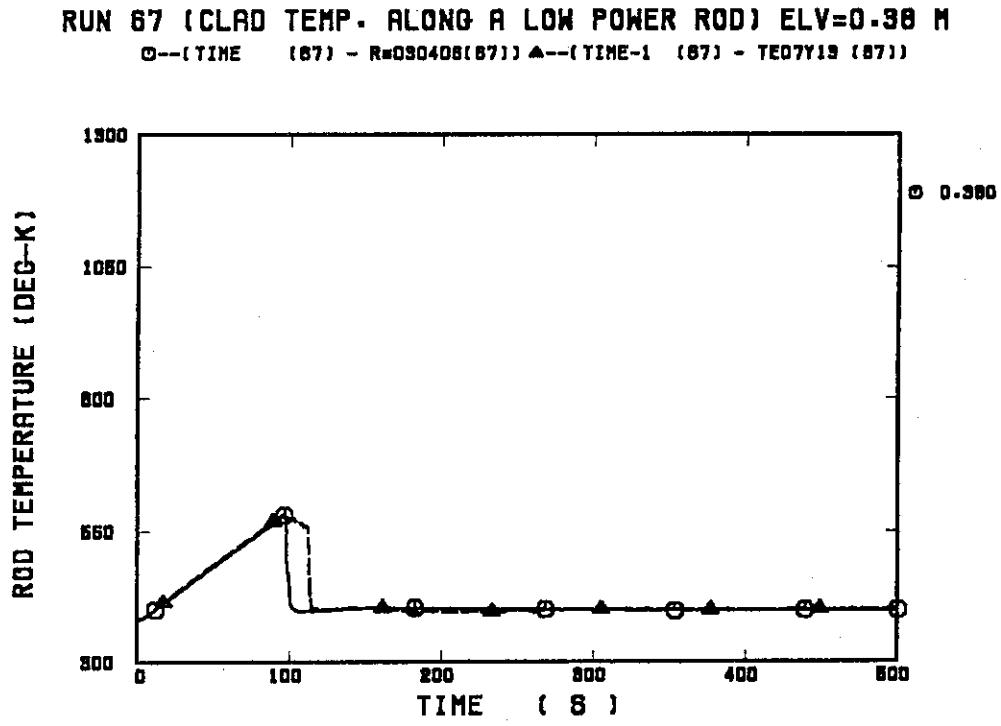

Fig. B.3.15 Clad temperature at elevation of 0.38 m along a low power rod

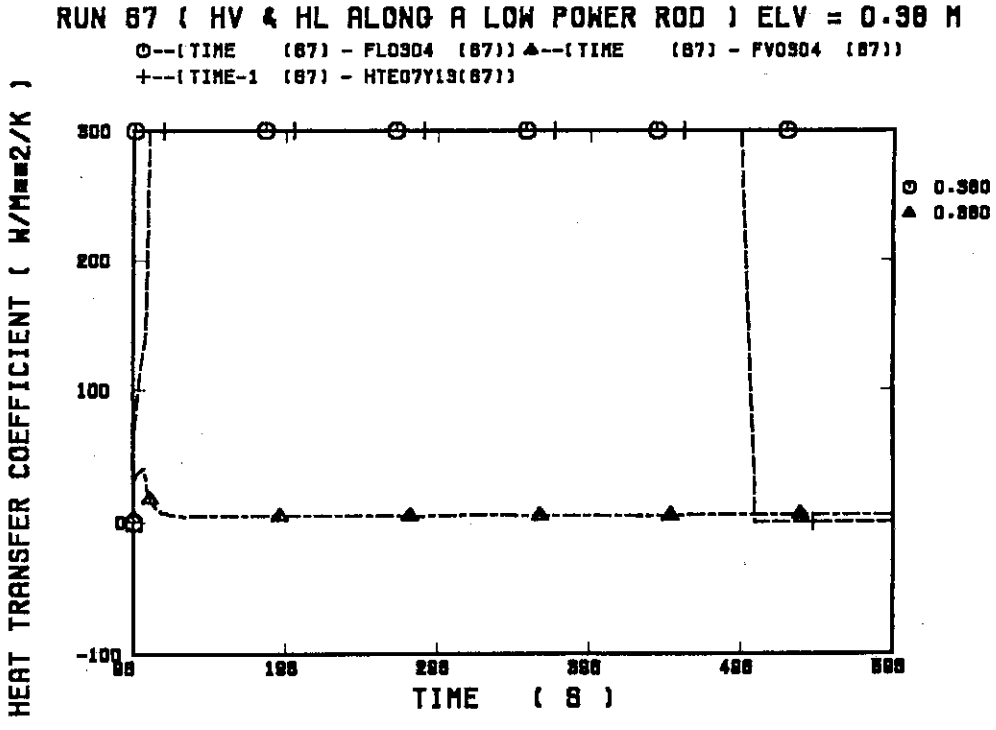

Fig. B.3.16 Heat transfer coefficient at elevation of 0.38 m along a low power rod

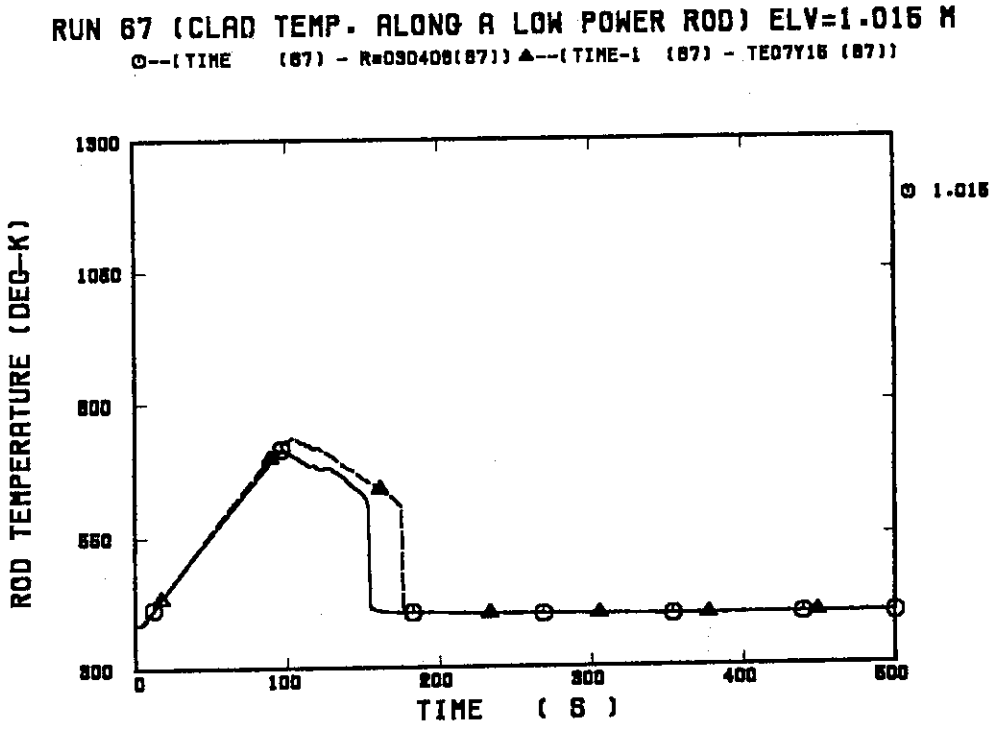

Fig. B.3.17 Clad temperature at elevation of 1.015 m along a low power rod

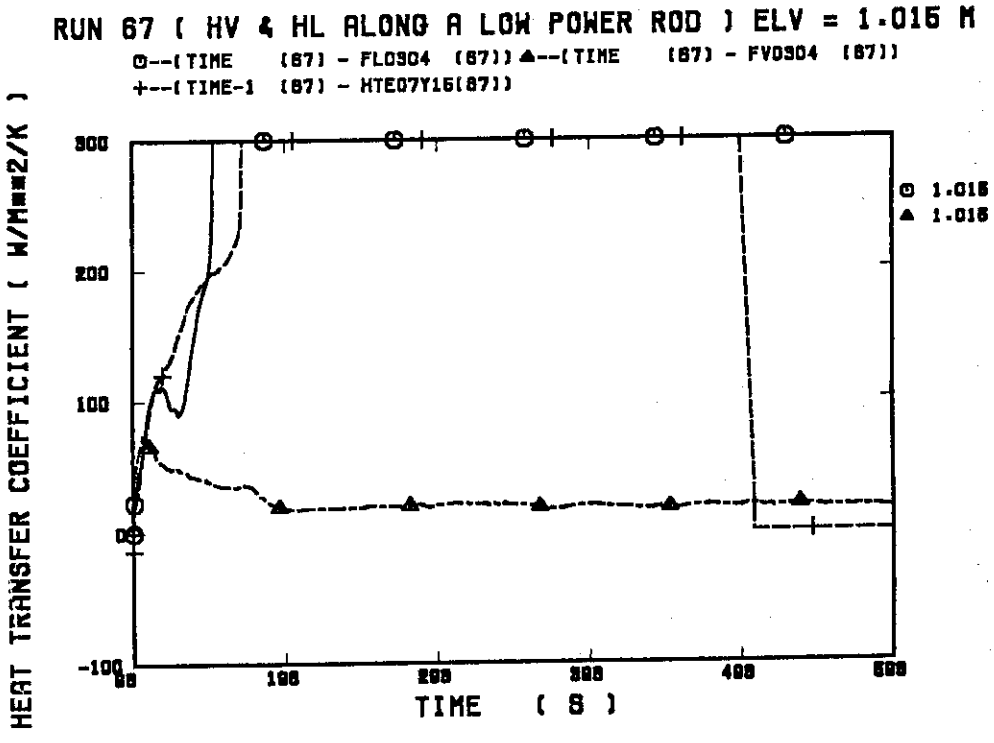

Fig. B.3.18 Heat transfer coefficient at elevation of 1.015 m along a low power rod

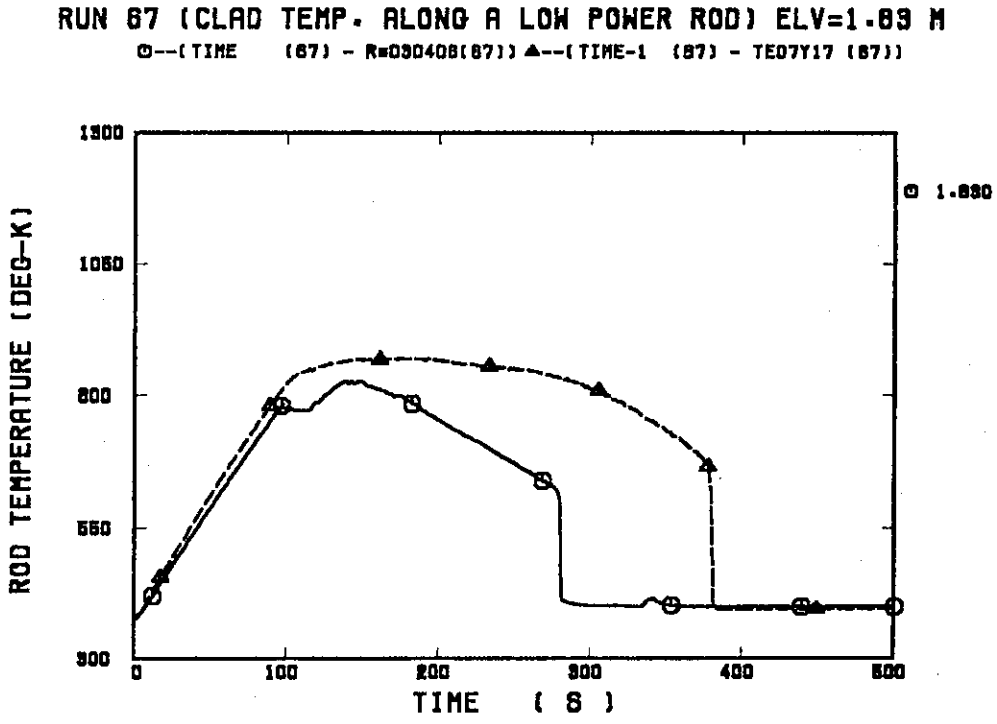

Fig. B.3.19 Clad temperature at elevation of 1.83 m along a low power rod

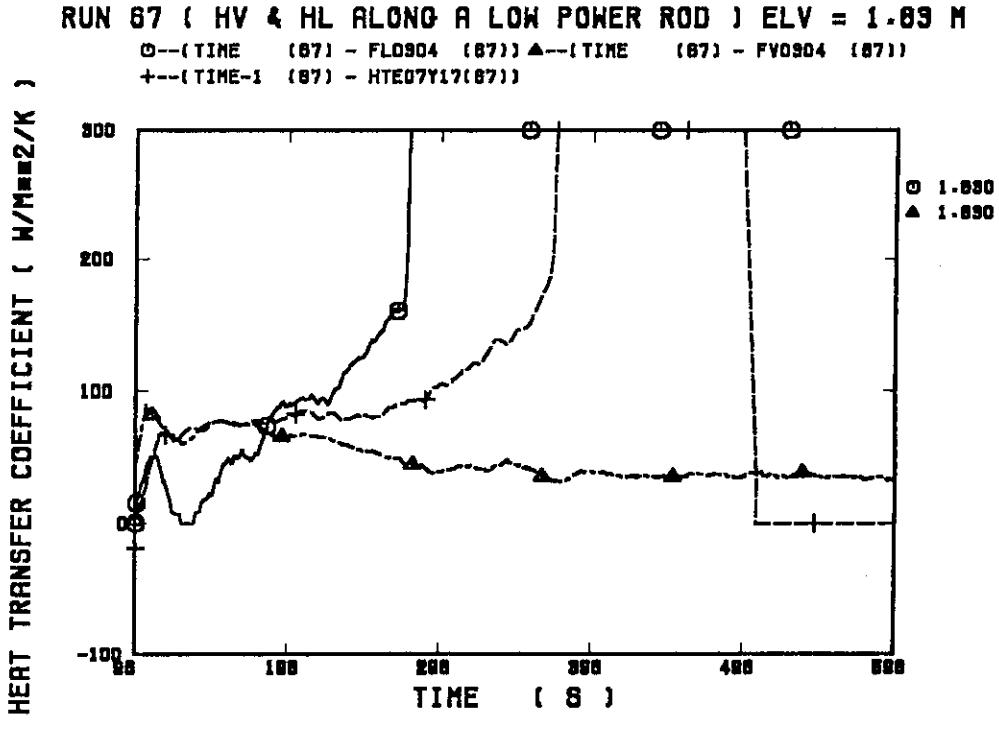

Fig. B.3.20 Heat transfer coefficient at elevation of 1.83 m along a low power rod

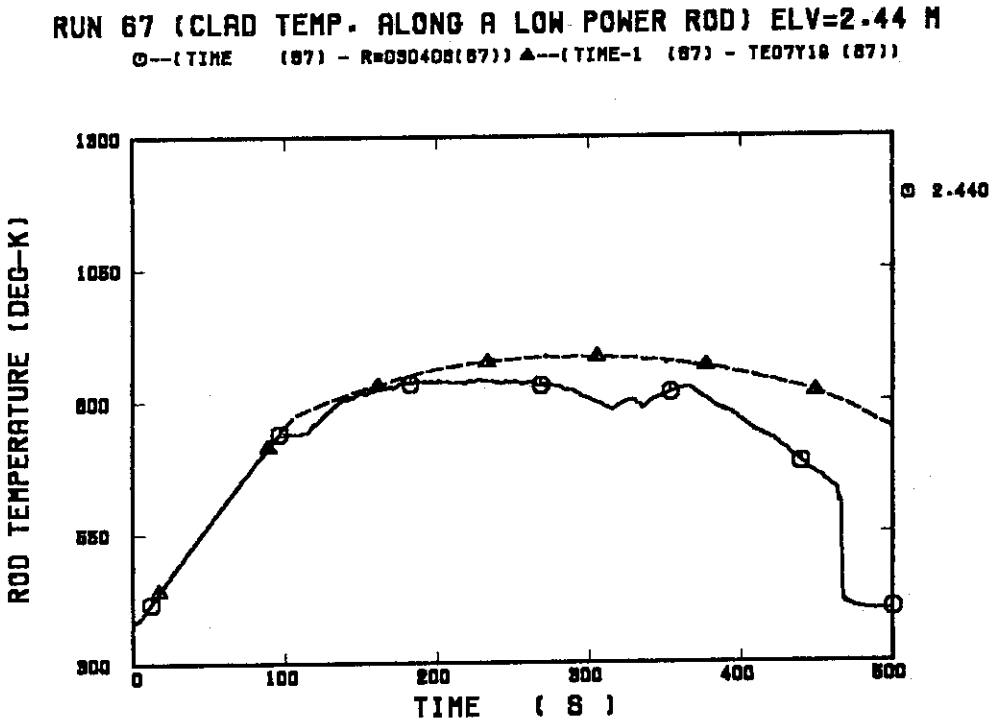

Fig. B.3.21 Clad temperature at elevation of 2.44 m along a low power rod

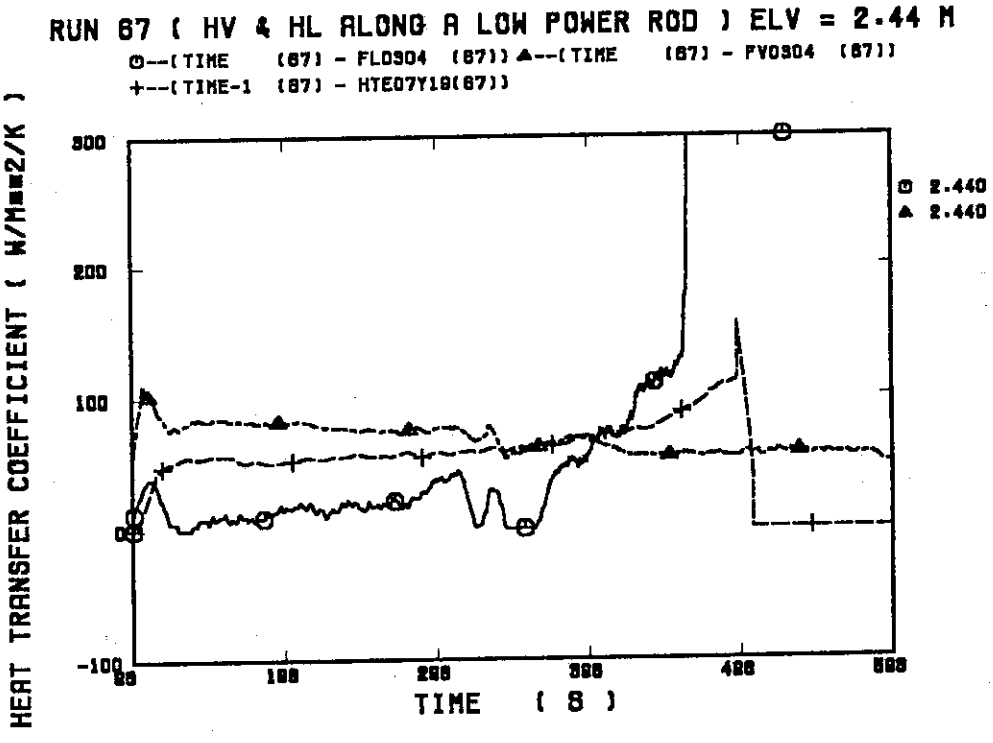

Fig. B.3.22 Heat transfer coefficient at elevation of 2.44 m along a low power rod

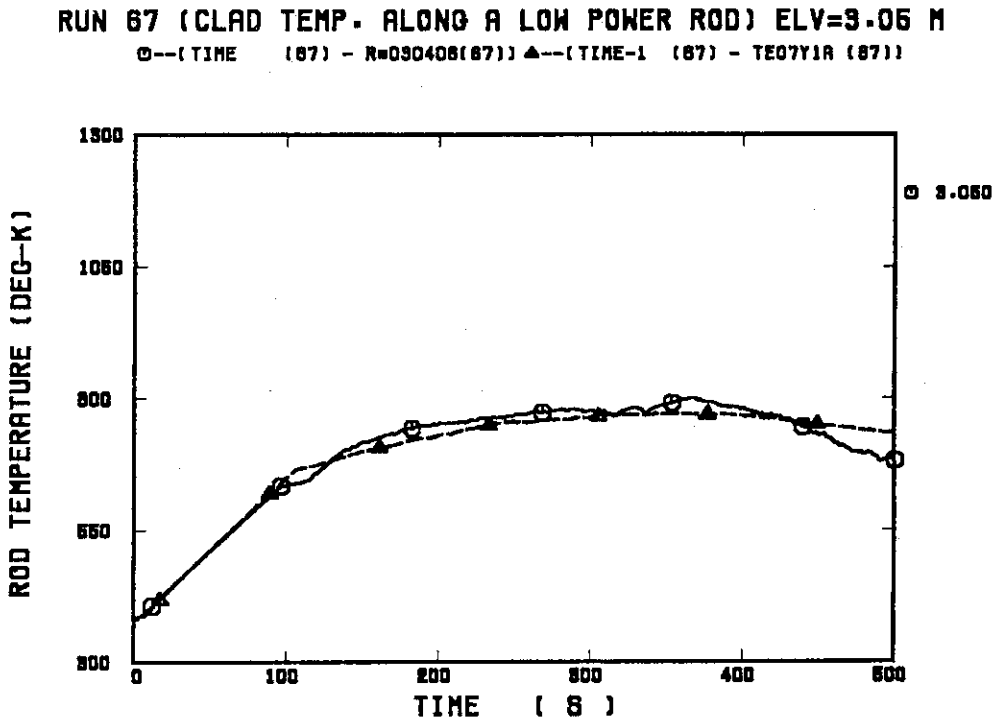

Fig. B.3.23 Clad temperature at elevation of 3.05 m along a low power rod

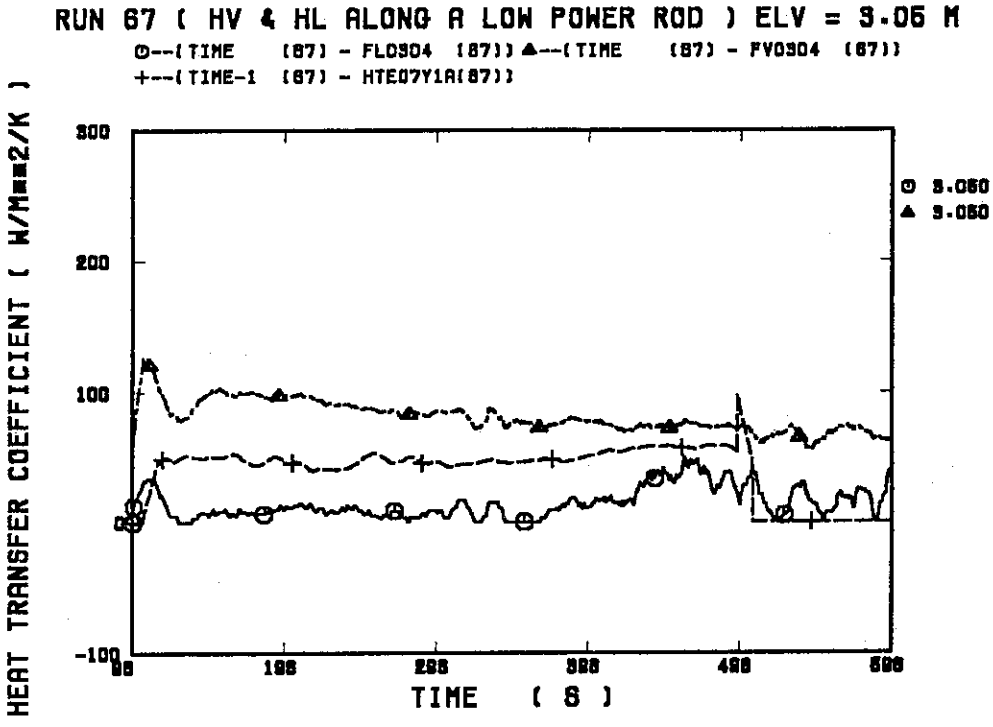

Fig. B.3.24 Heat transfer coefficient at elevation of 3.05 m along a low power rod

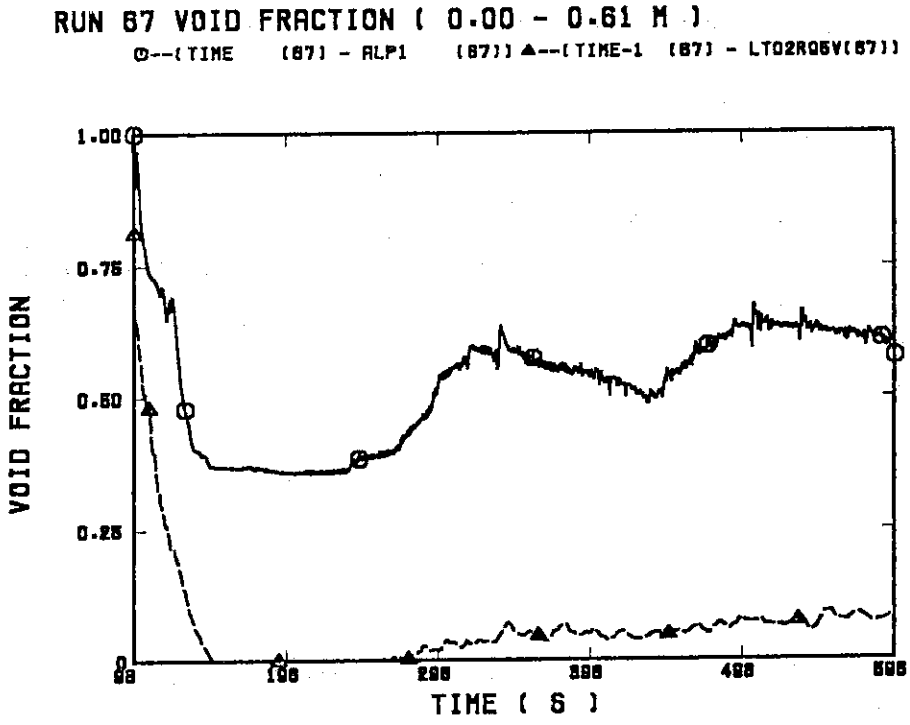

Fig. B.3.25 Average void fraction between 0.00 and 0.61 m

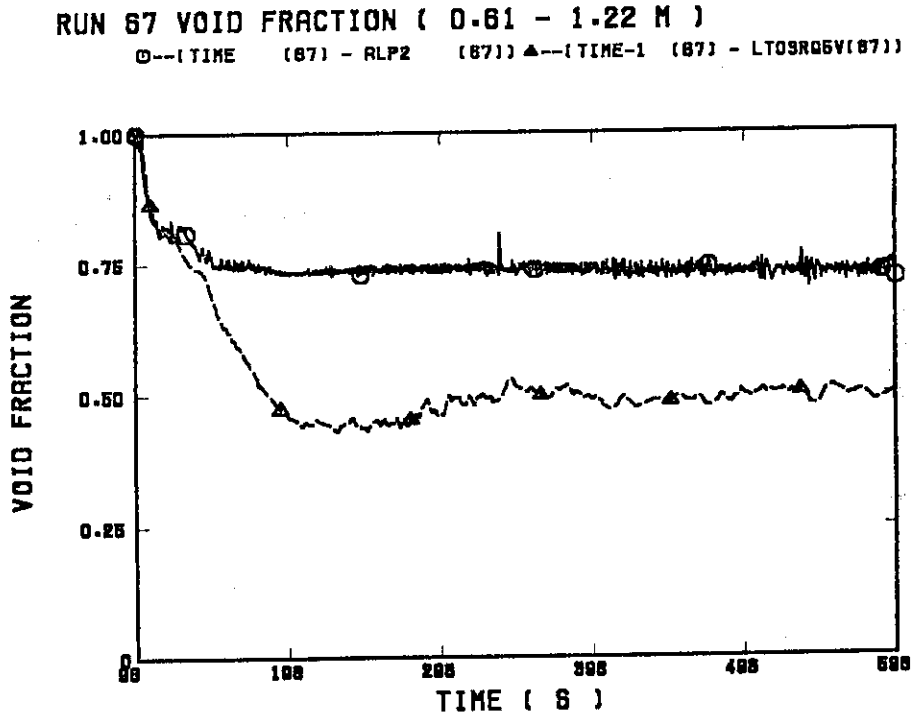

Fig. B.3.26 Average void fraction between 0.61 and 1.22 m

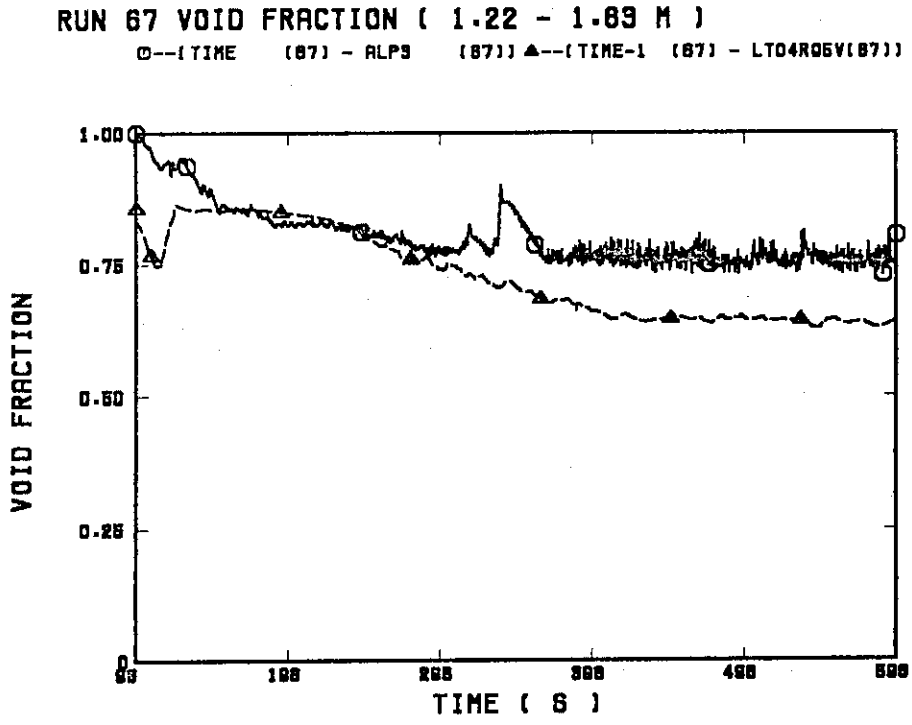

Fig. B.3.27 Average void fraction between 1.22 and 1.83 m

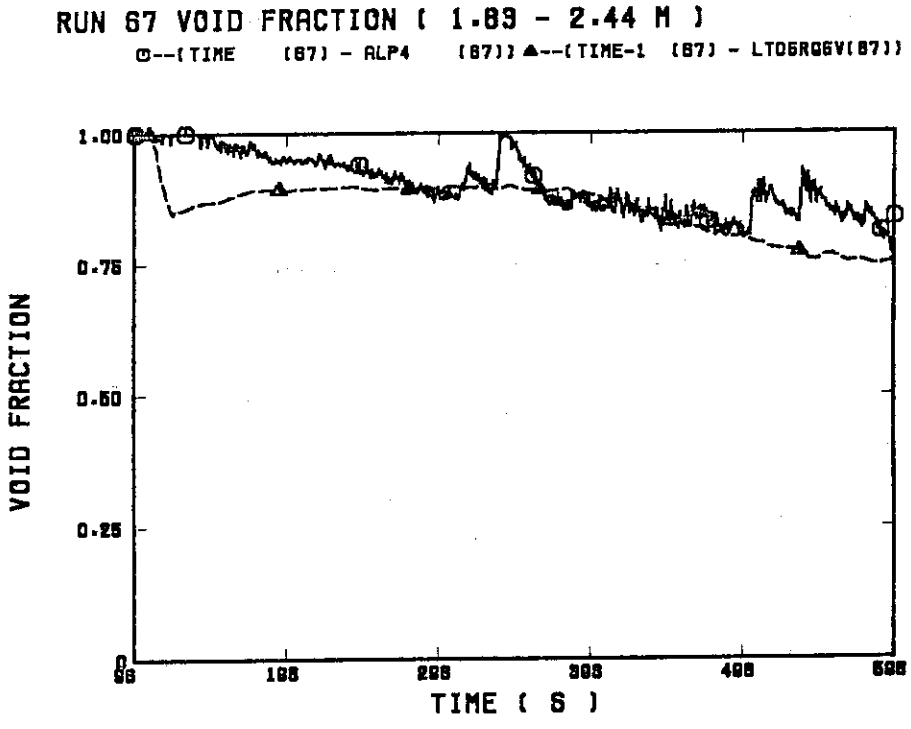

Fig. B.3.28 Average void fraction between 1.83 and 2.44 m

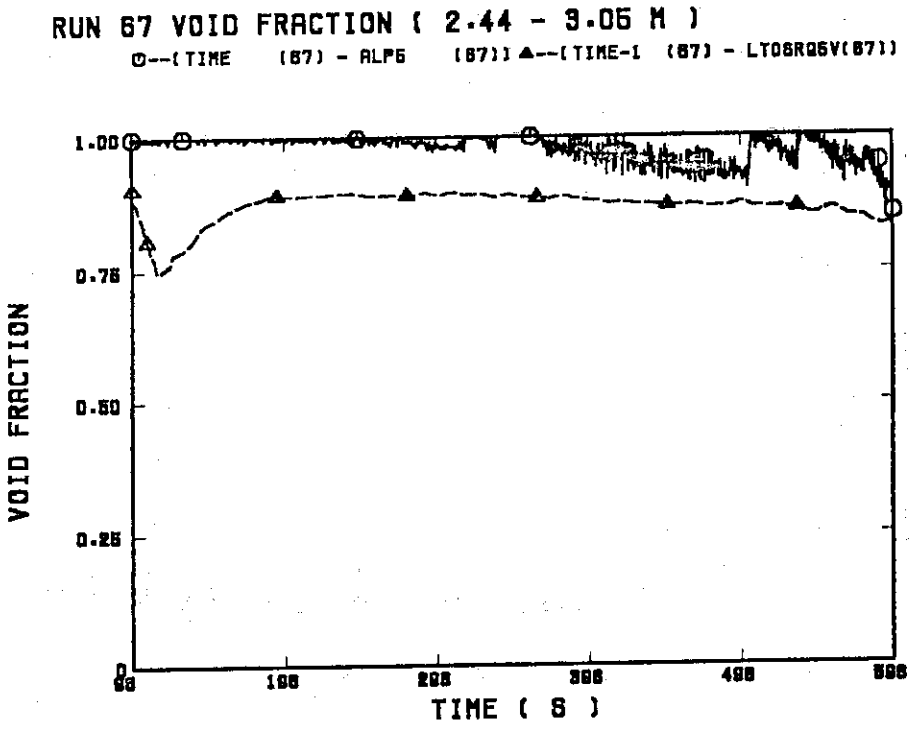

Fig. B.3.29 Average void fraction between 2.44 and 3.05 m

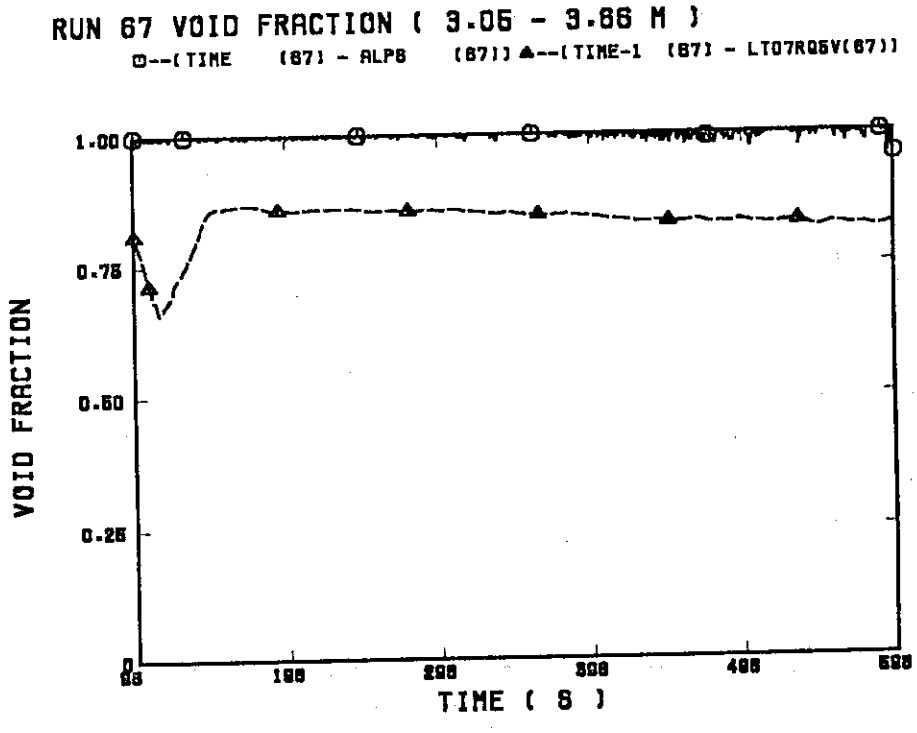

Fig. B.3.30 Average void fraction between 3.05 and 3.66 m

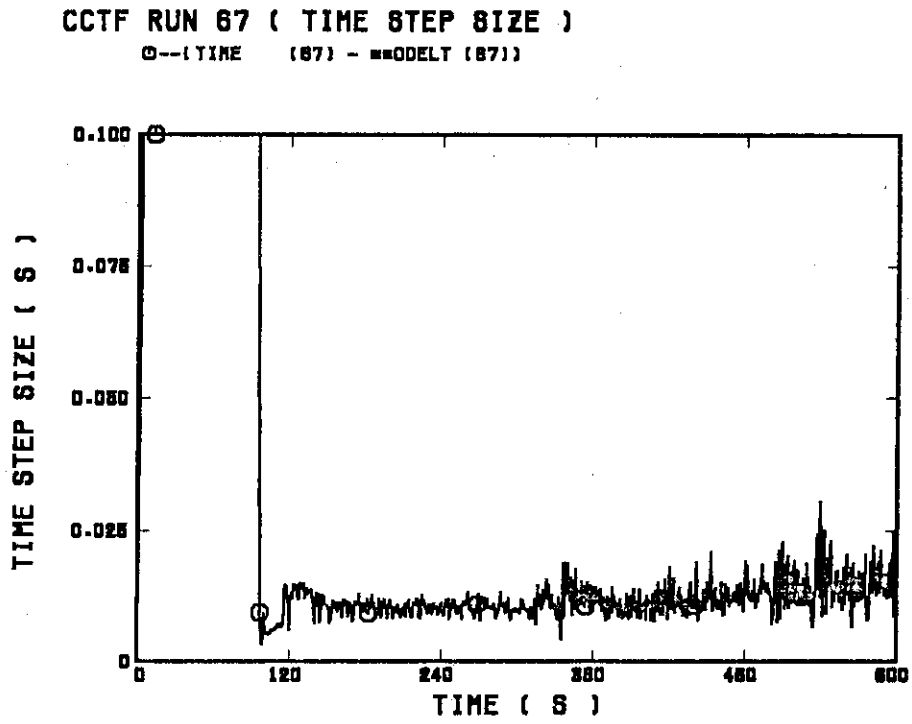

Fig. B.3.31 Time step size

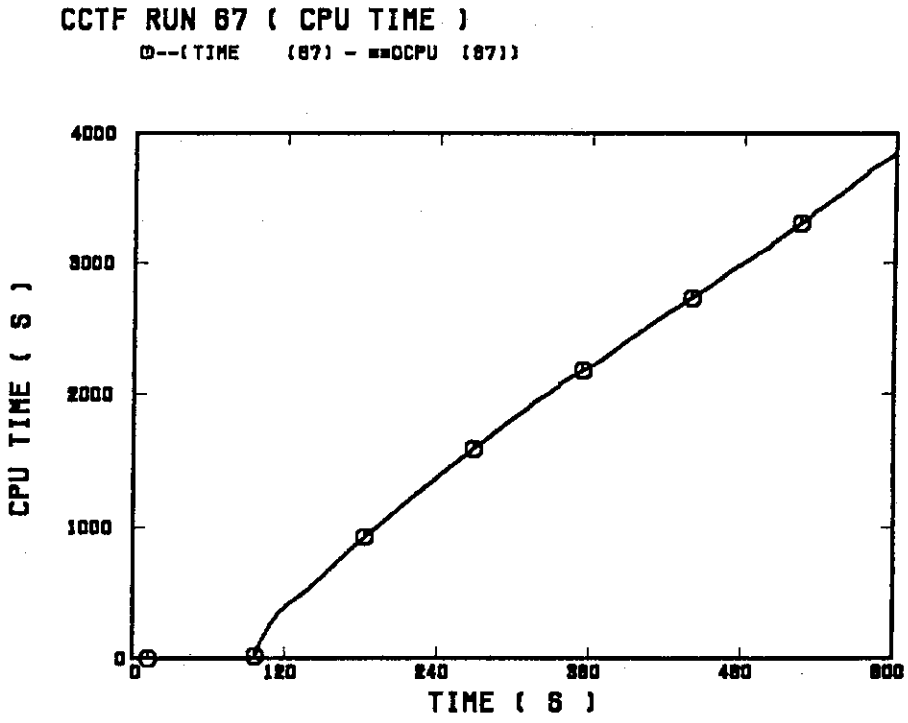

Fig. B.3.32 CPU time

(4) CCTF Low Power Test (Run 63)

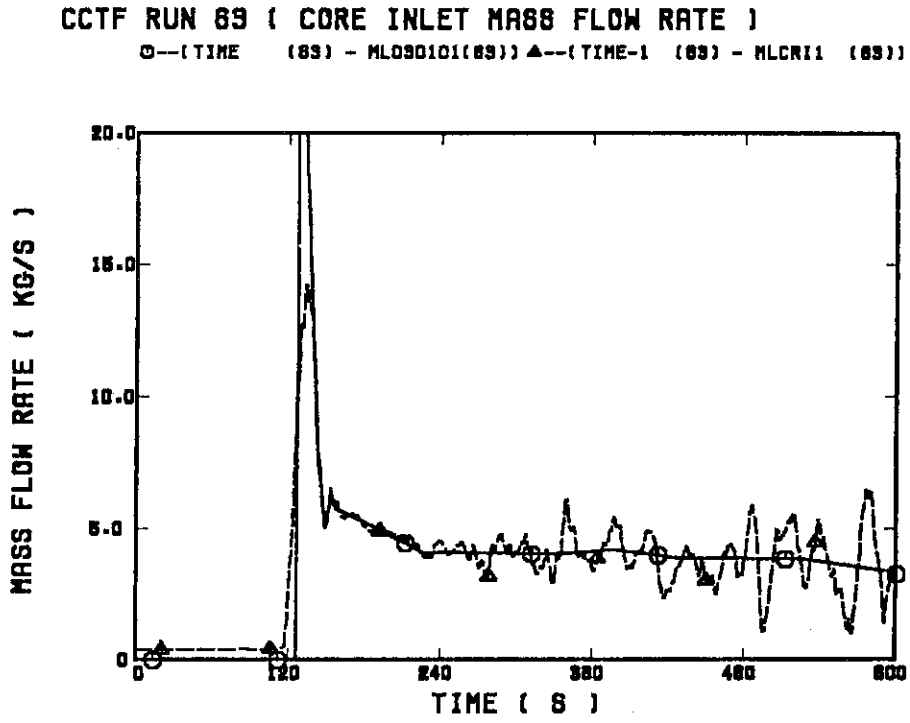

Fig. B.4.1 Core inlet mass flow rate (input)

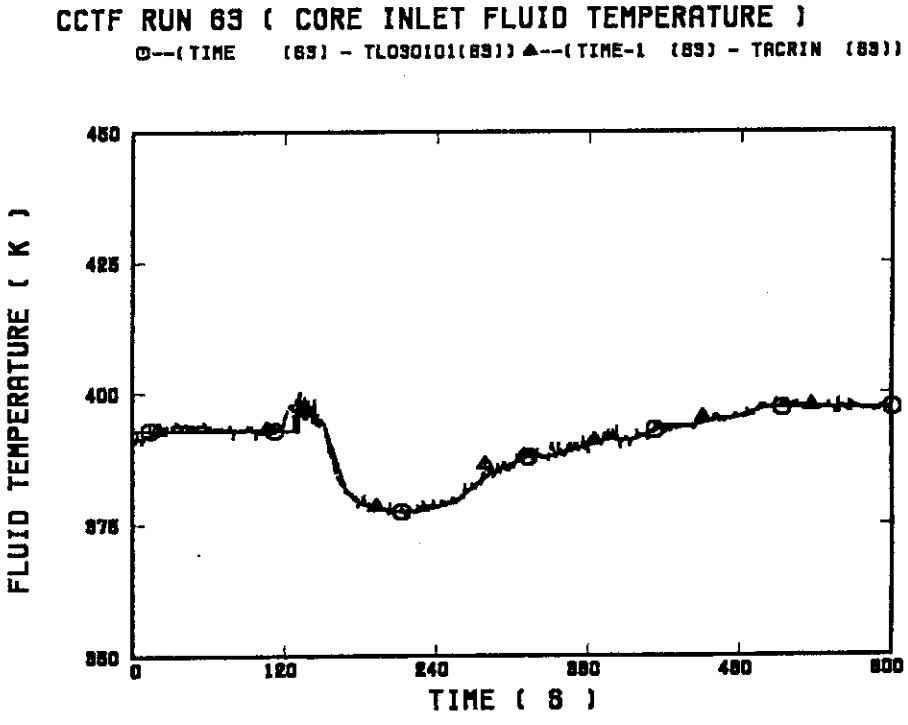

Fig. B.4.2 Core inlet fluid temperature (input)

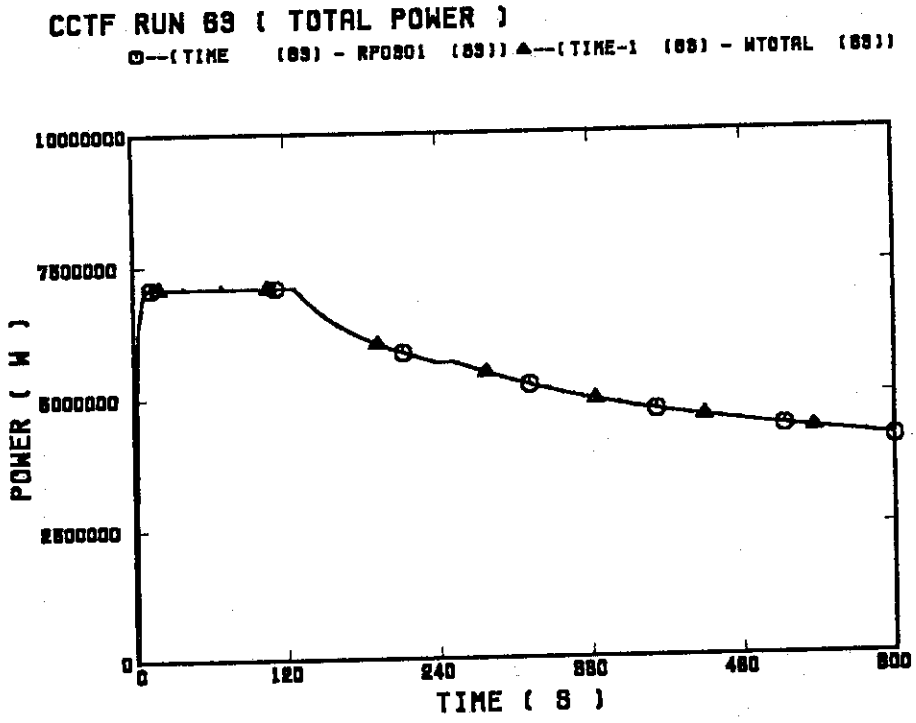

Fig. B.4.3 Total power supplied to core (input)

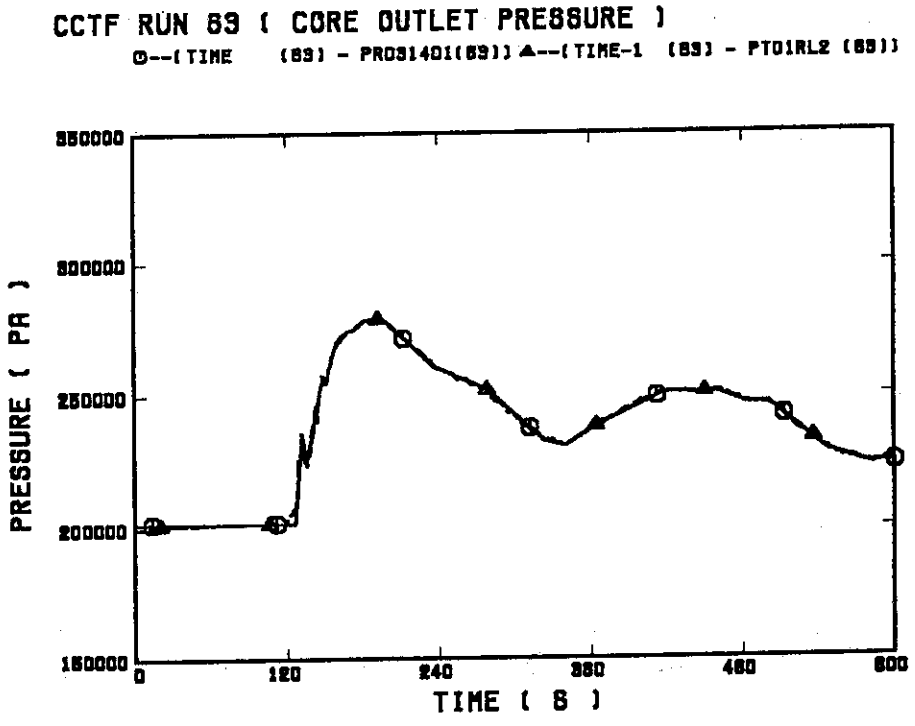

Fig. B.4.4 Core outlet pressure (input)

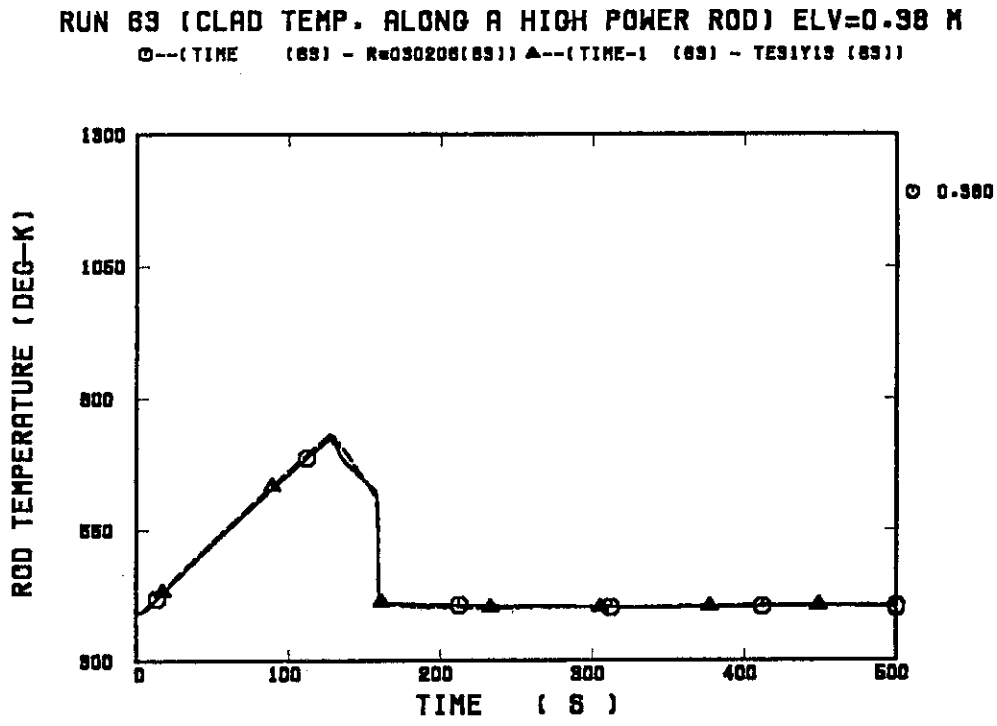

Fig. B.4.5 Clad temperature at elevation of 0.38 m along a high power rod

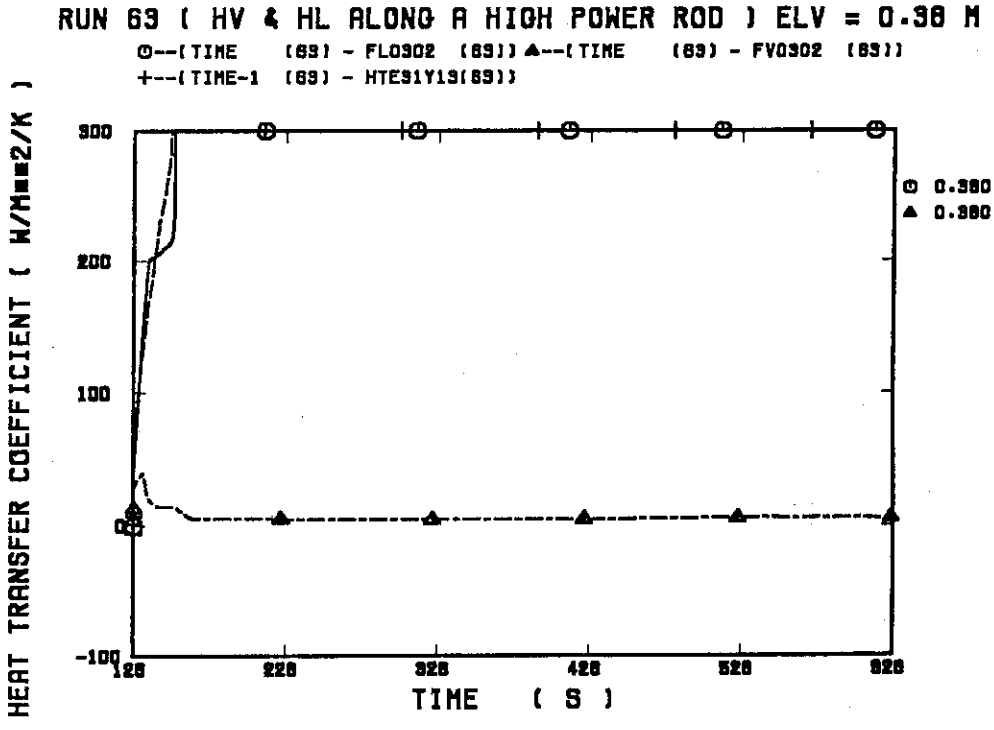

Fig. B.4.6 Heat transfer coefficient at elevation of 0.38 m along a high power rod

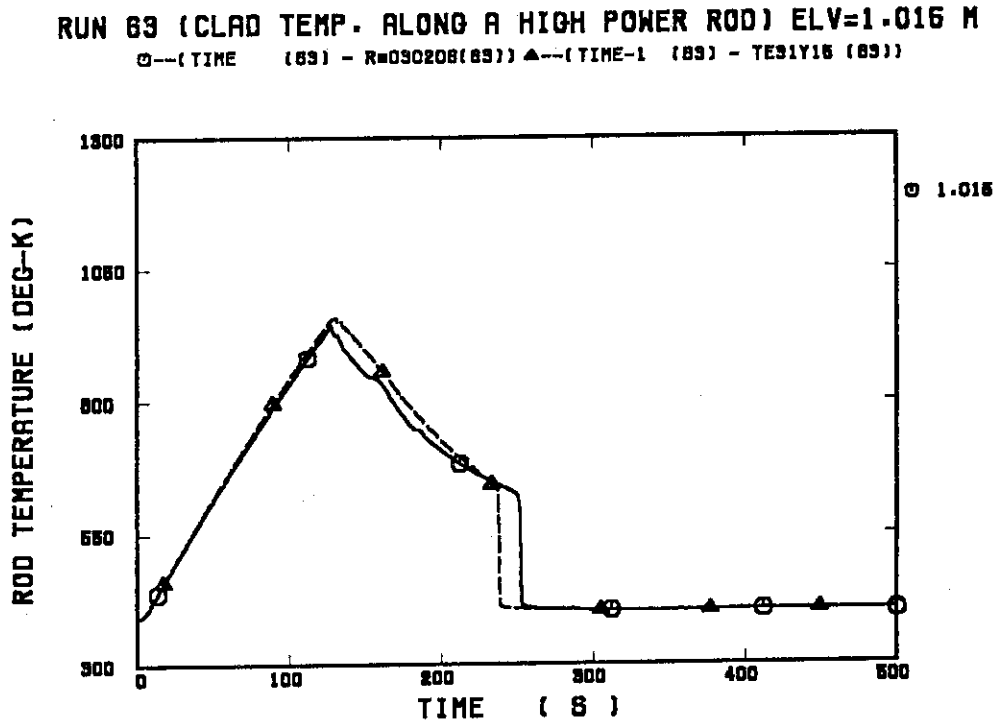

Fig. B.4.7 Clad temperature at elevation of 1.015 m along a high power rod

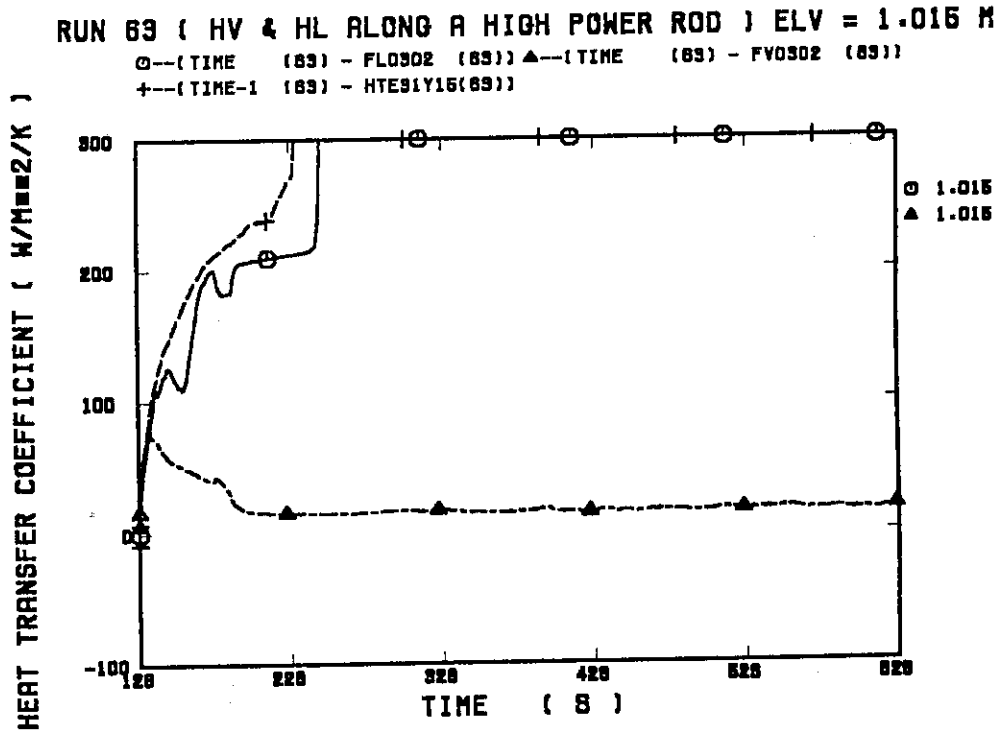

Fig. B.4.8 Heat transfer coefficient at elevation of 1.015 m along a high power rod

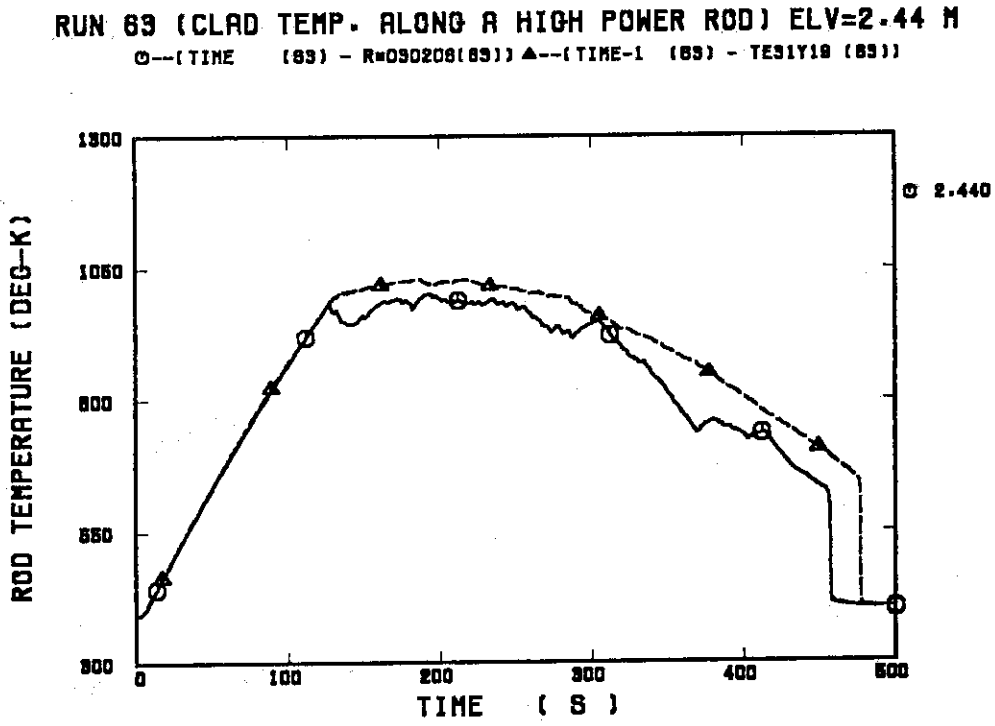

Fig. B.4.11 Clad temperature at elevation of 2.44 m along a high power rod

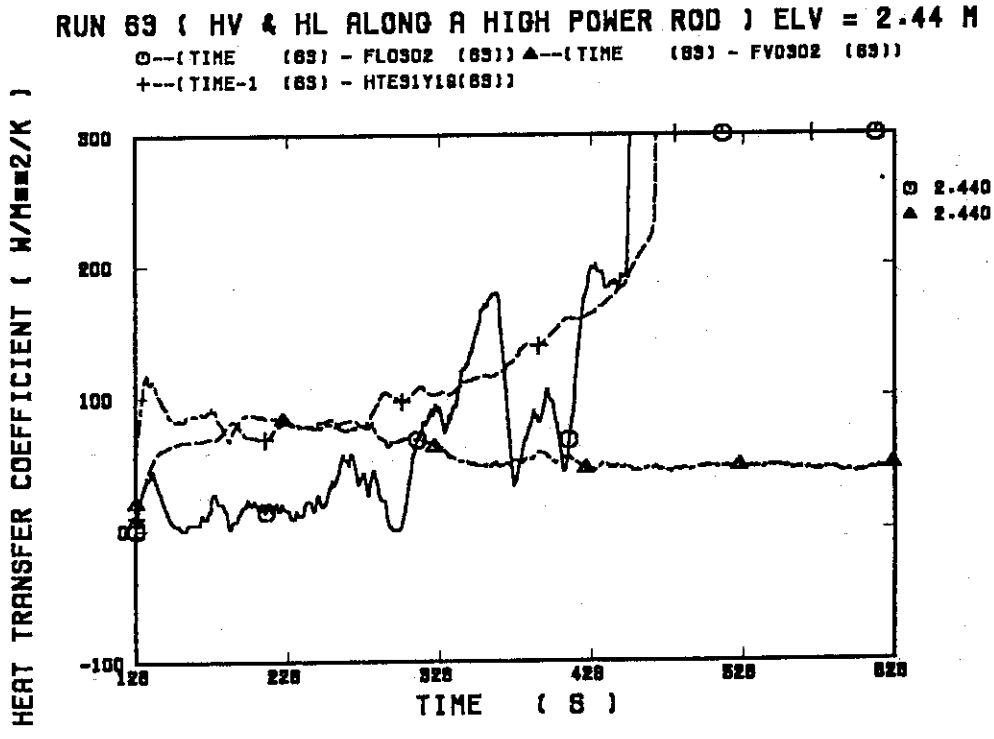

Fig. B.4.12 Heat transfer coefficient at elevation of 2.44 m along a high power rod

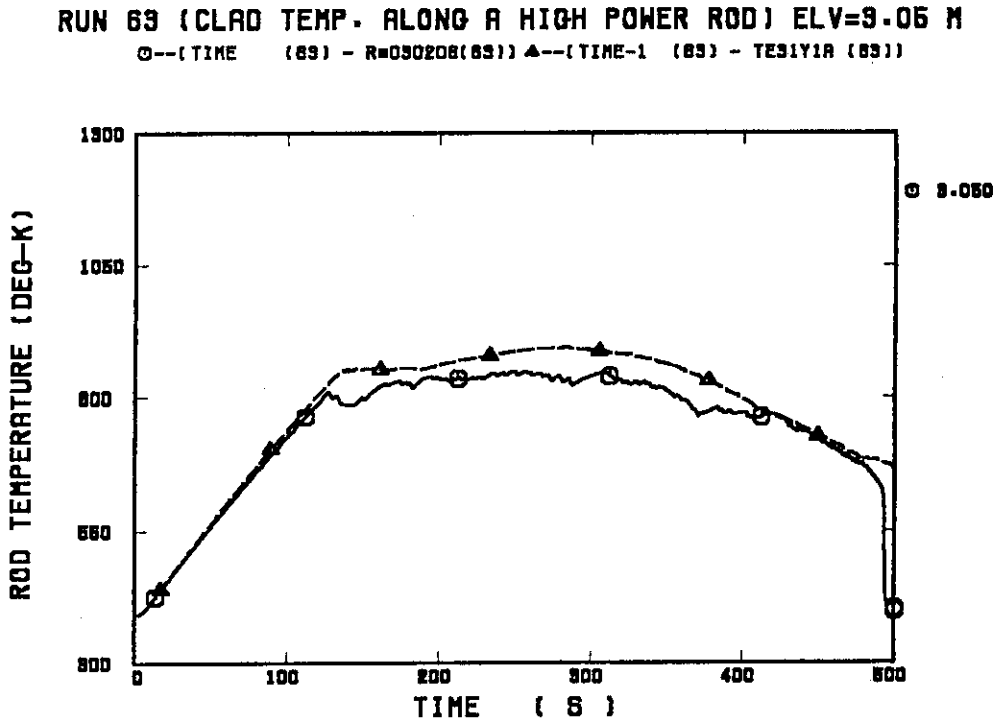

Fig. B.4.13 Clad temperature at elevation of 3.05 m along a high power rod

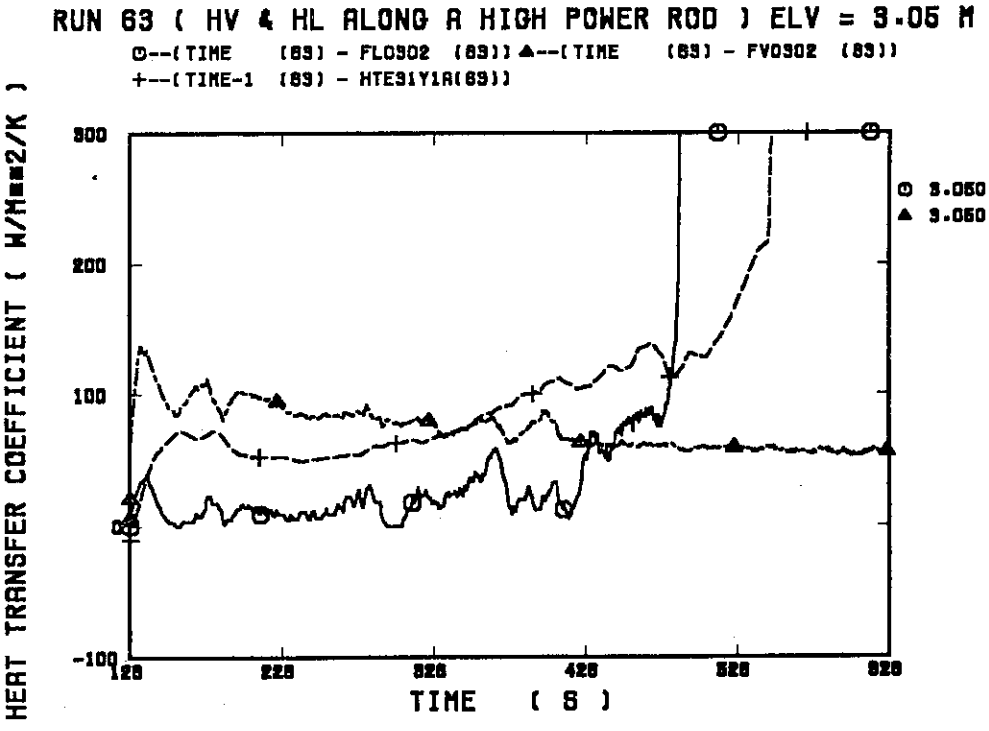

Fig. B.4.14 Heat transfer coefficient at elevation of 3.05 m along a high power rod

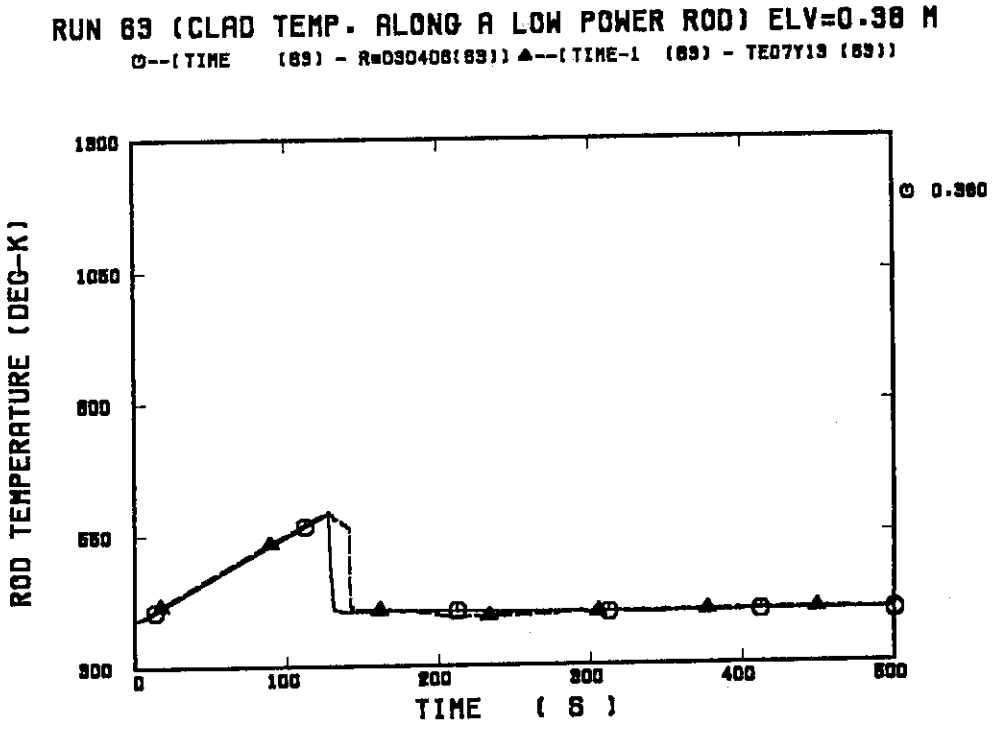

Fig. B.4.15 Clad temperature at elevation of 0.38 m along a low power rod

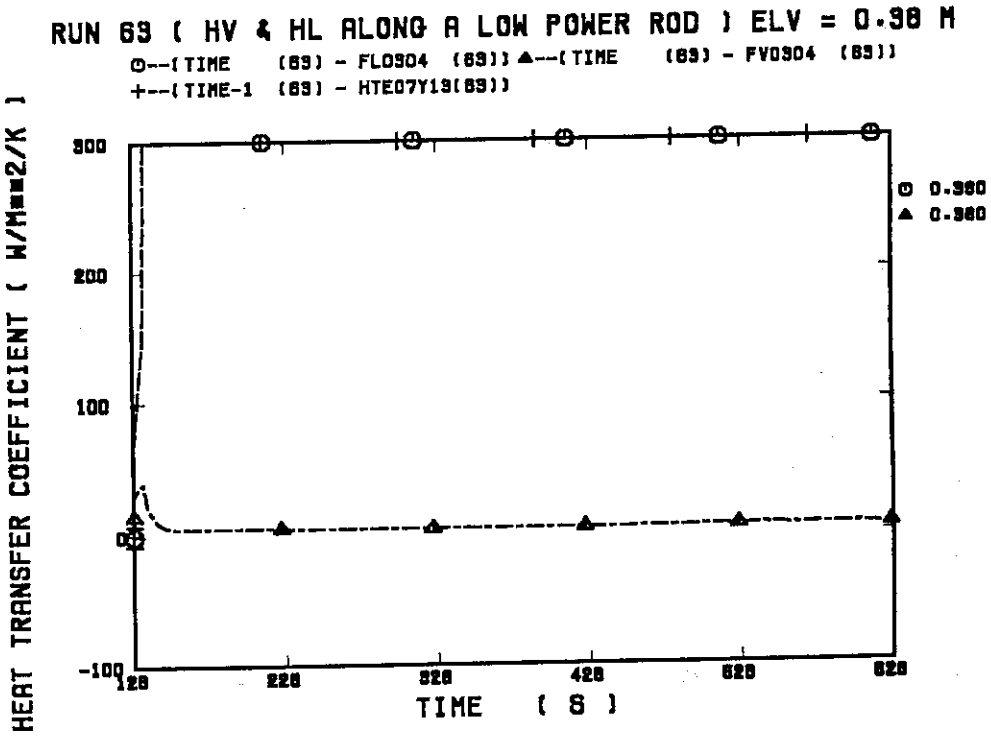

Fig. B.4.16 Heat transfer coefficient at elevation of 0.38 m along a low power rod

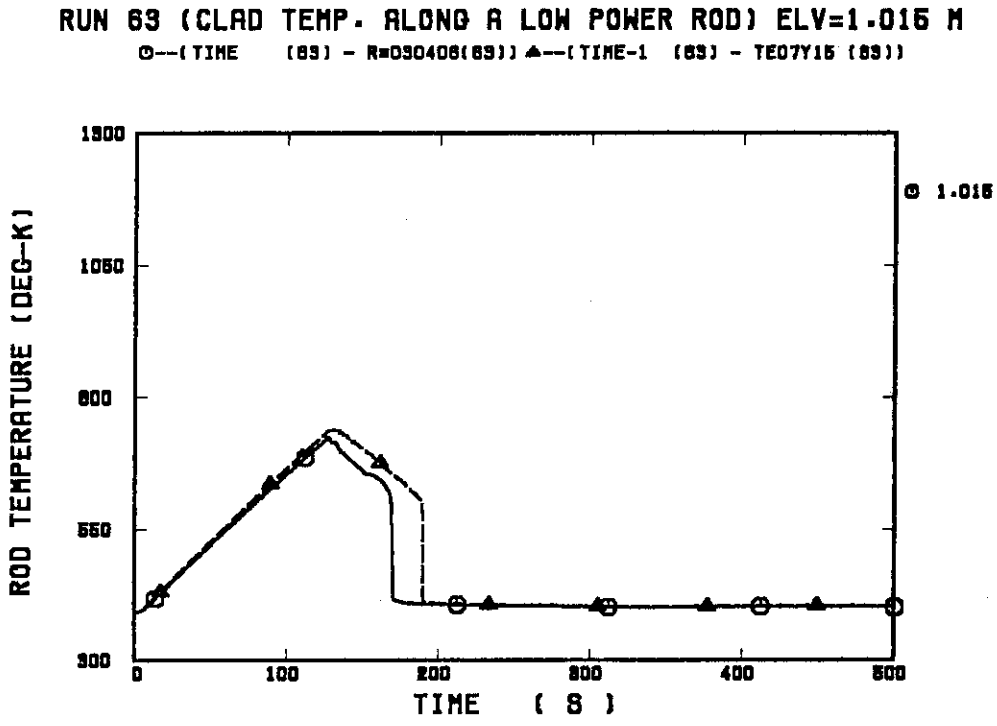

Fig. B.4.17 Clad temperature at elevation of 1.015 m along a low power rod

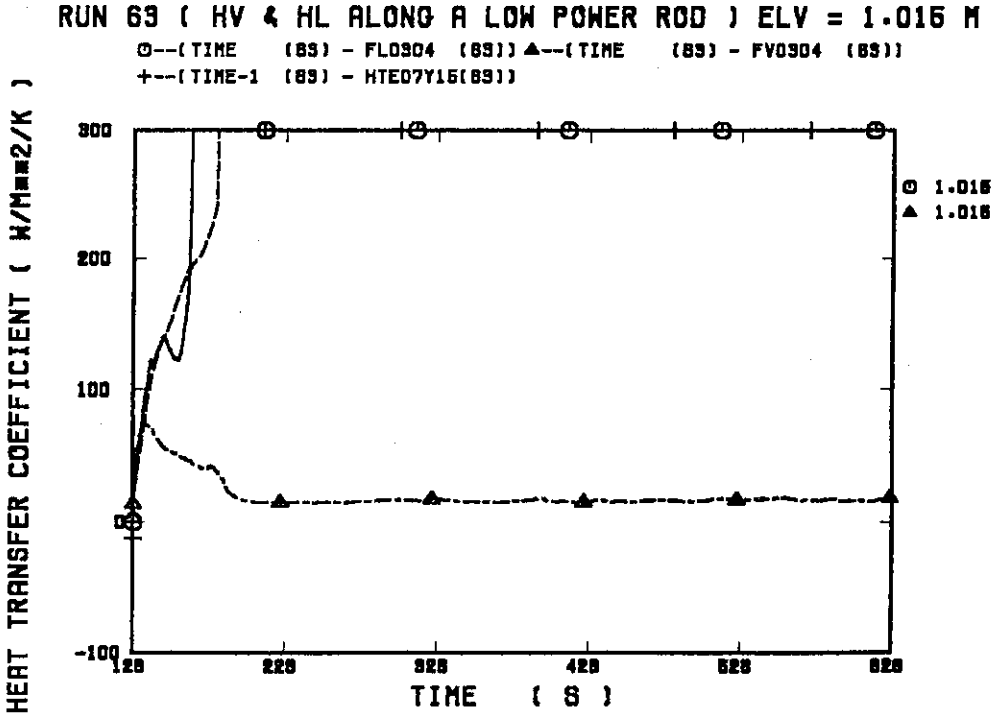

Fig. B.4.18 Heat transfer coefficient at elevation of 1.015 m along a low power rod

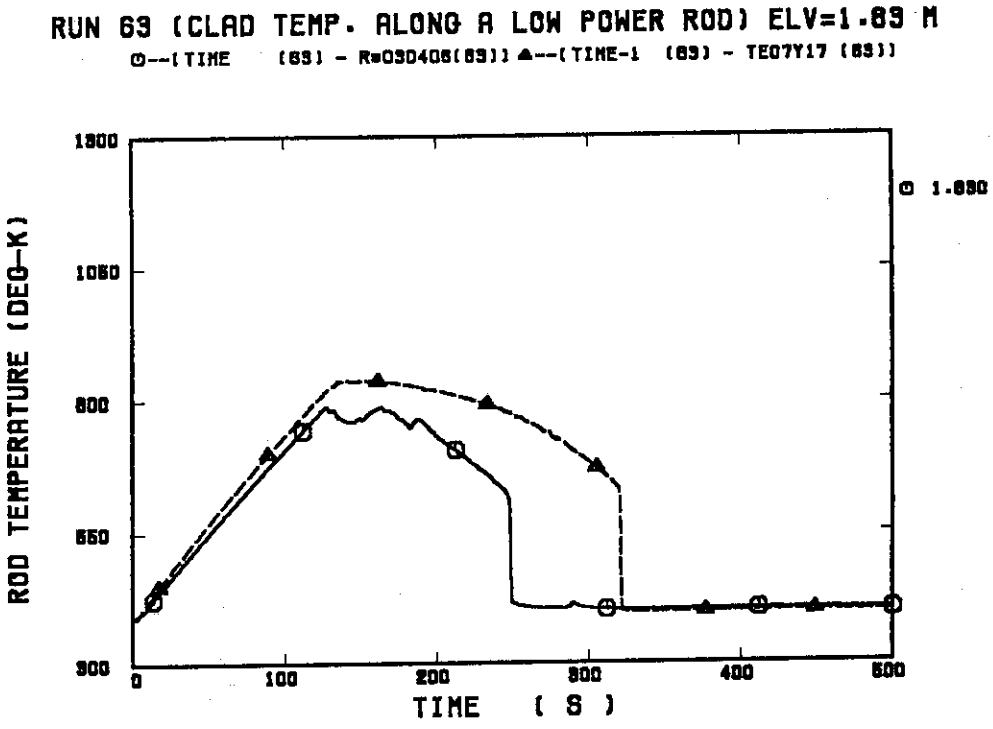

Fig. B.4.19 Clad temperature at elevation of 1.83 m along a low power rod

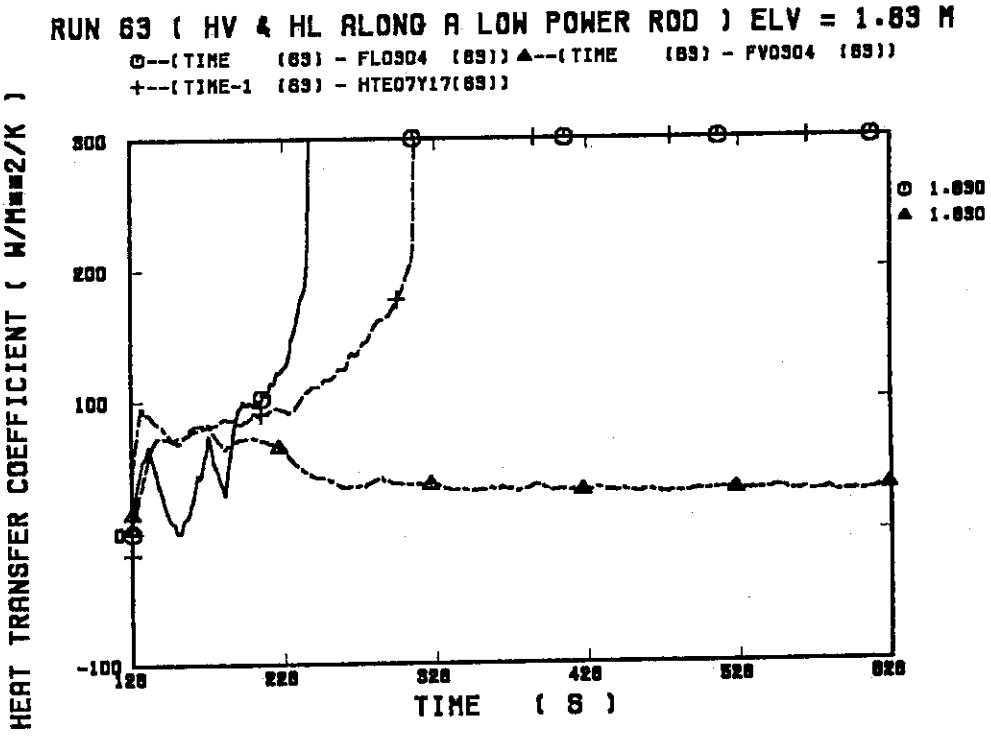

Fig. B.4.20 Heat transfer coefficient at elevation of 1.83 m along a low power rod

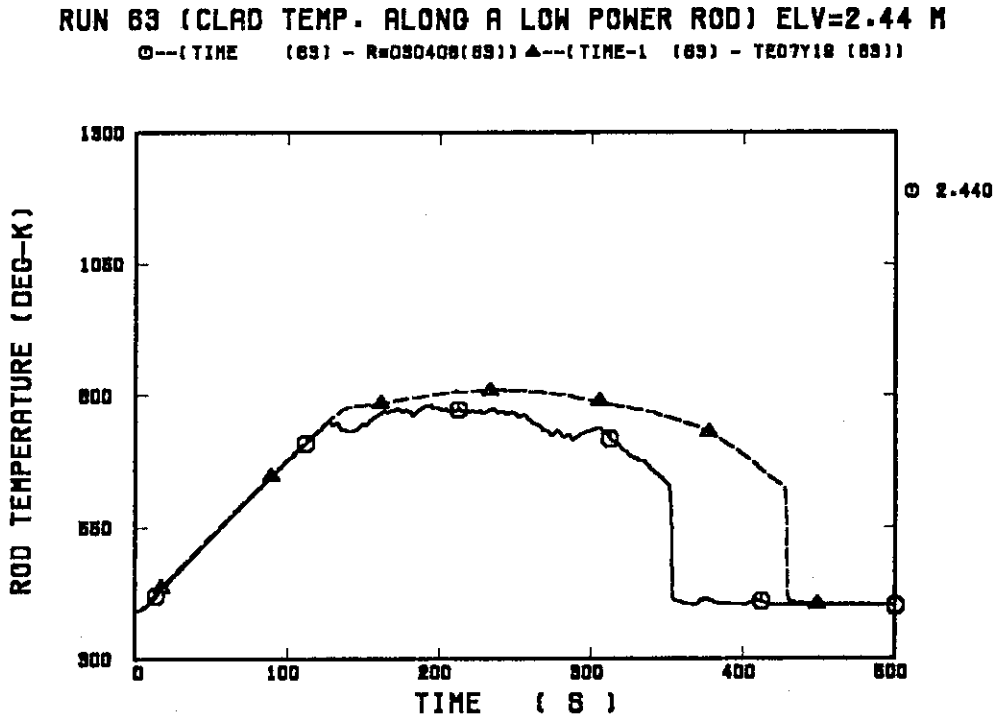

Fig. B.4.21 Clad temperature at elevation of 2.44 m along a low power rod

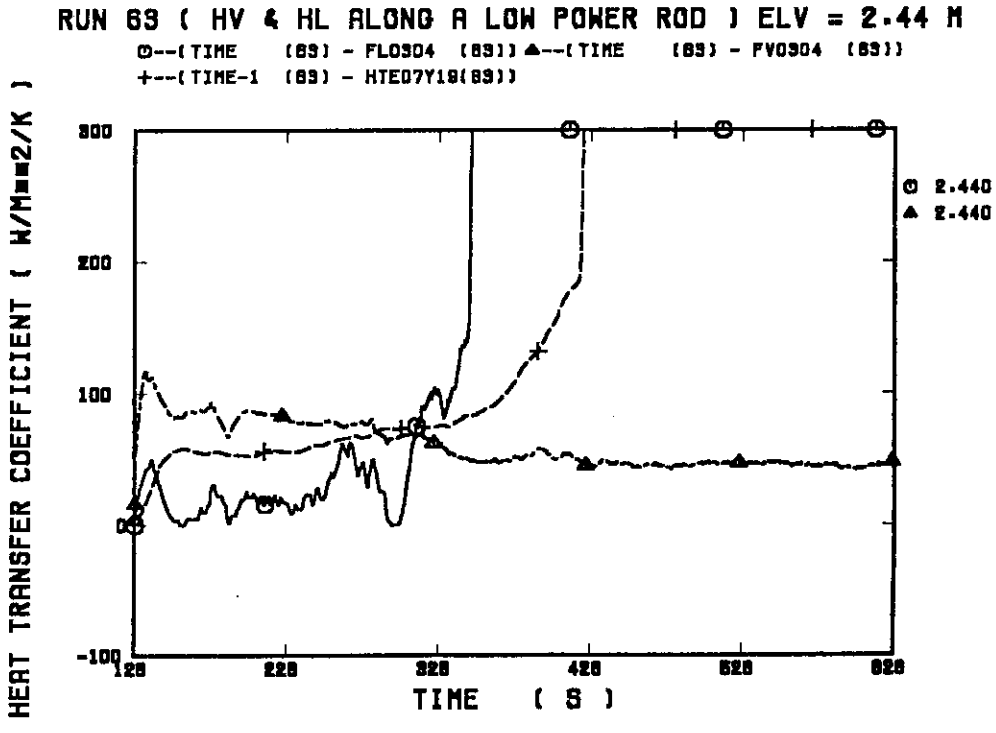

Fig. B.4.22 Heat transfer coefficient at elevation of 2.44 m along a low power rod

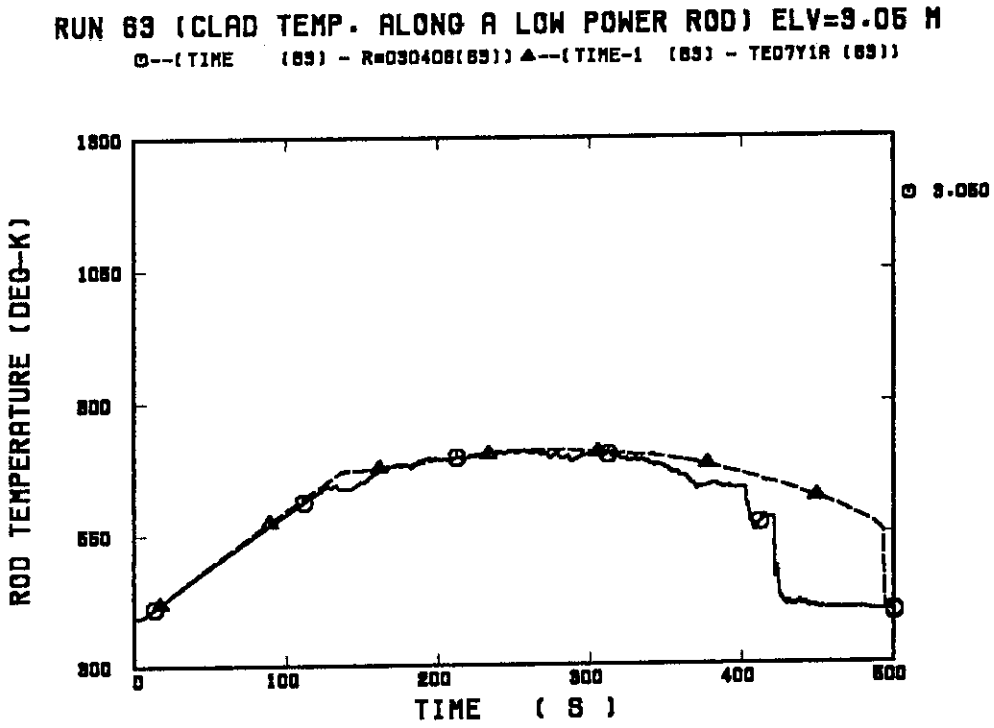

Fig. B.4.23 Clad temperature at elevation of 3.05 m along a low power rod

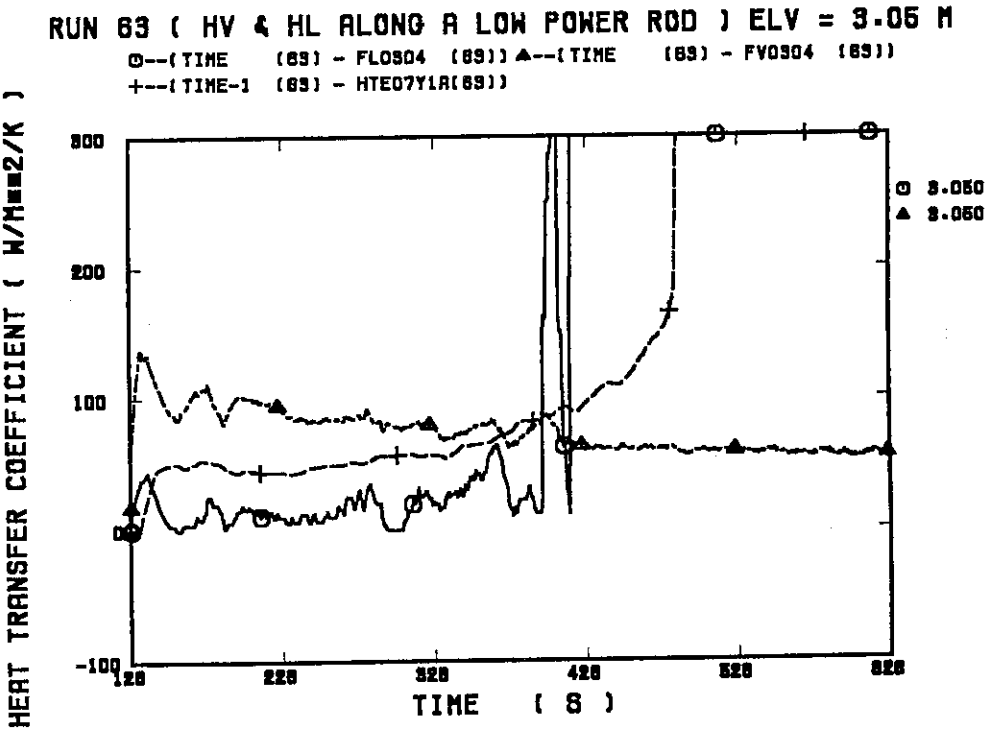

Fig. B.4.24 Heat transfer coefficient at elevation of 3.05 m along a low power rod

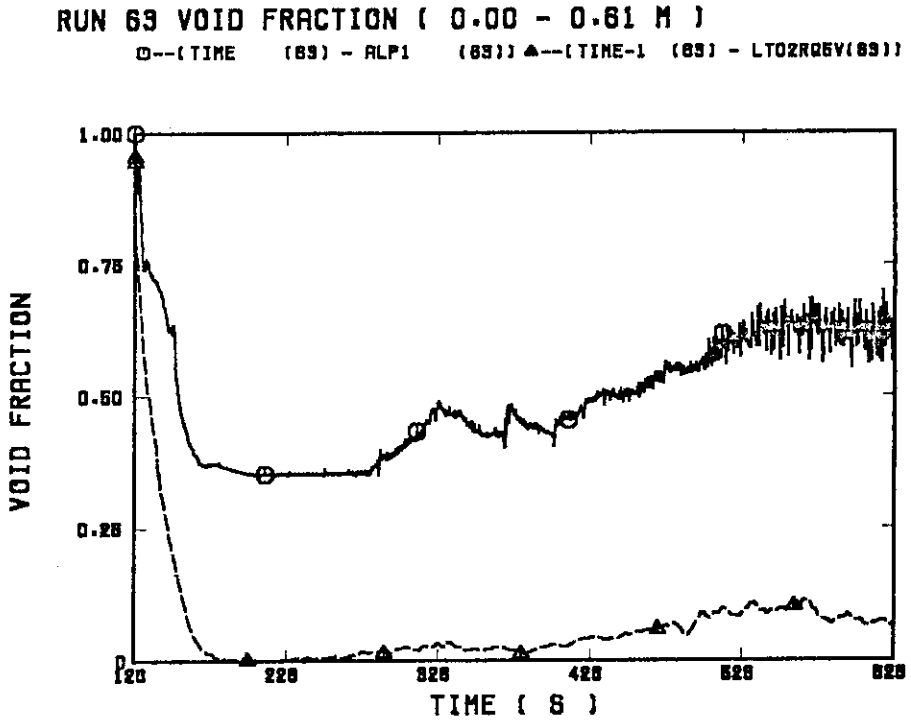

Fig. B.4.25 Average void fraction between 0.00 and 0.61 m

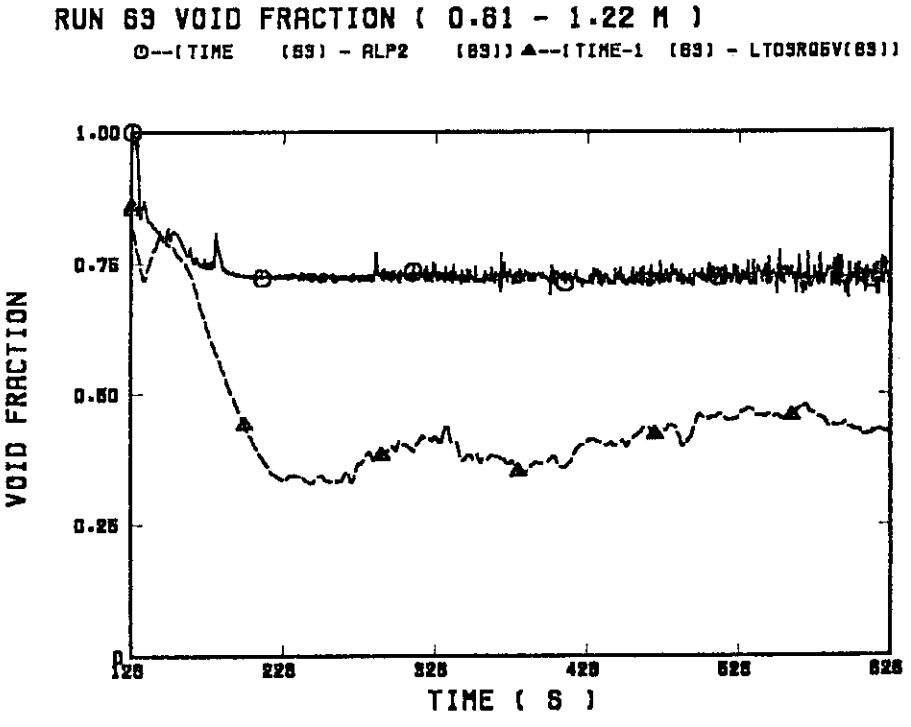

Fig. B.4.26 Average void fraction between 0.61 and 1.22 m

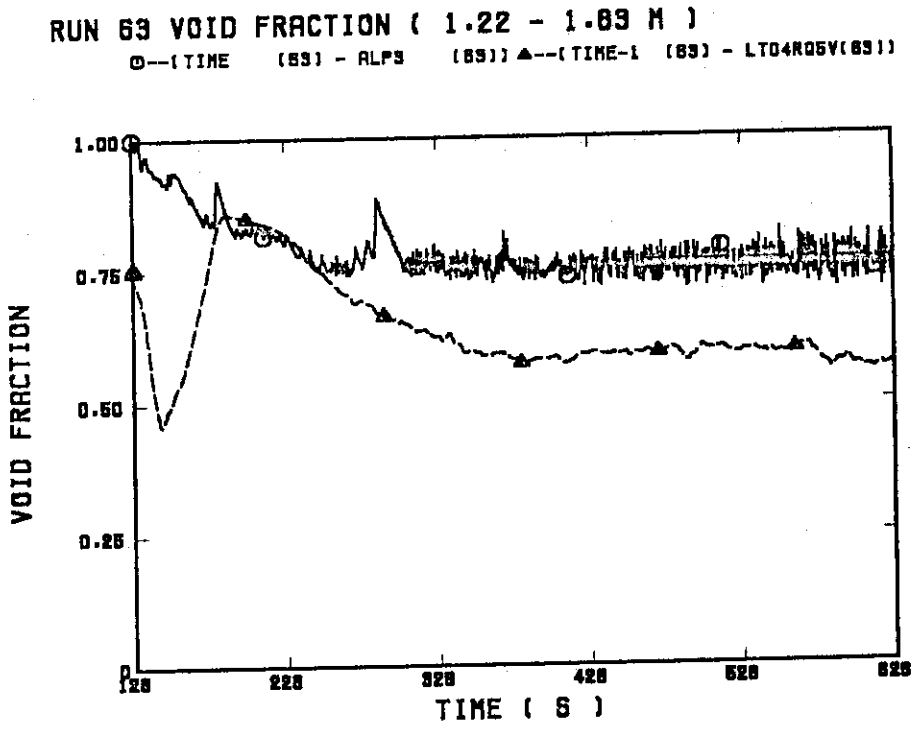

Fig. B.4.27 Average void fraction between 1.22 and 1.83 m

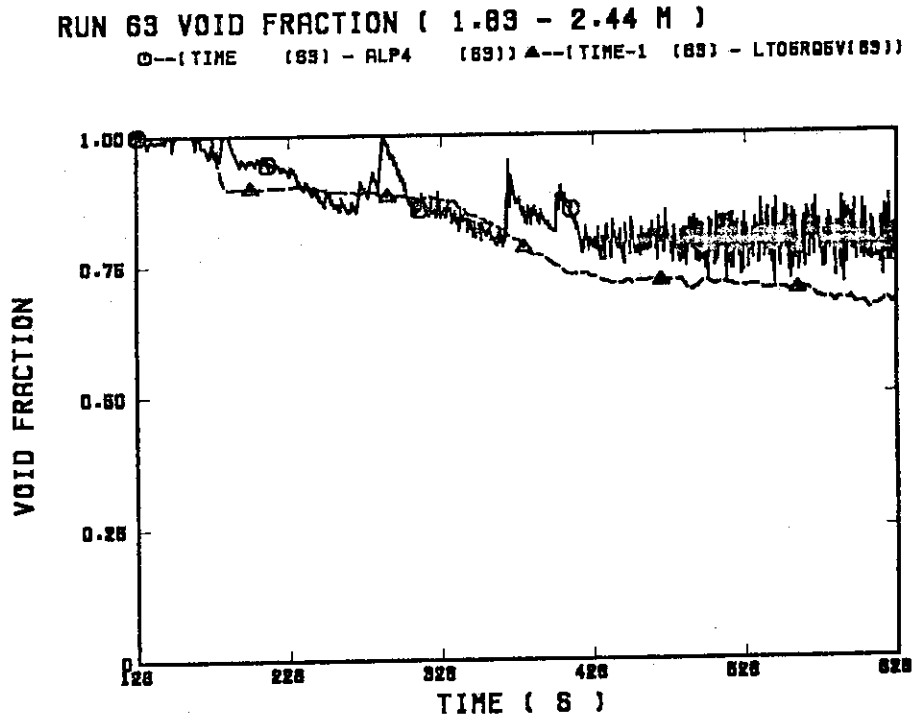

Fig. B.4.28 Average void fraction between 1.83 and 2.44 m

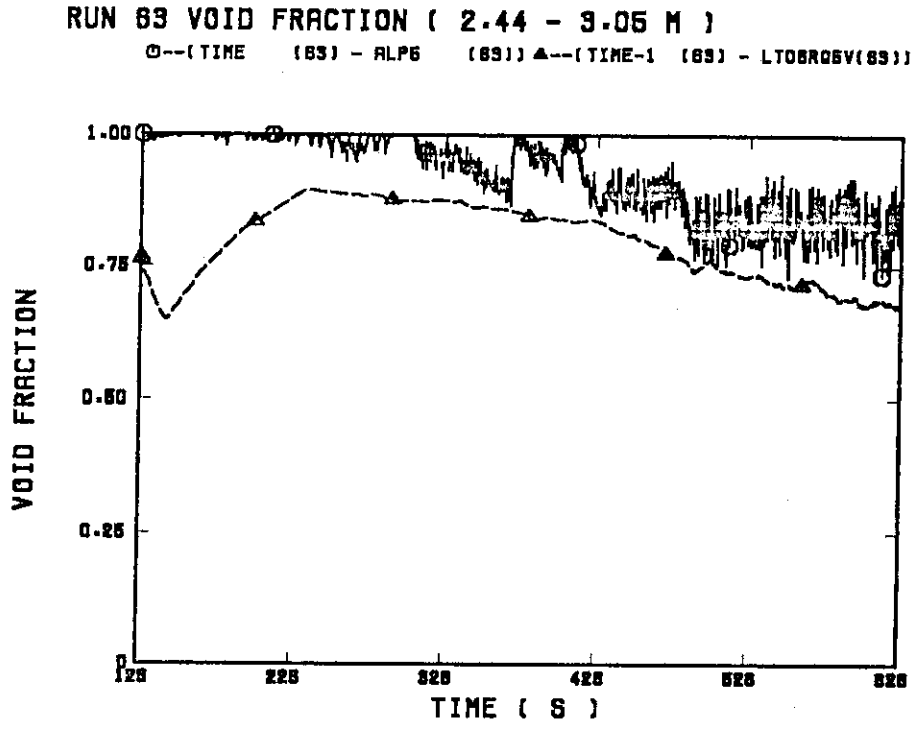

Fig. B.4.29 Average void fraction between 2.44 and 3.05 m

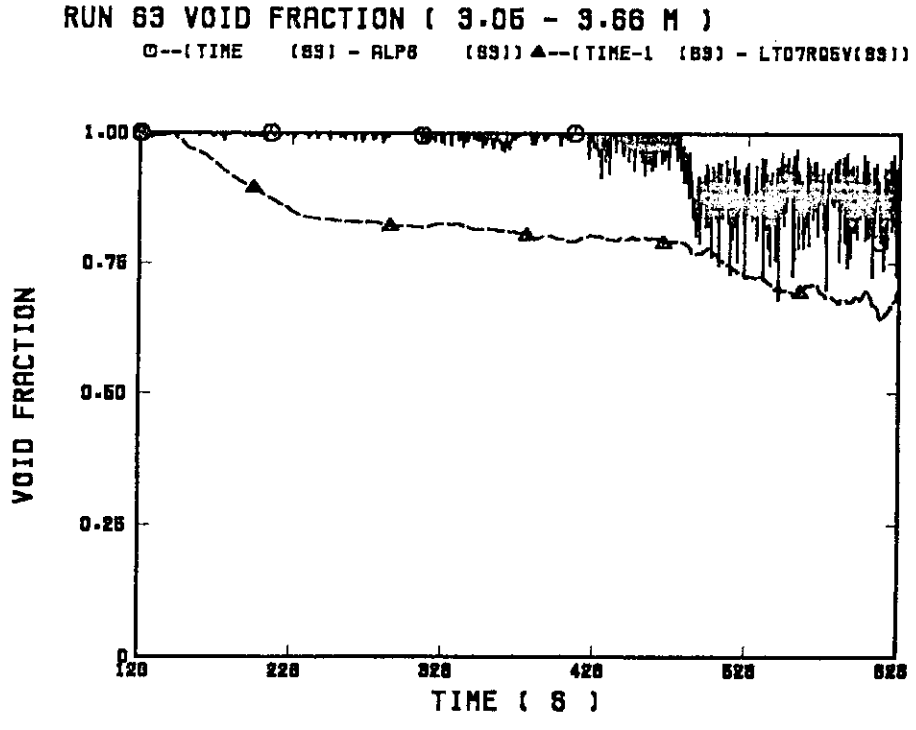

Fig. B.4.30 Average void fraction between 3.05 and 3.66 m

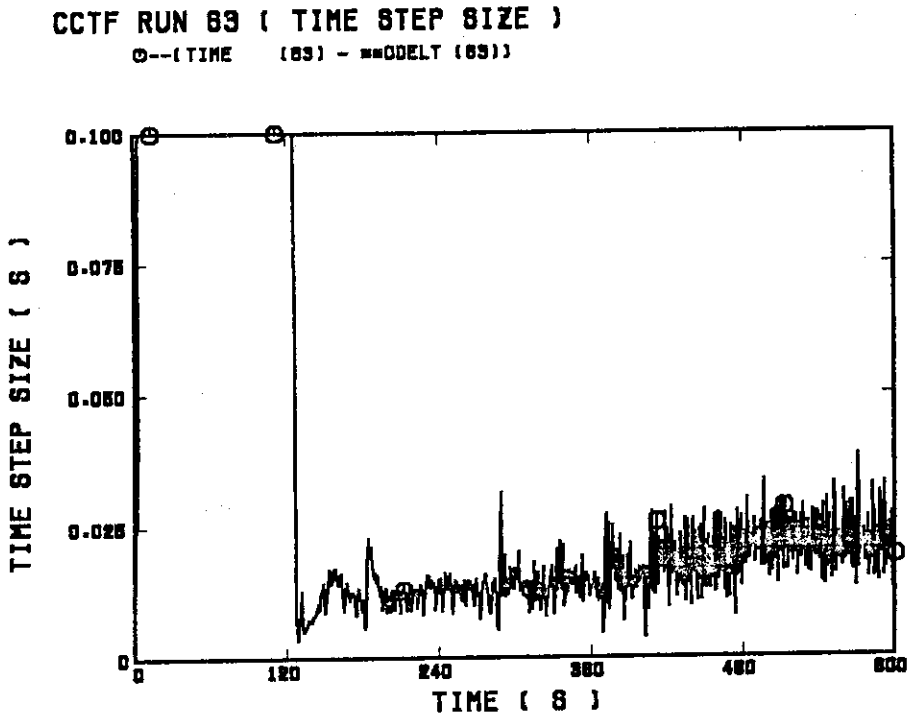

Fig. B.4.31 Time step size

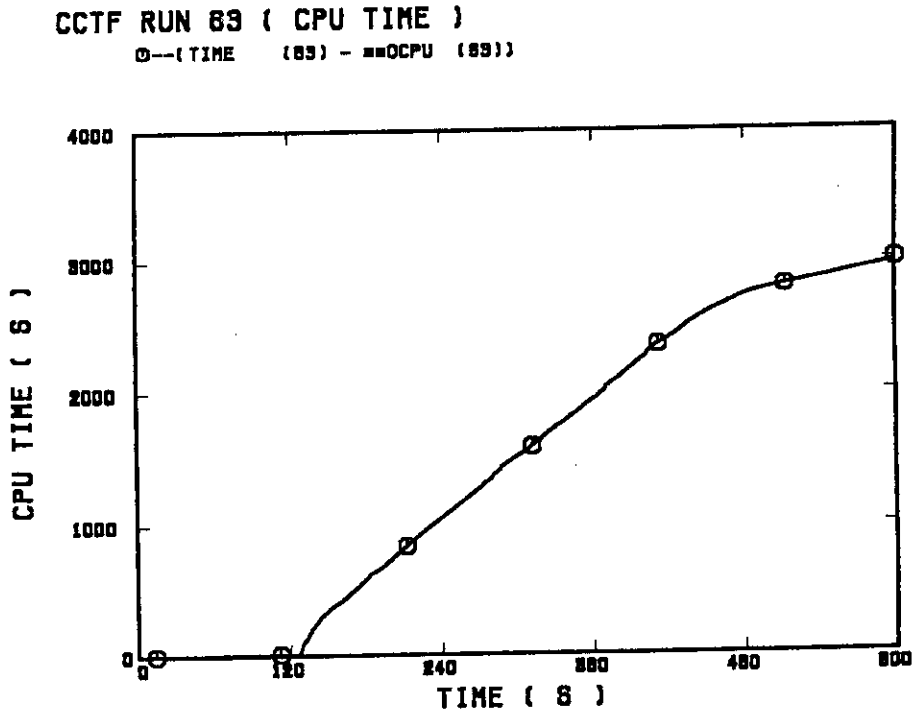

Fig. B.4.32 CPU time

(5) CCTF Best Estimate Test (Run 71)

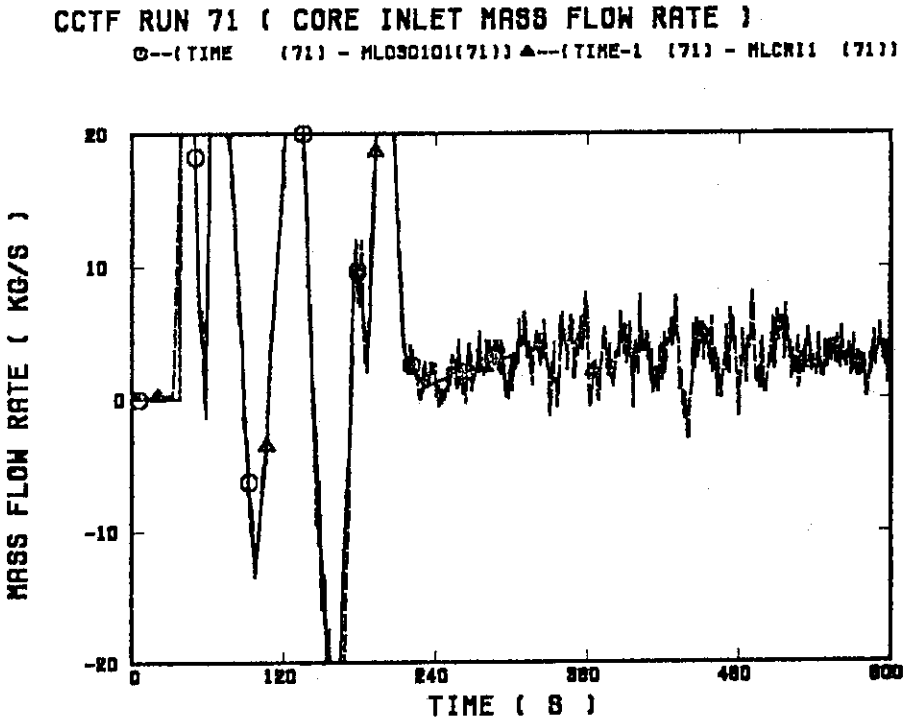

Fig. B.5.1 Core inlet mass flow rate (input)

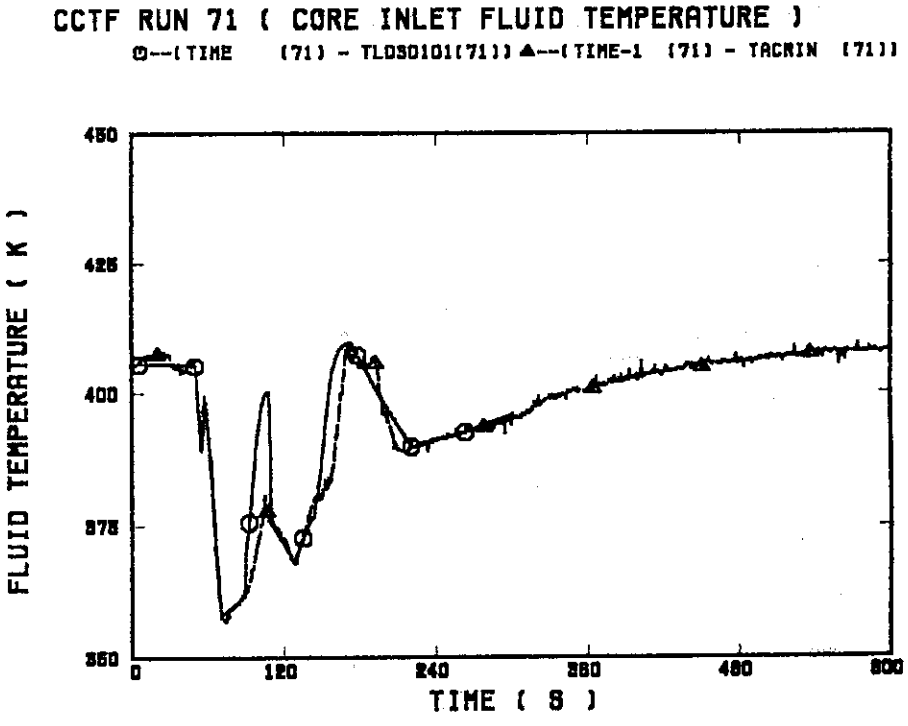

Fig. B.5.2 Core inlet fluid temperature (input)

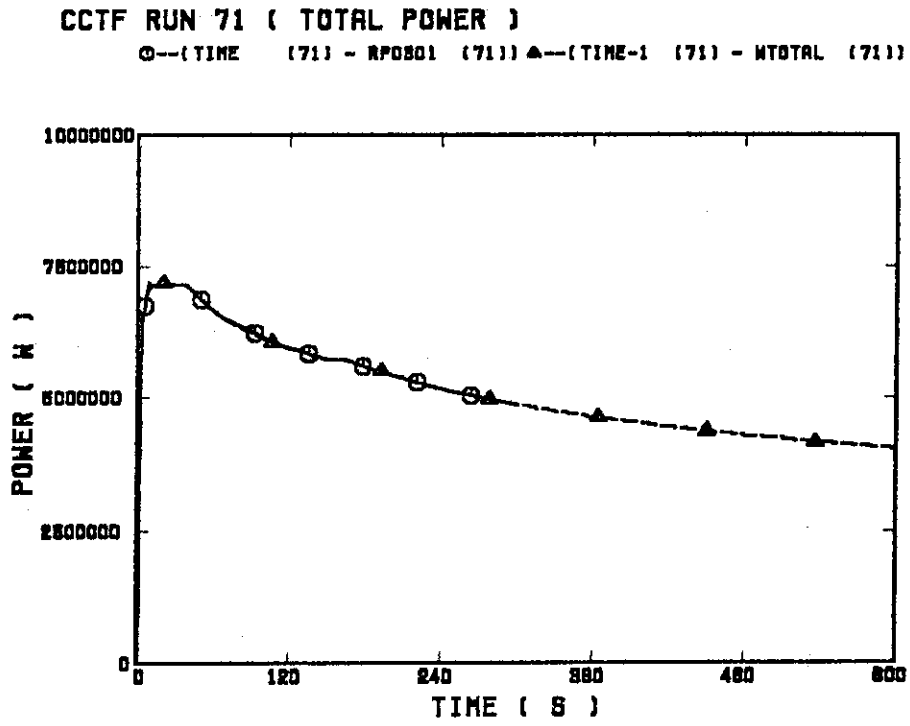

Fig. B.5.3 Total power supplied to core (input)

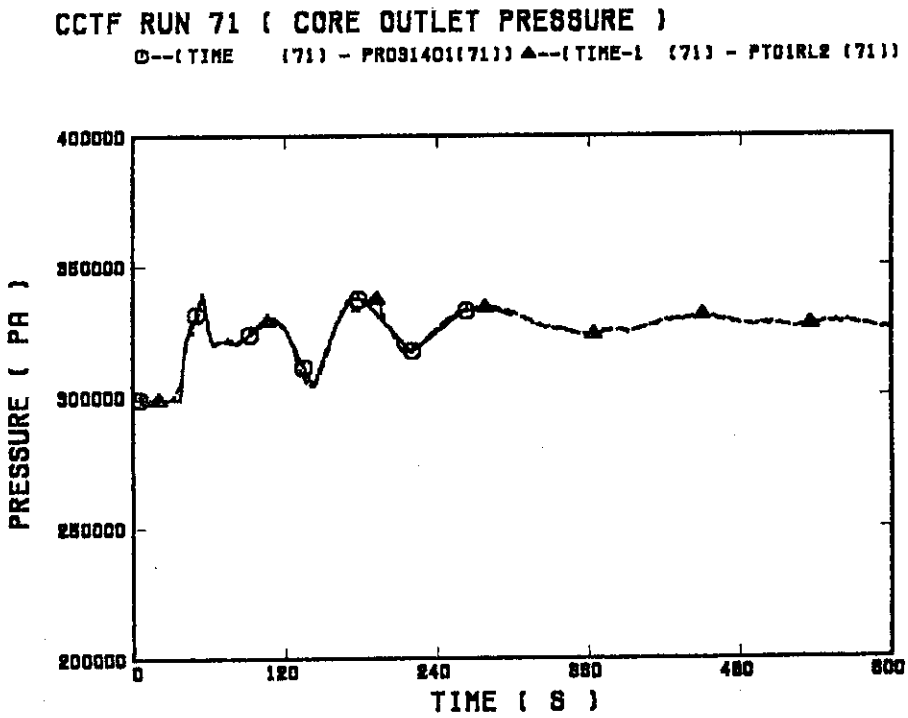

Fig. B.5.4 Core outlet pressure (input)

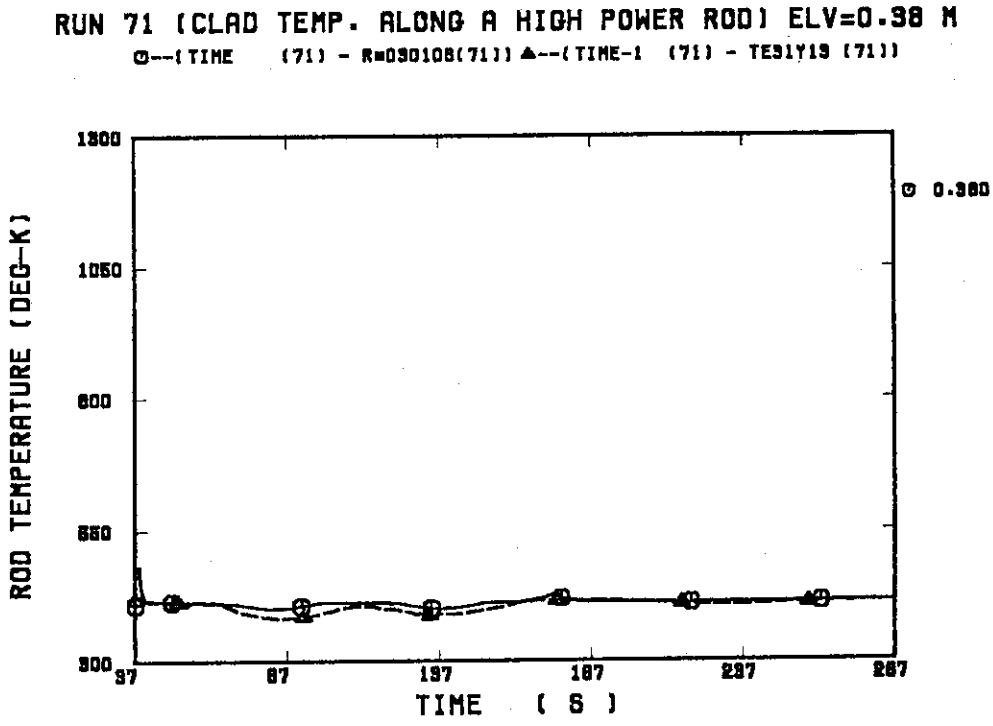

Fig. B.5.5 Clad temperature at elevation of 0.38 m along an average power rod

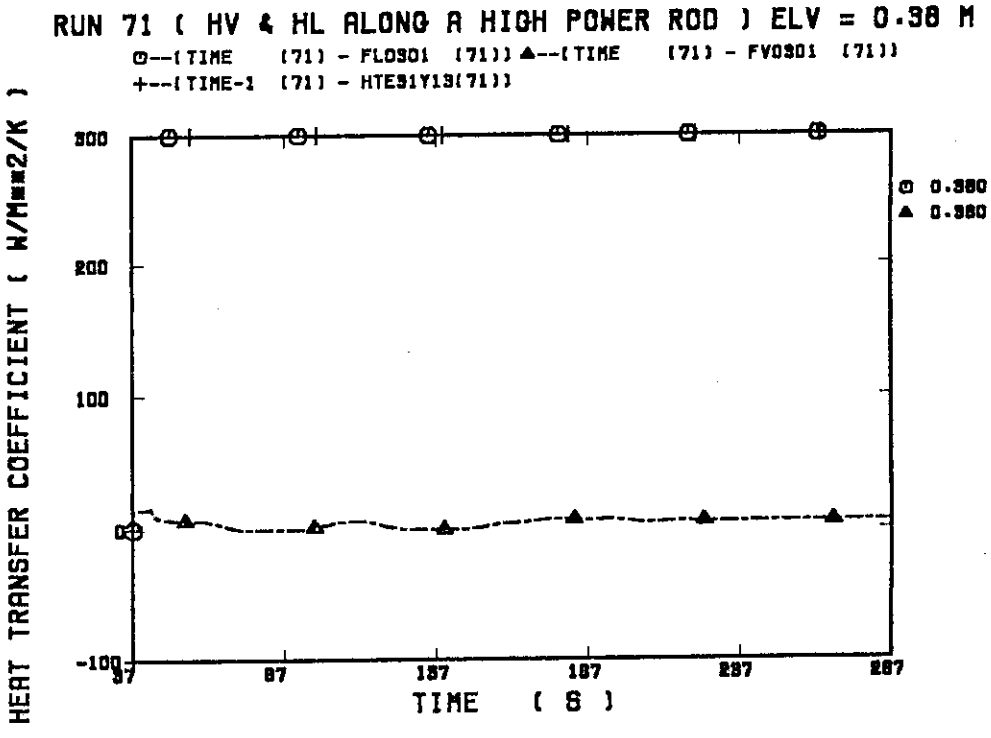

Fig. B.5.6 Heat transfer coefficient at elevation of 0.38 m along an average power rod

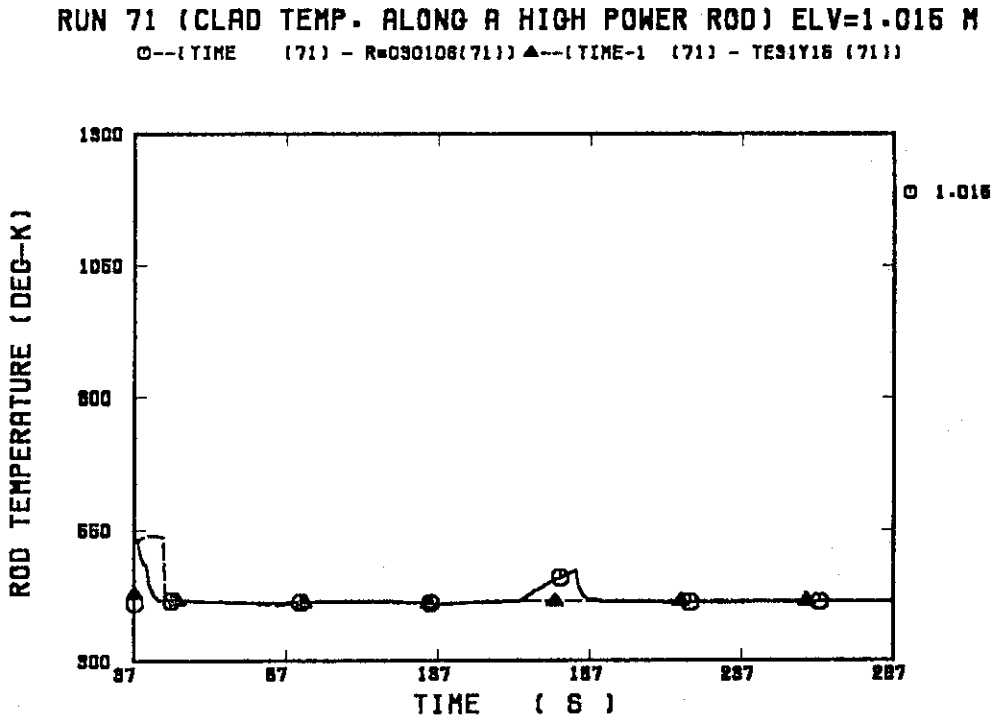

Fig. B.5.7 Clad temperature at elevation of 1.015 m along an average power rod

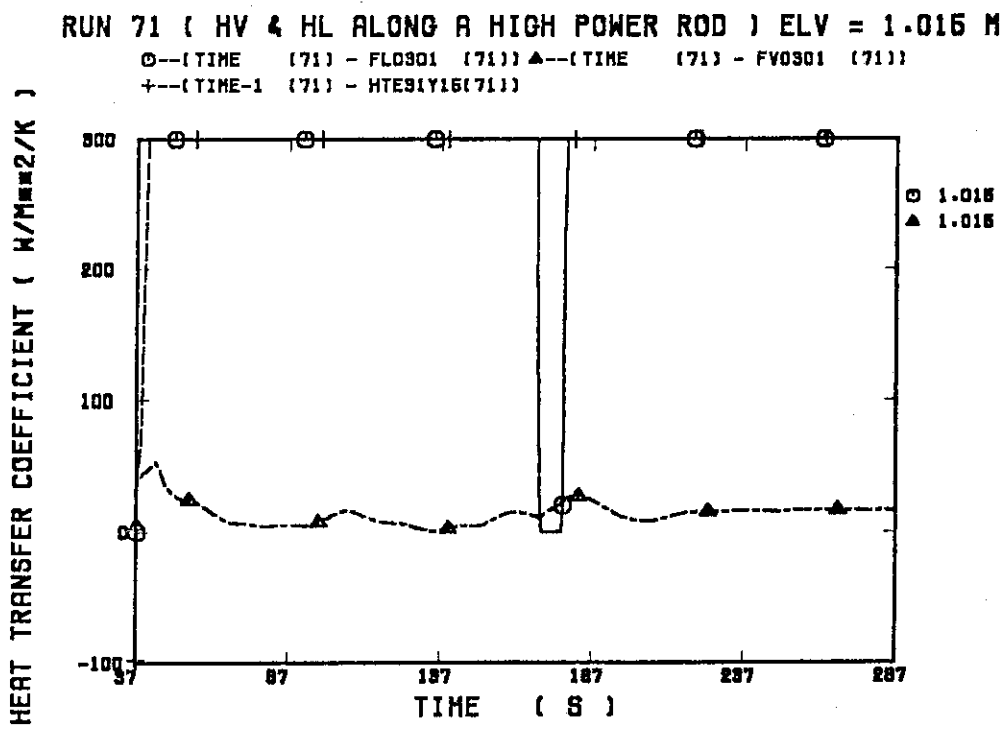

Fig. B.5.8 Heat transfer coefficient at elevation of 1.015 m along an average power rod

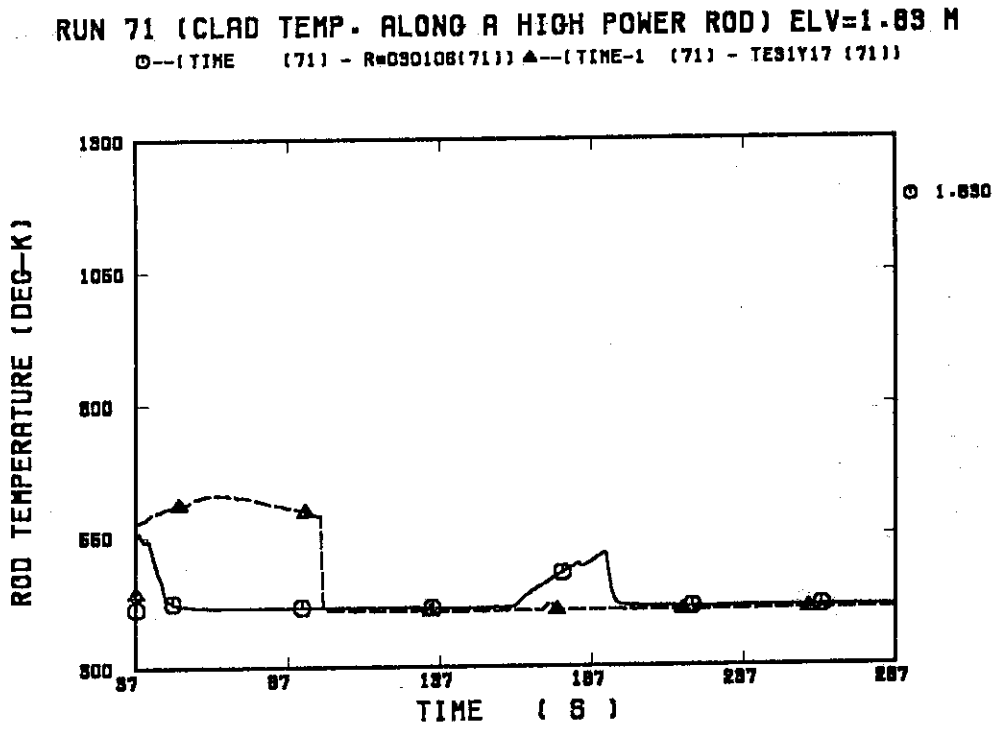

Fig. B.5.9 Clad temperature at elevation of 1.83 m along an average power rod

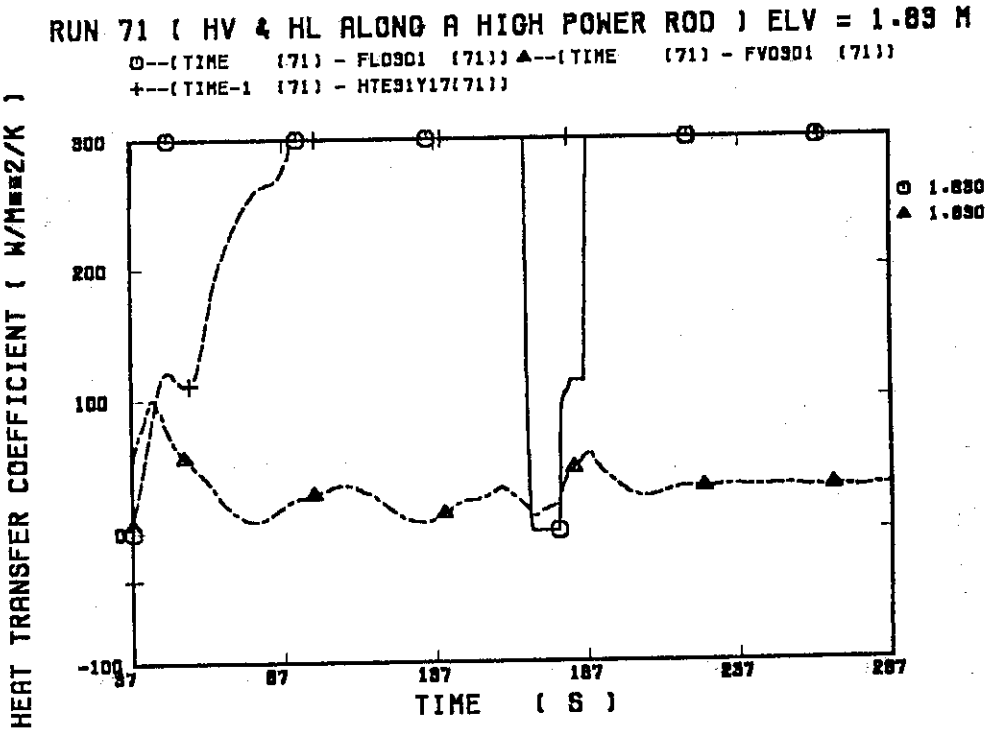

Fig. B.5.10 Heat transfer coefficient at elevation of 1.83 m along an average power rod

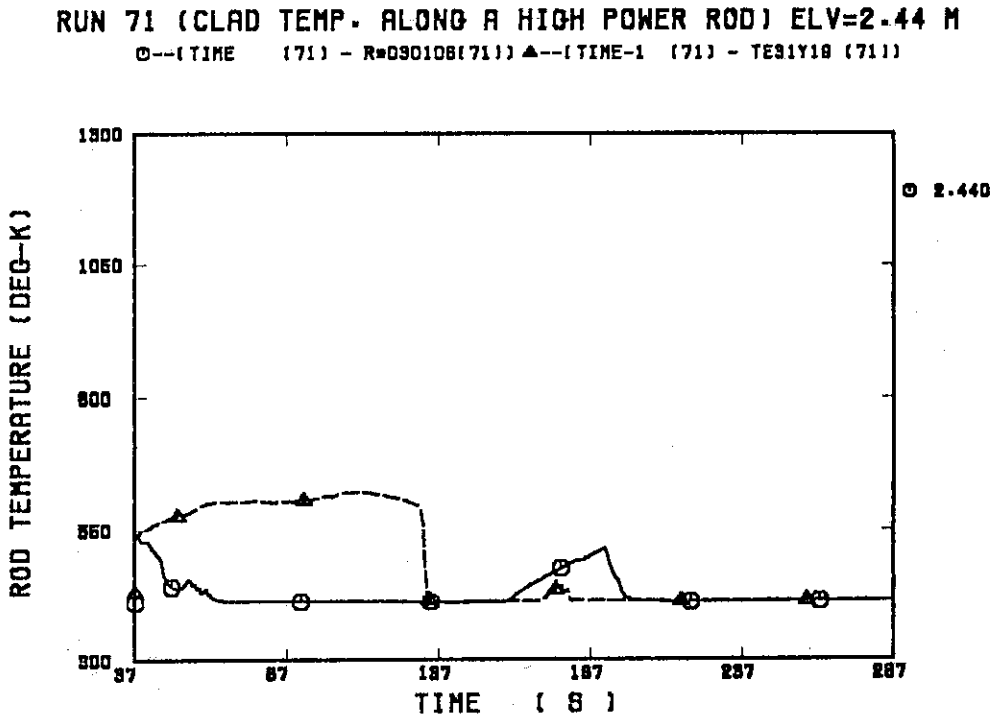

Fig. B.5.11 Clad temperature at elevation of 2.44 m along an average power rod

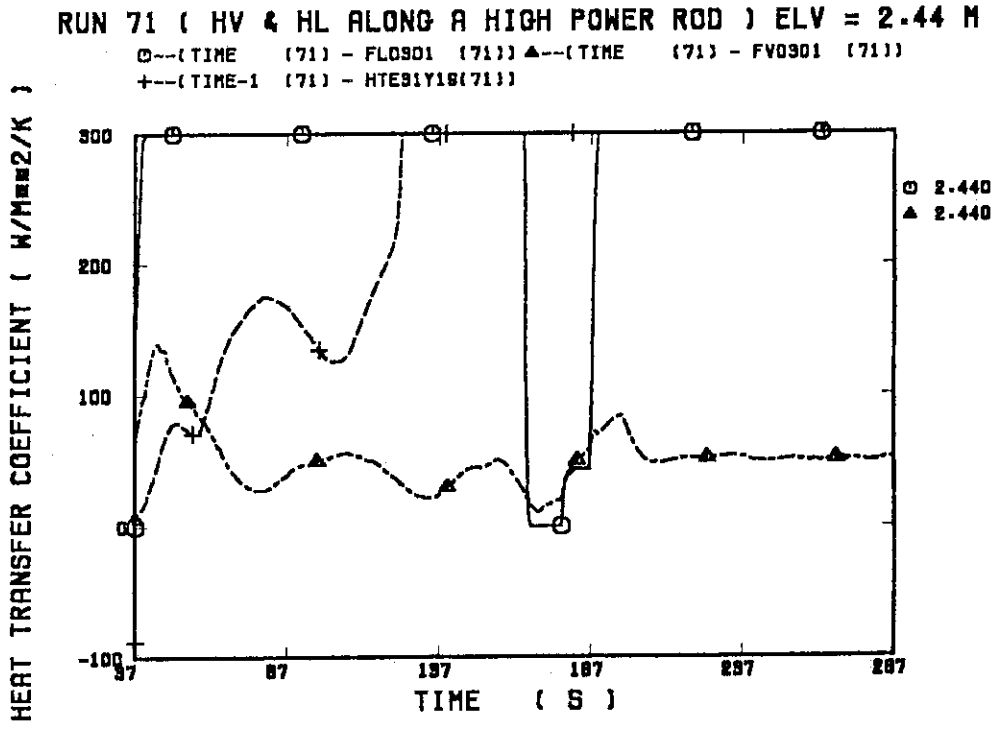

Fig. B.5.12 Heat transfer coefficient at elevation of 2.44 m along an average power rod

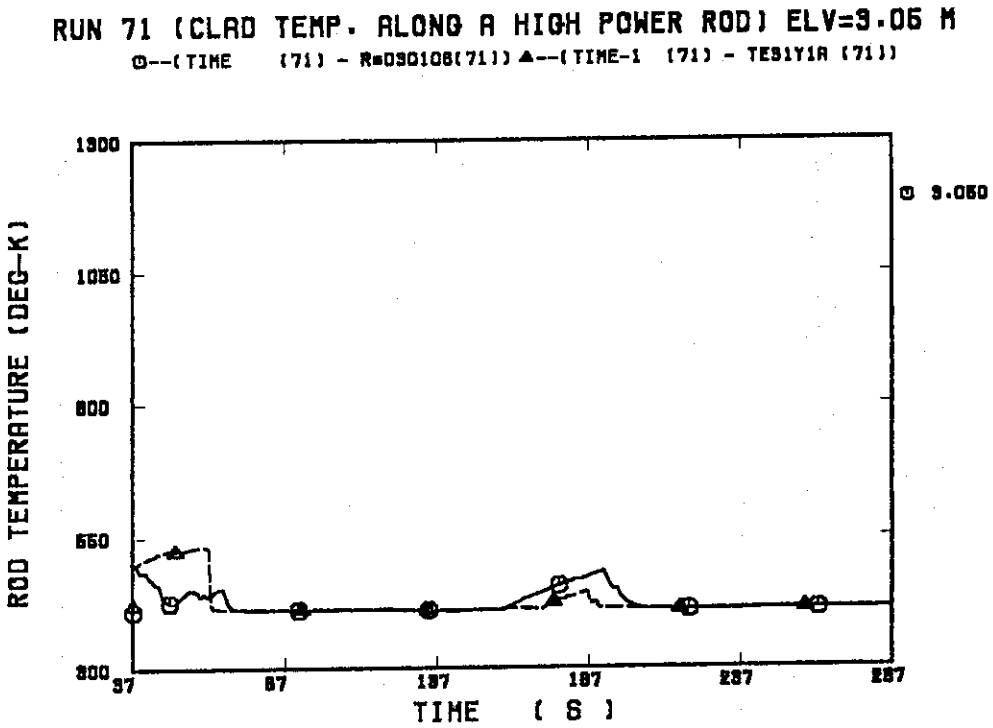

Fig. B.5.13 Clad temperature at elevation of 3.05 m along an average power rod

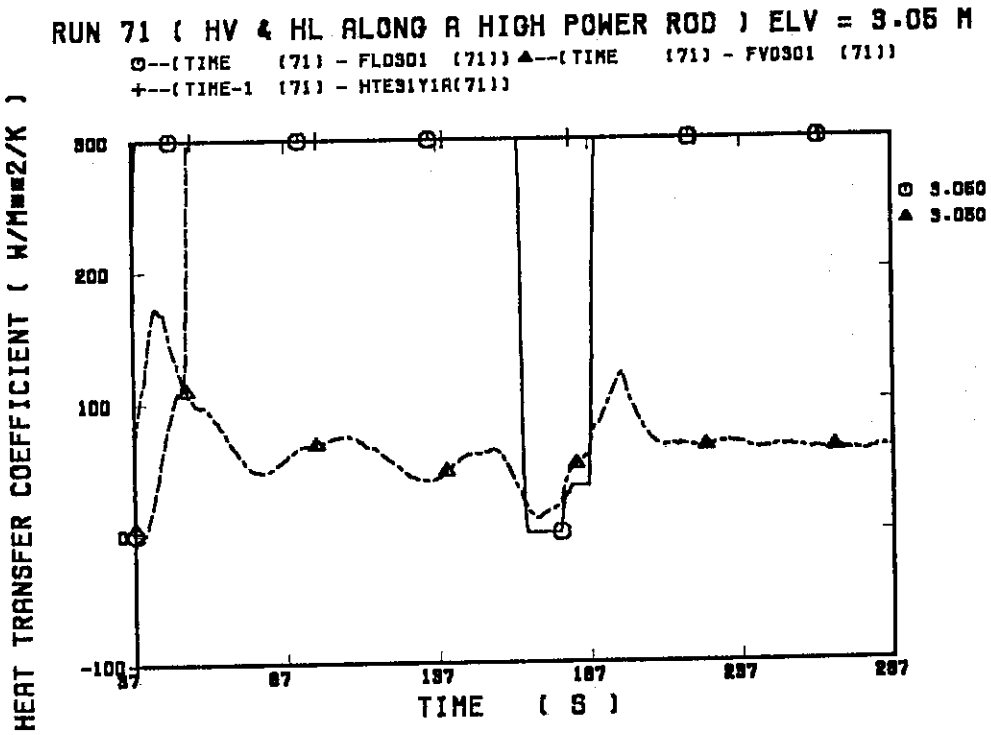

Fig. B.5.14 Heat transfer coefficient at elevation of 3.05 m along an average power rod

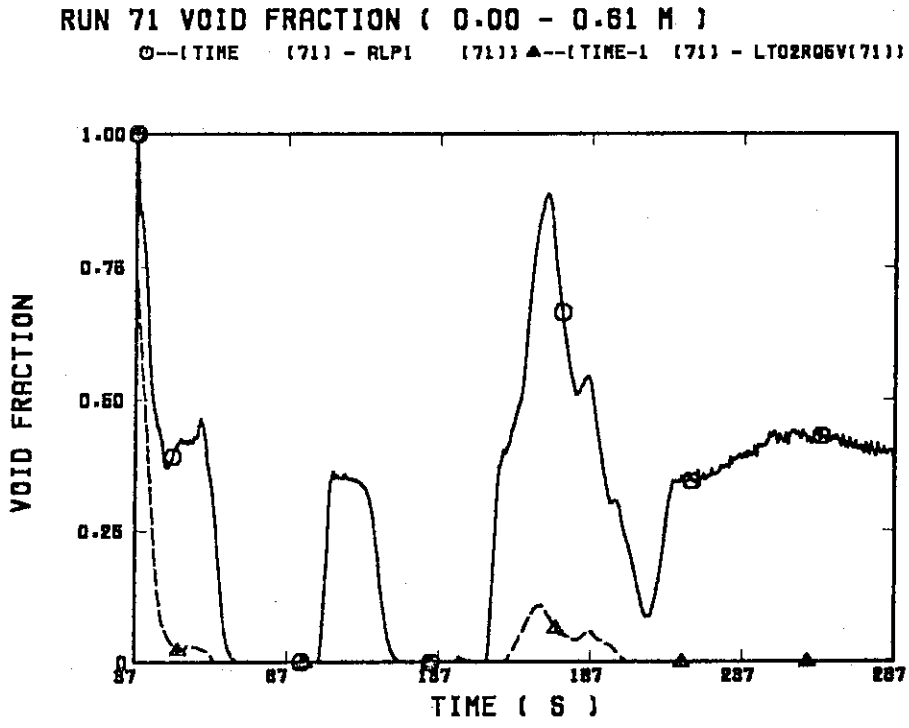

Fig. B.5.15 Average void fraction between 0.00 and 0.61 m

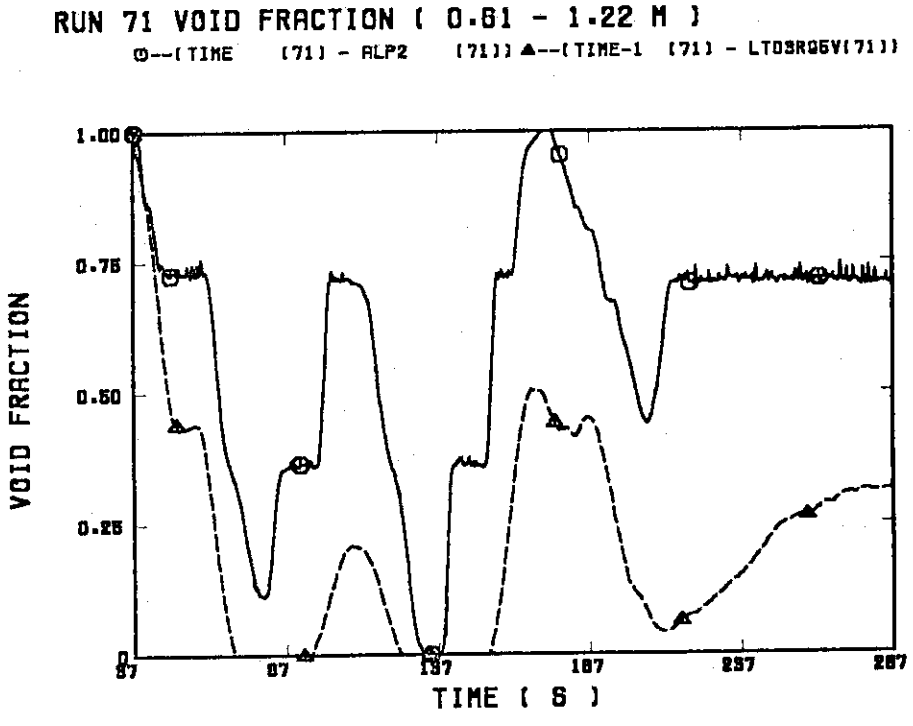

Fig. B.5.16 Average void fraction between 0.61 and 1.22 m

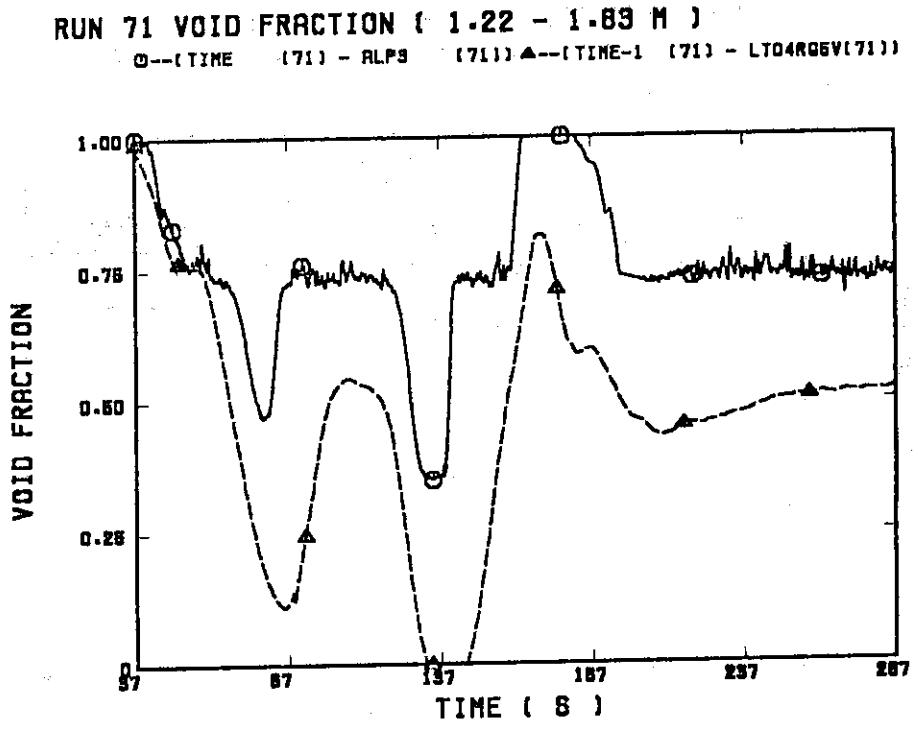

Fig. B.5.17 Average void fraction between 1.22 and 1.83 m

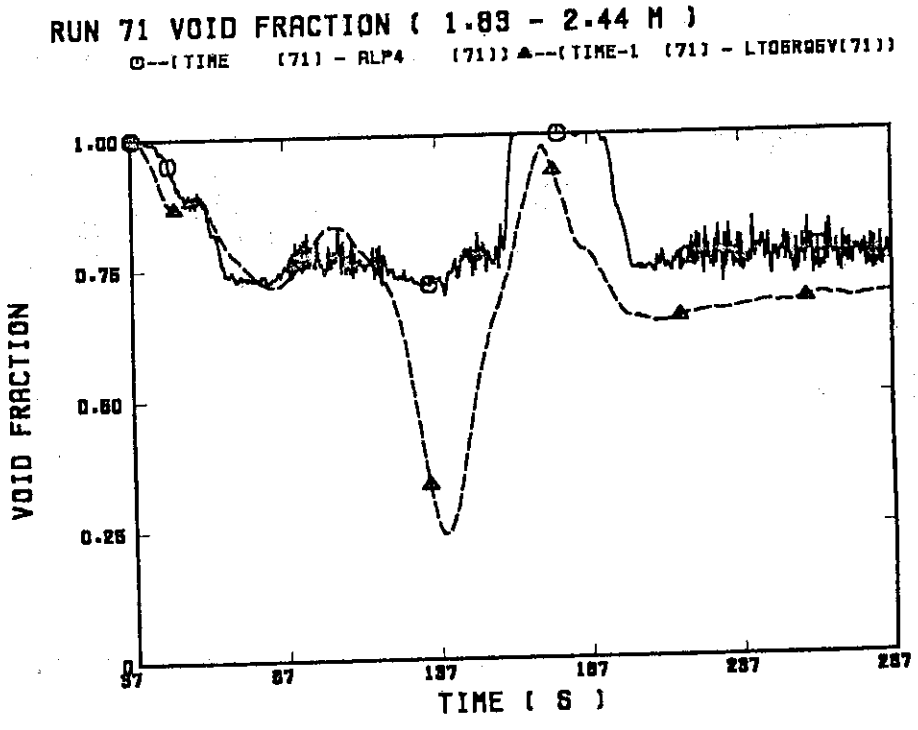

Fig. B.5.18 Average void fraction between 1.83 and 2.44 m

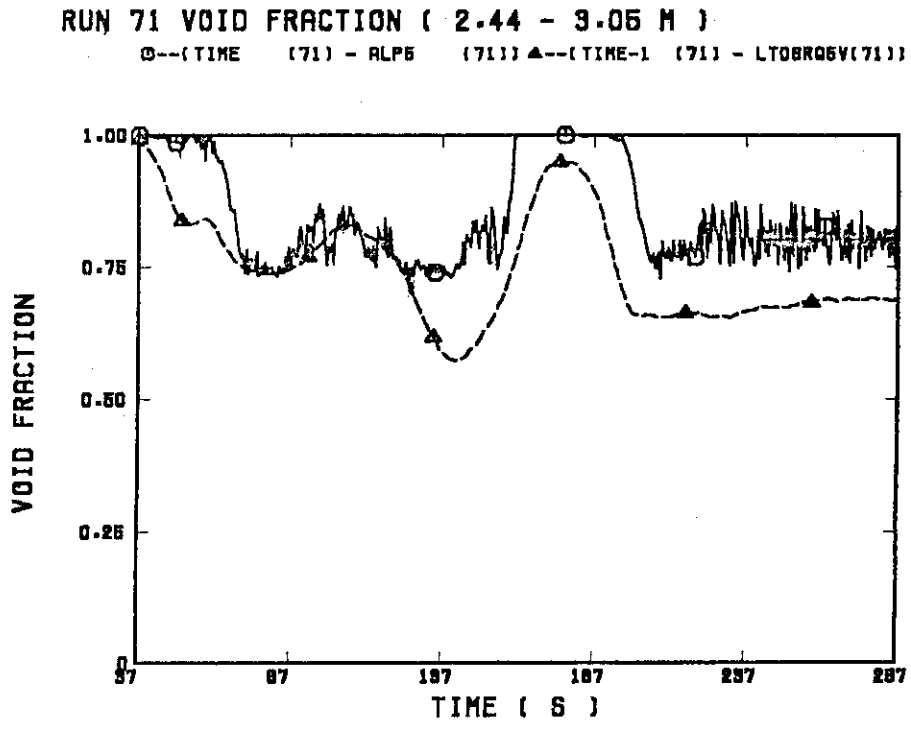

Fig. B.5.19 Average void fraction between 2.44 and 3.05 m

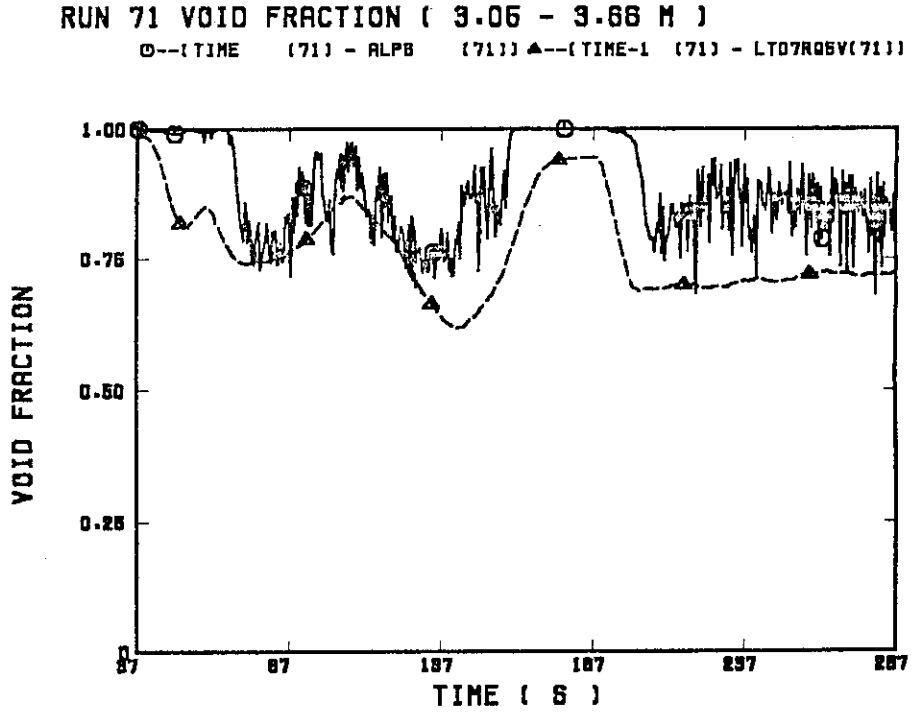

Fig. B.5.20 Average void fraction between 3.05 and 3.66 m

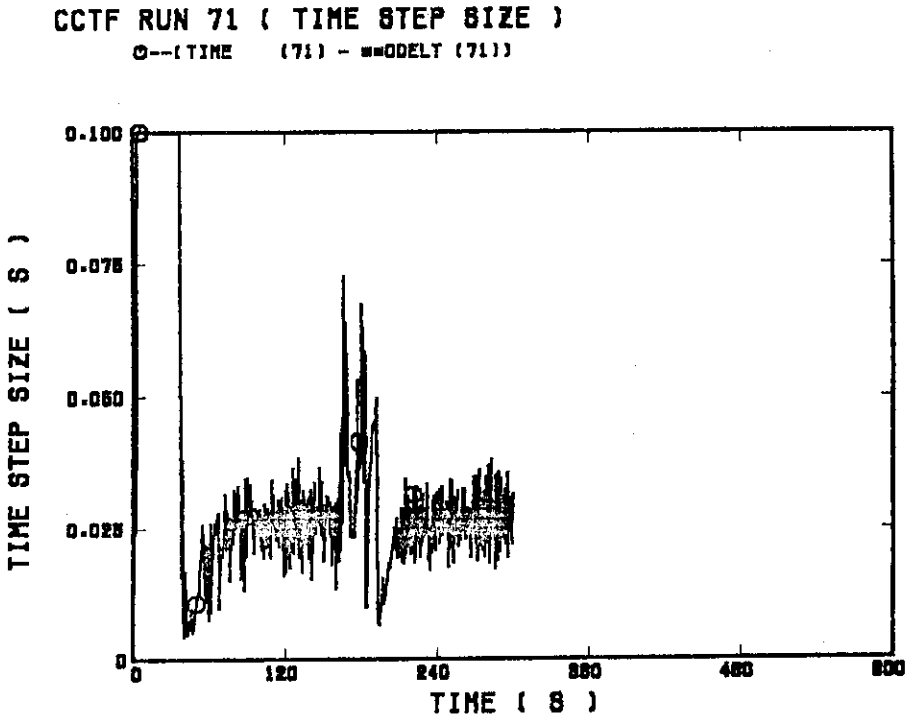

Fig. B.5.21 Time step size

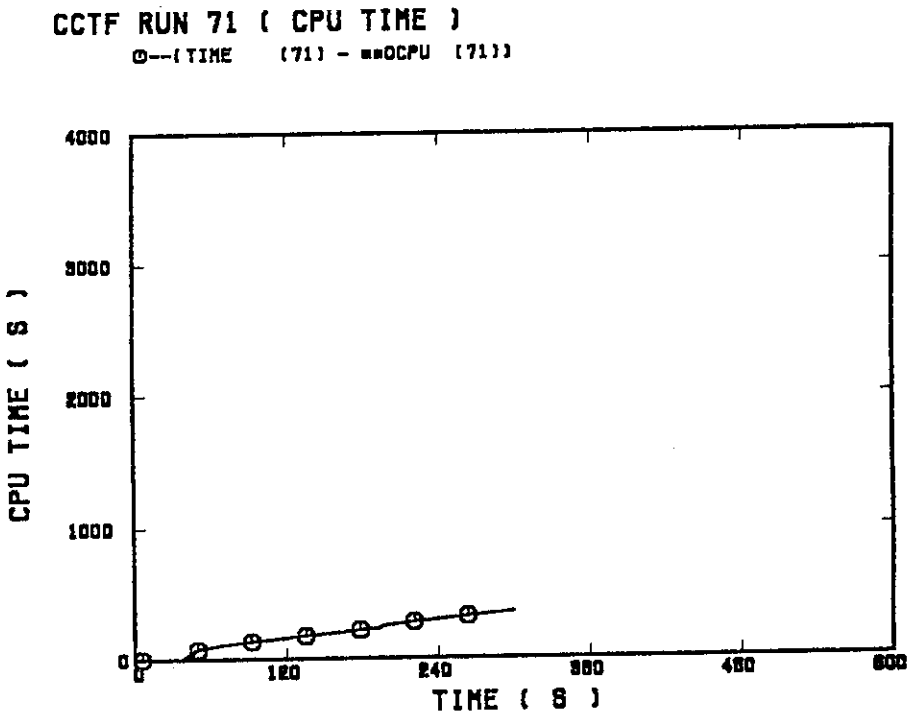

Fig. B.5.22 CPU time

(6) SCTF Flat Power Test (Run 619)

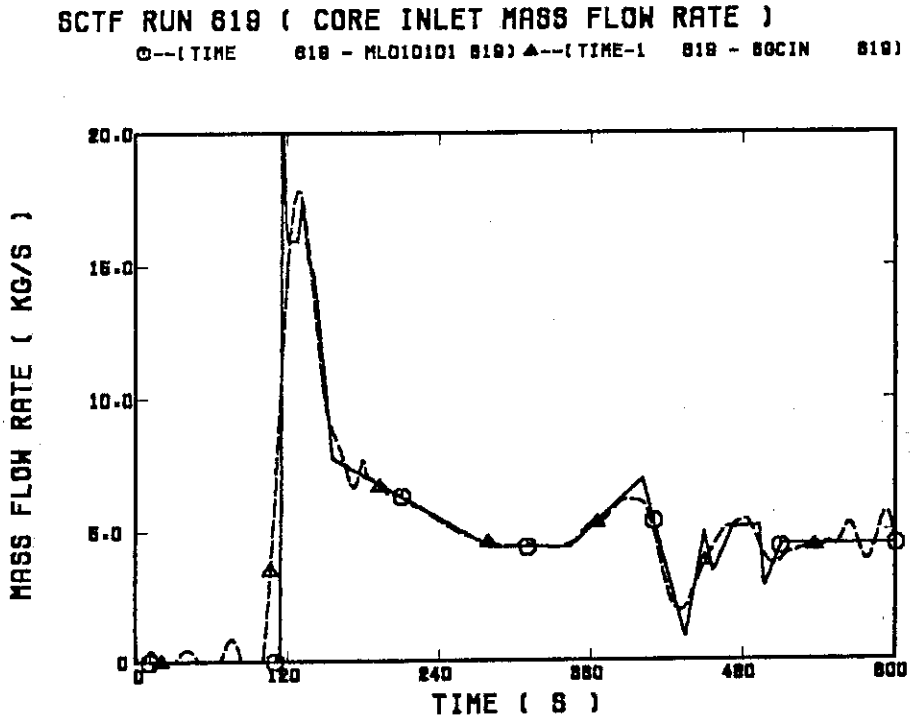

Fig. B.6.1 Core inlet mass flow rate (input)

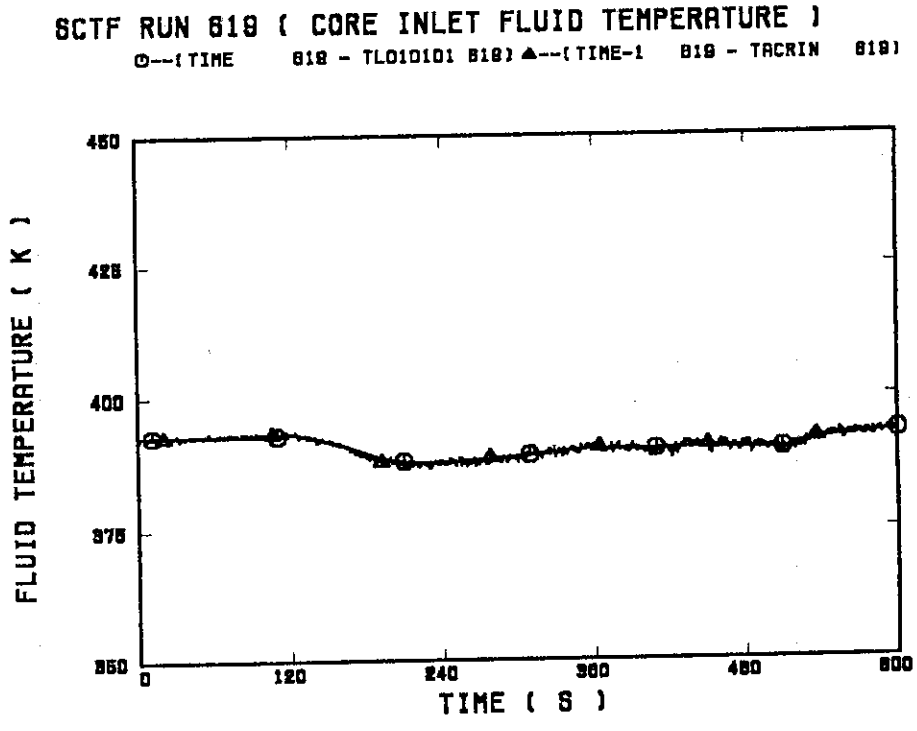

Fig. B.6.2 Core inlet fluid temperature (input)

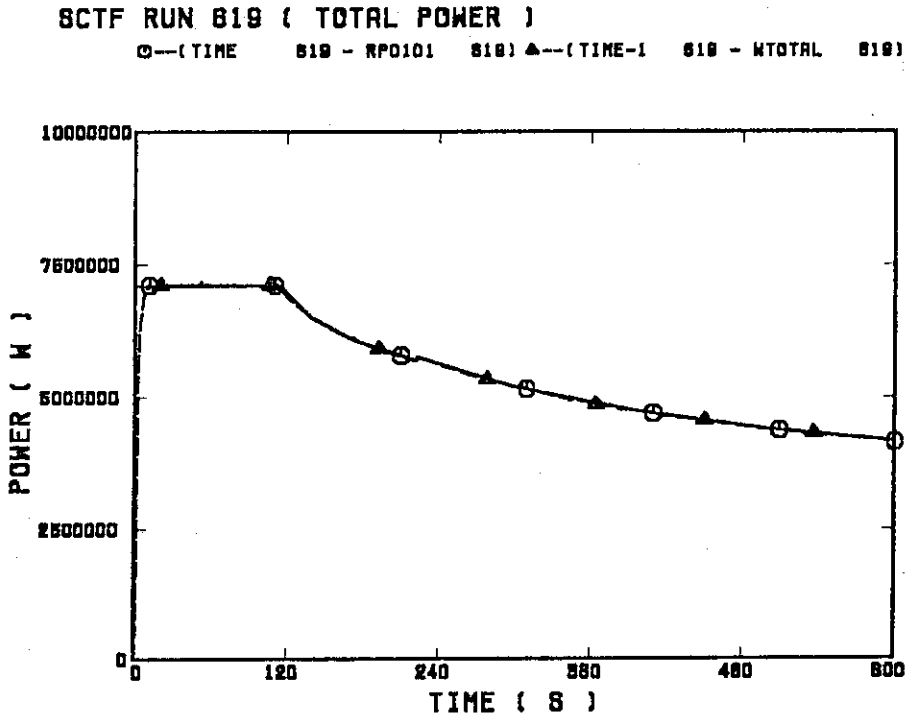

Fig. B.6.3 Total power supplied to core (input)

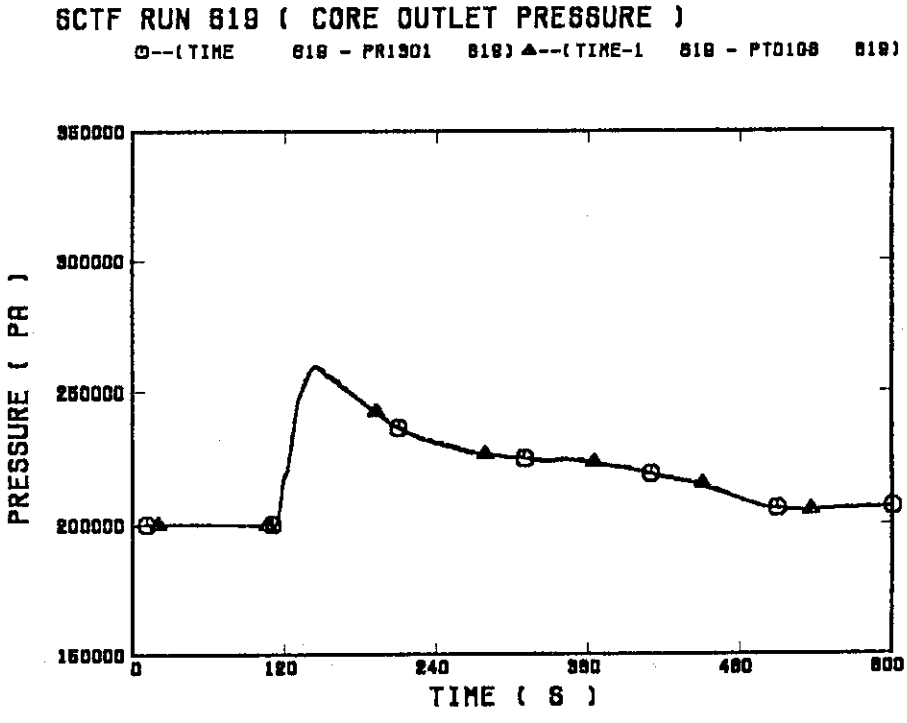

Fig. B.6.4 Core outlet pressure (input)

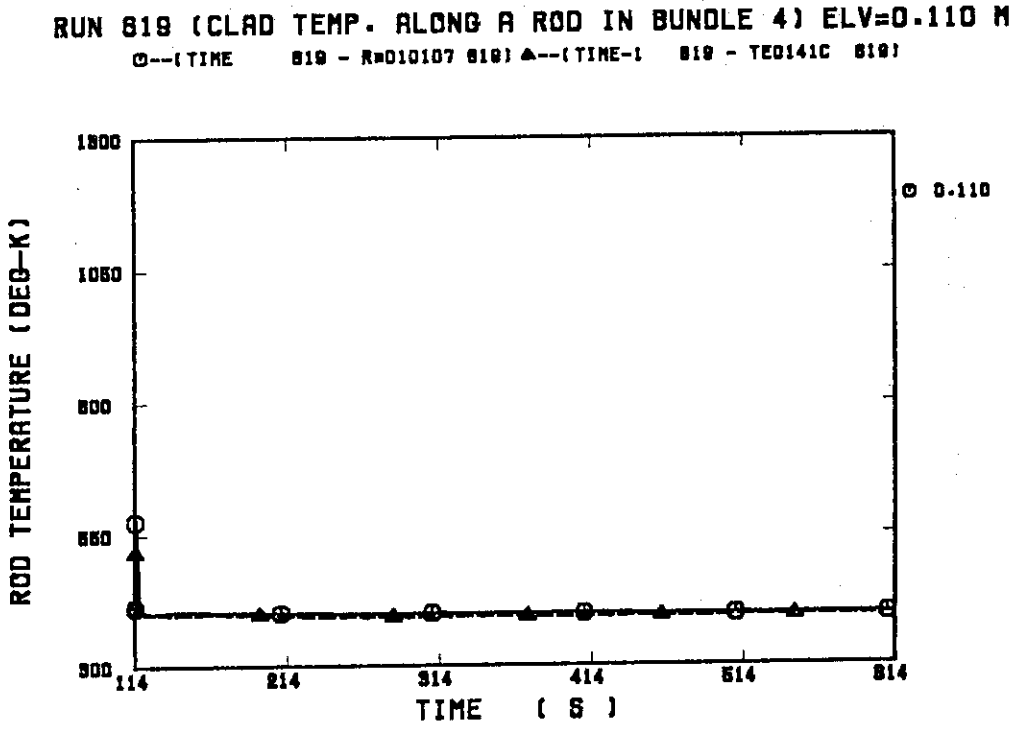

Fig. B.6.5 Clad temperature at elevation of 0.11 m along an average power rod

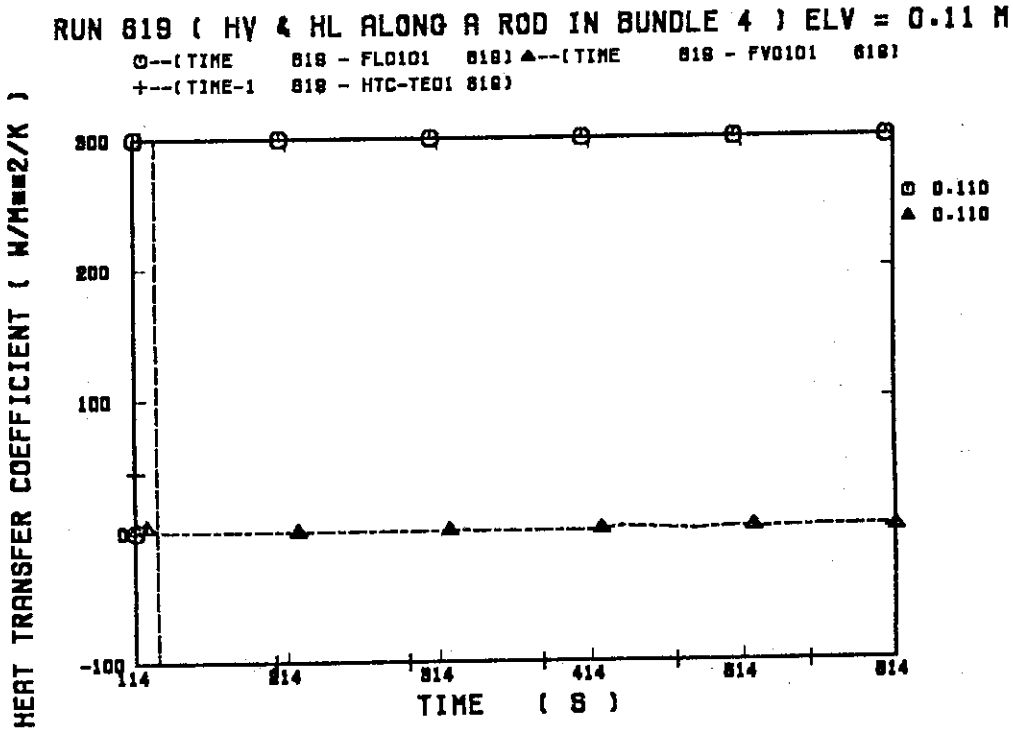

Fig. B.6.6 Heat transfer coefficient at elevation of 0.11 m along an average power rod

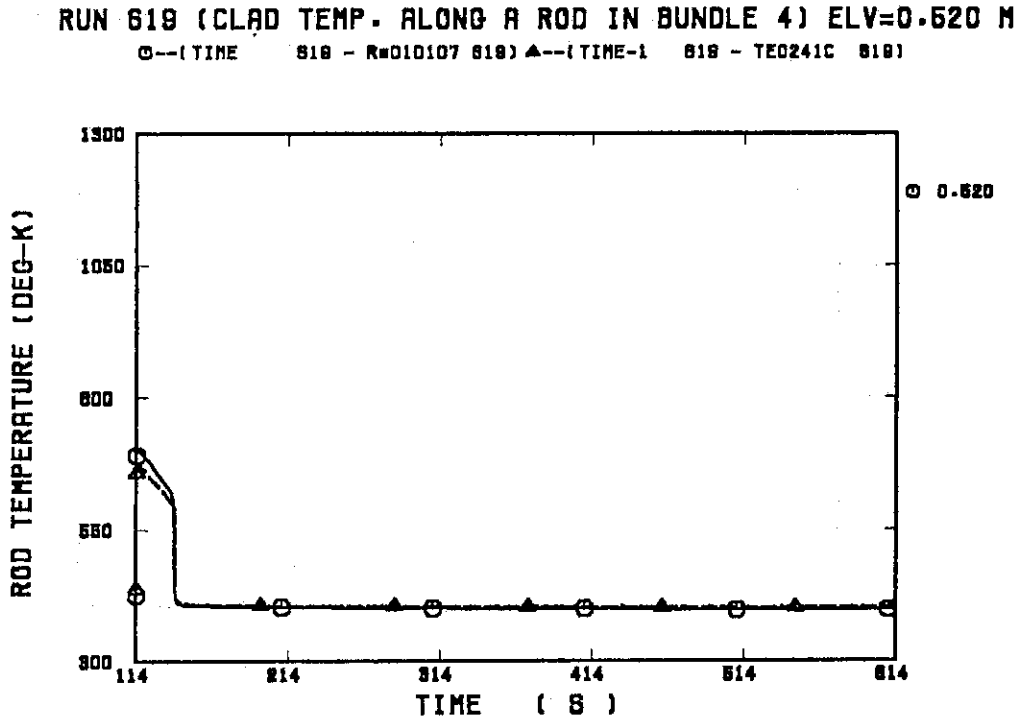

Fig. B.6.7 Clad temperature at elevation of 0.520 m along an average power rod

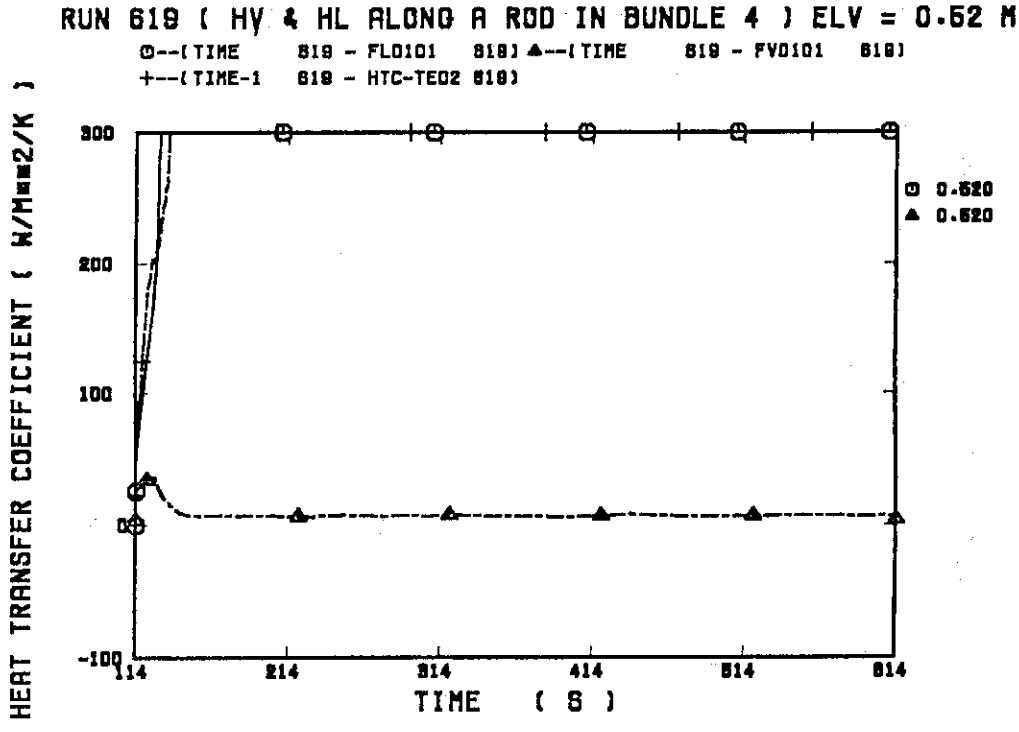

Fig. B.6.8 Heat transfer coefficient at elevation of 0.520 m along an average power rod

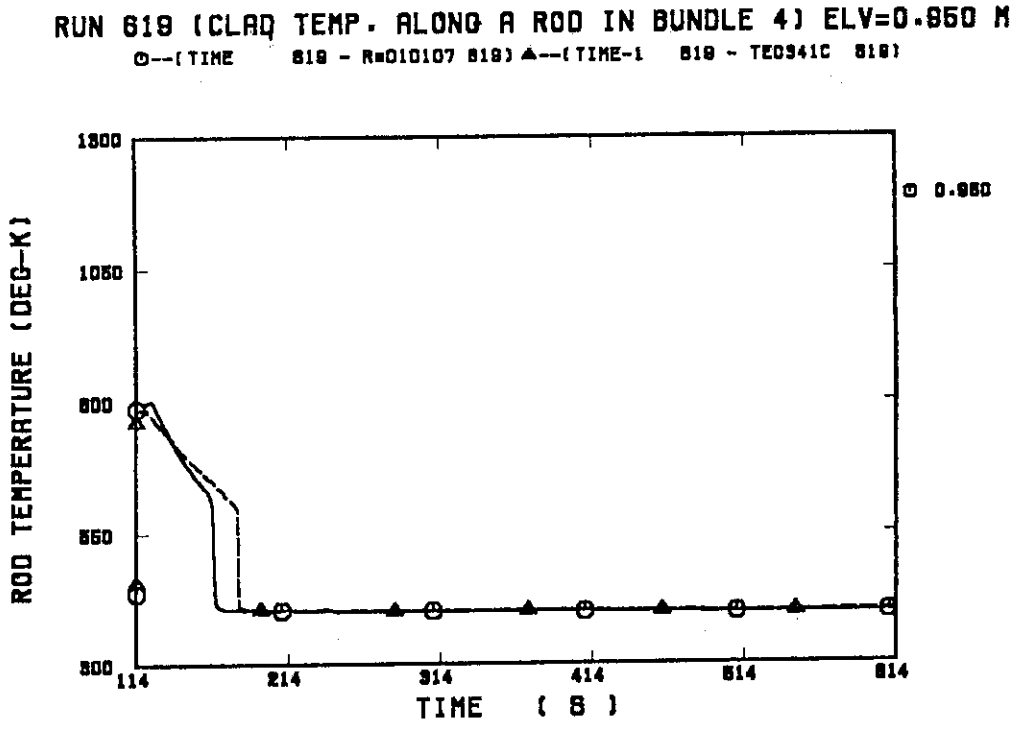

Fig. B.6.9 Clad temperature at elevation of 0.950 m along an average power rod

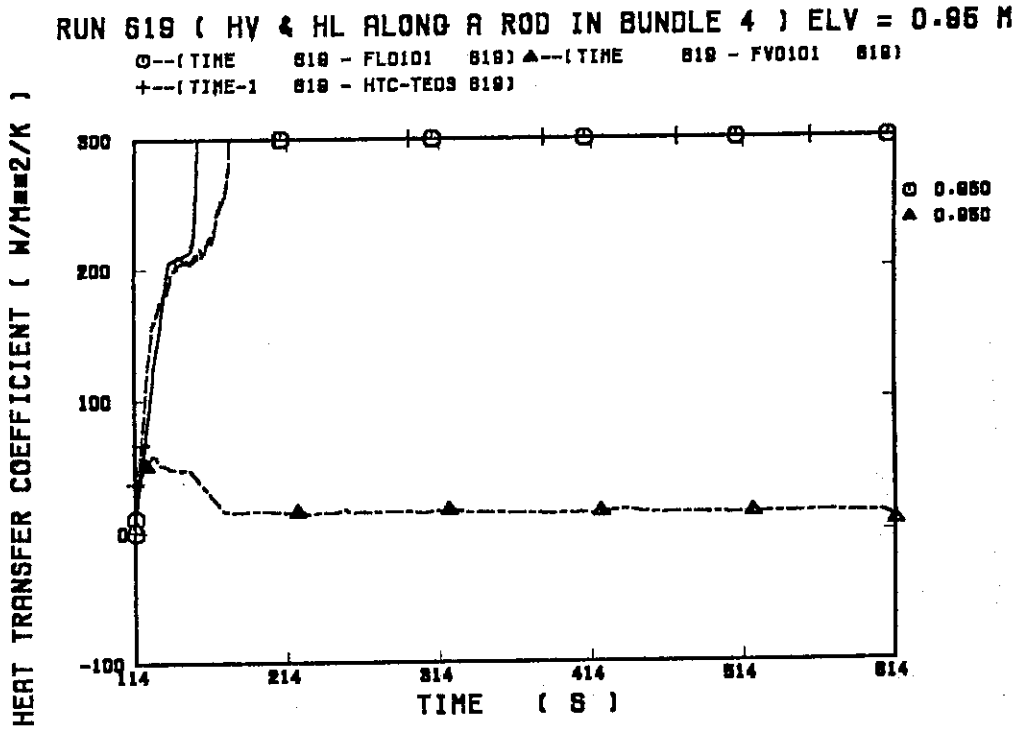

Fig. B.6.10 Héat transfer coefficient at elevation of 0.950 m along an average power rod

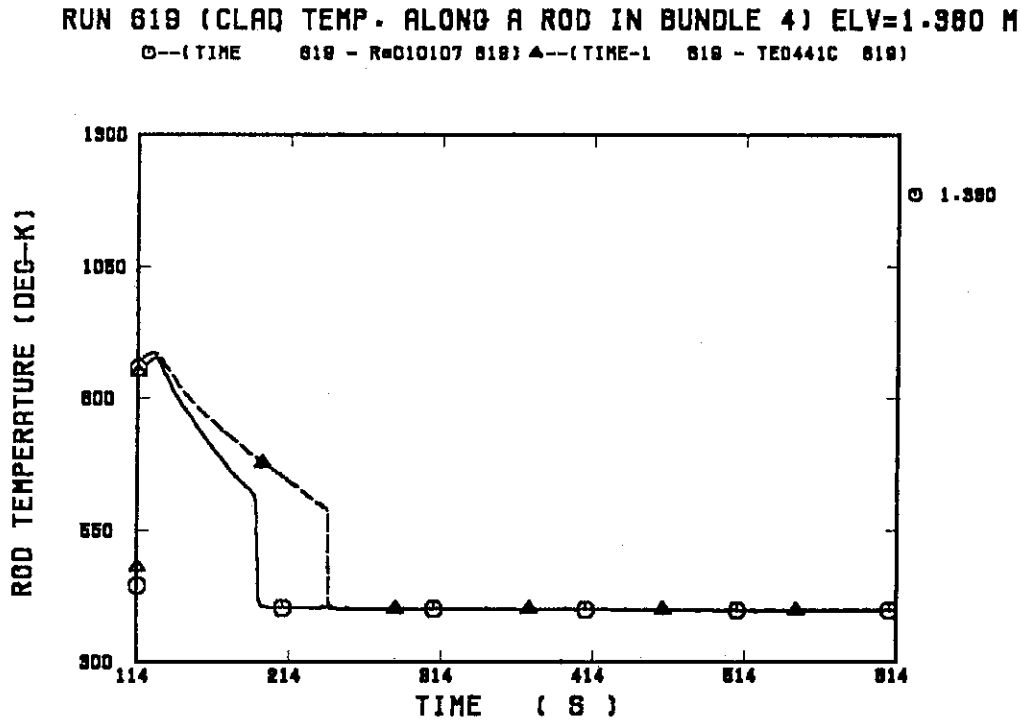

Fig. B.6.11 Clad temperature at elevation of 1.380 m along an average power rod

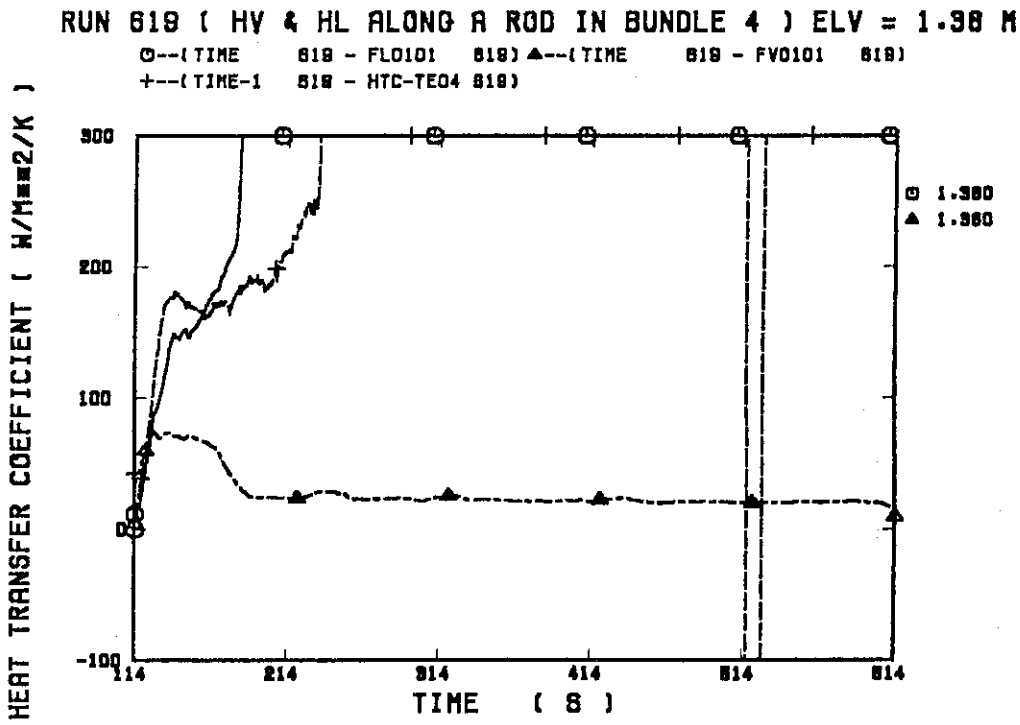

Fig. B.6.12 Heat transfer coefficient at elevation of 1.380 m along an average power rod

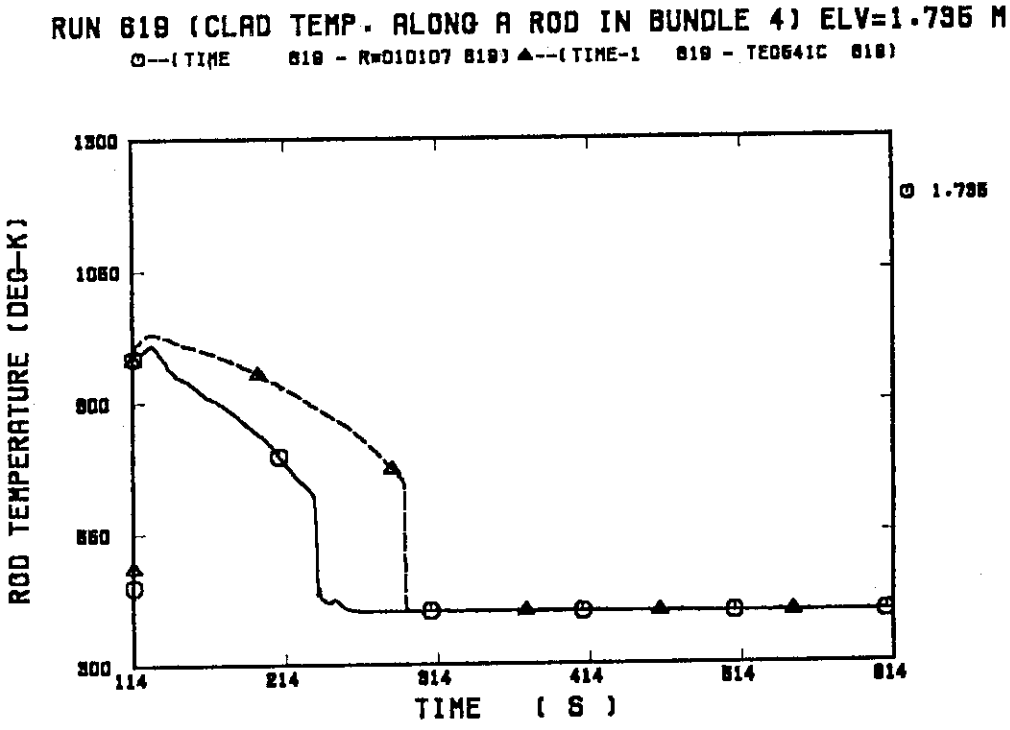

Fig. B.6.13 Clad temperature at elevation of 1.735 m along an average power rod

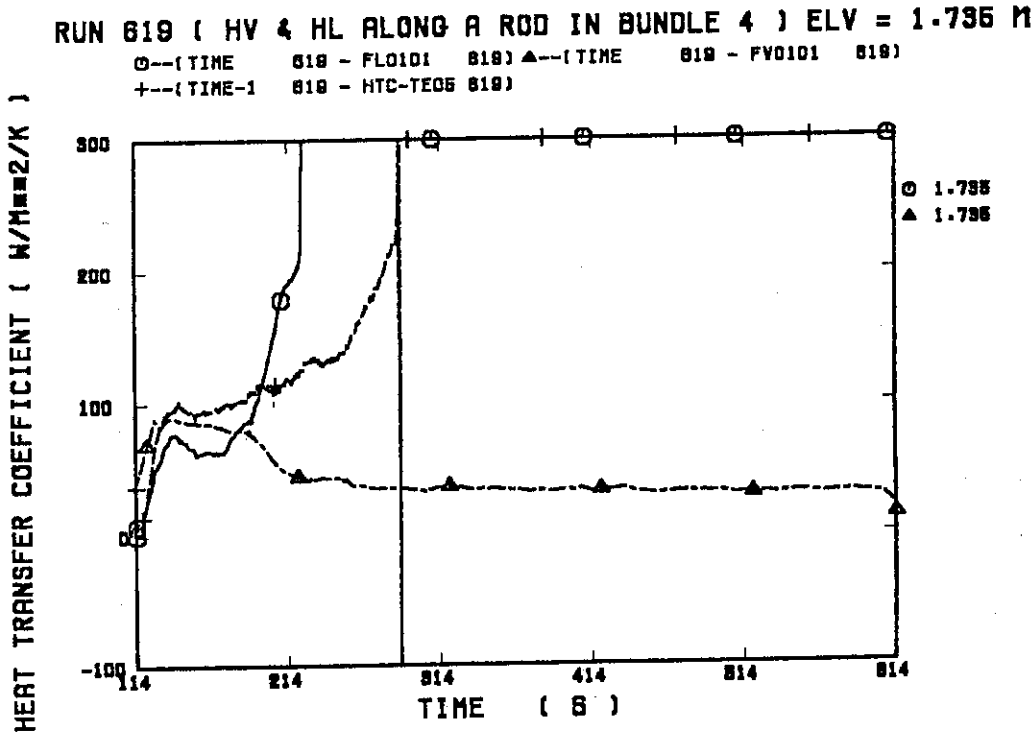

Fig. B.6.14 Heat transfer coefficient at elevation of 1.735 m along an average power rod

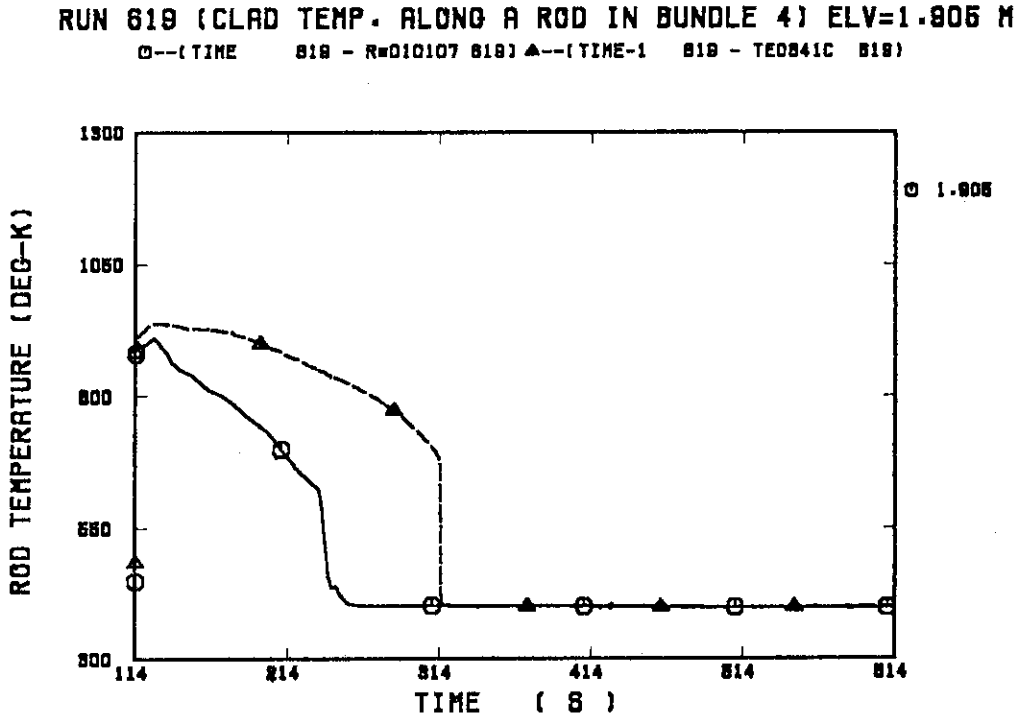

Fig. B.6.15 Clad temperature at elevation of 1.905 m along an average power rod

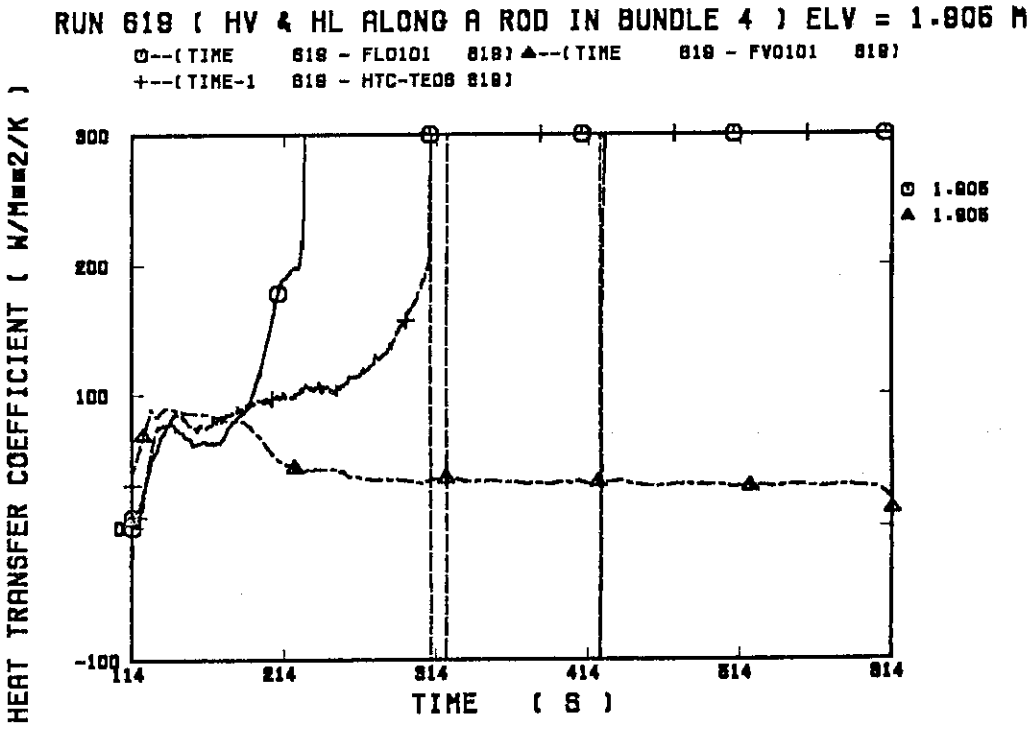

Fig. B.6.16 Heat transfer coefficient at elevation of 1.905 m along an average power rod

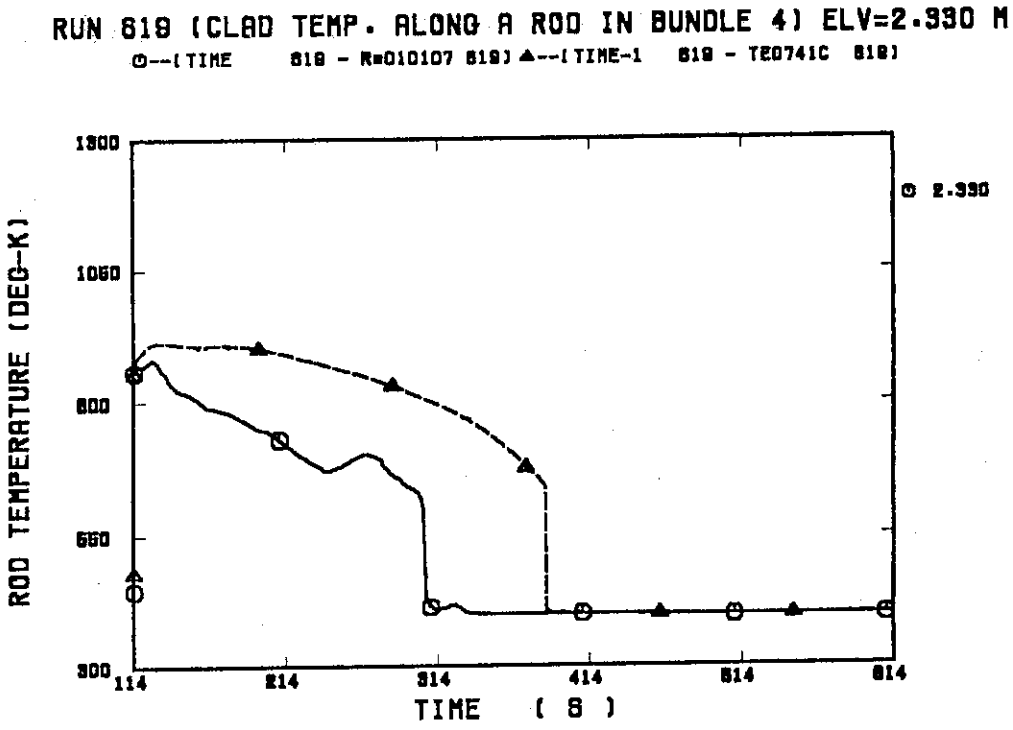

Fig. B.6.17 Clad temperature at elevation of 2.330 m along an average power rod

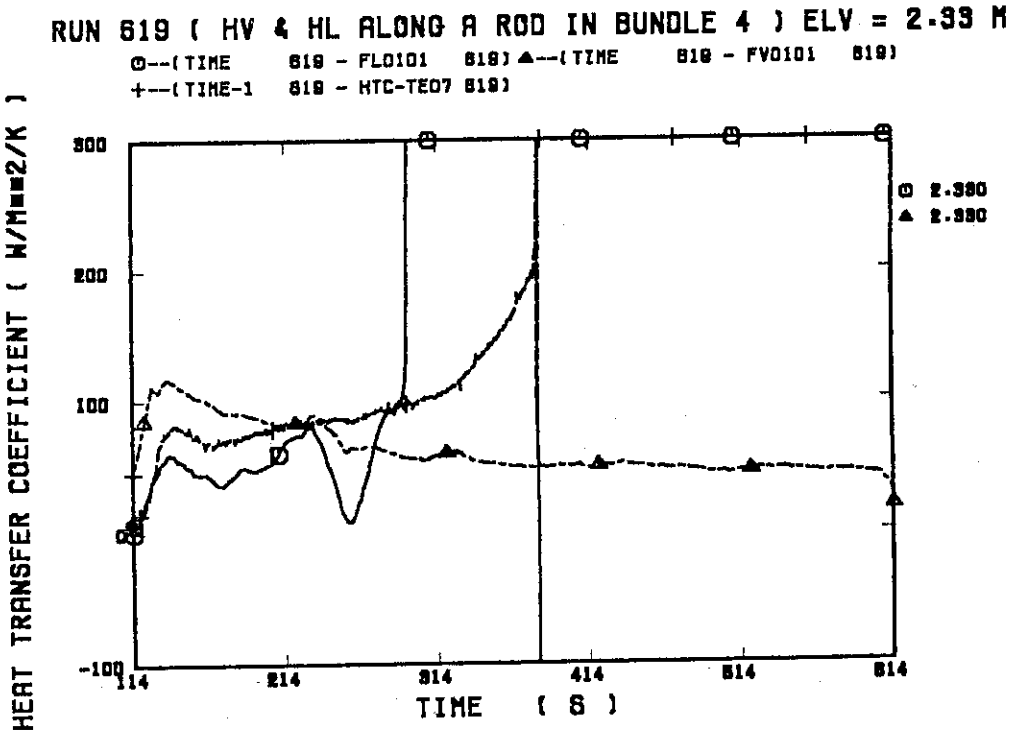

Fig. B.6.18 Heat transfer coefficient at elevation of 2.330 m along an average power rod

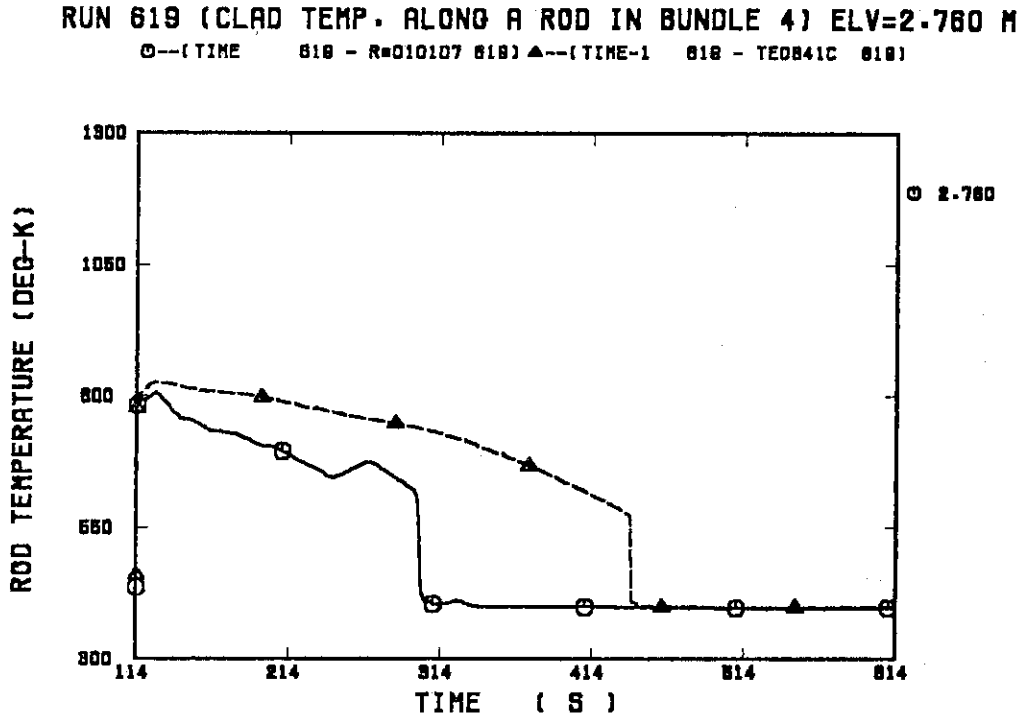

Fig. B.6.19 Clad temperature at elevation of 2.760 m along an average power rod

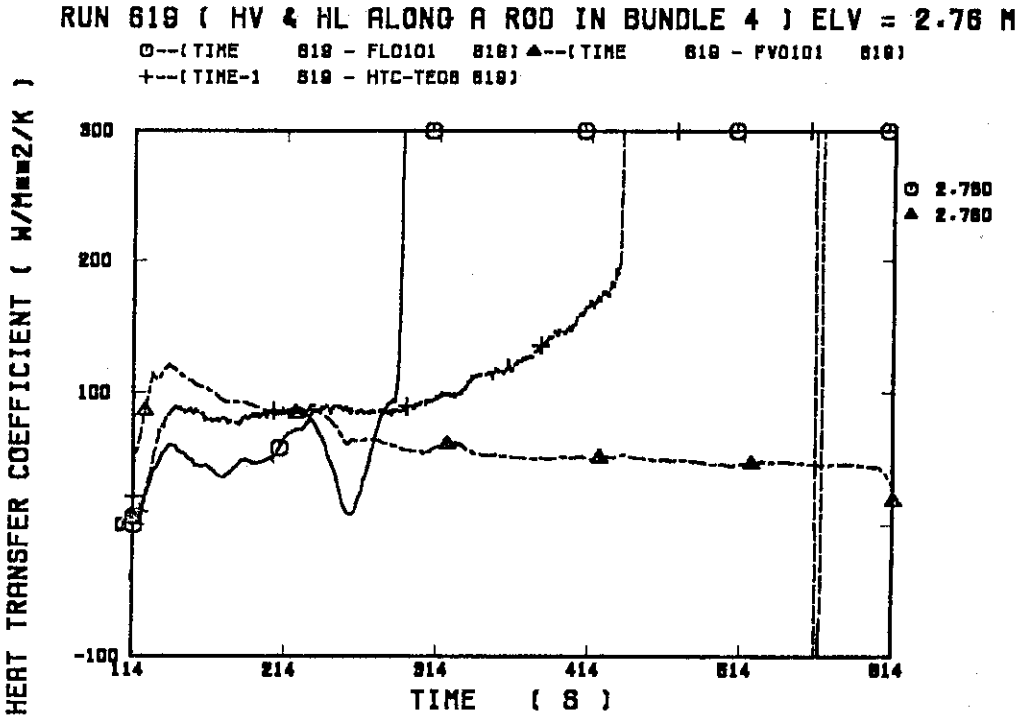

Fig. B.6.20 Heat transfer coefficient at elevation of 2.760 m along an average power rod

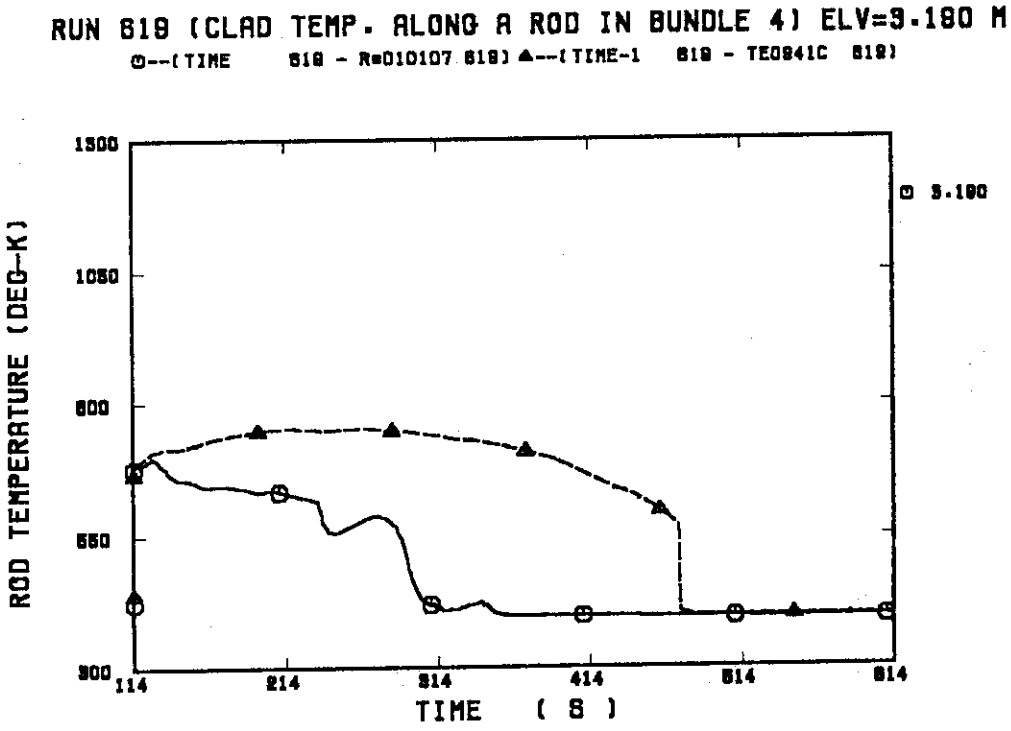

Fig. B.6.21 Clad temperature at elevation of 3.190 m along an average power rod

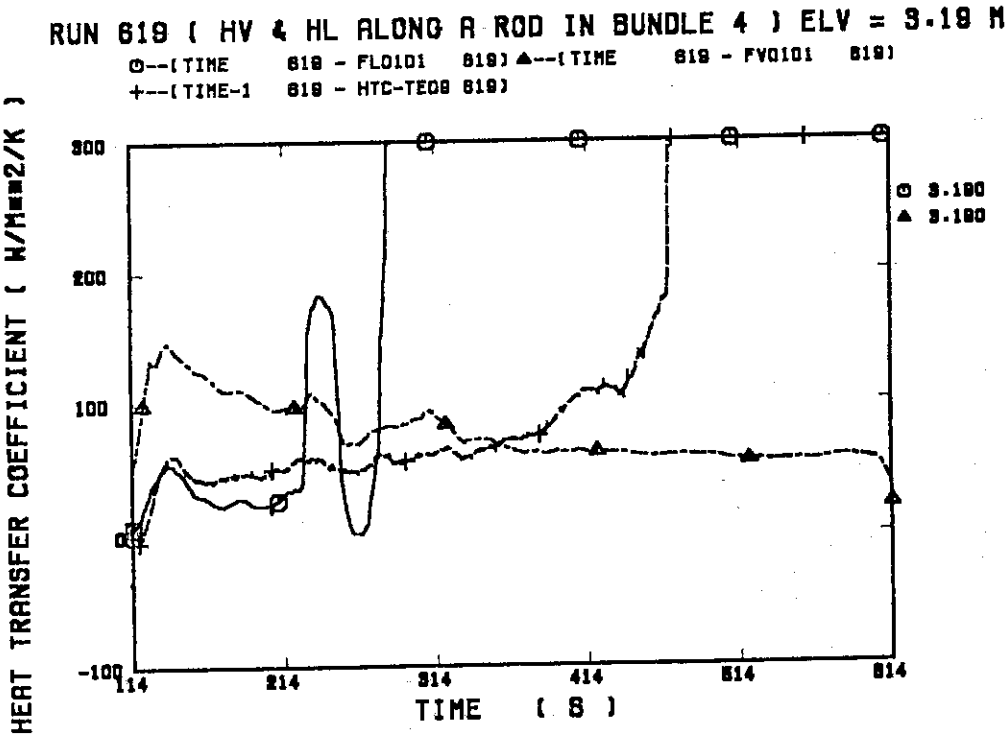

Fig. B.6.22 Heat transfer coefficient at elevation of 3.190 m along an average power rod

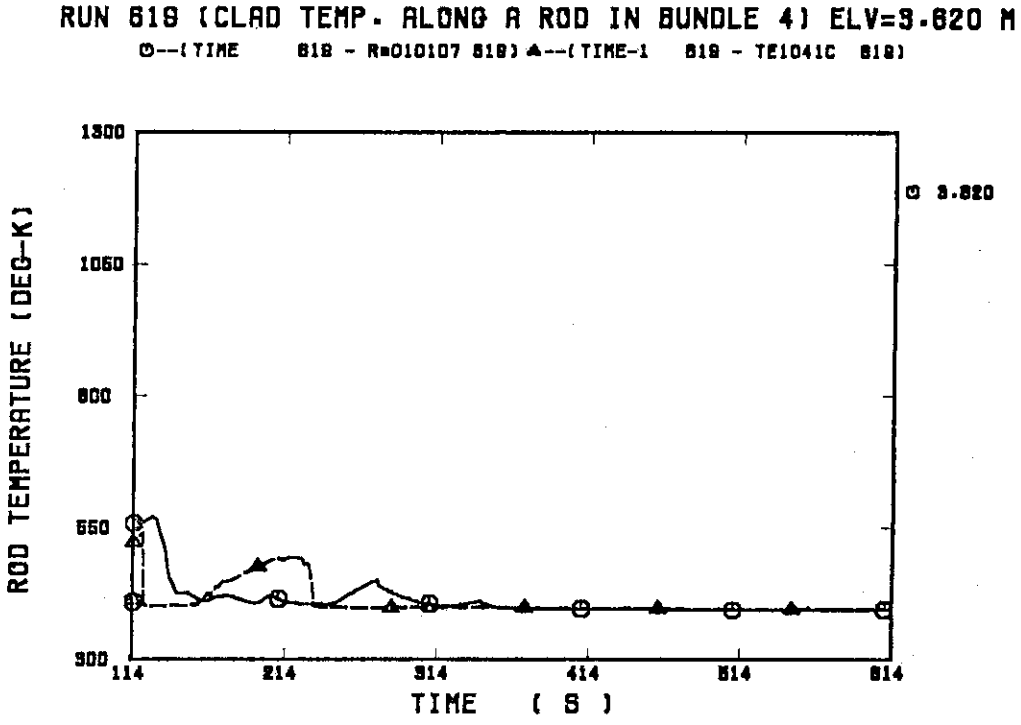

Fig. B.6.23 Clad temperature at elevation of 3.620 m along an average power rod

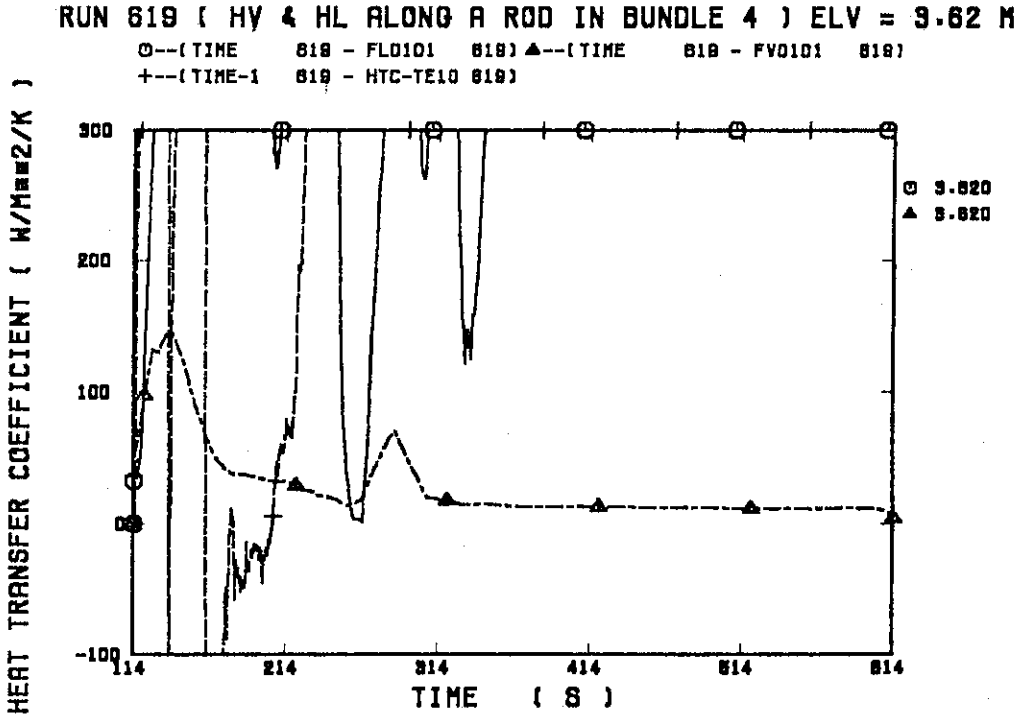

Fig. B.6.24 Heat transfer coefficient at elevation of 3.620 m along an average power rod

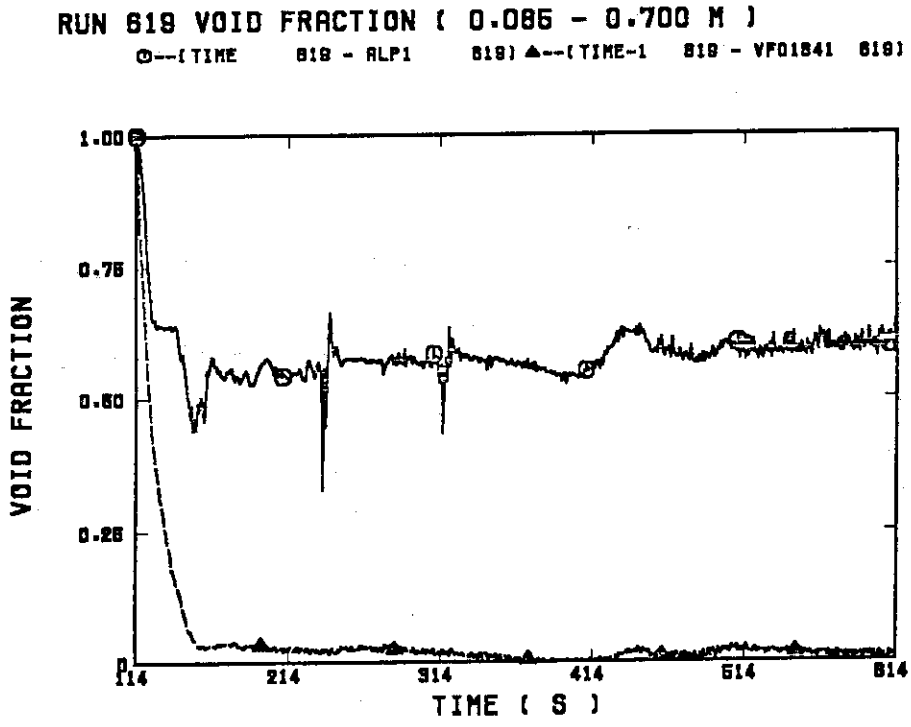

Fig. B.6.25 Average void fraction between 0.085 and 0.700 m

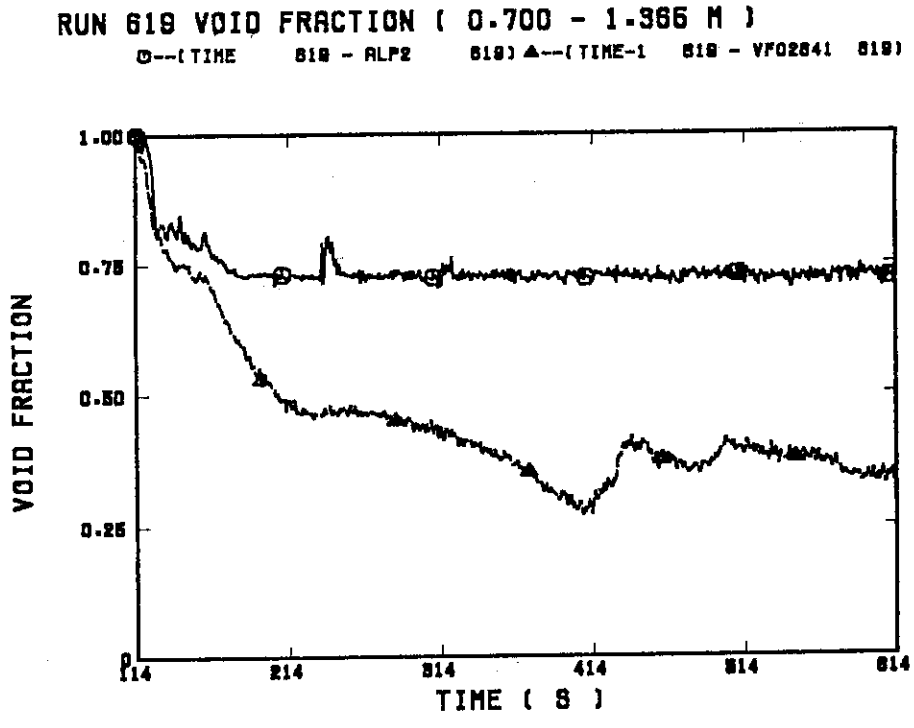

Fig. B.6.26 Average void fraction between 0.700 and 1.365 m

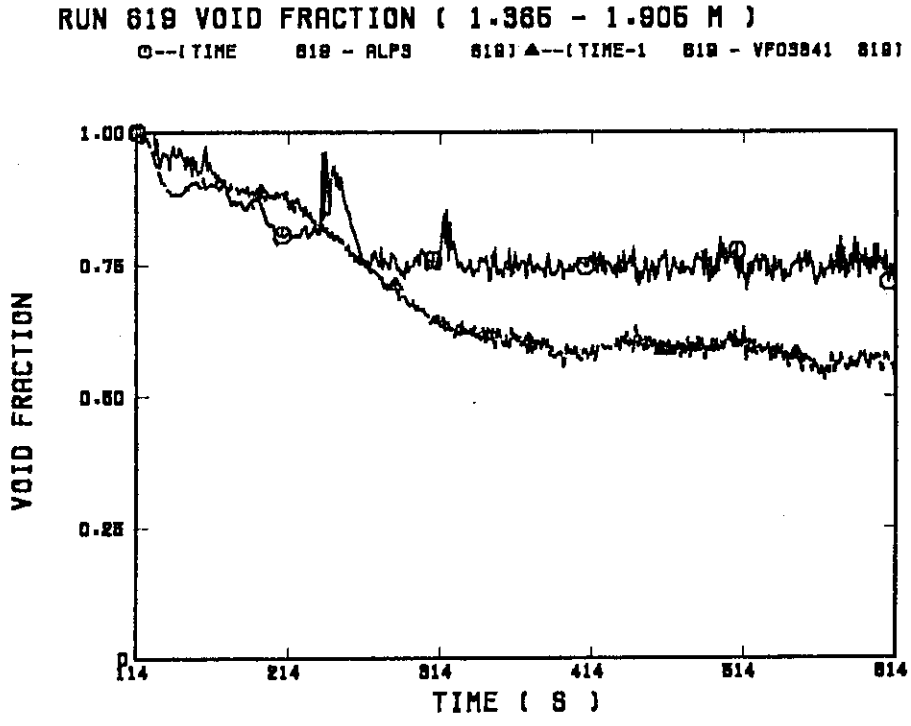

Fig. B.6.27 Average void fraction between 1.365 and 1.905 m

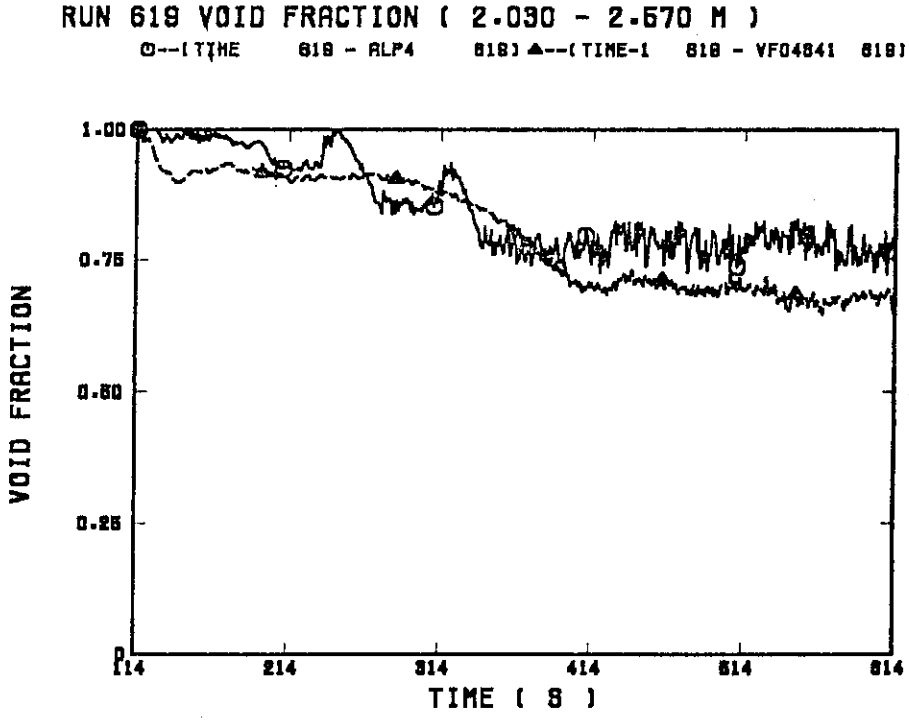

Fig. B.6.28 Average void fraction between 2.030 and 2.570 m

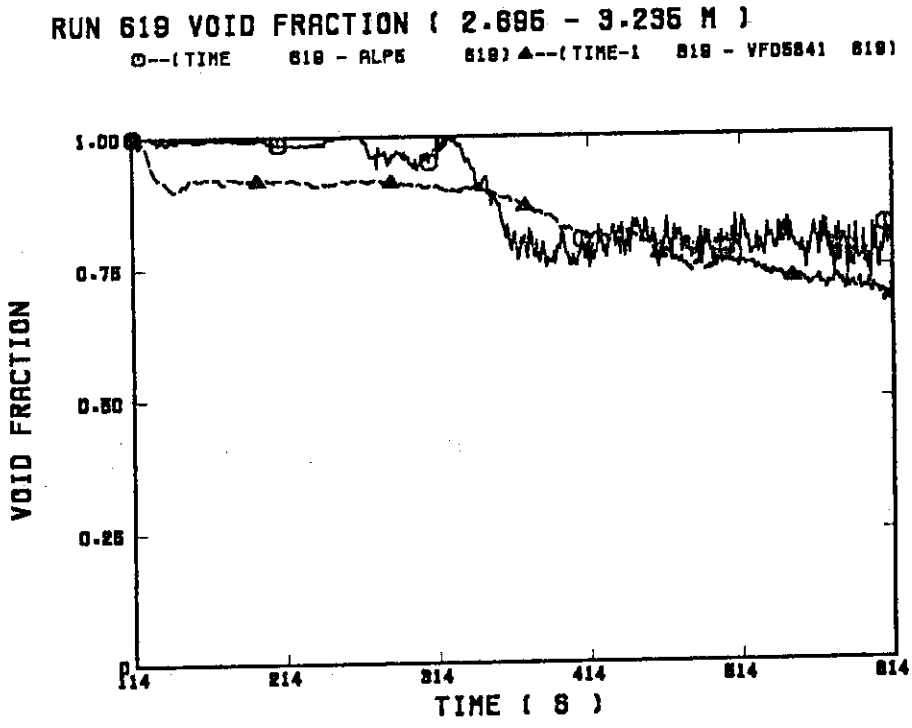

Fig. B.6.29 Average void fraction between 2.695 and 3.235 m

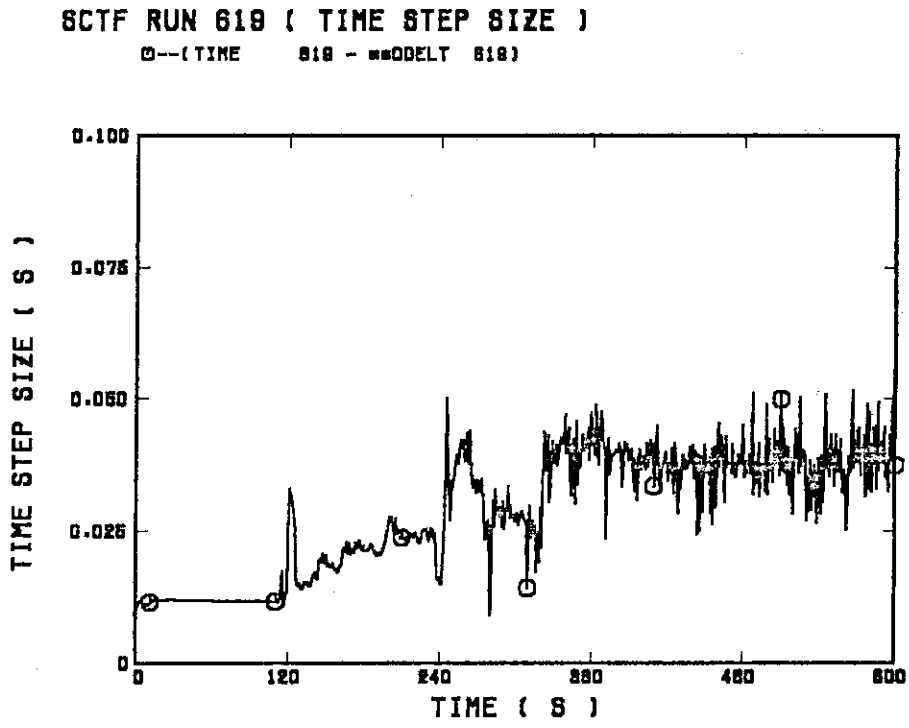

Fig. B.6.30 Time step size

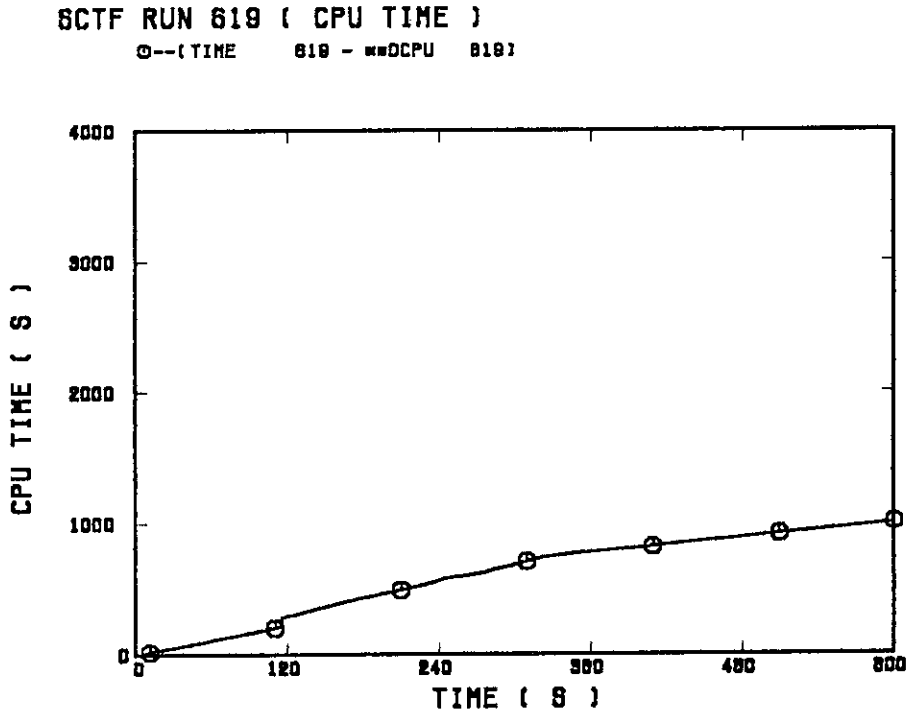

Fig. B.6.31 CPU time